2017-02-08

Dynamic Response and Residual Helmet Liner Crush Using Cadaver Heads and Standard Headforms

Stephanie Bonin
University of Miami, stephbonin@yahoo.com

UNIVERSITY OF MIAMI

DYNAMIC RESPONSE AND RESIDUAL HELMET LINER CRUSH USING CADAVER HEADS AND STANDARD HEADFORMS

By

Stephanie Julie Bonin

A DISSERTATION

Submitted to the Faculty
of the University of Miami
in partial fulfillment of the requirements for
the degree of Doctor of Philosophy

Coral Gables, Florida

May 2017

UNIVERSITY OF MIAMI

A dissertation submitted in partial fulfillment of
the requirements for the degree of
Doctor of Philosophy

DYNAMIC RESPONSE AND RESIDUAL HELMET LINER CRUSH USING CADAVER HEADS AND STANDARD HEADFORMS

Stephanie Julie Bonin

Approved:

Shihab Asfour, Ph.D. Professor of Industrial Engineering	Loren Latta, Ph.D. Director, Max Biedermann Institute for Biomechanics Mount Sinai Medical Center, Miami Beach, Florida
Moataz Eltoukhy, Ph.D. Assistant Professor of Kinesiology and Sport Sciences	Arzu Onar-Thomas, Ph.D. Associate Member St. Jude Children's Research Hospital Memphis, Tennessee
John Gardiner, Ph.D. Associate Member MEA Forensic Engineers & Scientists Laguna Hills, California	Guillermo Prado, Ph.D. Dean of the Graduate School

BONIN, STEPHANIE (Ph.D., Industrial Engineering)

Dynamic Response and Residual Helmet Liner Crush Using Cadaver Heads and Standard Headforms (May 2017)

Abstract of a dissertation at the University of Miami.

Dissertation supervised by Professor Shihab Asfour.
No. of pages in text. (239)

Biomechanical headforms are used for helmet certification testing and reconstructing helmeted head impacts; however, their biofidelity and direct applicability to human head and helmet responses remain unclear. In addition, proper helmet fit is important for optimizing head protection during an impact, yet many motorcyclists wear helmets that do not properly fit their heads. In the first phase of this research, the head dynamics and helmet foam liner deformations generated by cadaver heads and three headforms were compared during motorcycle helmet impacts. In the second phase of this research, the effect of a mismatch in headform and helmet size on the headform response and helmet residual foam liner deformation was examined. In Experiment 1, four cadaver heads and three headforms (50^{th} percentile Hybrid III, International Standards Organization (ISO), and Department of Transportation (DOT)) wearing a shorty-style motorcycle helmet were dropped onto the forehead region against a flat anvil using initial kinetic energies of 75, 150, and 195 J (impact speeds between 5.4 and 9.3 m/s). Computed tomography (CT) scans were used to quantify the maximum residual crush depth and residual crush volume of the helmet foam liners. General linear models were used to quantify the effect of head type and impact energy on peak linear head acceleration, head injury criterion (HIC), impact force, maximum residual liner crush

depth, and residual liner crush volume. Linear regression models were then used to separately quantify the relationship between the response variables (peak acceleration and impact speed) and the predictor variables (maximum crush depth and crush volume). The cadaver heads generated larger peak accelerations than all three headforms, larger HICs than the ISO, larger forces than the Hybrid III and ISO, larger maximum crush depth than the ISO, and larger crush volumes than the DOT. These significant differences between the cadaver heads and headforms showed that none of the headforms replicated all of the biomechanics of the cadaver heads, and that these differences need to be considered when attempting to estimate an impact exposure using a helmet's residual crush depth or volume. In Experiment 2, four sizes of a shorty-style helmet were tested on four sizes of ISO headforms during forehead impacts against a flat anvil using initial kinetic energies between 10 and 275 J (impact speed between 2.0 and 10.5 m/s). CT scans were again used to quantify maximum residual crush depth and residual crush volume of the helmet foam liners. Separate linear regression models were used to quantify how the response variables (peak acceleration, HIC, and impact speed) were related to the predictor variables (maximum crush depth, crush volume, and the difference in circumference between the helmet and headform). The results indicated that increasingly oversized helmets reduced peak headform acceleration and HIC for a given impact speed. Peak headform acceleration, HIC, and impact speed can be estimated from a helmet's residual crush for maximum residual crush depths less than 7.9 mm (31-34% of original foam thickness) and residual crush volumes less than 40 cm^3. Above these levels of residual crush, large variations in headform kinematics are present, possibly related to densification of the foam liner during the impact. Overall, this research has shown that

helmet impact kinematics can be estimated from residual helmet liner deformation under some conditions, although differences between the human head and biomechanical surrogates for the human head need to be considered when making these estimates.

To my children:

May you learn the value of tenacity

Acknowledgments

I would like to thank a number of individuals and organization for their support during my thesis research. Thank you to my academic advisor and committee member, Dr. Shihab Asfour, for your support and encouragement during my doctoral journey and for allowing me to continue my research in a non-traditional manner. Thank you to my committee members Drs. John Gardiner, Arzu Onar-Thomas, Moataz Eltoukhy, and Loren Latta, for your support and feedback during the research and thesis writing phases of my Ph.D. program. Thank you to the Injury Biomechanics Laboratory at Duke University including Drs. Dale Bass, Roger Nightingale, Jason Luck, and Mr. Jason Kait, for providing tissue specimens, resources, use of your facility, and testing support.

My doctoral research experience would not have been possible without the support of MEA Forensic Engineers & Scientists. I have been gifted the opportunity to learn how to become a researcher and critical thinker while developing my career. I am fortunate to have a supportive supervisor, Dr. John Gardiner, who has provided the resources I've needed to accomplish my goals. Thank you Dr. Gunter Siegmund for your unwavering mentorship, setting high standards, and the valuable education I've gained during this process. Thank you Mr. Jeff Nickel and Mr. Mircea Oala-Florescu for your endless technical and testing support and well-designed, handcrafted equipment. Thank you also to all my co-workers at MEA for your support, encouragement, and patience over the years.

Finally, thank you to my family. Without your support, completing this Ph.D. program would not have been possible.

Table of Contents

Page

List of Figures

List of Tables

Table Page

CHAPTER 1: Introduction

Head protection in motorcycle accidents

Helmets reduce the risk of head injury by 47 to 69 percent and the risk of death by 42 to 58 percent during motorcycle accidents (Hurt et al., 1981, Rowlands et al., 1996, Liu et al., 2008). Unhelmeted motorcyclists cost more to treat at the hospital, spend a longer time in rehabilitation, have higher disability rates, have reduced lifetime earning potential and quality of life, and are more likely to require some form of public assistance to pay for medical bills and rehabilitation (Murdock and Waxman, 1991, Lawrence et al., 2002). Average hospital costs for unhelmeted motorcyclists are approximately 30 to 200 percent higher than for helmeted motorcyclists (Murdock and Waxman, 1991, Nelson et al., 1992, Offner et al., 1992) and motorcyclists with a head injury cost 79 to 178 percent more than those without a head injury (Orsay et al., 1995, Max et al., 1998). In 1991, prior to enacting its helmet law, California's state medical insurance program paid $40 million for the treatment of motorcycle-related head injuries; however, that figure dropped to $24 million after enactment of a universal helmet law (National Highway Traffic Safety Administration, 1996).

Motorcycles account for only 3 percent of vehicle registrations and 0.7 percent of all vehicle miles traveled in the United States, but motorcycle collisions account for 14 percent of traffic deaths (U.S. Department of Transportation, 2013). The National Highway Traffic Safety Administration (NHTSA) estimates that helmets saved the lives of 1,630 motorcyclists in 2013; however, if all motorcyclists had worn helmets, an additional 715 lives could have been saved (U.S. Department of Transportation, 2013).

Parts of a helmet

An approved motorcycle helmet consists of three primary safety components: a stiff outer shell, an energy absorbing liner and a retention system (Figure 1). The outer shell distributes the impact load across the helmet, resists penetration of a foreign object and dissipates energy by cracking (Mills et al., 2009, Pinnoji et al., 2010). The energy absorbing liner attenuates energy by compressing and/or crushing and increases the distance and time over which the impact occurs, thereby reducing head acceleration and the risk of head and brain injuries (Beusenberg and Happee, 1993). Energy-absorbing liners are typically made of expanded polystyrene (EPS) foam and during an impact, the foam compresses and then partially rebounds (Kroeker et al., 2014). The permanent deformation to the foam is called the residual crush and can be quantified using parameters such as maximum crush depth or crush volume. There is an additional soft, low-density foam layer, called the comfort liner, between the energy absorbing liner and the head. The comfort liner does not absorb any significant energy or play a protective role; instead it is used to more comfortably fit the helmet to heads of different sizes and shapes (Pinnoji et al., 2010). The retention system secures the helmet on the head and minimizes helmet motion before, during and after an impact (Beusenberg and Happee, 1993). The past fifteen years have seen significant advances in motorcycle helmet materials and design and the newer helmets afford a greater degree of protection against potentially fatal head injuries (U.S. Department of Transportation, 2004, 2010).

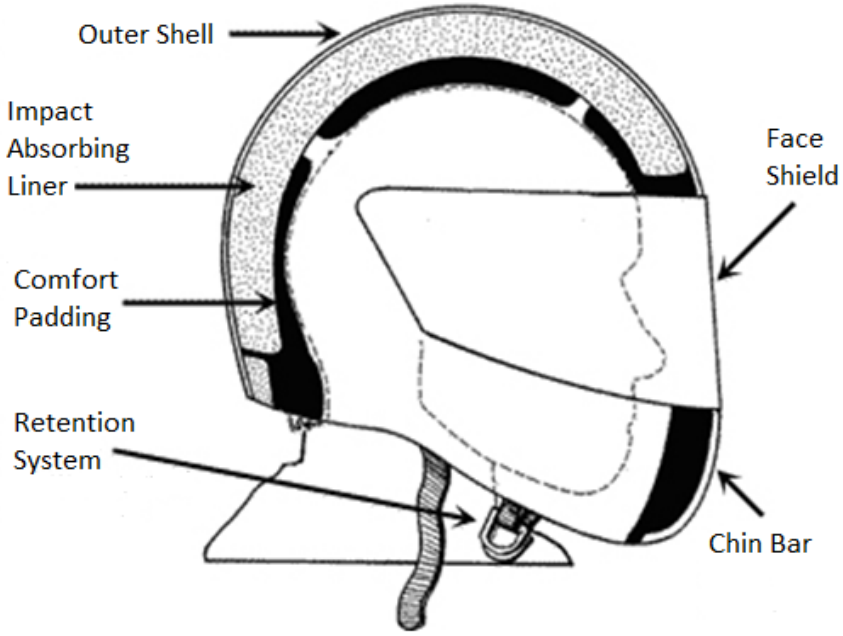

Figure 1: The components of a full-face motorcycle helmet

Helmet testing for certification

Laws that require motorcyclists to wear a helmet exist in only some US states. In states where motorcyclists are required to wear a helmet, it must meet the minimum requirements of certification testing standards established by the US Department of Transportation (DOT). Other countries and independent organizations publish similar motorcycle helmet certification requirements (British Standards Institute, 1985, United Nations Economic Commission for Europe, 2002, Australian/New Zealand Standard, 2006, Snell Memorial Foundation, 2015). Most motorcycle helmet standards prescribe minimum requirements for the amount of the head that must be covered by the helmet, impact attenuation performance, resistance to penetration, retention system strength, and labeling requirements. This thesis is focused on factors related to the impact attenuation performance of motorcycle helmets.

To test a helmet's impact attenuation performance, the helmet is placed on an instrumented metallic headform (Figure 2a, b) and dropped from a prescribed height onto a flat or shaped anvil (Figure 3). Headform acceleration is measured and recorded during the impact and then compared to the pass/fail criteria of the performance standard (Smith et al., 1994, Thom et al., 1996, Consumer Product Safety Commission, 1998, U.S. Department of Transportation, 2006, Snell Memorial Foundation, 2015). Metallic headforms serve as surrogates for the human head for impact attenuation testing (Figure 2a, b). Despite their widespread usage, these metallic headforms lack the biofidelity testing and validation undergone by other headforms, such as the Hybrid III head (part of the Hybrid III automotive crash test dummy, Figure 2c), whose calvarium geometry, overall inertial properties, and impact response have been validated against human heads (Hodgson and Thomas, 1971, Hubbard and McLeod, 1974, Prasad and Mertz, 1985, Becker, 1998). One of the goals of this thesis is to investigate if a human head crushes the foam liner differently than a metallic headform during an impact.

Figure 2: Examples of common head forms. (a) The metallic headform defined by the US Department of Transportation standard (DOT headform); (b) The metallic headform defined International Organization for Standardization (ISO headform); (c) The vinyl-covered metallic headform used for the Hybrid III anthropomorphic test device or crash test dummy. The latter headform is commonly used during automotive crash testing.

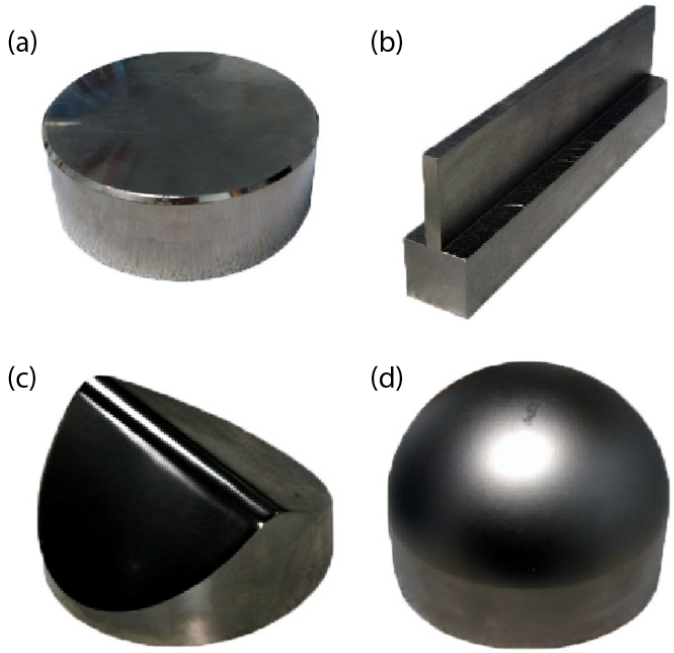

Figure 3: Four anvils used in impact attenuation testing: (a) flat anvil, (b) edge anvil, (c) curbstone anvil and (d) hemispherical anvil

Headform comparisons through helmet testing

Drop tests have also been used to compare the dynamic response between different headforms and between headforms and cadaver heads. Loyd et al. (2014) compared the impact response of a Hybrid III 50th percentile male headform to adult male cadaver heads in unhelmeted free-fall drops from 15 and 30 cm at five impact locations: vertex, occiput, forehead, and right and left parietal regions. They found that the peak linear accelerations and head injury criterion (HIC) of the Hybrid III headform and cadaver heads were not significantly different. In contrast, drop tests using early football helmets showed that the responses of other metallic headforms and cadaver heads were significantly different (Hodgson, 1975). This difference led to the development of the compliant, glycerin-filled headform used by the National Operating Committee on

Standards for Athletic Equipment (NOCSAE) for testing football helmets (National Operating Committee on Standards for Athletic Equipment, 2013). To date, no similar testing has compared the impact responses of cadaver heads to the metallic headforms currently prescribed by the various standards for testing motorcycle helmet impact performance.

Motorcycle accident reconstruction

Helmets and helmet standards are designed and developed to prevent head injuries in the field, and therefore studying the field performance of motorcycle helmets is an important component for evaluating motorcycle helmet safety. The field performance of helmets is also an important factor in civil litigation involving head injuries caused by motorcycle accidents. Accident investigators can use the laws of physics and other engineering principles to interpret physical evidence from a crash and draw conclusions regarding specific crash factors such as vehicle speed, crash severity and the performance of safety equipment. Considerable work has gone into crashing cars and developing models to estimate the severity of a car crash from the permanent or residual damage to the vehicles. Comparatively little work has gone into estimating the severity of a helmet impact based on the residual damage to the helmet.

Hugh Hurt launched the field of motorcycle accident research in the mid-1970s (Hurt et al., 1981). Hurt and colleagues studied many different aspects of motorcycle crashes and were responsible for one of the first comprehensive studies showing that the use of motorcycle helmets meeting official specifications drastically reduced head injuries (Hurt et al., 1981). Specific to helmet performance, Hurt et al. observed that the location and extent of damage to a helmet, including crush or cracking to the helmet liner

and cracking and scratches to the external shell, could provide information about how a rider's helmet interacted with the surroundings during the crash. They also observed that the amount of residual liner crush could be used to estimate the head acceleration during a head impact, although their work in formulating this relationship was limited.

Helmet testing to replicate damage and estimate impact severity

Researchers have attempted to reproduce the residual liner crush observed in an accident-involved helmet by iteratively impacting new, exemplar helmets with a single impact until the damage is replicated. The exemplar helmet is placed on an instrumented metallic headform and dropped from varying heights to generate damage to the energy absorbing liner (Figure 4). The motorcyclist's head acceleration and impact speed are then estimated from the exemplar test that best replicates the accident-involved helmet's damage (Hurt and Ouellet, 1976, Hope and Chinn, 1990, Smith et al., 1994, Wobrock et al., 2003, McIntosh and Patton, 2012).

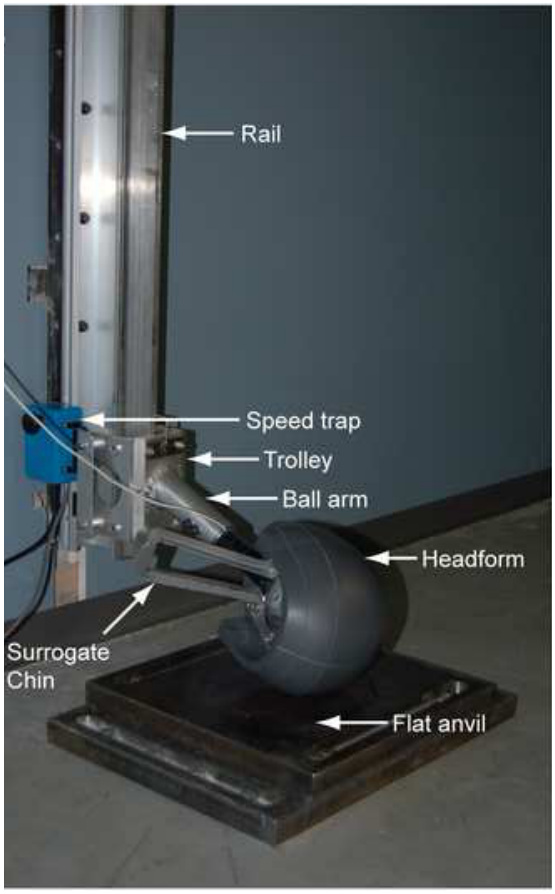

Figure 4: Monorail system with a DOT headform attached to a ball arm on a flat anvil.

Schuller et al. (1993) drop-tested five types of motorcycle helmets with polystyrene foam liners and shells made of either polycarbonate, polyamide, acrylonitrile-butadiene-styrene, or glass-reinforced plastic. The helmets were tested using an ISO headform at 4.4 to 10 m/s at four impact sites (front, lateral, parietal, and occiput) onto five anvil types (flat, hemispherical, edge, curbstone, and semi-cylindrical). Despite variability in impact location and shell material, Schuller et al. (1993) found that head acceleration could be reliably estimated by replicating residual liner deformation provided that the residual deformation was less than 27% of the initial liner thickness.

Additional residual deformation was associated with highly variable headform accelerations.

McIntosh and Patton (2012) found that residual liner deformation correlated with both impact speed and resultant headform linear acceleration for bicycle helmets, but not for motorcycle helmets. This poor correlation for motorcycle helmets may have been caused by various factors, including pooling results across different helmet models with varying material properties, measuring residual crush at only four points around the impact area and thus potentially missing the maximum crush, and/or comparing the accident-involved helmets to only one new helmet and therefore potentially not capturing manufacturing variability in the undeformed liner thickness.

Hope and Chim (1990) determined the impact severity of accident-involved motorcycle helmets by reproducing liner crush and shell cracking through iteratively drop-testing new, equivalent helmets attached to an instrumented headform, at varying impact speeds until the damage was reproduced. The impact speed believed to recreate the damage was reported; however, liner deformation was not quantified – only a visual inspection of the shell and liner confirmed that the deformation pattern had been matched.

Smith et al. (1994) replicated damage to 10 accident-involved bicycle helmets by attaching new exemplar helmets to properly sized instrumented ISO headforms and dropping the helmet/headform unit from heights that were predicted to impart the same impact energy experienced by the accident-damaged helmet. Direct measurements of liner crush were made and compared to the case helmets. Impact speeds ranged from 2.2 to 5.4 m/s, maximum liner crush ranged from 0.8 to 6.6 mm and peak headform

accelerations ranged from 38 to 179 g. The relationship between impact severity and liner crush, however, was not explored.

The limitations of these investigations support the need for a comprehensive study to examine the relationship between head/headform kinematics and residual helmet liner crush. Based on the work of Schuller et al. (1993), this relationship may be limited to a range of impact severities smaller than the range a helmet can experience in the field. The relationship between head/headform acceleration and residual crush may not be accurate at low impact severities where there is little residual crush or at high impact severities where the foam bottoms out, i.e., densifies, and head acceleration increases rapidly with small increases in impact speed (DeMarco et al., 2010, Kroeker et al., 2016). Both the relationship between headform kinematics and residual liner crush, and the range over which this relationship holds, will be investigated in this thesis.

Helmet fit

Gilchrist and Mills (1994) observed that the extent of liner crush is affected by how well the metallic headform fits inside the helmet. They found considerable crushing of the inside surface of the liner by headforms due to the lack of an exact fit between the liner and the headform surface. They stated that in reality, the deformable head of a motorcyclist makes a good fit to the inside of the foam liner and this interior crushing mechanism rarely occurs.

Damage replication of accident-involved helmets is generally conducted with a correctly sized headform (Smith et al., 1994, Wobrock et al., 2003); however, motorcyclists often wear helmets that do not fit properly. Improper helmet fit makes the helmet more prone to move out of position or roll off during a crash, potentially leaving

portions of the head unprotected and more vulnerable to injury (Hurt et al., 1998, Rivara et al., 1999, Thai et al., 2015a, 2015b). A recent study of motorcycle helmet fit found that 40.7 percent of motorcycle riders wore helmets that were too large and 21.8 percent wore helmets that were too small (Thai et al., 2014). These researchers considered a helmet to be correctly sized if the wearer's head circumference fell within the range specified on the helmet's label. They also found that the lengths of their riders' heads were between 2.9 cm shorter and 2.1 cm longer than the ISO headform appropriate for testing the helmets, and the widths of their heads were between 2.0 cm narrower and 2.2 cm wider than the ISO headform appropriate for testing the helmets. These findings suggest that motorcycle riders are wearing helmets outside the manufacturer's specified range to accommodate differences in their head length and width.

Helmets are not generally tested with mismatched headforms and therefore the effect of this mismatch on impact performance is not well understood. Using finite element analysis, Chang et al. (2001) found lower peak accelerations and HIC with increasingly smaller headforms within a fixed helmet size; however, these findings were not verified experimentally. In contrast, Rivara et al. (1999) postulated that the gap between the head and the liner of an oversized helmet may undermine the liner's ability to absorb the impact and thus increase the risk of brain injury. To date, there is no systematic study of the effect of helmet size mismatch on headform kinematics or the impact performance of motorcycle helmets. This thesis will examine if liner crush is a reliable estimate of impact severity across a range of helmet/headform size combinations.

Research goals

In order to use the residual crush to a helmet's energy absorbing liner to estimate the motorcyclist's head acceleration and head impact speed, we first need to establish if metallic headforms respond like human heads during helmeted impacts. In addition, we need to establish if a motorcycle helmet's liner, when impacted with a metallic headform, has the same amount of residual crush when impacted with a human head under equivalent conditions. And finally, we need to establish if head acceleration and impact speed can be reliably estimated from residual liner crush and over what range of impact speeds and helmet/headform size combinations this relationship holds.

To accomplish these goals, two experiments were conducted. In Experiment A, helmeted cadaver heads and headforms were tested to determine if the headforms respond to impacts like human heads. The residual crush of the energy absorbing liner was measured to determine if headforms produce the same amount of crush as a human head, and if head/headform acceleration and impact speed can be estimated from the amount of residual crush. Experiment B addressed how to estimate head acceleration and impact speed from the residual liner crush for different combinations of headform and helmet sizes. The range of impact speeds over which the relationship between headform kinematics and residual crush holds was also explored.

Hypotheses

This thesis examines four hypotheses. Experiment A addresses the first two hypotheses and Experiment B addresses the second two hypotheses.

Experiment A

Hypothesis 1: Metallic headforms experience different peak dynamics and generate different levels of residual crush than cadaver heads under helmeted impact conditions.

Hypothesis 2: (a) The amount of residual maximum crush depth and crush volume increases with impact energy levels and (b) residual liner crush can be used to estimate peak head/headform acceleration and impact speed.

Experiment B

Hypothesis 1: For a given impact speed, the peak headform acceleration and HIC will decrease as the relative helmet size increases.

Hypothesis 2: Peak acceleration, HIC, and impact speed can be estimated from maximum residual crush depth and crush volume.

CHAPTER 2: Literature Review

Helmet laws and use

In 1966, the U.S. Federal Government introduced the Highway Safety Act that, in part, required states to have mandatory helmet laws in order to receive federal funds for highway maintenance and construction and by 1975, 47 states complied (U.S. Department of Transportation, 1966). However, when the funding was reduced or eliminated, many states abandoned laws requiring helmet use for motorcyclists. Today, helmet laws for motorcyclists vary from state to state: only 19 states have universal helmet laws for all riders, 28 have partial helmet laws, typically requiring helmets for riders 18 and younger, and 3 have no helmet laws. In 2013, it was estimated that the use of DOT-compliant helmets was 88% in states requiring all riders wear helmets and 49% in other states. Overall, 60% of motorcyclists wore DOT-compliant helmets, 7% wore non-compliant and 33% wore no helmet at all in 2013 (U.S. Department of Transportation, 2013).

Helmet styles

There are a variety of helmet styles on the market: full-face, open-face, shorty, modular, and beanie (Figure 5). All but he beanie style helmets, also known as skull caps or novelty helmets, are typically certified by one or more testing standards. Helmets that meet DOT testing requirements are labeled with “DOT” at the back of the helmets. Beanie style helmets typically lack an adequate energy absorbing liner and do not meet DOT standards; however, consumers have obtained counterfeit DOT stickers and applied them to unapproved helmets to create the appearance that the helmet is approved (Peek-Asa et al., 1999).

Figure 5: Examples of the most common motorcycle helmet styles.

Helmet components

Approved motorcycle helmets consist of three primary components: an outer shell, an energy absorbing liner and a retention system (Figure 1). The shell and the energy absorbing liner play a role in impact attenuation and are described here.

Helmet shell

Helmet shells are typically made of thermoplastics, usually Acrylonitrile Butadine Styrene (ABS), a polycarbonate, or composites of epoxy with fibers of glass, carbon, or Kevlar. Helmet shells are typically 3-5 mm thick (Pinnoji et al., 2010). Thermoplastic

shells are constructed by injection molding whereas composite shells have a more lengthy manufacturing process (Gilchrist and Mills, 1994). Fiberglass shells require mixing coarse ceramic particles into a thermoset resin and then impregnating the resin into fiberglass sheeting. The impregnated sheeting is then molded into the shape of the helmet shell and the substrate is cured. More modern fiber reinforced shells are formed by layering Kevlar or carbon fiber cloth and a resin on top of a mold. These latter materials result in high-strength, lightweight, and stiff shells. Kevlar and carbon-fiber based motorcycle helmets are often marketed as superior to thermoplastic shells because of their greater strength; however, helmet testing has shown that fiber reinforced shells result in more severe headform accelerations compared to thermoplastic shells (Beusenberg and Happee, 1993).

Energy Absorbing Liner

Current crushable energy absorbing helmet liners were patented in 1953 by Herman Roth and Charles Lombard and was initially designed for the United States Air Force (Oliver, 1990). Typical energy absorbing foam liners are made from polystyrene, polyurethane or Ensolite, a blend of polyvinyl chloride and nitrile butadiene rubber. Foams are cellular solids that are comprised of an interconnected network of solid struts or plates that make up the edges and faces of cells (Gibson and Ashby, 1999), with primary applications in the areas of thermal insulation, packaging/energy absorption, buoyancy, and structures. Any material (polymer, metal, ceramic, glass) can be considered a cellular solid if it is less than full density and if it has a void volume uniformly distributed throughout (Williams, 1991).

Although almost any material can be foamed, polymers are the most common. The foaming process begins by melting pellets of the base material and introducing a blowing agent, either chemical or physical, into the hot liquid polymer. Liquid chemical agents decompose by way of a chemical reaction with the polymer and give off a gas, or, the gas that has been introduced (physical agent) expands under the action of heat that is applied as steam. The gas bubbles grow, stabilize and solidify the polymer by cross-linking during cooling (Suh and Skochdopole, 1980). During the forming process, surface tension can draw the material into the cell edges, leaving a membrane across the faces of the cell. By controlling the surface tension, either open or closed-cell foams can be produced (Gibson and Ashby, 1999). As foam is processed, the gas will rise, creating cells that are elongated in the rise direction, providing anisotropic material properties. Inherent anisotropy can also arise from the cell wall material itself. Strength and stiffness will be higher in the rise direction and as the ratio of height to width increases, the compressive and tensile strength also increases by the same amount (Gibson, 1989). The cell structures are not entirely uniform throughout foam materials – there is a range of cell sizes and combinations of open and closed-cells, with one structure dominating. The foaming process greatly extends the range of material properties and creates applications for foams that cannot be easily fulfilled by fully dense solids (Gibson and Ashby, 1999). Foams used for energy absorption, such as the helmet liner, are typically closed-cell. Foam material properties, density, and compression rate vary with the production procedure and the additives used (Kostopoulos et al., 2002). Thus, foam in helmet liners can vary from one manufacturer to the next, even within the same base material.

Foam material properties

The energy absorbing capability of a helmet primarily depends on the foam liner thickness and material properties (Kroeker et al., 2016). The properties of foam and of cellular solids in general, can vary depending on: 1) The type of foam, i.e., elastomeric, elastic-plastic, or elastic-brittle; 2) the internal structure of the foam, i.e., open or closed cell, cell geometry, relative density; 3) the loading mode, i.e., uni-, bi- axial stress, or uni-axial strain (Ben-Dor et al., 1996); and 4) the loading rate. Foams used as impact absorbing liners fall under the elastic-plastic category. The most important feature of foams is the relative density ρ^*/ρ_s , where ρ^* is the density of the cellular material and ρ_s is the density of the solid from which the cell walls are made. Relative density is equivalent to the volume fraction of solids, and is known to have a significant effect on mechanical response (Gibson, 1989, Ouellet et al., 2006). Foam stiffness increases as the relative density increases.

During foam compression, the stress-strain response of elastic-plastic foams shows three distinct regions: a linear elastic region at low strains, a long collapse plateau at medium strains, and a densification region at high strains (Figure 6). The mechanical response within the linear elastic region is controlled by cell wall bending and cell face stretching. The response in the plateau region is associated with the collapse of the cells by buckling for elastomeric foams, plastic yielding for elastic-plastic foams, and brittle fracture for ceramic foams. Densification occurs when the cells collapse and opposing cell walls touch. The onset of densification causes a non-linear increase in stress with strain, and ultimately reaches a point where the solid itself is being compressed. (Gibson and Ashby, 1999). Every foam material has a limit to its energy-absorbing capability.

When a helmet liner has reached densification, it becomes stiff, the forces become high and unabsorbed energy is transferred to the head (Hui and Yu, 2002).

Foam materials also rebound following compression. Elastomeric foams will rebound fully from being compressed into all three regions, whereas elastic-plastic and elastic brittle will only rebound fully from the linear elastic region. If the latter two foams entered the collapse plateau, then some residual compression of the foam will remain after the load is released. The amount of residual compression will increase as the degree of maximum compression increases, but will reach a point where greater amounts of maximum compression will not generate further increases in residual compression. Above this point, the amount of maximum compression (and presumably maximum force) generates no further increase in residual compression.

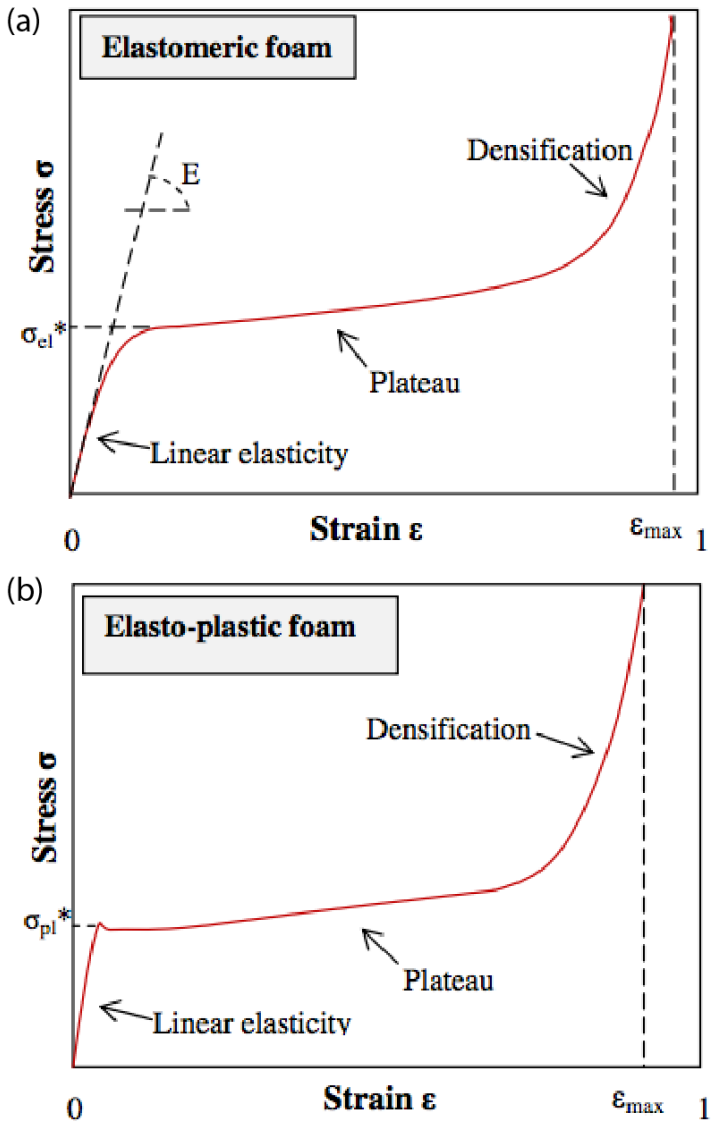

Figure 6: Schematic compressive stress-strain curves for foam, showing the three regions of linear elasticity, collapse plateau, and densification for (a) an elastomeric foam; (b) elastic-plastic foam (de Vries, 2009). Elastic-plastic behavior (b) is typical of the foams using in motorcycle helmets.

Quantifying helmet liner residual crush

Quantifying the amount of residual crush to the energy absorbing liner is an important aspect of the damage replication process. Different methods of quantifying residual liner deformation can yield different results, and thus can affect the

relationship—or lack thereof—between residual crush and impact severity. Some researchers have measured residual crush directly by removing the foam liner from the shell of the accident-involved helmet and comparing it to an undamaged exemplar liner (Wobrock et al., 2003, McIntosh and Patton, 2012). Others have used techniques that vary from simple visual inspection (Hope and Chinn, 1990) to computed tomography (CT) (Cooter, 1990, Loftis et al., 2011). Loftis et al. (2011) used CT scans to quantify the foam liner thickness of impacted motorcycle helmets, but found that the artifact from the helmets' metal components limited their analysis. CT scanning has the ability to examine a helmet non-destructively, account for potential gaps or geometry changes between the foam liner and shell, and create three-dimensional geometries for finite element analyses.

Helmet certification testing

Motorcyclists donning an approved helmet are ensured that the helmet has met minimum performance standards, including impact performance. The regulating body setting the minimum standard for approved helmets in the United States is the DOT. Neither the DOT nor NHTSA approves motorcycle helmets, however, NHTSA has the statutory authority to issue Federal Motor Vehicle Safety Standards (FMVSS) applicable to motor vehicles and related equipment such as motorcycle helmets. The law establishes a self-certification process in which helmet manufacturers certify that their products are in compliance with FMVSS 218, a standard that defines minimum requirements that motorcycle helmets must meet, including the amount of the head that must be covered by the helmet, impact attenuation performance and the headform type and size required for impact attenuation testing, resistance to penetration, retention system strength, and labeling requirements. The manufacturer places a DOT sticker on the back of helmets

that meet this standard. NHTSA enforces the standard by randomly selecting helmets from distribution stocks and testing them to the standard at independent test labs (U.S. Department of Transportation, 2012).

During the impact attenuation portion of the FMVSS 218 certification process, helmets are attached to a DOT magnesium headform (Figure 2a) that is attached via a ball arm to a cart or rig that is guided by a monorail or twin-wire system onto an anvil (Figure 3). The drop height is selected such that the helmet impacts a flat and hemispherical anvil at 6.0 m/s and 5.2 m/s respectively (Figure 4). The headform has an accelerometer mounted at its center of gravity to measure acceleration during the impact attenuation tests and these data are then compared to the pass/fail criteria of the helmet standard (Consumer Product Safety Commission, 1998, U.S. Department of Transportation, 2006, Snell Memorial Foundation, 2015).

For the FMVSS 218 tests, the peak accelerations experienced by the headforms must be less than 400g. In addition, the duration of the acceleration greater than 150 g must not exceed 4 ms (dwell time) and the duration of the acceleration greater than 200 g must not exceed 2 ms (U.S. Department of Transportation, 2006). Other components of the standards include shell penetration, retention system strength, labeling, and helmet positioning.

The Snell Memorial Foundation offers a set of performance standards that are generally considered more rigorous than those established in the FMVSS 218 standard. The Snell Foundation was formed in 1957 in memory of William Snell, a fatally injured sports car racer, to provide independent helmet testing. Some manufacturers choose to voluntarily comply with the Snell performance standard and submit helmet samples to

Snell for certification testing. Once a helmet is tested and approved by Snell, the helmet is labeled as such and Snell enforces its standard by testing randomly selected sample helmets from distribution stocks. (Snell Memorial Foundation, 2010).

The Snell standard calls for the helmet to be tested with an ISO headform (Figure 2b) and helmeted headforms are dropped using either a monorail or guide-wire system onto a flat, hemispherical and edge anvil (Figure 3). Helmets are tested twice on both flat and hemispherical anvils and must impact at 7.7 m/s for the first impact and 7.0 m/s for the second impact. Helmets are also tested once with the edge anvil at 7.7 m/s. In all cases, peak accelerations are not to exceed 300g (Snell Memorial Foundation, 2010). In addition to the components tested in FMVSS 218, the Snell standard includes roll-off, face shield penetration, and chin bar deflection tests. A variety of standards exist across the world with similar aims to the standards prevalent in North America (British Standards Institute, 1985, United Nations Economic Commission for Europe, 2002, Australian/New Zealand Standard, 2006).

There are alternative techniques for performing helmet drop tests in addition to the monorail and guide-wire methods specified in the DOT and Snell standards. The United Nations Economic Commission for Europe (ECE) 22 standard for motorcycle helmet testing requires the helmeted ISO headform to be placed in a basket-like apparatus and guided until impact (United Nations Economic Commission for Europe, 2002). The unrestrained rebound is only limited by the basket walls (Thom et al., 1996). Another approach to drop testing, although not prescribed by any helmet standards, includes suspending an instrumented, helmeted headform by a thin string. When the string is released, the headform free-falls on an anvil while acceleration data are recorded. This

method provides good velocity repeatability as the variability due to trolley or guide-wire friction is eliminated.

Headforms

The DOT and ISO headforms used for impact attenuation testing are made of magnesium K1A alloy (Figure 2a,b, Figure 7), selected by the standards committee due to the alloy's ability to transfer energy throughout the headform and it's reproducibility in testing (Gilchrist and Mills, 1994). They are low-resonance, rigid castings, that differ in size, shape, and weight (Thom et al., 1996). The DOT headform has 4 standard sizes ranging from 1.73 to 4.37 kg in mass and 49 to 60 cm in circumference (Figure 7a). The ISO headforms are available in 15 sizes ranging from 1.52 to 3.26 kg in mass and 50 to 64 cm in circumference; however, only 6 of these sizes are used in most of the testing standards (Figure 7b).

Headforms have reference planes scored onto their surface that define where the headform circumference is measured and these planes are referred to when aligning a helmet onto a headform for testing. The basic plane is defined as an anatomical plane through the centers of the right and left external ear openings and the inferior orbital rims whereas the reference plane is above and parallel to the basic plane. The distance from the basic plane depends on the headform type and size (National Highway Traffic Safety Administration, 1997).

Current helmet standards prescribe impact attenuation tests using different size headforms for different size helmets; however, differences exist between standards in how to select the appropriate headform size. The DOT standard for motorcycle helmets defines three headform sizes and prescribes that a helmet be tested with the headform that

matches the range of helmet circumferences specified by the manufacturer or with multiple headforms if more than one headform size falls into the helmet's size range (U.S. Department of Transportation, 2006). The Snell standard for motorcycle helmets includes six headforms (ISO A, C, E, J, M, O) and allows for a helmet to be tested with any headform that falls within the size range specified by the helmet's manufacturer, or the next smaller size headform (Snell Memorial Foundation, 2015). The British standard includes four headforms (ISO A, E, J, M) and requires that the helmet be tested with the smallest headform appropriate to the size range of the helmet (British Standards Institute, 1985). The Australian/New Zealand standard includes five headforms (ISO A, E, J, M, O) and requires the appropriate size headform be selected based on the inner circumference of the helmet measured 12.7 mm above the headform's reference plane. These differing headform-size selection requirements mean that a single helmet model and size could be tested with different size headforms to comply with these different standards. Perhaps more importantly, helmets may not be tested using the range of headform sizes that represent the riders who are actually wearing the helmets in the field (Thai et al., 2014).

The Hybrid III headforms are part of the Hybrid III anthropomorphic test device (ATD). The Hybrid III head's geometry and moments of inertia match particular segments of the population, including 5th percentile females, 50th percentile males, and 95th percentile males (Figure 2c). There are also Hybrid III dummies for the child and infant populations. The Hybrid III headform was developed with the purpose of having a head capable of sustaining multiple impacts during motor vehicle crash testing while still producing data within the range found in cadaveric head drop studies (Hodgson and

Thomas, 1971). This headform can be instrumented with accelerometers to measure 3 linear and 3 angular accelerations at the head's center of gravity and is covered with a vinyl skin to simulate human skin. The Hybrid III headform is not used for any standardized helmet testing, but it is often used for other types of helmet testing when rotational accelerations are of interest (Cobb et al., 2014, Siegmund et al., 2014).

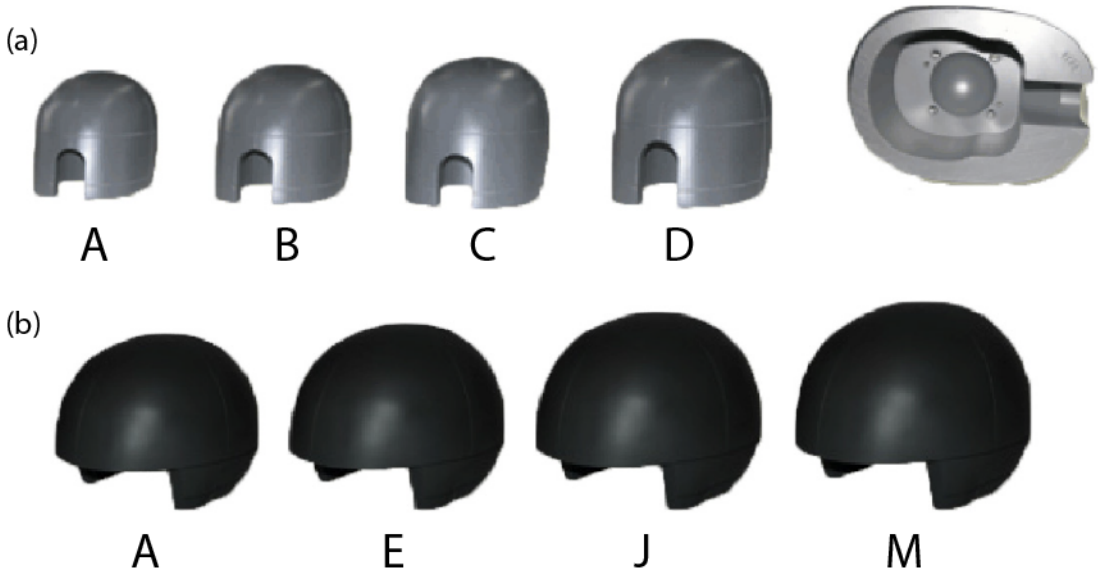

Figure 7: Examples of (a) DOT family of headforms and (b) four commonly used ISO headforms. The letters below each headform designate the headform size.

Cadaver testing

Cadaver heads have been studied in helmet drop testing to validate finite element (FE) models, quantify skull damage at impact, and validate the stiffness of compliant headforms. Kang et al. (1997) aimed to validate a 3D anatomic human head model and replicate a head impact involved in a motorcycle accident to correlate the model response with the clinical observations. An instrumented Hybrid II headform was fitted inside an exemplar helmet and dropped from different heights onto a flat surface to reproduce the impact location and damage sustained to accident-involved helmet. A FE model was

developed and a comparison between numerical and experimentally measured accelerations of the Hybrid II headform validated the model. The model's predicted intracranial pressure was compared to intracranial pressure measurements obtained in cadaver impact testing by Nahum et al. (1977).

Skull fracture tolerance was investigated by Mills and Gilchrist (2008) while evaluating the protection that bicycle helmets provide to the temporal region through a finite element analysis. Impact severities that resulted in skull fractures were determined by striking the side of cadaver heads wearing a bicycle helmet with a flat anvil. Experimental cadaver head testing compared the results of slow lateral compression tests of cadaver skulls with that of a NOCSAE headform and determined the lateral stiffness of cadaver skulls to be 1.59 kN/mm (Hodgson and Thomas, 1971). Allsop et al. (1991) delivered impacts to the temporo-parietal region of thirty-one human cadaver heads. Impacts were delivered to stationary cadavers by two flat, rigid impactors, one with a circular surface area of a 5 cm^2 and the other a rectangular surface of 52 cm^2. Skull stiffness and fracture tolerance values were 1800 N/mm, and 5000 N respectively when using the circular impactor and 4200 N/mm and 12,500 N with the rectangular impactor.

Nusholtz et al. (1984) examined the response of the head to impacts on live anesthetized and post-mortem Rhesus monkeys and repressurized cadavers. Eighteen cadaver impacts at 3.8 – 5.5 m/s resulted in only 2 skull fractures when impacted with padded impactors weighing 10 – 65 kg. To date, cadaver heads have not been tested in motorcycle impact attenuation testing.

Head Injury Criteria

Head injury criteria is a metric used to quantify the risk of a skull fracture and/or brain injury during a head impact and is calculated from the acceleration pulse acquired during a head impact (Equation 1) (Prasad and Mertz, 1985, Mertz and Irwin, 2003). The first data set used to establish HIC came from research at Wayne State University (WSU) where instrumented and pressurized cadaver heads were impacted against rigid and padded surfaces (Lissner et al., 1960). Head acceleration and intracranial pressure vs. time recorded during six head impacts were used to create the original WSU tolerance curve. Additional research established the relationship between head injuries and HIC using a variety of impact pules shapes, cadaver tests, animal models, and human volunteer studies. Skull fracture and brain injury were correlated to head acceleration and HIC, contributing to the final form of the tolerance curve (Hodgson and Thomas, 1977, Got et al., 1978, Tarriere et al., 1982).

HIC is calculated by integrating the acceleration-time history and searching for the maximum value over a 15 ms window (Equation 1). Prasad, et al. (1985) suggested that the time duration over which HIC is calculated should be 15 ms because the majority of HIC durations associated with head impacts that produced either brain damage or skull fractures were less than 10 ms and no brain damage or skull fracture data existed where HIC durations were greater than 15 ms. In this thesis, HIC is computed over a 15 ms window.

$$HIC = max\left[\frac{1}{t_2-t_1}\int_1^2 a(t)dt\right]^{2.5} \quad (1)$$

CHAPTER 3: Methods

Helmet Testing

Experiment A

Cadaver Heads

Four fresh-frozen and thawed near-50th percentile (Young, 1993) male cadaver heads (Table 1) were disarticulated from their spines at the atlanto-occipital joint and used in this study. The cadaver tests were conducted at the Injury and Orthopaedic Biomechanics Laboratory at Duke University and the use of cadavers was approved by Duke's Institutional Review Board. Each head was CT scanned at 120 kV and 680 mA with a slice thickness of 0.625 mm and 0.469 x 0.469 mm pixel spacing. The distance between the two occipital condyles (Figure 8a) and a comparable distance on the posterior side of the foramen magnum was measured on each specimen (Figure 8b). A custom aluminum plate (53 x 53 x 6.5 mm) was fitted over the foramen magnum and secured to the occipital bone with four wood screws and polymethyl methacrylate (PMMA) (Figure 8c). The plate covered the foramen magnum and the PMMA sealed the intracranial contents. The cadaver heads were CT scanned again with the mounting plate intact and the images were viewed in OsiriX, a medical imaging software (v.6.5.2, Pixmeo SARL, Bernex, Switzerland). Each cadaver head's coordinate system was created from anatomical landmarks and the plate was located relative to that coordinate system (Figure 9).

Table 1: Description of tested cadaver heads and headforms. Measurements were taken in the Frankfort (cadaver) or reference (headforms) plane.

Headform	Mass (kg)	Mass with instrumentation (kg)	Circumference (mm)	Head length (mm)	Head breadth (mm)
Cadavers	4.36 ± 0.18	4.77 ± 0.26	574 ± 3	197 ± 7	155 ± 3
Hybrid III (50^{th} male)	4.54	4.99	597	203	155
ISO M	2.95	4.74	600	212	168
DOT D	4.20	4.75	600	212	156

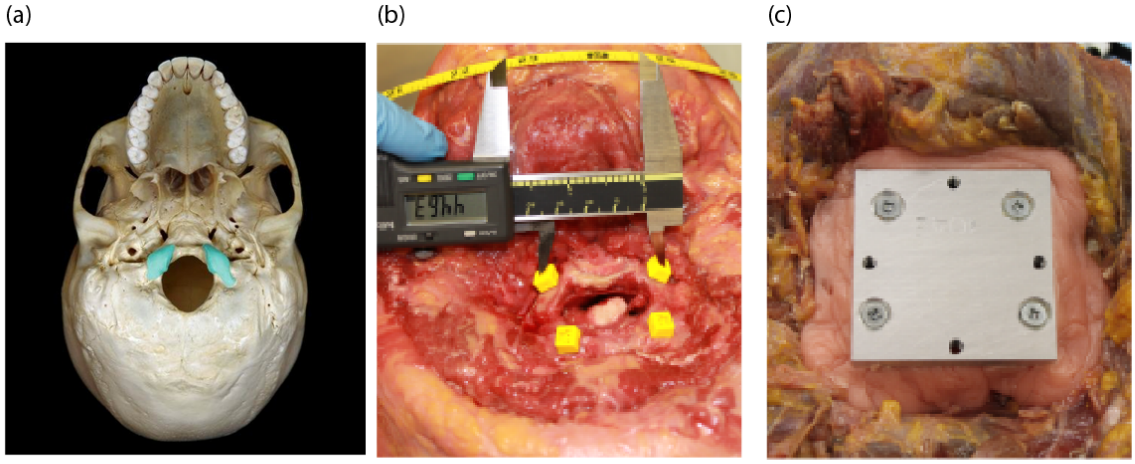

Figure 8: (a) Inferior view of the skull with the occipital condyles highlighted in blue, (b) measurements of bony landmarks surrounding the foramen magnum, (c) plate screwed over foramen magnum with PMMA to seal intercranial contents

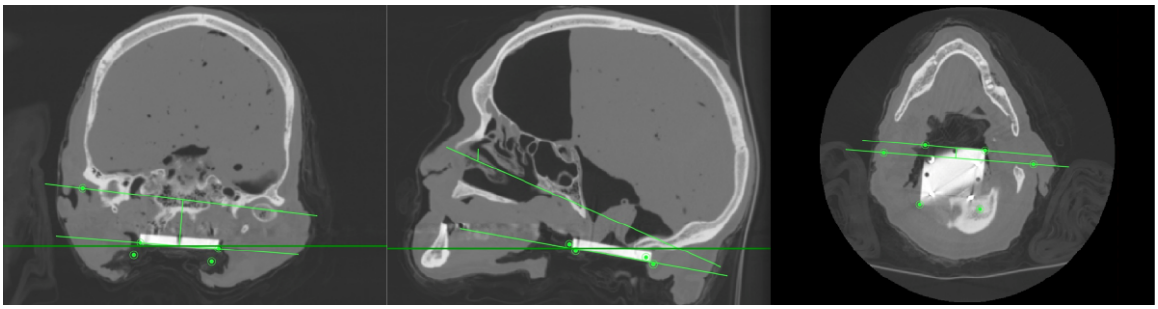

Figure 9: The head coordinate system was identified from the left and right external acoustic meatuses and the left inferior orbital rim. The mounting plate was located relative to the head coordinate system.

The cadaver heads remained inverted in a forehead-down orientation throughout preparation and testing to ensure the brain remained against the forehead region of the skull and thus did not generate a secondary impact against the skull interior during testing. Three uni-axial linear accelerometers (64C-2000-360T-001, Measurement Specialties, Hampton, VA) and three angular rate sensors (ARS PRO-8k, 600 Hz bandwidth, Diversified Technical Systems, Seal Beach, CA) were mounted on the plate's inferior surface (Figure 10a). The sensors were connected to a data acquisition (DAQ) system (SLICE NANO base, 3 SLICE NANO bridges (MCS-07), and a SLICE NANO stack battery; Diversified Technical Systems, Seal Beach, CA) that was installed in a structure fastened to the aluminum plate (Figure 10b). The total mass of the mounting plate, sensors, DAQ and support structure was 501 gm. The sensors and DAQ were wrapped in plastic and the neck skin of the cadavers was then secured around the DAQ-mounting structure with a large cable tie (Figure 10c).

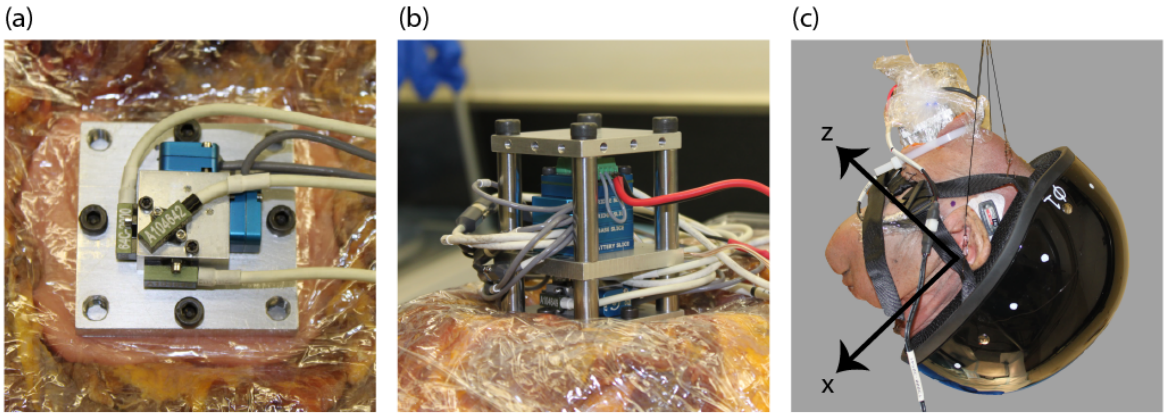

Figure 10: (a) Instrumentation mounted to occipital condyles over foramen magnum, (b) instrumentation and DAQ system fully assembled, and (c) suspended helmet and cadaver head showing its pre-release orientation and coordinate system.

Headforms

Three headforms were used in this study: a size D DOT headform, an ISO M headform, and a 50th percentile male Hybrid III headform (Table 1, Figure 11). The DOT and ISO headforms are made of magnesium K1A alloy and are used for motorcycle and bicycle helmet certification respectively. The Hybrid III headform, part of the Hybrid III dummy developed for automotive crash testing, is an aluminum headform and was included because a compliant, vinyl skin covers it. The same sensors used for the cadaver tests were mounted on a steel plate (119 x 82 x 25 mm) or on an aluminum plate (74 x 76 x 10 mm), which was fastened to the ISO and DOT headforms respectively. The DAQ system was fastened to the inferior side of the plate. The mass of these mounts added 1790 and 551 gm to the ISO and DOT headforms respectively, and brought their total masses near the mean of the instrumented cadaver heads (Table 1). For the Hybrid III headform, the sensors and DAQ were mounted onto a smaller steel plate (100 x 85 x 10 mm) to more closely match the mass of the instrumented cadaver heads (Table 1). To ensure that the sensors were located at the headforms' center of mass (COM), each headform was hung by twine and photographed in two orientations. These photographs were overlaid and the intersection of the twine was used to confirm that the COM and seismic center of the sensors of the instrumented headforms was within 3 mm of headforms' COM without the instrumentation.

Helmets

Large Daytona Skull Cap motorcycle helmets (Daytona Helmets, Daytona, FL) were used for all tests (Figure 10c). The large size was chosen to fit the cadaver heads according to the manufacturer's recommended sizing. This helmet model was chosen

because it had a smooth exterior shell (no vents or ribs) and a near-constant thickness, single density foam liner. The shell was 5 mm thick and made of acrylonitrile butadiene styrene (ABS) and the foam liner was 23-25 mm thick in the impact region and made of expanded polystyrene (EPS). The foam liner was adhered to the interior surface of the shell with glue around the helmet's perimeter and there was an air gap of 4.8 ± 0.6 mm between the liner and shell near the vertex, based on measurements of five undamaged helmets (Figure 11, bottom row). The helmet mass, including straps, buckles and internal comfort liner was 703 gm. A new helmet was snugly attached to each head/headform prior to each test by looping and securing the helmet's restraining straps with similar tension while the helmet was inverted.

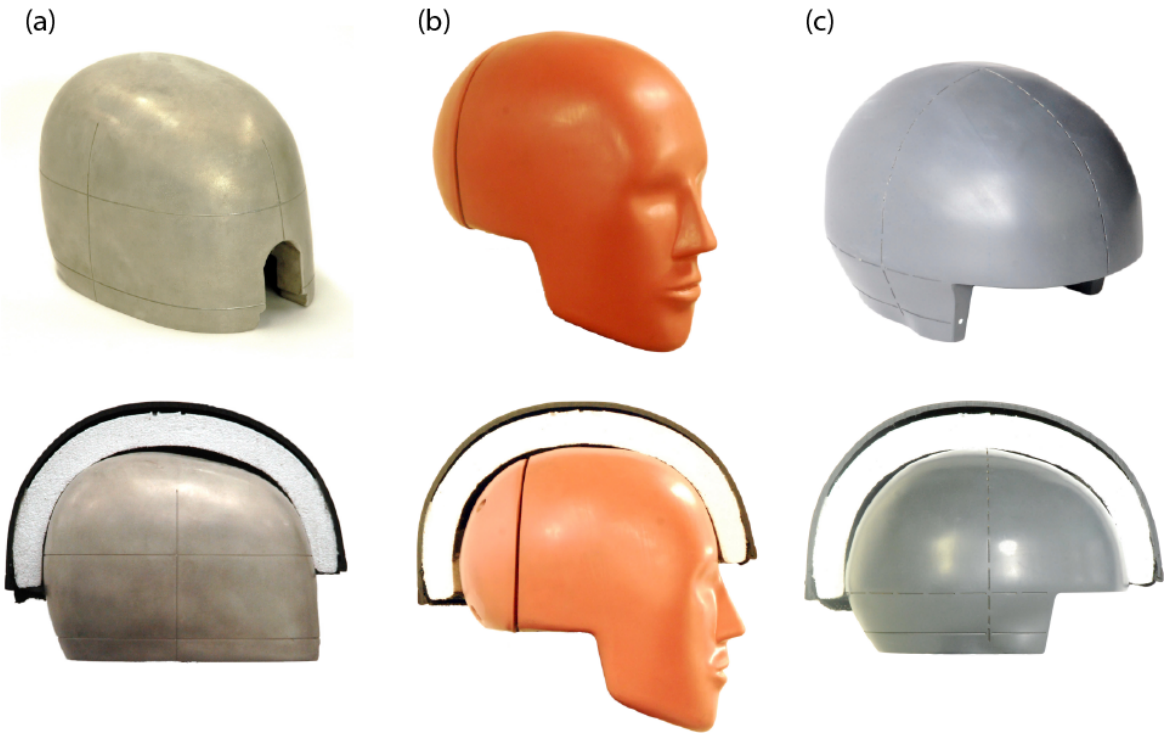

Figure 11: Oblique and sagittal view of tested headforms with cross-sections of a large Daytona Skull Cap helmet: (a) DOT D (b) Hybrid III 50th percentile (c) ISO M.

Test Procedures

To conduct free-fall drop tests, the helmeted heads/headforms were suspended by a custom harness made from lightweight fishing tackle that attached to the helmet straps and tilted the Frankfort plane of the heads/headforms 45° ± 3° from horizontal in the sagittal plane (Figure 10c). The mediolateral axis of the heads/headforms and helmets remained horizontal. The harness was attached to fishing line that ran through a ceiling-mounted pulley to a spool used to adjust the drop height. Drop tests were initiated by cutting the line at the spool, and this technique did not induce any discernable motion or rotation to the helmeted heads/headforms. All helmeted heads/headforms were dropped onto the forehead region (midway between brow and vertex) against a flat anvil at three impact energies: 75 J (low), 150 J (medium) and 195 J (high). These impact energies were selected because, based on pilot testing, the foam liner remained on the fracture plateau of the liner's stress-strain response.

Headform testing was conducted in a different laboratory than the cadaver testing and therefore two different load cells and high-speed video cameras were used. The impact force on a flat anvil (cadavers: aluminum, 127 x 127 x 19 mm, 0.64 kg; headforms: steel, 178 mm diameter, 3.65 kg) was measured using a load cell (cadavers: 40 kN, model 9067, Kistler, Amherst, NY; headforms: 80 kN, model 41, Honeywell, Morristown, NJ) mounted through a steel base to a concrete slab and connected to a separate DAQ system. Both load cells were calibrated prior to testing. The load cell and sensor DAQ systems were configured to initiate data collection simultaneously prior to head/headform release. Helmeted headforms experienced three impacts at each energy level (in randomized order), whereas each helmeted cadaver head experienced each

impact energy level once (in increasing severity). Cadaver heads were palpated after each test, radiographed between the medium and high drops and then CT scanned and dissected after testing was complete to ensure that no fractures had occurred and that the accelerometer plate remained rigidly attached.

All transducer signals were sampled at 50 kHz with a 10 kHz hardware antialiasing filter. The acceleration and load cell signals were then digitally low-pass filtered at 1650 Hz using a 4^{th}-order, zero-lag Butterworth filter (SAE Channel Class 1000). MATLAB 2014a, MathWorks, Natick, MA). For the cadaver heads, a fast Fourier transform determined the appropriate filtering cut-off frequency for the angular rate signals, which was consistent with other studies (Newman et al., 2005, Kang et al., 2011). Angular rate data were low-pass filtered (8 pole, zero-lag, 300 Hz Butterworth filter), then differentiated using a central difference algorithm by averaging over a moving 1 ms window to obtain angular acceleration (Equation 2)

$$\alpha = \frac{f}{2n}(\omega_{i+n} - \omega_{i-n}) \tag{2}$$

where f = sampling frequency (50 kHz), i = sample number, and n = 25 (half window-width for 1 ms). These angular kinematics were used to resolve the linear accelerations to each cadaver head's COM using rigid body kinematics (Martin et al., 1998) (see sample data in Figure 12). The head's COM was estimated to be 0.867 cm forward and 3.157 cm above the intra-aural axis (Beier et al., 1980), which was located relative to the seismic center of the linear accelerometers using the CT scans. HIC_{15} was computed from the resultant linear acceleration using a 15 ms window (Prasad and Mertz, 1985). High-speed digital video recorded the cadaver impacts at 5,000 fps (Phantom V711, Vision Research,

Wayne, NJ) and the headform impacts at 500 fps (X-PRI F2, AOS Technologies AG, Baden, Switzerland).

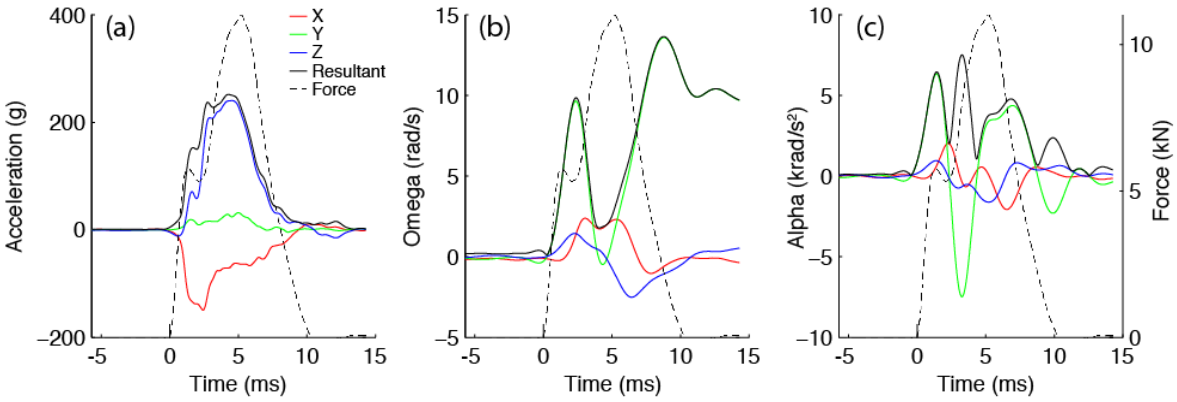

Figure 12: Example cadaver data for a 75 J impact resolved to the head COM. (a) filtered x, y, z and resultant linear acceleration, (b) filtered x, y, z and resultant angular rate, and (c) filtered x, y, z and resultant angular acceleration. The force trace from the load cell is superimposed onto each panel. Impact occurred at time=0. The reference frame is shown in Figure 10c.

Experiment B

Helmets

Four sizes of helmets (extra small, XS; large, L; extra large, XL; and extra extra large, 2XL) (Skull Cap, Daytona Helmets, Ormond Beach, FL) were tested on four sizes of ISO half headforms (A, C, J, M) (Cadex Inc., Quebec, Canada). A hat-size measuring tool (Guangzhou Capable Machinery, China) was used to measure the inner circumference of the EPS liner in the reference plane of 14 new untested helmets (3 of sizes XS, XL and 2XL, and 5 of size L) with the 4.5 mm thick (uncompressed) low-density comfort liners removed (Table 2). The circumference of each headform was measured at the reference line and these measurements matched the circumference specified in the standard governing the ISO headforms (International Standards Organization, 1983). The difference (Δ) between the measured liner circumference and

the headform circumference was used to represent the degree of helmet/headform mismatch (Table 2).

Table 2: Specifications of the helmets and headforms used in this study, including circumference range on the manufacturer's label, initial foam thickness in the forehead region, inner helmet liner circumference after removing the comfort liner, and headform sizes and circumferences. The circumference difference (Δ) between helmet and headform circumferences is specified for the conditions tested.

Helmet size	Manufacturer's labeled size (cm)	Initial foam thickness (mm)	Measured liner circumference (cm)	Circumference difference Δ (cm) (N[a])			
				ISO A (50 cm)[b]	ISO C (52 cm)[b]	ISO J (57 cm)[b]	ISO M (60 cm)[b]
XS	48.6 – 50.8	22.6 ± 0.28	57.60 ± 0.13	7.60 (7)	5.60 (10)	-	-
L	56.2 – 58.4	23.9 ± 0.25	60.25 ± 0.25	10.25 (6)	8.25 (6)	3.25 (10)	-
XL	58.7 – 61.0	25.6 ± 0.28	62.01 ± 0.25	12.01 (2)	-	5.01 (6)	2.01 (21)
2XL	61.3 – 63.5	25.3 ± 0.26	62.25 ± 0.29	-	10.25 (10)	5.25 (6)	2.25 (9)

a. N = number of impacts performed at each helmet/headform combination
b. Circumference of the headform
"-" indicates a helmet/headform combination that was not tested.

Some of the helmets were equipped with three male studs for attaching a visor at the front edge of the helmet shell, but these studs did not interfere with the impacts. All helmets were tested with the visor removed. The chinstrap was secured snugly over a custom-made chin bar attached to the underside of the headform.

Test Procedures

A 3.2 m tall monorail and trolley assembly guided the helmets during the drop tests. A uni-axial ± 2000 g accelerometer (7264B-2000T, Endevco, San Juan Capistrano, CA) was located at the headform's center of mass and oriented vertically. The total mass of the trolley, ball arm and each headform was about 5 kg (ISO A = 4.977 kg, ISO C = 4.981 kg, ISO J = 4.999 kg, ISO M = 5.000 kg). Impact speed was measured with a speed trap located within 40 mm of impact, and impact speed accuracy was better than ± 0.5%

at 10 m/s. Speed trap and accelerometer signals were simultaneously acquired at 100 kHz with a 1 kHz hardware antialiasing filter. Accelerometer data were digitally low-pass filtered at 1650 Hz using a 4^{th}-order, zero-lag Butterworth filter (SAE Channel Class 1000). Peak acceleration was extracted and HIC_{15} was computed from the filtered acceleration data (MATLAB 2014a, MathWorks, Natick, MA).

The impact location was in the mid-sagittal plane and to the forehead region with the Frankfort plane oriented 40° ± 1° from the horizontal plane, approximately the same orientation used in Experiment A (Figure 13). The helmets struck a flat anvil at speeds between 2.0 and 10.50 m/s. For impact speeds above 7.7 m/s, elastic cables were added as a slingshot to increase the impact speed. The forehead impact location minimized interaction with the edge of the helmet while striking a common impact site reported in the literature (Hurt et al., 1981, Hope and Chinn, 1990).

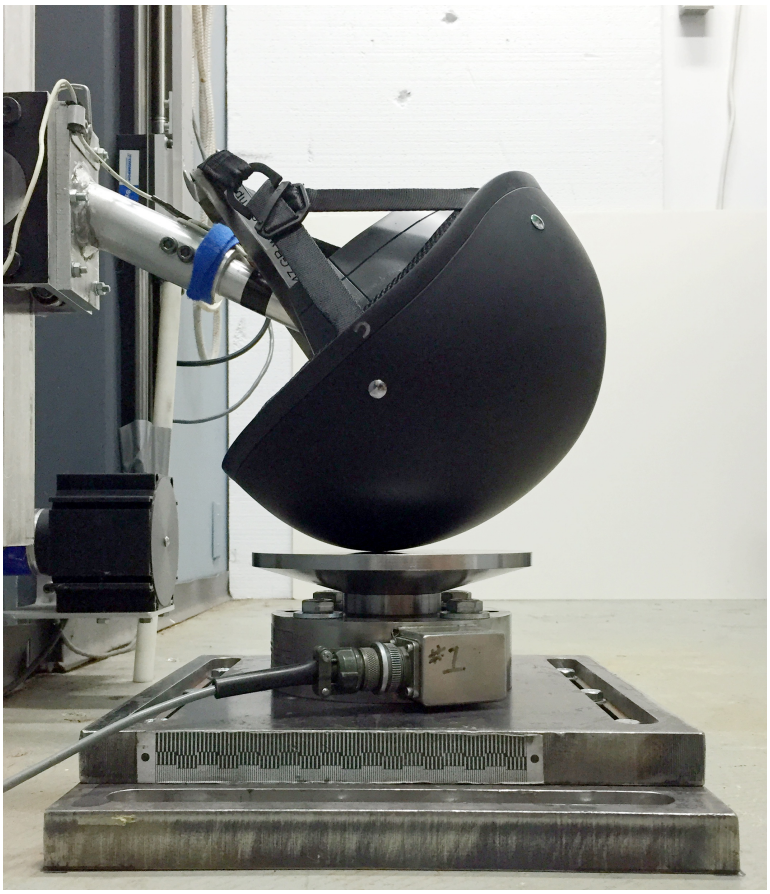

Figure 13: Helmet positioned on headform, attached to monorail.

Foam Crush Analysis

Helmet Scanning

Computed tomography (CT) scans were used to measure the thickness of the foam liner in both Experiments A and B. All tested helmets and the 14 untested reference helmets (3 size SX, XL, 2XL and 5 size L) were scanned. The untested helmets served as templates against which the tested helmets were compared. All helmets were CT scanned at 135 kV and 500 mA with a slice thickness of 0.5 mm and pixel spacing of 0.617 x 0.617 mm (Aquilion One TSX-301A, Toshiba America Medical Systems, Tustin, CA) and stored in a Digital Imaging and Communication in Medicine (DICOM) format. To

ensure consistent helmet position and orientation in the scanner, helmets were placed upright in a container with a 2 cm bed of poured silicone rubber (Mold Max 60, Smooth-On, Inc., Macungie, PA) molded to the helmet's lower perimeter. A wooden dowel threaded through a crossbar at the top of the container restrained the helmet at its vertex (Figure 14). The helmets were submerged in a water solution of NaCl (20 g/L) and surfactant (0.008% vol/vol Triton X-100, EMD Millipore, Billerica, MA) with a radiodensity of 25 ± 75 Hounsfield units (HU) to better distinguish the foam liner (-950 ± 20 HU) from air (-1000 HU) (Figure 15). The saline solution also helped to obscure the shell (-30 ± 30 HU), and thereby improved the ability to segment the foam from both the surrounding shell and saline solution, and the surfactant minimized the air bubbles that adhered to the foam surface. A 2-cm diameter hole was drilled through the shell and a 3-mm diameter hole was drilled through the foam (both at the vertex) to allow the solution to flow between the foam liner and shell, and to allow air to escape. Without a thru-hole in the foam, air can collect on the inside surface of the foam at the vertex. The air is indistinguishable from the foam during the segmentation process and the foam appears thicker than it actually is (Figure 15c).

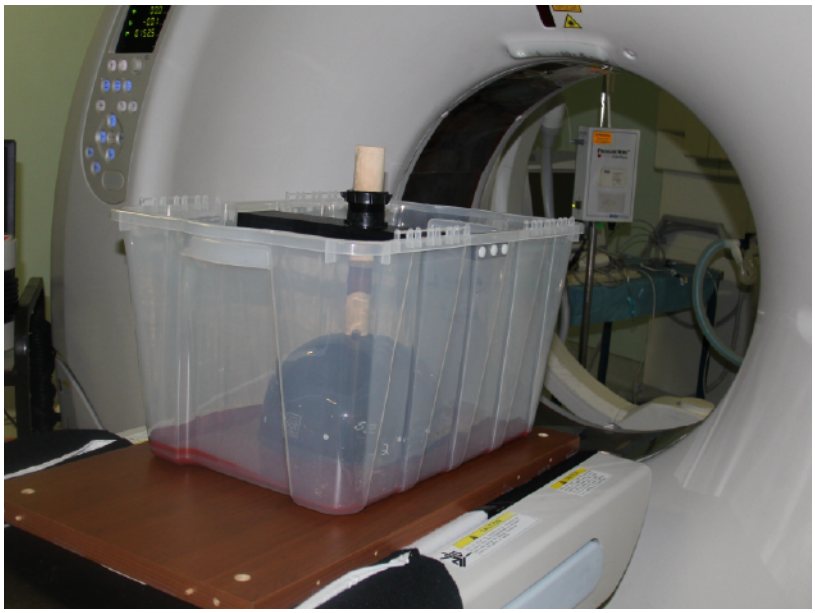

Figure 14: Helmet positioned in fixture with poured silicone rubber as the base and a wooden dowel to maintain the helmet's position. No saline solution has been added here.

The CT scanner settings, fixture materials, and saline and surfactant concentrations were iteratively adjusted during preliminary scans of an exemplar helmet until the foam could be independently segmented in the images (Table 3, Figure 15). The steel rivets were removed to eliminate artifacts that locally obliterated the images and the comfort liners were removed to improve segmentation (Figure 15a,b). A silicone rubber base and a wooden dowel (Figure 15e) were selected over poured urethane and a Delrin® dowel (Figure 15c) for the helmet fixture because they did not create artifacts in the images and their radiodensities were different from the foam liner.

Table 3: CT scanner settings range and concentrations combinations used to determine optimum settings and concentrations for foam segmentation. Bold numbers indicate values used for helmet scanning.

Voltage (kV)	Current (mA)	Solution concentration (g/L)	Surfactant concentration (%)
100-135	100-500	No solution	None
80-135	50-500	100	None
80-135	50-500	50	None
135	50-**500**	**20**	0 – **0.008**

Scan Segmentation

Initially, CT segmentation was attempted algorithmically in a slice-by-slice manner using MATLAB's Image Processing Toolbox with the goal of identifying the x, y, and z coordinates of the inner and outer surfaces of the foam liner. However, this approach was error-prone and OsiriX, was selected to process the images instead. The foam was segmented in OsiriX by selecting the foam region in one image, then specifying and propagating a lower (-1300) and upper (-600) HU threshold through the entire series using the Grow/Region tool (Figure 15e). Using the Brush tool, a 5-pixel dilatation and subsequent erosion process filled the inter-foam gap created by drilling a hole at the foam's vertex (Figure 15e). All non-foam pixels were set to black and a 3D surface was rendered from the foam volume using a marching cubes algorithm (Lorensen and Cline, 1987) where the 3D surface rendering options that produced the highest resolution surface were: Resolution = high, Decimate = 0.1, and Smooth = 50 (Figure 15f). The 3D surface was exported as a 3D object file and opened in CloudCompare (v2, Télécom ParisTech, Paris, France) where the x, y, z location of the verticies were saved as a .txt file (Figure 16a).

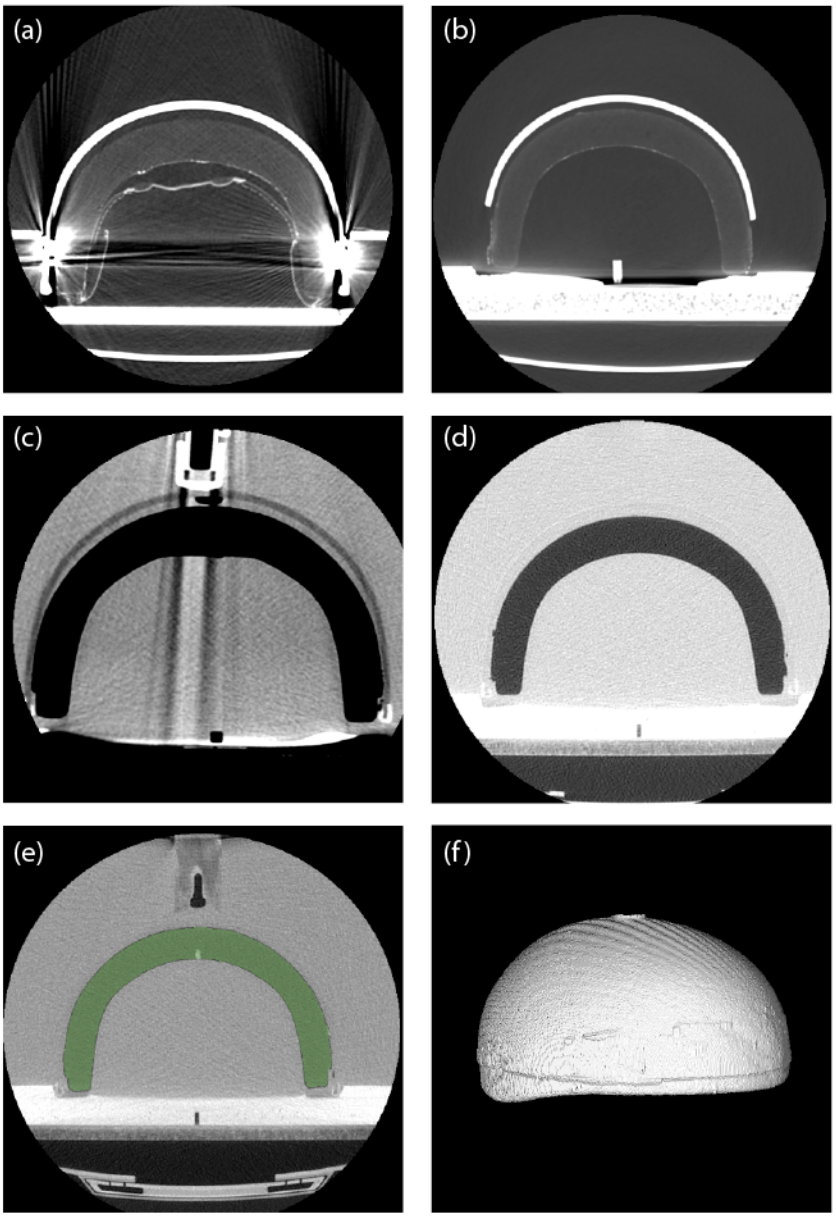

Figure 15: Helmet cross-sections after scanning in (a) air with helmet intact, (b) in air with rivets removed and a urethane base, (c) in water with a PVC dowel, (d) in final saline solution, (e) in final saline solution with wooden dowel, showing foam segmentation, and (f) 3-D surface of foam. All images were viewed in OsiriX.

Within CloudCompare, the point clouds for each helmet size were aligned to a reference frame based on the average of the template helmets. To avoid the geometry

irregularities observed along the bottom edge of the liner, data representing this region (approximately ½ inch wide) was deleted (Figure 16a). The segment tool was used to separate the inner (~500,000 points) and outer (~700,000 points) surfaces (Figure 16b). In order to quantify the foam's thickness, and therefore the amount of residual crush, the coordinates of the inner surface were compared to the coordinates of the outer surface. The Euclidean distance from every point on the foam's inner surface to the closest point on the outer surface was computed using the nearest neighbor distance algorithm (Figure 16b,c). The x, y, z, and foam thickness value of each point on the inner surface was imported into MATLAB where a custom algorithm partitioned the foam thickness data from the front half of the helmet into a grid defined by 5° increments in azimuth and elevation over the region from 5° to 80° in elevation and ± 65° in azimuth either side of the mid-sagittal plane. The foam thickness at each 5° x 5° element was calculated as the average thickness at all points within the element and plotted at the element's center (Figure 17, Figure 18). The foam thickness of the template helmets was averaged for each helmet size and used as the reference value against which the test helmets were compared (Table 2). The difference between a test helmet's thickness and the reference thickness at each element represented the residual crush for that test helmet at that location. The maximum crush depth was the largest amount of residual crush amongst all of the elements analyzed. The product of each element's area on the inner foam surface multiplied by its residual crush was used to estimate the volume of residual crush of each element. These element volumes were then summed over the entire grid to compute total crush volume.

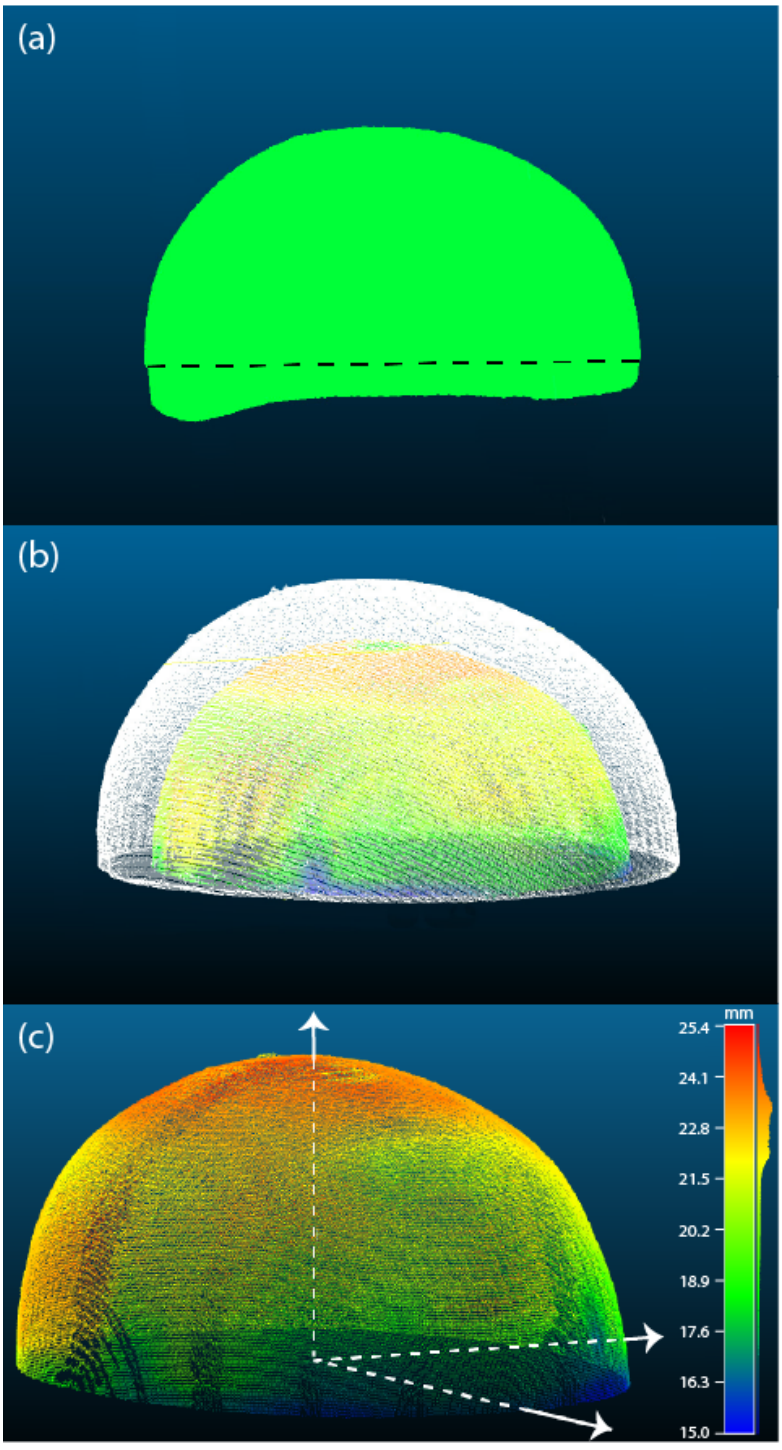

Figure 16: Point cloud data viewed in CloudCompare showing (a) the surface data of entire helmet where data below the dashed line was removed, (b) surface data separated into an inner and outer surface with computed thickness represented by the color gradient on inner surface, and (c) oblique view of a point cloud of the inner foam surface with the liner thickness displayed as a color gradient.

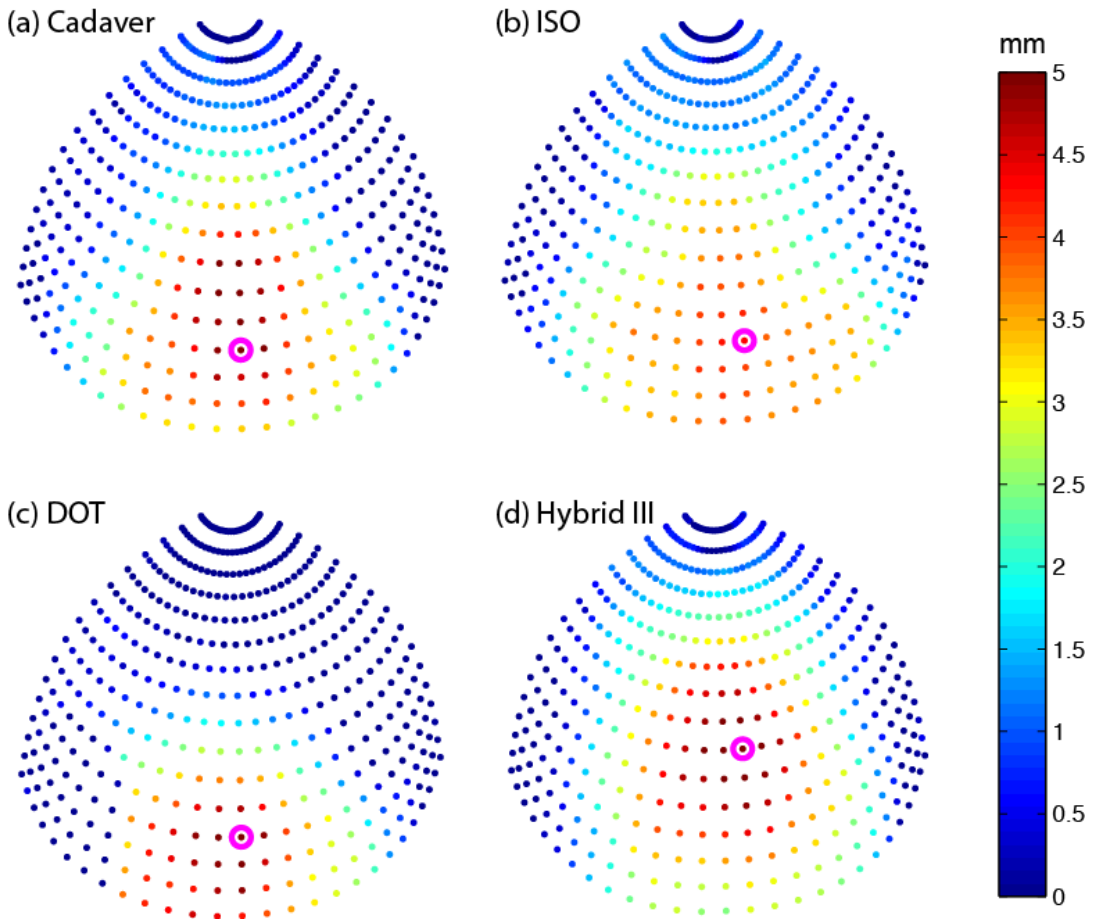

Figure 17: Anterosuperior views of the residual foam liner deformation averaged over 5° x 5° elements after a representative Experiment A 150 J impact for (a) cadaver, (b) ISO headform, (c) DOT headform, and (d) Hybrid III headform. The circled point represents the maximum crush depth.

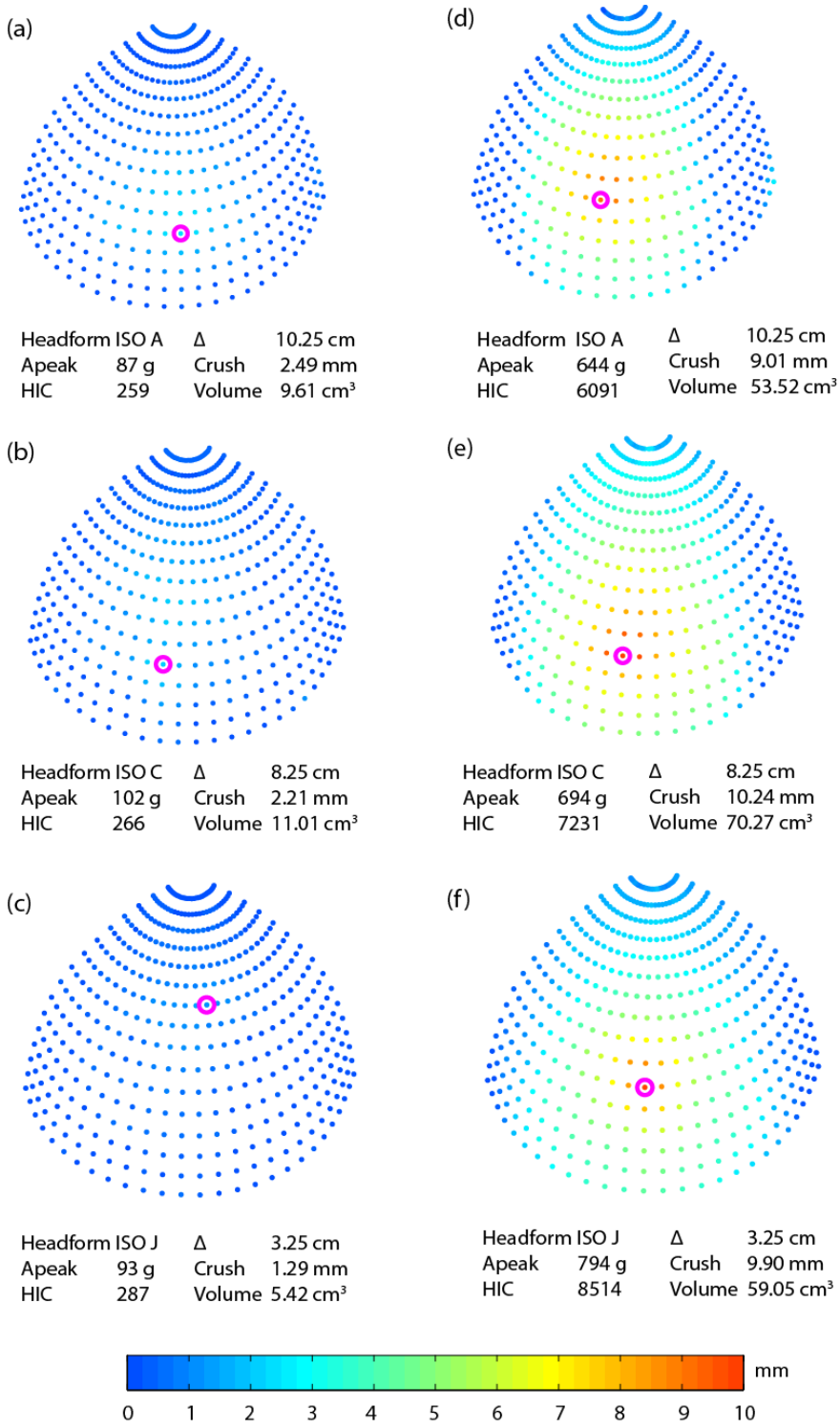

Figure 18: Anterosuperior views of the foam liner deformation averaged over 5° x 5° elements after representative Experiment B 3.3 m/s (left side) and 10 m/s (right side) impacts using one helmet size (L) and three headform sizes (ISO C, J, M). The circled point represents the maximum crush depth. Δ = circumference difference, Amax = maximum acceleration, HIC = head injury criterion Crush = maximum residual crush depth, Volume = residual crush volume.

Statistical Analyses

Experiment A

The first hypothesis of Experiment A stated that metallic headforms experience different peak dynamics and generate different levels of residual crush than cadaver heads under helmeted impact conditions. Experiment A assessed the effect of head/headform type (cadaver, DOT, Hybrid III and ISO) and impact energy level (75 J, 150 J, 195 J) on the dependent variables (peak resultant linear acceleration (g), HIC, peak impact force (N), maximum residual liner crush depth (mm) and crush volume (cm^3)) using general linear models. The mathematical model to test this hypothesis can be written as:

$$R_{ij} = \mu + D_i + E_j + DE_{ij} + \varepsilon_{k(ij)} \quad (3)$$

where R_{ij} is the response for i = 1, 2, 3, 4 for the heads/headforms, j = 1, 2, 3 for the three energy levels, and k = 1, 2, 3 for the three observations at each treatment condition, μ is the overall mean, D_i is the main effect of headform, E_i is the main effect of energy level, DE_{ij} is the effect of their interaction, and $\varepsilon_{k(ij)}$ is the error term.

Assessment of maximum crush depth and crush volume across all three headforms:

H_{01}: $\mu_{\text{Cadaver}} = \mu_{\text{Hybrid III}} = \mu_{\text{DOT}} = \mu_{\text{ISO}}$

H_{a1}: At least one mean is different from the other two

Assessment of liner deformation across all three energy levels:

H_{02}: $\mu_{\text{Energy1}} = \mu_{\text{Energy2}} = \mu_{\text{Energy3}}$

H_{a2}: At least one mean is different from the other two

Assessment of the interaction for each treatment:

H_{03}: $DE_{ij} = 0$; H_{a3}: $DE_{ij} \neq 0$

The treatment means will be ranked by conducting a post-hoc Tukey's test post-hoc.

The second hypothesis stated (a) the amount of residual maximum crush depth and crush volume increases with impact energy levels and (b) residual liner crush can be used to estimate peak head/headform acceleration and impact speed. Separate linear regression models were used to quantify the relationship between maximum resultant acceleration and impact speed (the response variables) and either maximum crush depth or crush volume (the predictor variables) to estimate the average head acceleration and impact speed from residual helmet liner crush. The regression models also included head/headform type and interaction terms as predictor variables to allow for different intercepts and slopes for each head/headform, and these terms were then removed from the models if their coefficients were not significant. The regression models were of the form shown in Equation 4, where R_i is the response of the i^{th} helmet, β_0 is the intercept, β_1 is the coefficient for the residual crush variable c_i (either maximum residual crush depth or residual crush volume), β_2 is the coefficient for the head/headform h_j, β_3 is the coefficient for the interaction term $c_i h_j$, and ε_i is the residual.

$$R_i = \beta_0 + \beta_1 c_i + \beta_2 h_j + \beta_3 c_i h_j + \varepsilon_i \quad (4)$$

All statistical analyses were conducted in Minitab (version 17, Minitab, State College, PA) using a significance level of $\alpha = 0.05$.

Experiment B

The first hypothesis of Experiment B stated that for a given impact speed, the peak headform acceleration and HIC will decrease as the relative helmet size increases.

The second hypothesis stated that peak acceleration, HIC, and impact speed can be estimated from maximum residual crush depth and crush volume. Six separate linear regression models were used to quantify the relationship between each of the three response variables (peak acceleration (A_{peak}) (g), HIC_{15}, and impact speed (m/s)) and two groups of predictor variables: (i) maximum residual crush depth (mm) and circumference-difference (cm), and (ii) residual crush volume (cm^3) and circumference-difference (cm)). The regression models were of the form shown in Equation 5, where R_i is the response of the i^{th} helmet, β_0 is the intercept, β_1 is the coefficient for the residual crush variable c_i (either maximum residual crush depth or residual crush volume), β_2 is the coefficient for the circumference difference Δ_i, β_3 is the coefficient for the interaction term $c_i \Delta_i$, and ε_i is the residual. Box-Cox power transformations were applied to A_{peak} and HIC because the residuals of their untransformed regression models were not normally distributed when tested using an Anderson-Darling test ($\alpha = 0.05$). The impact speed regressions did not require a Box-Cox transformation because the distribution of their residuals was not significantly different from normal. The A_{peak} and HIC regressions were then back transformed for the figures presented here.

$$R_i = \beta_0 + \beta_1 c_i + \beta_2 \Delta_i + \beta_3 c_i \Delta_i + \varepsilon_i \quad (5)$$

For the regression models that included crush volume, 9 of the 25 2XL helmets were excluded because they contained an extra piece of foam (25 x 10 x 0.5 cm) between the energy absorbing liner and the shell. This extra foam was aligned longitudinally in the mid-sagittal plane and its forward edge partly and variably overlapped the impact-related crush (Figure 19). The radiodensity of the extra foam was similar to the EPS liner and therefore the extra foam could not be distinguished from the EPS liner during

segmentation. The extra foam did not overlap the location of maximum crush depth and therefore these helmets were not excluded from the regression models that included maximum crush depth. The remaining 16 2XL helmets did not have any additional foam between the liner and shell at the forehead or vertex region and were included in the crush volume regressions.

Figure 19: Foam liner from 2XL helmet containing additional foam segment at vertex.

The foam liner densified at high impact speeds and caused rapid increases in peak acceleration and HIC with small increases in impact speed, and therefore these densification-affected data were excluded from the linear regression models. The boundary between the included and excluded data was chosen by visual inspection and finding the value of maximum crush and crush volume that corresponded to a large increase in acceleration (Appendix A). All statistical analyses were conducted in Minitab (v17, Minitab, State College, PA) using a significance level of $\alpha = 0.05$.

CHAPTER 4: Results

Experiment A

The time-varying nature of the resultant accelerations and impact forces within each head/headform showed consistent patterns; however, the cadaver heads showed higher initial accelerations than the headforms (Figure 20). The general linear model showed all dependent variables increased significantly with increasing impact energy ($p<0.005$, Table 4). Post-hoc testing showed differences between the responses of the cadaver heads and each of the headforms, but there was no consistent pattern across the dependent variables (Table 5).

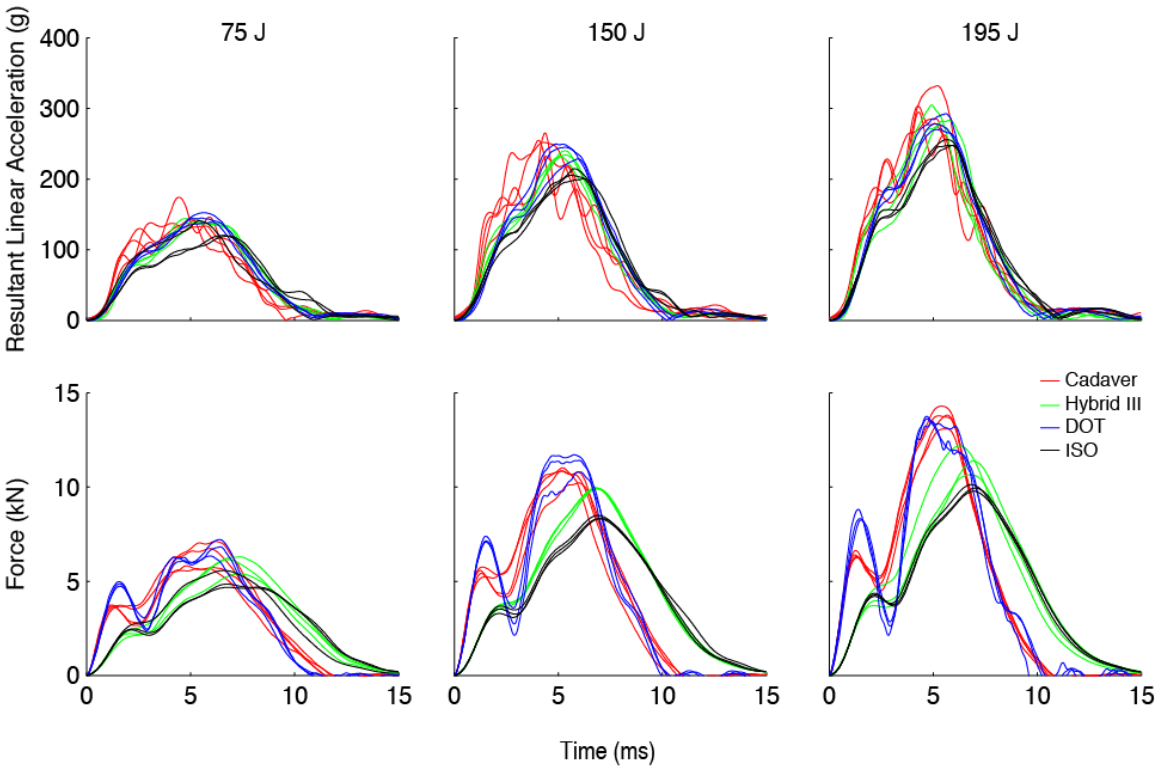

Figure 20: Resultant acceleration and force traces during all impacts. Impact occurred at time=0.

Table 4: Average ± standard deviation for maximum values of each response variable at the low (75 J), medium (150 J), and high (195 J) impact energies.

	Amax (g)	HIC_{15}	Force (kN)	Max Crush Depth (mm)	Crush Volume (cm^3)
Cadaver					
low	149 ± 18	912 ± 104	6.35 ± 0.68	4.0 ± 0.5	18.4 ± 2.8
medium	251 ± 14	2611 ± 468	10.73 ± 0.35	5.1 ± 0.9	34.6 ± 1.4
high	318 ± 25	4277 ± 635	13.74 ± 0.50	6.1 ± 0.3	47.4 ± 3.7
Hybrid III					
low	141 ± 3	850 ± 16	5.94 ± 0.48	2.9 ± 0.7	14.8 ± 5.5
medium	235 ± 4	2355 ± 38	9.93 ± 0.03	5.1 ± 0.4	39.8 ± 3.7
high	288 ± 15	3478 ± 234	11.40 ± 0.76	6.4 ± 0.1	50.3 ± 0.9
DOT					
low	145 ± 7	883 ± 45	6.79 ± 0.44	3.1 ± 0.3	10.4 ± 0.6
medium	241 ± 11	2683 ± 281	11.31 ± 0.46	4.8 ± 0.5	23.3 ± 1.2
high	280 ± 11	3806 ± 124	13.62 ± 0.13	5.2 ± 0.5	32.8 ± 3.4
ISO					
low	127 ± 12	643 ± 88	5.03 ± 0.48	3.3 ± 0.9	18.6 ± 4.8
medium	207 ± 7	1963 ± 40	8.38 ± 0.10	4.6 ± 0.6	37.8 ± 2.7
high	250 ± 5	2945 ± 92	9.95 ± 0.18	4.6 ± 0.1	48.3 ± 4.1

Table 5: Mean differences between cadaver heads (CAD) and headforms (DOT, HIII, ISO) and post-hoc Tukey's test p-values for all dependent variables pooled across impact energy levels. Bold values indicate a significant difference.

Comparison	Acceleration (g)	HIC_{15}	Force (kN)	Max Crush Depth (mm)	Crush Volume (cm^3)
CAD-DOT	**17.19** **p=0.054**	143 p=0.748	-0.297 p=0.698	0.712 p=0.059	**11.28** **p<0.0005**
CAD-HIII	**18.07** **p=0.040**	372 p=0.061	**1.185** **p=0.001**	0.290 p=0.708	-1.52 p=0.787
CAD-ISO	**44.87** **p<0.0005**	**750** **p<0.0005**	**2.488** **p<0.0005**	**0.936** **p=0.008**	-1.4 p=0.815
DOT-HIII	0.88 p=0.999	229 p=0.443	**1.482** **p<0.0005**	-0.422 p=0.464	**-12.81** **p<0.0005**
DOT-ISO	**27.68** **p=0.002**	**607** **p=0.002**	**2.786** **p<0.0005**	0.223 p=0.866	**-12.72** **p<0.0005**
HIII-ISO	**26.80** **p=0.002**	378 p=0.081	**1.304** **p<0.0005**	0.645 p=0.136	-0.09 p=1.000

The regression of maximum linear acceleration (A_{peak}) against maximum residual crush depth ($Crush_{max}$) generated a simple linear equation as neither the head/headform type nor the head/headform-type × max crush depth interaction was significant and both terms were therefore removed from the model (Equation 6, Table 6, Figure 21). There were significant slope differences between the head/headform types and between head/headform-type × crush volume interaction when maximum linear acceleration was regressed against crush volume ($Crush_{vol}$) and therefore the additional terms were kept in the model (Equation 7, Table 6, Figure 22). A comparison of the head/headform-specific slopes showed that the cadaver heads had a greater slope, i.e., acceleration increased more with increasing residual crush volume, than the Hybrid III and ISO headforms. The results of both regressions are shown in Equations 6 and 7, wherein the indicator

variables DOT, HIII, and ISO take on the value of 1 to indicate their presence and 0 otherwise.

$$A_{peak} = 1.8 + 47.37 \times Crush_{max} \quad (6)$$

$$A_{peak} = 54.4 + 5.533 \times Crush_{vol} + \begin{Bmatrix} DOT \times (37.8 + 0.337 \times Crush_{vol}) \\ HIII \times (30.2 - 1.619 \times Crush_{vol}) \\ ISO \times (0.4 - 1.525 \times Crush_{vol}) \end{Bmatrix} \quad (7)$$

Table 6: Results of the peak head acceleration linear regression models showing the coefficients ± standard errors and p-values for the predictor variables maximum crush depth and crush volume. P-values < 0.05 are in bold.

Predictor Variable	Constant β_0	Crush Coefficient β_1	Headform Coefficient β_2	Interaction Coefficient β_3
Max Crush Depth	1.8 ± 23.2 p=0.939	47.37 ± 4.86 **p<0.0005**		
Crush Volume	54.4 ± 16.8 **p=0.003**	5.533 ± 0.473 **p<0.0005**	DOT 37.8 ± 24.0 p=0.126	DOT ×Crush Vol 0.337 ± 0.853 p=0.696
			HIII 30.2 ± 23.7 p=0.212	HIII ×Crush Vol -0.619 ± 0.643 **p=0.017**
			ISO 0.4 ± 25.7 p=0.988	ISO ×Crush Vol -1.525 ± 0.704 **p=0.038**

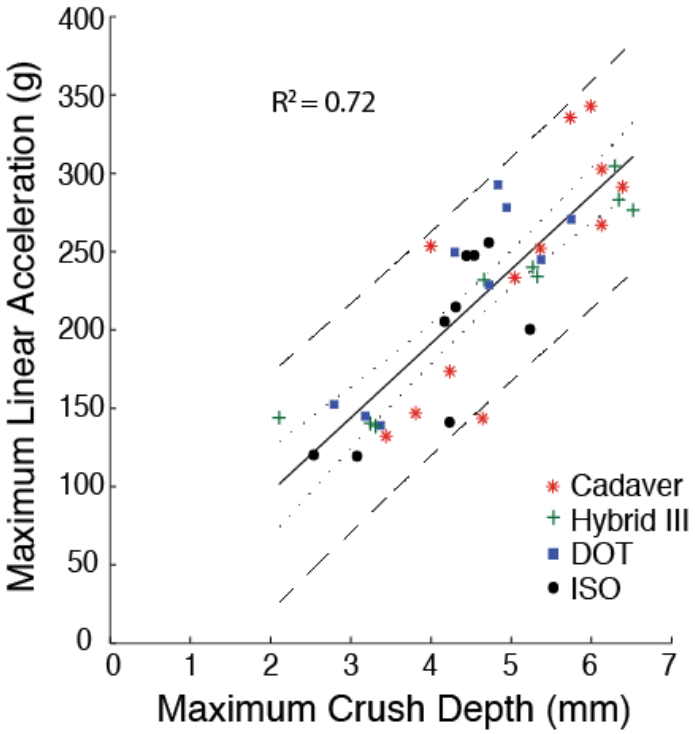

Figure 21: Maximum resultant acceleration vs. maximum crush depth for each headform with regression line (solid), confidence interval (dotted) and prediction interval (dashed). Adjusted R^2 is reported.

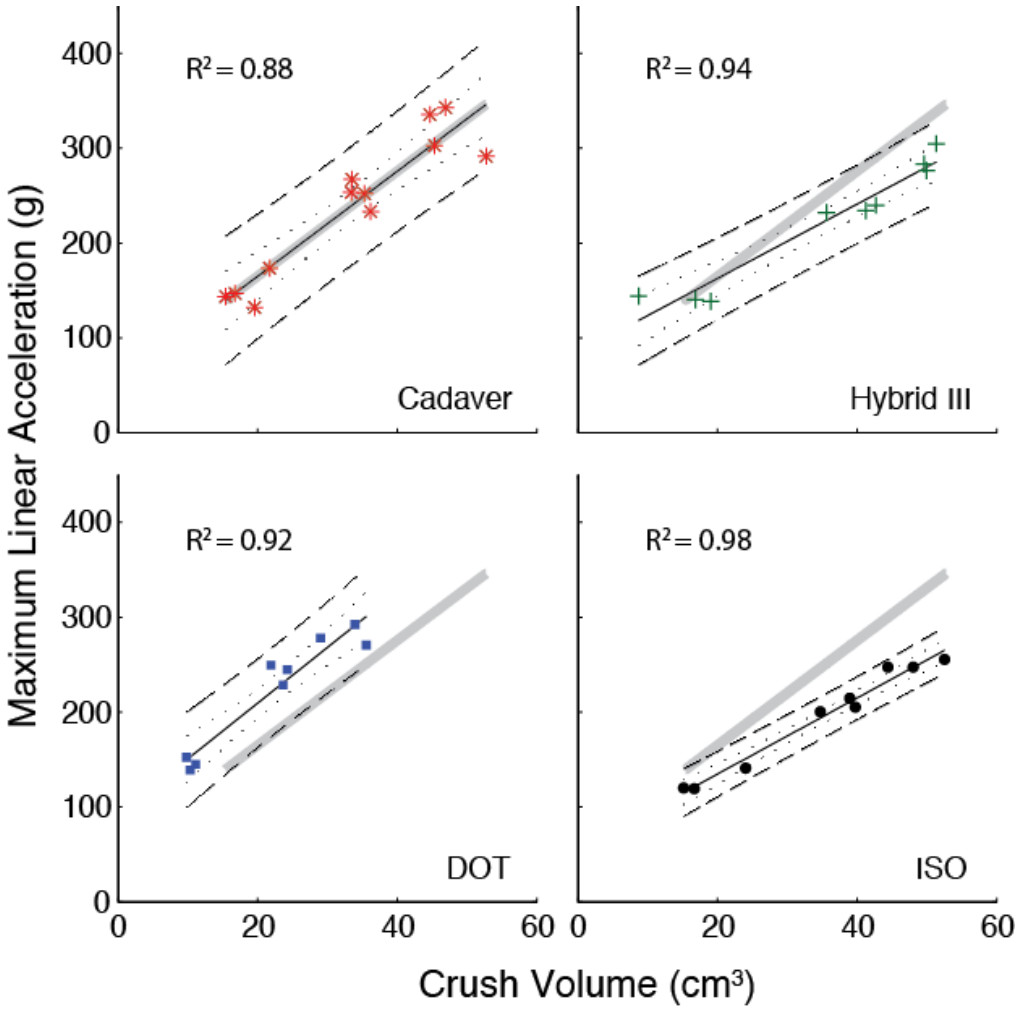

Figure 22: Maximum resultant acceleration vs. crush volume for each headform with regression line (solid), confidence interval (dotted) and prediction interval (dashed). The thick grey line represents the cadaver regression line for ease of comparison. Adjusted R^2 is reported in each panel.

The regression of impact speed (*Speed*) against maximum residual crush depth ($Crush_{max}$) included the head/headform term, but the head/headform-type × max crush depth interaction was not significant and was therefore removed from the model (Equation 8, Table 7, Figure 23). There were significant slope differences between the head/headform types and between head/headform type × crush volume interaction when impact speed was regressed against crush volume ($Crush_{vol}$) and therefore these terms

were kept in the model (Equation 9, Table 7, Figure 24). The results of both regressions are shown in Equations 8 and 9, wherein the indicator variables DOT, HIII, and ISO take on the value of 1 to indicate their presence and 0 otherwise.

$$Speed = 1.860 + 1.119 \times Crush_{max} + \begin{Bmatrix} DOT \times 0.898 \\ HIII \times 0.143 \\ ISO \times 1.108 \end{Bmatrix} \quad (8)$$

$$Speed = 3.646 + 0.1163 \times Crush_{vol} + \begin{Bmatrix} DOT \times (0.678 + 0.0332 \times Crush_{vol}) \\ HIII \times (0.564 - 0.0264 \times Crush_{vol}) \\ ISO \times (0.116 - 0.0064 \times Crush_{vol}) \end{Bmatrix} \quad (9)$$

Table 7: Results of the head impact speed linear regression models showing the coefficients ± standard errors and p-values for the predictor variables maximum crush depth and crush volume. P-values < 0.05 are in bold.

Predictor Variable	Constant β_0	Crush Coefficient β_1	Headform Coefficient β_2	Interaction Coefficient β_3
Max Crush Depth	1.860 ± 0.667 **p=0.009**	1.119 ± 0.123 **p<0.0005**	DOT 0.898 ± 0.376 **p=0.023**	
			HIII 0.143 ± 0.367 p=0.700	
			ISO 1.108 ± 0.383 **p=0.007**	
Crush Volume	3.646 ± 0.323 **p<0.0005**	0.1163 ± 0.0091 **p<0.0005**	DOT 0.678 ± 0.460 p=0.151	Crush Vol ×DOT 0.0332 ± 0.0164 p=0.051
			HIII 0.564 ± 0.454 p=0.224	Crush Vol ×HIII -0.0264 ± 0.0123 **p=0.040**
			ISO 0.116 ± 0.492 p=0.816	Crush Vol ×ISO -0.0064 ± 0.0135 p=0.641

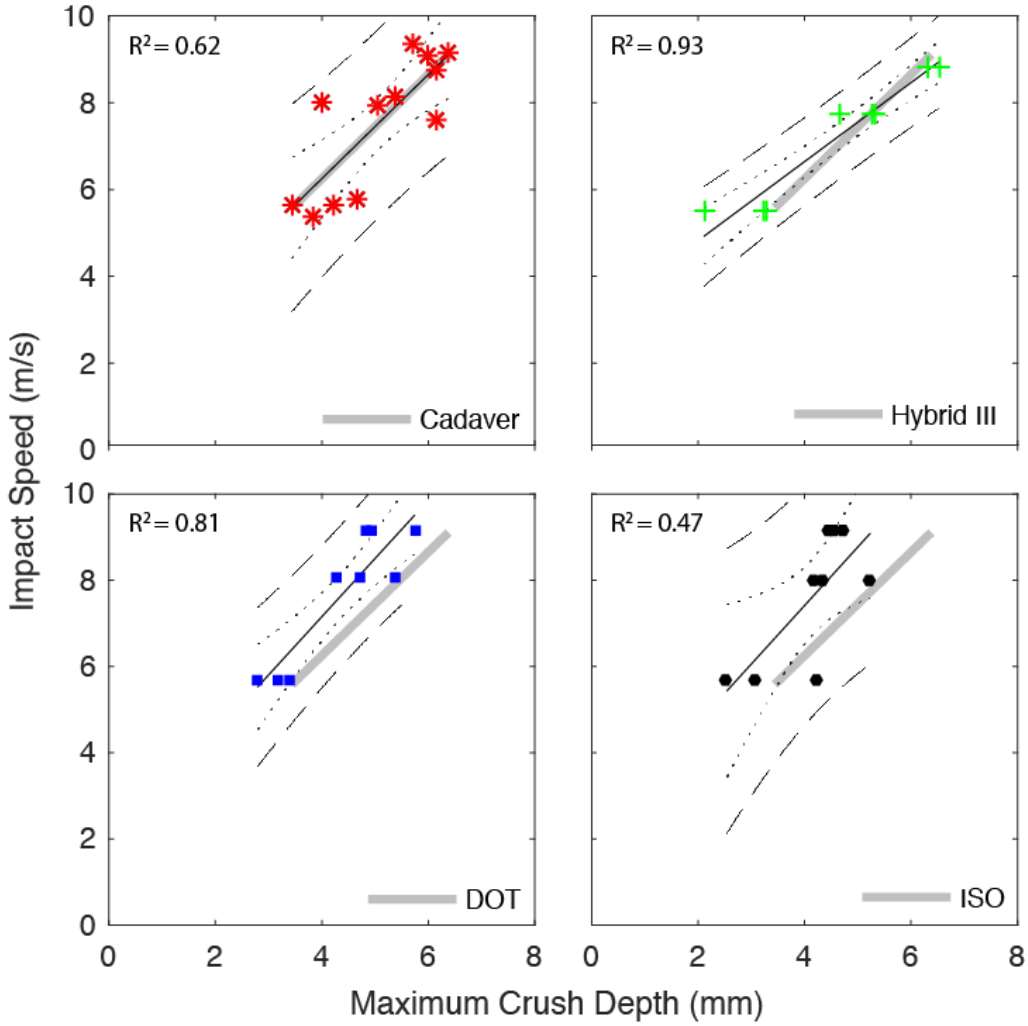

Figure 23: Impact speed (m/s) vs. Maximum crush depth (mm) for each headform with regression line (solid), confidence interval (dotted) and prediction interval (dashed). The thick grey line in each panel represents the cadaver regression line for ease of comparison. Adjusted R^2 is reported in each panel.

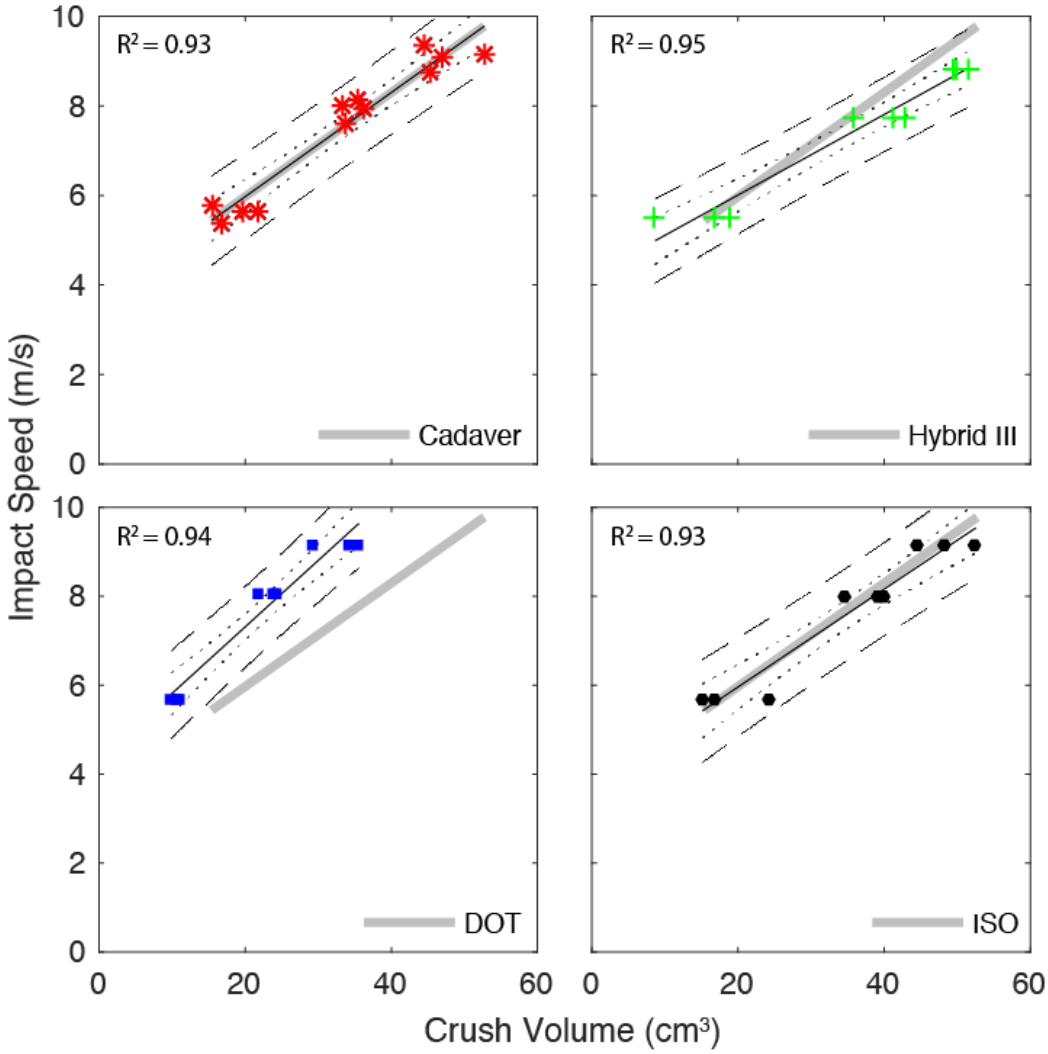

Figure 24: Impact speed (m/s) vs. crush volume (cm^3) for each headform with regression line (solid), confidence interval (dotted) and prediction interval (dashed). The thick grey line in each panel represents the cadaver regression line for ease of comparison. Adjusted R^2 is reported in each panel.

Experiment B

Three of the 93 impacts were excluded from the analysis. Two of these impacts involved helmets with focal areas of deformation (2 cm x 5 cm, and 2 to 4 mm deep) on the outer surface of the liner. These focal areas overlapped the impact region but did not appear to be related to the impact. A third helmet was excluded because it rotated during testing and the deformation was concentrated along the front edge of the liner.

The relationships between peak headform acceleration and residual crush were relatively well behaved up to a maximum crush depth of about 7.9 mm and a crush volume of about 40 cm^3. Above these levels, the relationships became highly variable (Figure 25, Appendix E1 and E4). As a result of this response pattern, the regression analyses were restricted to impacts below 7.9 mm of maximum residual crush depth (64 helmets) and 40 cm^3 of residual crush volume (40 helmets). The coefficients for all six of the regression analyses were significantly different from zero ($p<0.0005$; Equations 10-15, Table 8, Figure 26 and Figure 27) and indicated that peak headform acceleration, HIC, and impact speed were positively correlated with both crush measurements and negatively correlated with the difference in circumference between the helmet and headform.

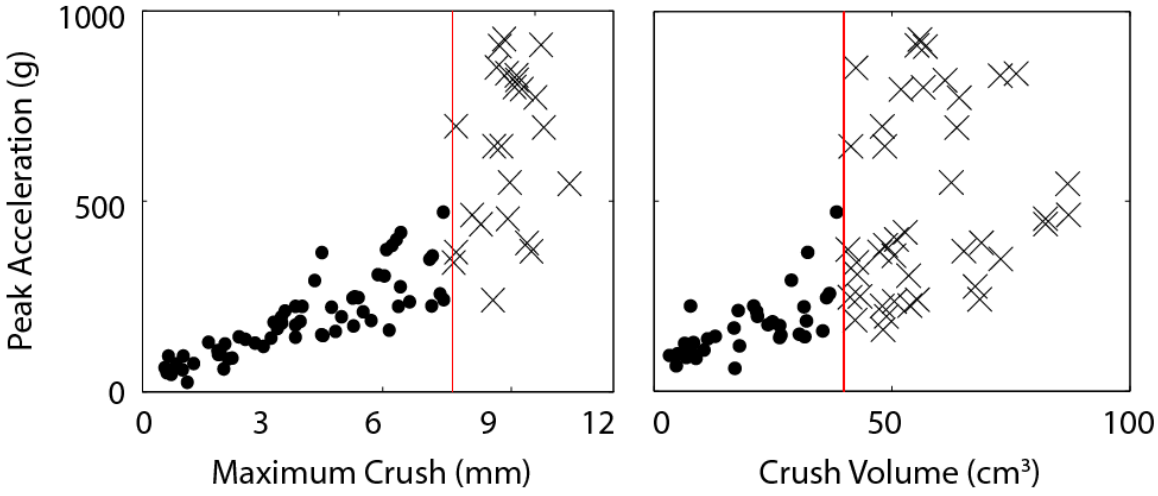

Figure 25: Peak acceleration (g) vs. maximum residual crush depth (mm) and residual crush volume (cm^3) for all impacts. A vertical red lines separate the dots, which represent impacts with a maximum residual crush depth below 7.9 mm and a residual crush volume below 40 cm^3, from the x-marks, which represent impacts above these thresholds. Only the data represented by the dots were used in the regressions.

$$\sqrt{A_{max}} = 9.222 + 1.464 \times Crush_{max} - 0.440 \times Diff \quad (10)$$

$$HIC^{0.26353} = 4.132 + 0.771 \times Crush_{max} - 0.229 \times Diff \quad (11)$$

$$Speed = 2.977 + 1.019 \times Crush_{max} - 0.280 \times Diff \quad (12)$$

$$\sqrt{A_{max}} = 8.975 + 0.226 \times Crush_{vol} - 0.280 \times Diff \quad (13)$$

$$HIC^{0.20864} = 3.100 + 0.067 \times Crush_{vol} - 0.101 \times Diff \quad (14)$$

$$Speed = 3.154 + 0.150 \times Crush_{vol} - 0.197 \times Diff \quad (15)$$

Table 8: Results of the linear regression models showing the coefficients ± standard errors for each response variable for the maximum crush depth regression (top half) and crush volume regression (bottom half). Also shown are the Anderson-Darling normality test p-values for the residuals of the transformed response variables, and the adjusted coefficients of determination (R^2).

Response Variable *R*	Constant β_0	Max Crush Coefficient β_1	Difference Coefficient β_2	Anderson-Darling	Adjusted R^2 (%)
$\sqrt{A_{peak}}$	9.222±0.451	1.464±0.081	-0.440±0.060	0.239	85.18
$HIC^{0.26353}$	4.132±0.205	0.771±0.037	-0.229±0.027	0.146	88.52
Speed	2.977±0.258	1.019±0.047	-0.280±0.034	0.078	89.29
Response Variable *R*	Constant β_0	Crush Volume Coefficient β_1	Difference Coefficient β_2	Anderson-Darling	Adjusted R^2 (%)
$\sqrt{A_{peak}}$	8.975±0.604	0.226±0.021	-0.280±0.089	0.396	76.64
$HIC^{0.20864}$	3.100±0.159	0.067±0.005	-0.101 ±0.024	0.265	81.15
Speed	3.154±0.364	0.150 ±0.013	-0.197±0.054	0.732	80.25

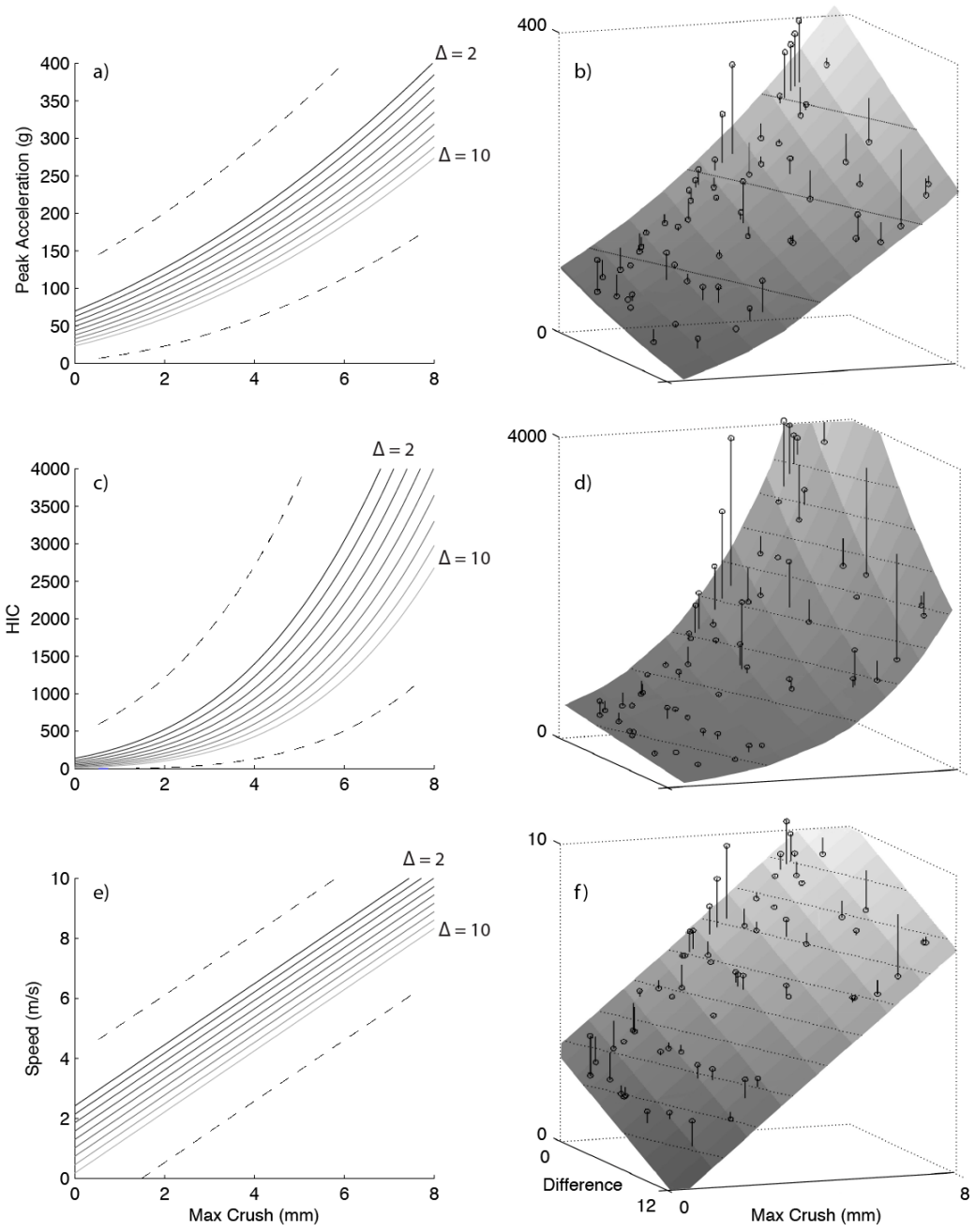

Figure 26: The regression results for peak acceleration (g) (a,b), HIC (c,d), and speed (m/s) (e,f) regressed against maximum residual crush (mm) (Max Crush) and helmet/headform mismatch (Δ). The left column of graphs (a,c,e) shows the regression results for 1 cm increments of mismatch from 2 to 10 cm and the +95th and -95th percentile prediction intervals for the 2 cm and 10 cm mismatch conditions respectively (shown by dashed lines). The right column of graphs (b,d,f) shows surface plots of the regression models and the data, wherein the vertical lines represent the residuals between each data point and the surface, the shaded gradations represent 1 mm increments of maximum crush depth, and the dashed lines represent increments of each vertical axis: (b) 100 g, (d) 500, (f) 1 m/s. Note that peak acceleration and HIC have been back-transformed for these figures.

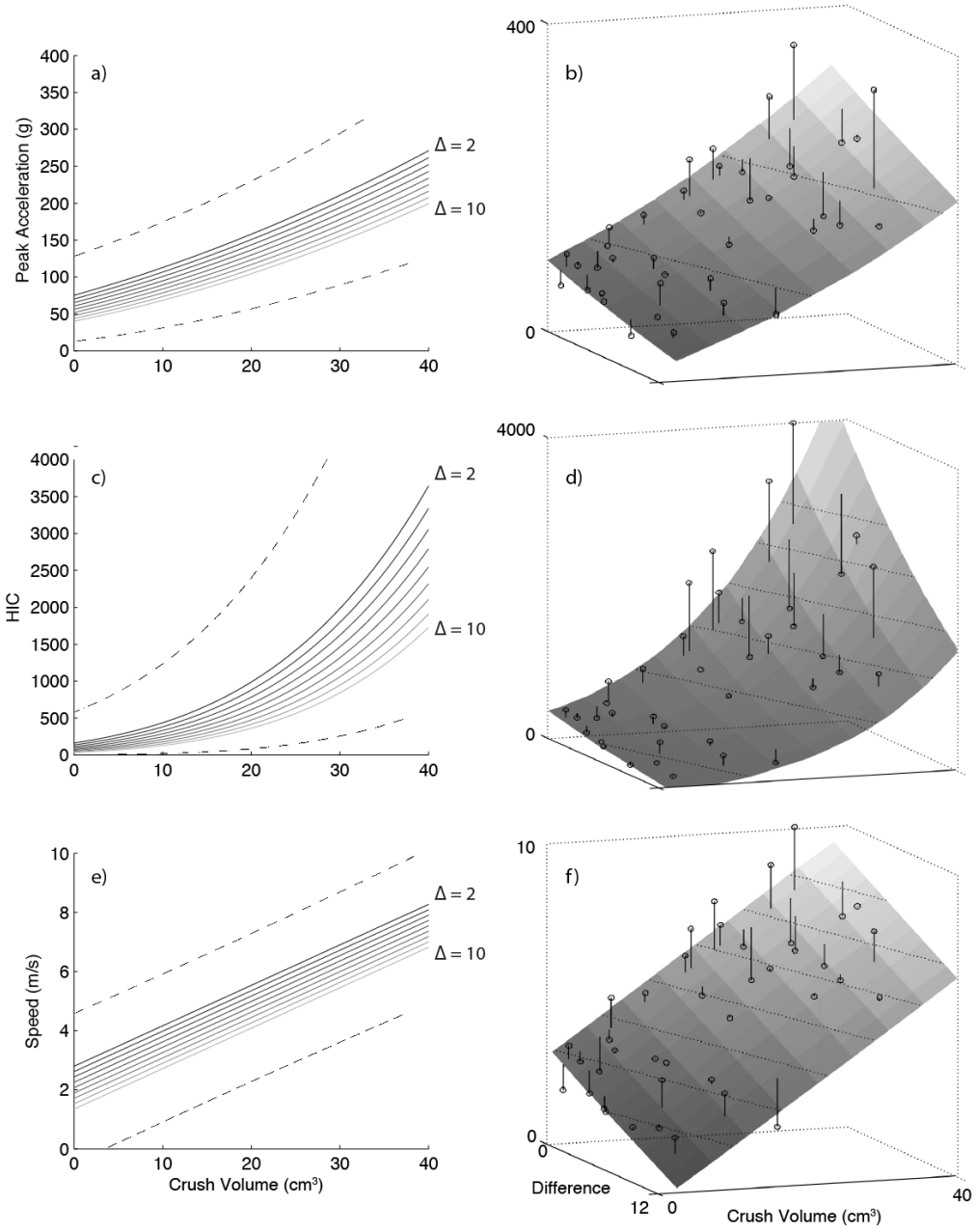

Figure 27: The regression results for peak acceleration (g) (a,b), HIC (c,d), and speed (m/s) (e,f) regressed against crush volume (cm) and helmet/headform mismatch (Δ). The left column of graphs (a,c,e) shows the regression results for 1 cm increments of mismatch from 2 to 10 cm and the $+95^{th}$ and -95^{th} percentile prediction intervals for the 2 cm and 10 cm mismatch conditions respectively (shown by dashed lines). The right column of graphs (b,d,f) shows surface plots of the regression models and the data, wherein the vertical lines represent the residuals between each data point and the surface, the shaded gradations represent 10 cm^3 increments of crush volume, and the dashed lines represent increments of each vertical axis: (b) 100 g, (d) 500, (f) 1 m/s. Note that peak acceleration and HIC have been back-transformed for these figures.

CHAPTER 5: Discussion

Experiment A

The goals of experiment A were to compare the dynamic responses and residual helmet liner deformations between cadaver heads and three headforms during helmeted drop tests, and to develop a relationship to estimate peak head/headform acceleration and impact speed from residual helmet liner maximum crush depth and crush volume. These goals attempted to quantify prior concerns that a metallic headform may not duplicate the impact dynamics of the human head and therefore may be a poor surrogate for the human head in helmet testing (Schuller et al., 1993, Becker, 1998, Willinger et al., 2000). The first hypothesis stated that metallic headforms experience different peak dynamics and generate different levels of residual crush than cadaver heads under helmeted impact conditions. The second hypothesis stated that (a) the amount of residual maximum crush depth and crush volume increases with impact energy levels and (b) residual liner crush can be used to estimate peak head/headform acceleration and impact speed. Overall, peak dynamics, maximum crush depth, and crush volume increased with increasing impact energy, and these responses differed between the cadaver heads and the three headforms. Using these data, a relationship was developed to estimate both peak head/headform acceleration and impact speed from either maximum residual crush depth or residual crush volume.

With respect to the first hypothesis, each headform differed from the cadaver heads for at least two of the five dependent variables. As a result, I failed to reject the first hypothesis that the headforms' dynamic responses and residual liner deformations differ from those of the cadaver heads. All three headforms generated peak linear

accelerations and HICs that were lower than the cadaver heads (Table 4). These differences are important because both linear acceleration and HIC are used as injury criteria and all headforms underestimated these values (Mertz and Irwin, 2003). Both the Hybrid III and ISO headforms generated peak forces that were lower than those of the cadaver heads, however force is not used as an injury metric and this difference in response may not be as meaningful from an injury perspective (Table 5). Differences in the residual crush parameters were also present. The Hybrid III headform was not significantly different from the cadaver heads for both maximum crush depth and crush volume, whereas the ISO and DOT headforms generated less maximum crush depth and lower crush volumes respectively than did the cadaver heads. While the lack of statistically significant difference in both maximum crush depth and crush volume between the Hybrid III headform and cadaver heads was encouraging, the sample size in this study was too small to interpret this lack of difference as equivalence or non-inferiority. The varying combination of differences amongst the three headforms and five dependent variables indicates that none of the headforms accurately models all of the cadaver head responses, and that the best headform for a particular application may depend on the parameter of interest (Table 5). Further work and larger studies are needed to better understand these relationships and determine which headform responds most similarly to the cadaver heads.

One possible explanation for the observed response and crush differences is how the heads/headforms fit into the Daytona Skull Cap helmet (bottom row of Figure 11). For example, all of the force traces displayed a local maximum about 1 to 2 ms after contact followed by a local minimum about 2 to 3 ms after contact (Figure 20). The force

traces then increased to their absolute peaks about 5 to 7 ms after contact. A review of the high-speed video showed that these first maxima occurred because the helmets started rebounding upward from the anvil while the heads/headforms were still descending. The heads/headforms then crushed into the helmet liners and produced the absolute peak forces. A comparison of the force traces in Figure 20 with the gaps between the upper forehead and helmet liner in Figure 11 showed that the DOT headform had the largest force decrement following the initial force peak and the largest forehead-to-liner gap, whereas the Hybrid III headform had the smallest force decrement following the initial force peak and the smallest forehead-to-liner gap. These gaps between the headforms and inner surface of the helmet liner were present even though the heads and headforms were securely fastened into the upside-down helmets and kept in this inverted posture prior to testing. Other factors such as a looser/tighter fit around the perimeter of the helmet also may have affected how well the dynamic response and residual crush of the headforms compared to the cadaver heads. The greater maximum crush depth produced by the cadaver heads compared to the headforms suggests that the cadaver heads' smaller average circumference reduces the effective loading area, producing increased maximum crush depth but not necessarily crush volume (Table 5).

Differences in the shape of the forehead region may have also contributed to the observed differences in headform acceleration or liner crush. To explore this in the future, the external surface of the headforms and cadaver heads could be quantified after digitizing the headform surfaces with a 3D digitizer (e.g. FaroArm) or from reconstructed CT scans of the cadaver heads. The radius of curvature at the forehead region could be included as a regression predictor variable to assess its effect on head/headform

acceleration and residual crush. In addition, further work is needed to characterize the biofidelity of these headforms using other impact locations, sizes and helmet models.

The Hybrid III headform's shape is specified from the average three-dimensional locations of anatomical landmarks obtained from a sample of 16 average-sized adult American male skulls combined with additional landmark data from one "average skull" from within the sample (Hubbard and McLeod, 1972). The DOT and ISO headforms are also intended to represent Western head anthropometry, although there are many differences between them. The specification of the external surface of the DOT C (medium) headform is presumed to come from 1940s anthropometric data of U.S. soldiers, though its actual genesis is uncertain (Becker, 1998). The A (small) and D (large) DOT headforms are scaled from the medium headform, even though the length-to-width ratio of human heads is independent of head circumference and a single scalable headform shape cannot be assumed (Gilchrist et al., 1988). The ISO family of headforms is not scaled from a single reference and has a smaller anterior-to-posterior length, wider breadth, and shorter head height than the DOT headform of the same circumference (Becker, 1998). Experiment B determined whether these results extend to different sized ISO headforms.

The second hypothesis stated that there would be increased residual crush at increased impact energy levels, and that this relationship could be used to estimate head/headform acceleration and impact speed from predictor variables residual maximum crush depth and crush volume. The regression models supported this hypothesis and showed that the relationship between acceleration, impact speed and residual crush was linear over the impact energies tested. This response indicated that the severities were

sufficient to produce residual crush in the helmet liner without bottoming out the foam, i.e., collapsing of cell walls and reaching the densification region where a small increase in foam strain has a large increase in stress at the high energy level (DeMarco et al., 2010, Kroeker et al., 2016). Experiment B further explored higher and lower impact severities to determine when this relationship breaks down.

Both maximum crush depth and crush volume increased significantly with impact energy, but based on the post-hoc tests, the change in maximum crush depth was smaller, though still significant, between the medium and high impact energies than between the low and medium impact energies. This trend suggests that the foam is approaching densification at the high energy level. The maximum residual crush depth values at the high impact energy were between 4.4 and 6.5 mm, which equates to about 18% to 28% of the helmet's initial liner thickness of 23.9 ± 0.25 mm. This is near the 27% level above which Schuller et al. (1993) showed that headform acceleration no longer correlated to residual deformation. Despite this potential problem with maximum crush depth at high impact severities, the crush volume measurements displayed good separation for all heads/headforms between the medium and high impact levels (Table 4). This finding suggests that residual crush volumes continue to grow as a greater area of the foam liner is recruited at higher impact severities, even if maximum residual crush depth saturates near the middle of the impact area, up to a severity where both maximum crush depth and crush volume are saturated. This finding also suggests that crush volume may be a more useful parameter than maximum crush depth for estimating peak headform acceleration at higher impact severities.

The intercept for the A_{peak} vs. crush volume regression was significantly different from zero. This is consistent with the linear elastic toe region in the stress-strain curve for expanded polystyrene foam and indicates an acceleration of 54.4 g for the cadavers and up to 92.2 g for the DOT headform can occur before permanent damage to the foam liner occurs. In contrast, the intercept for peak acceleration vs. maximum crush depth was not significantly different from zero, suggesting that maximum crush depth—at least for the pooled data—is unable to capture this aspect of the foam's material properties. The intercepts for the speed vs. maximum crush depth and crush volume regressions were also significantly different from zero, suggesting that an impact speed of at least 1.86 m/s and 3.65 m/s is necessary before maximum crush depth and crush volume can be quantified respectively. This difference suggests that maximum crush depth may be a more useful parameter than crush volume for estimating head impact speed at lower severities. Experiment B quantified crush values below the impact energies tested in Experiment A to better define the response in the toe region.

The regression models show that peak linear head/headform acceleration and impact speed can be estimated from the foam liner's maximum crush depth or crush volume. The regression model of A_{peak} vs. maximum crush depth was independent of head/headform type, but had the largest prediction interval (± 71 g at a maximum crush of 4.5 mm). The regression models of A_{peak} vs. crush volume had smaller prediction intervals (cadavers ± 63 g, DOT ± 48 g, Hybrid III ± 41 g, and ISO ± 23 g at a crush volume of 30 cm^3), but they were head/headform specific and come with the added cost of CT imaging and complex post-processing algorithms. Similarly wide prediction intervals exist for the speed vs. maximum crush depth regression (cadavers ± 2.2 m/s,

DOT ± 1.6 m/s, Hybrid III ± 1.0 m/s, and ISO ± 2.8 m/s at a maximum crush depth of 4.5 mm) and the speed vs. crush volume regressions (cadavers ± 0.92 m/s, DOT ± 0.94 m/s, Hybrid III ± 0.83 m/s, and ISO ± 1.05 m/s at a crush volume of 30 cm^3). While the prediction intervals for the headforms may narrow with more test data, it remains unclear whether the larger prediction intervals for the cadavers will also narrow or whether they simply represent a larger underlying variability in these data (Figure 21 and Figure 22).

From prior studies, we know that density significantly affects the impact attenuation properties of foam and the density within a single helmet can vary up to about 7% (Kroeker et al., 2014, Kroeker et al., 2016). Although the inter- and intra-helmet variability in foam density of the tested helmets was not measured, it was assumed that the density across all Daytona Skullcap helmets was the same. Some of the variability present in the large prediction intervals may be due to density differences. To examine if density differences between helmets affect peak acceleration and/or residual crush values, foam density could be quantified from cores extracted from the foam liners of tested helmets and included as a regression predictor variable.

To reduce the variance in the data, the current work was limited to a single helmet model and size, and used cadaver heads that approximated only one size of each metallic headform. A comparison of the actual time-varying acceleration and force signals showed that there was generally more variability in the cadaver signals than in the headform signals, which is expected given the inherent variability of biological tissue and the fact that different heads were tested. Part of this increased variability may be due to the angular kinematics in the rigid body transformation of linear acceleration to the center of mass of the cadaver heads; however, the contribution of the angular components was low

and variability was also present in the untransformed cadaver acceleration traces, suggesting that skull compliance and skull vibration also may have contributed. There was no artifact in the cadaver signals to indicate that the brain shifted during impact and therefore the observed differences are not likely related to the cadaver preparation methods. In contrast to prior work by Thom et al. (1996), the peak acceleration observed here was significantly higher for the DOT headform than for the ISO headform. Thom et al. tested five motorcycle helmets at varying impact locations and their data were pooled from multiple headform sizes, helmet models and test conditions. As a result, a direct comparison between results may not be appropriate.

Experiment A compared dynamic responses of cadaver head and 3 different headforms during helmeted impacts at three energies and quantified helmet liner residual crush depth and volume. For an equivalent impact energy, the peak acceleration and HIC for a cadaver head is different from that of the three metallic headforms tested here. Linear regression models allowed head/headform acceleration, HIC, and impact speed to be estimated from residual crush depth and volume.

Experiment B

The goal of Experiment B was to understand how helmet/headform size mismatch affects headform impact kinematics and residual crush to a motorcycle helmet liner. This goal was achieved by examining how three kinematic variables (peak acceleration, HIC, and impact speed) varied with three predictor variables (maximum residual crush depth, residual crush volume, and helmet-headform circumference mismatch). In support of our first hypothesis, the regression analyses showed that all three kinematic variables significantly decreased as the mismatch between the helmet and headform

circumferences increased. The regression analyses also showed that all three kinematic variables significantly increased as maximum residual crush depth and residual crush volume increased. This latter finding supported the second hypothesis of Experiment B, that the three kinematic variables can be estimated—albeit with wide prediction intervals—from a combination of helmet-headform mismatch and one of the two variables quantifying helmet crush: maximum residual crush depth below 7.9 mm or residual crush volume less than 40 cm^3. Overall, these findings mean that both helmet fit and residual crush need to be considered when estimating the peak headform acceleration, HIC, and impact speed from a damaged motorcycle helmet.

When compressed, the EPS foam used in most motorcycle helmet liners has a characteristic stress-strain curve with three regions: a linear-elastic region, a fracture plateau, and a densification region (Mills and Gilchrist, 1991, Zhang et al., 1998, Ouellet et al., 2006). During impact attenuation testing, incremental increases in impact speed (or energy) cause linearly increasing amounts of foam compression and headform acceleration while in the fracture plateau region of the stress-strain curve. Within the densification region, additional increases in impact speed (or energy) cause proportionally smaller increases in foam compression and proportionally larger increases in headform acceleration because the foam stiffens as it densifies and unabsorbed energy is transferred to the head (Hui and Yu, 2002, DeMarco et al., 2010, Kroeker et al., 2016). In this study, some impacts that produced more than about 7.9 mm of maximum residual crush depth and 40 cm^3 of residual crush volume had peak accelerations that indicated the densification region was reached (Appendix E1 and E4). These observations were echoed when the root mean squared (RMSE) error for the regressions of $\sqrt{A_{peak}}$ (Equations 10

and 13) were plotted across the range of observed maximum crush depth (mm) and crush volume (cm^3) (Figure 28a and b). The differences between the actual and predicted acceleration increased at 7.9 mm of crush depth and 40 cm^3 of crush volume and this provided further support for limiting the use of the regression equations to crush values below these thresholds.

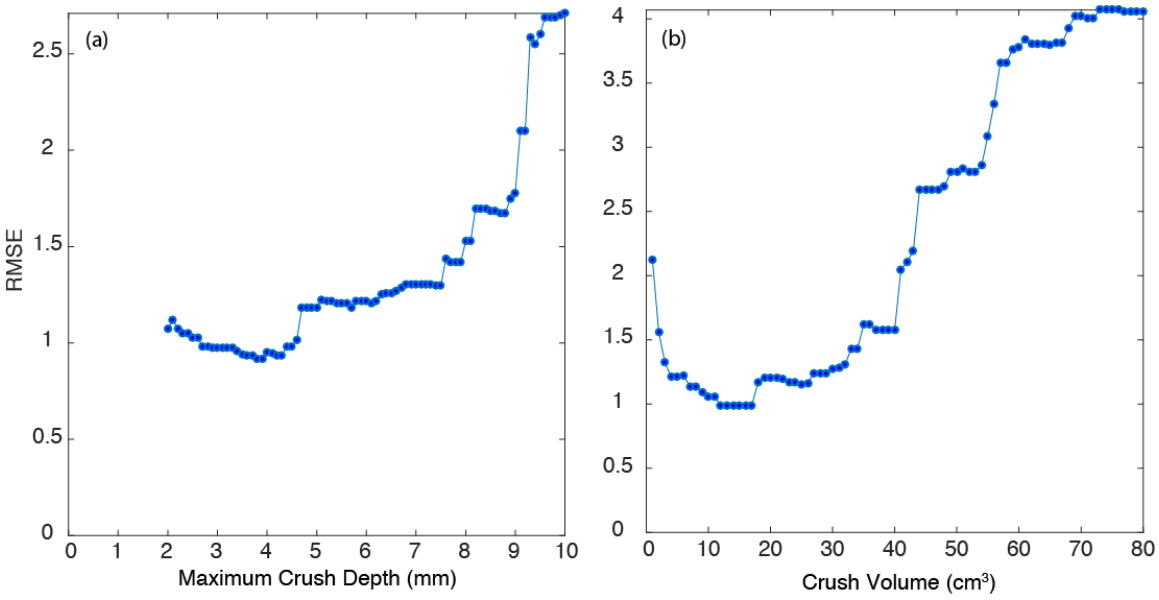

Figure 28: RMSE vs. (a) maximum crush depth (mm) and (b) crush volume (cm^3) for linear regressions with $\sqrt{A_{peak}}$ as the response variable and circumference-difference, (a) maximum crush depth (b) and crush volume as predictor variables. RMSE rapidly increases around 8 mm and 40 cm^3. A similar trend was observed when HIC was the response variable.

For a given maximum residual crush depth or residual crush volume, the kinematic variables studied here significantly decreased as helmet-headform mismatch increased. Based on the regression models, 5 mm of maximum residual crush depth corresponded to an estimated head acceleration of 248 g, HIC of 2148 and impact speed of 7.5 m/s for a 2 cm mismatch (which would likely be considered a properly fitting helmet with the comfort foam in place) whereas the same 5 mm of maximum residual

crush depth corresponded to a head acceleration of 147 g, HIC of 734 and impact speed of only 5.3 m/s for a 10 cm mismatch (which would be considered a poor fitting helmet even with the comfort foam in place). This comparison shows the importance of including helmet-headform mismatch when estimating impact kinematics from maximum residual crush depth.

The results also indicated that a headform penetrates further into the foam of an oversized helmet than a properly sized helmet for a given impact speed. For example, at an impact speed of 7 m/s, a 2.25 cm mismatch produced a maximum crush depth of 6.6 mm and a peak acceleration of 275 g in one of the test helmets whereas a 10.25 cm mismatch at the same impact speed produced a maximum crush depth of 8.9 mm and a peak headform acceleration of 240 g in a different test helmet. The headform likely penetrated further into the foam liner of the oversized helmet because the contact area was reduced by the larger difference in the radii of the interacting surfaces, and this additional penetration likely contributed to the reduced peak acceleration. This phenomenon was also observed in Experiment A where the slightly smaller cadaver heads produced more maximum crush depth than the headforms (Table 1, Table 4). Although this example suggests that wearing an oversized helmet can be protective, it fails to highlight the added risk of an oversize helmet rolling off the head during a crash and the detrimental effect of the foam liner bottoming-out at a lower impact speed than it would for a properly fitting helmet. For example, at an impact speed of 8.5 m/s, a test with a 5.6 cm mismatch produced a residual crush depth of 8.9 mm and a peak acceleration of 644 g whereas a different test at the same impact speed with a 2 cm mismatch produced only 4.4 mm of residual crush depth and a peak acceleration of 291

g. These examples show that the large benefit of wearing a well-fitting helmet in a serious impact far outweighs the small benefit of wearing an oversize helmet in a low severity impact.

The finding of decreasing headform acceleration and HIC with increasing helmet-headform mismatch is consistent with prior FE modeling work of motorcycle helmet impacts (Chang et al., 2001). Our finding is not entirely consistent with Rivara et al. (1999), who examined the relationship between bicycle helmet fit and head injuries in children and found that individuals with a "poor fit" had a 1.96 (95% confidence interval: 1.10 to 3.73) times increased risk of head injury. In the Rivara et al. study, the average circumference mismatch across all age groups was 4.2 to 5.3 cm, which lies in the middle of the range of mismatches studied here. Rivara et al. suggested that when a helmet is too large, the distance between the head and helmet is increased, potentially allowing the head to accelerate (relative to the helmet) during a crash before it contacts the energy absorbing liner thereby undermining the liner's ability to absorb the forces of the impact. Our study is not well suited for evaluating Rivara's hypothesis because our inverted drop configuration and impact location likely created similar gaps between the headforms and helmets in the impact region across all test conditions. Although we did not quantify this pre-impact gap between the liner and headform, our tests did not replicate the range of gaps that could exist over the entire interface between the head and helmet during actual use. From this perspective, our results are limited to impacts to regions of the head that are in close proximity to the helmet liner and may not apply to other regions where a large pre-impact gap between the head and liner exists.

Further work is needed to explore the effect of these gaps on the relationships developed here.

The regression analyses showed that the response variables significantly increased with maximum residual crush depth and residual crush volume. This finding agrees with other studies that found increased residual foam crush with increased impact energy (Schuller et al., 1993, McIntosh and Patton, 2012). Within the regressed data, our maximum residual crush depths (< 7.9 mm) did not exceed 33% of the initial foam thickness. Although we observed maximum residual crush depth that reached 45% of the initial foam thickness, levels above 33% were associated with a wide range of peak accelerations and HIC values. Schuller et al. (1993) determined that head acceleration could be reliably estimated only for residual liner deformations less than 27% of the initial liner thickness; additional residual deformation was associated with a wide range of headform accelerations. Both their findings and our findings suggest that there is a ceiling to the amount of residual deformation that can be used to estimate headform acceleration, despite the fact that helmet foam liners can potentially crush up to 90% during an impact (Kroeker et al., 2016). This ceiling may be related to foam thickness, density, densification during the impact, and visible cracking of the foam liner that was observed in the higher speed impact tests.

Application to field helmets and limitations

The Daytona Skull Cap used here was a DOT-approved, shorty-style helmet that was selected for its simple design and lack of ventilation holes. This study focused on a single helmet that had a relatively constant foam thickness and a smooth shell without vents, and a single impact location was chosen away from the foam's edge. The utility of

the regression coefficients presented here for different helmets, other impact locations, other foam thicknesses, larger mismatches, impacts to a vent, ridge or rivet, and impacts near the foam's edge remains unknown.

Quantifying foam thickness through CT scans accounted for the air gap between the foam and shell and any residual crush to the outer surface of the foam liner. Aside from the cost, the primary limitations of CT are metallic artifact and creating the necessary contrast between the polystyrene foam (-950 HU) and air (-1000 HU). To address these problems, the metal rivets were removed from the helmets prior to scanning, small holes were drilled through the shell and foam at the vertex, and then helmets were submerged in a saline solution with a surfactant (Figure 15). These procedures worked well for research purposes, but may not be possible in forensic cases where evidence cannot be altered. Other techniques to minimize metal artifact in CT (Boas and Fleischmann, 2011) or combining CT and laser scanning could yield less-destructive approaches to quantifying residual helmet crush.

The small variations (about ± 0.25 mm) that were observed in the undamaged liner thicknesses suggest that a single undamaged helmet could have been used to estimate the residual damage in our test helmets. It is not known whether other helmets have similarly narrow manufacturing tolerances. Data from two helmets were excluded from the analysis because of what appeared to be pre-existing crush near the impact location. This kind of unrelated damage may not be detectable if it is wholly contained within the impact region. Other helmets may use different foam densities (and sometimes more than one density in a single helmet), and the compression level where densification

begins varies with foam density (Kroeker et al., 2016). Investigators should consider these factors when applying the data presented here to other conditions.

Headform and helmet circumferences were measured in the horizontal plane rather than at the impact site because these measurements are more likely to be available following real-world exposures. For my impact location, these surrogate measurements were reasonable estimates of the impact site geometry, but investigators should ensure this assumption is valid for their impact location.

The XL and 2XL EPS liners had similar foam thicknesses and circumferences (Table 2) but were assembled inside different sized shells with additional foam placed between the liner and 2XL shell. As per the manufacturer, this supplemental foam was added during the helmet assembly process to improve the fit of the EPS liner in the 2XL shell. Upon dismantling various 2XL helmets, it was apparent that different techniques were used to improve the fit of the foam liner into the shell for different samples of the same size helmet. One technique used an additional layer of low-density foam, approximately 2 inches wide, at the lower edge around the circumference of the helmet (Figure 29a). Another technique placed a piece of foam, with a different density than that used in the first technique, near the vertex and into the forehead region by variable amounts (Figure 19, Figure 29b). The supplemental foam at the vertex could not be distinguished from the energy absorbing liner during segmentation and consequently, these helmets were not used in the crush volume analysis. Relying solely on the manufacturer's sizing labels to identify a properly fitting helmet should be done cautiously as a single size EPS liner can be used in different sized shells with supplemental foam spacers to improve the fit between the liner and shell.

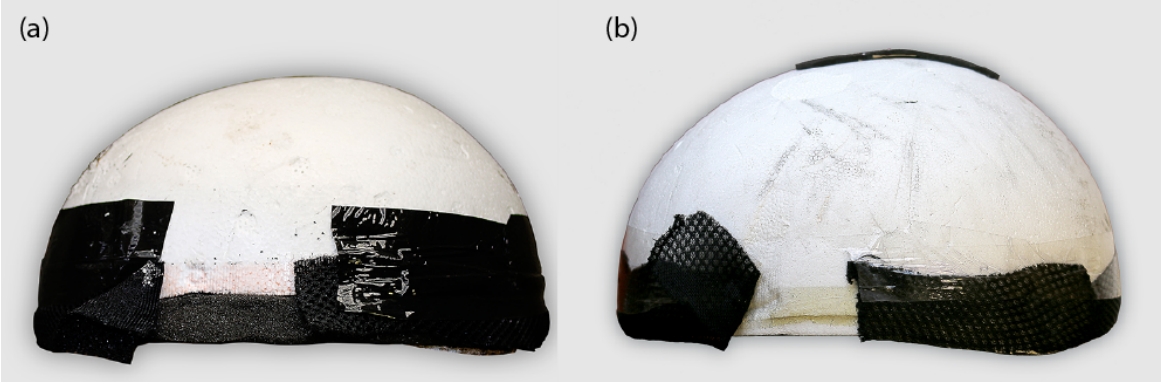

Figure 29: Foam liner from two dismantled size 2XL helmets with a section of black tape and mesh removed. (a) Supplemental low-density foam placed around the EPS liner circumference at the bottom edge. (b) A supplemental piece of foam, of a different density than in (a) placed at the liner's vertex and into the forehead region by variable amounts.

A typical goal in motorcycle helmet forensic investigations is to estimate the head acceleration and/or impact speed experienced by the motorcyclist during a head impact. Estimating the head acceleration allows conclusions to be made about the risk of head injury and estimating the head impact speed can be useful in the accident reconstruction process. To that end, an investigator may attempt to replicate helmet damage by placing an exemplar helmet on an instrumented headform and then perform a drop test at a given impact speed while recording headform acceleration. This process is then repeated with a new exemplar helmet until the investigator is satisfied that the damage sustained in the accident helmet has been replicated. The motorcyclist's head impact speed and acceleration during the accident are assumed to be the values obtained during the drop test that best replicated the accident-related helmet damage (Cooter, 1990, Hope and Chinn, 1990, Smith et al., 1994, Wobrock et al., 2003, Loftis et al., 2011, McIntosh and Patton, 2012). Based on the data presented here, the peak acceleration experienced by a human head is different from that experienced by a headform in equivalent impact conditions and the residual crush experienced by the helmet liner is different when

impacted by a human head than by a headform. Thus additional interpretation of accident-specific test data is needed before drawing conclusions about the accident itself. The amount of interpretation depends on assumptions made by the investigator regarding the similarities and differences between the accident helmet and the test helmets used here.

To directly use the data reported here, an investigator must assume that the field helmet responds similarly to the helmets tested. These assumptions include that the field helmet has similar foam density and thickness and shell material as the helmets tested here. If these assumptions are met, then one can measure the maximum residual crush or crush volume of that field helmet and refer to the cadaver data to estimate the head acceleration (Equations 5 & 6, Figure 21, Figure 22a). Additional steps can be performed to help ensure the field helmet responds similarly to the test helmets. Exemplar field helmets can be tested over the range of impact energies or speeds tested here with a metallic headform and the acceleration and crush values can be compared to our findings to establish if the response is the same. If the response is the same, then one can rely on the cadaver data with more confidence. If a field helmet is different from the helmets tested here, i.e. different foam density or thickness or different shell material, then it may be necessary to establish an acceleration–crush relationship with the different helmet through additional drop-testing over a range of impact speeds with instrumented cadaver heads.

The regression models from Experiment A highlight potential problems when estimating a motorcyclist's peak head acceleration and injury risk by reconstructing collision-induced helmet damage using one of the headforms (Hurt and Ouellet, 1976,

Hope and Chinn, 1990, Schuller et al., 1993, Smith et al., 1994, Wobrock et al., 2003). For example, if one of the cadaver impacts (252 g, 5.4 mm and 35.3 cm^3 residual crush) is taken to represent a real-world impact, then a reconstruction based on maximum residual crush depth would yield a peak head acceleration (mean ± 95%ile prediction intervals) of 252 ± 71 g, and reconstructions based on crush volume using the cadaver heads, Hybrid III, DOT and ISO headforms would yield peak head accelerations (mean ± 95%ile prediction intervals) of 250 ± 63 g, 222 ± 41 g, 300 ± 50 g and 196 ± 22 g respectively. These ranges yield skull fracture risks from 4% to 96% (Mertz and Irwin, 2003). These numbers show that head acceleration and injury risk estimates based on the reconstructions of accident-involved helmets should account for the larger prediction intervals when using maximum crush and the differences between the response of headforms and cadaver heads when using crush volume.

Future Work

The following future work will build on the foundation established in this research and improve the ability to estimate a motorcyclist's head impact severity from residual liner crush.

Cadaver testing

The low, medium, and high impact energies of the cadaver testing in Experiment A correspond to 5.61 ± 0.164 m/s, 7.93 ± 0.233 m/s, and 9.08 ± 0.254 m/s. The low energy impacts were within the range of head impact speeds of motorcyclists falling from a seated height. A typical center of gravity head-height while seated on a motorcycle is approximately 1.5 m, which corresponds to a vertical head impact speed of 5.5 m/s when falling is uninhibited. Falls from lower heights or body contacts with the ground or

surrounding objects prior to head contact may reduce the head impact speed. Additional cadaver testing at lower severities will account for potential lower head impact speeds and improve the range over which the cadaver regression equations remain valid. Additional testing across the range of 1 to 10 m/s will potentially reduce the overall variability in the data, providing a narrower range of head injury risk for a given impact. Testing other impact locations and additional helmet models will expand the application of these results to other helmets and additional impact locations. With additional cadaver data it may be possible to develop a method to relate head accelerations of a metallic headform from reconstructed impacts to human head accelerations at locations and for helmets not tested here.

Finite element modeling

An additional area of future work is to develop a validated FE model of a helmeted head/headform to simulate impacts and assess the effect of different headform sizes and shapes, and foam and shell materials on head acceleration. A model requires geometry and material properties of the head/headform and helmet. The headforms tested here are made from a single material, although the Hybrid III headform is covered with a vinyl nitrile skin, and their geometries are easily obtained. Many validated human head FE models are currently being used to study brain injury and these models can be utilized for helmeted human head impact simulations (Patton et al., 2013). Helmet geometry can be obtained from reconstructed CT scans while shell and foam material properties can be determined from testing. Shell material properties can be determined through 3-point bending tests while foam material properties, which are strain rate dependent, can be

determined from impact attenuation tests of extracted foam coupons at various impact speeds. Simulated impacts can then be validated with the data collected here.

Summary

In this research, Experiment A compared the dynamic responses, maximum residual helmet liner crush depth, and residual crush volume between three common surrogate headforms and similarly sized cadaver heads during helmeted drop tests onto a flat anvil. The cadaver heads and all three headforms responded differently, and the nature and size of these differences varied between headforms and the variables of interest. Residual maximum crush depth and crush volume can be used to estimate peak head/headform acceleration and head impact speed; however, headform acceleration and injury risk estimates based on the regression analyses should account for the large prediction intervals (Figure 26 and Figure 27). Overall, the results showed that significant differences between the cadaver heads and headforms need to be accounted for when attempting to estimate a helmeted impact exposure using the residual crush generated by a headform; however, more work is needed to determine how to accurately account for these differences.

In Experiment B, impact attenuation tests were performed on a range of headform and helmet sizes across of range of impact speeds. Peak headform acceleration, HIC, and impact speed were all reduced as the mismatch between the helmet liner and headform circumference increased. Peak headform acceleration, HIC, and impact speed can be estimated from maximum residual crush depths less than 7.9 mm or residual crush

volumes less than 40 cm^3. These findings provide the foundation for researchers and forensic investigators to estimate head kinematics from the residual crush of a helmet's liner.

References

Allsop, D.L., Perl, T.R., Warner, C.Y. (1991) Force/deflection and fracture characteristics of the temporo-parietal region of the human head. Society of Automotive Engineering Transactions 100 (6), 2009-2018

Australian/New Zealand Standard (2006) AS/NZS 1698:2006 Protective Helmets for Vehicle Users.

Becker, E.B. (1998) In: Narayan Yoganandan, F.a.P., Sanford J. Larson, Anthony Sances ed. Frontiers in head & neck trauma clinical and biomechanical. IOS Press, Washington D.C.

Beier, G., Schuller, E., Schuck, M., Ewing, C.L., Becker, E.D., Thomas, D.J. (1980) Center of gravity and moments of inertia of human heads. IRCOBI Conference, Graz, Austria, 218-28

Ben-Dor, G., Cederbaum, G., Mazor, G., Igra, O. (1996) Well tailored compressive stress-strain relations for elastomeric foams in uni-axial stress compression. Journal of Materials Science 31, 1107-1113

Beusenberg, M.C., Happee, R. (1993) An experimental evaluation of crash helmet design and effectiveness in standard impact tests. In: Proceedings of the International IRCOBI Conference on the Biomechanics of Impacts, Eindhoven, The Netherlands.

Boas, F.E., Fleischmann, D. (2011) Evaluation of two iterative techniques for reducing metal artifacts in computed tomography. Radiology 259 (3), 894-902

British Standards Institute (1985) Specification for Protective Helmets for Vehicle Users. BS 6658.

Chang, L.-T., Chang, C.-H., Chang, G.-L., 2001. Fit effect of motorcycle helmet - a finite element modeling. JSME 44 (1), 185-192

Cobb, B.R., Macalister, A., Young, T.J., Kemper, A.R., Rowson, S., Duma, S.M. (2014) Quantitative comparison of hybrid III and national operating committee on standards for athletic equipment headform shape characteristics and implications on football helmet fit. Journal of Sports Engineering and Technology 229 (1), 39-46

Consumer Product Safety Commission (1998) 16 CFR Part 1203 Safety Standard for Bicycle Helmets. Federal Register 63 (46).

Cooter, R.D. (1990) Computed tomography in the assessment of protective helmet deformation. The Journal of Trauma 30 (1), 55-68

De Vries, D.V. (2009) Characterization of polymeric foams. Department of Mechanical Engineering, Eindhoven University of Technology.

Demarco, A.L., Chimich, D.D., Gardiner, J.C., Nightingale, R.W., Siegmund, G.P. (2010) The impact response of motorcycle helmets at different impact severities. Accident Analysis & Prevention 42, 1778-1784

Gibson, L.J. (1989) Modelling the mechanical behavior of cellular materials. Materials Science and Engineering A110, 1-36

Gibson, L.J., Ashby, M.F. (1999) Cellular solids. Cambridge University Press, New York, NY.

Gilchrist, A., Mills, N.J. (1994) Modeling of the impact response of motorcycle helmets. International Journal of Impact Engineering 15 (3), 201-218

Gilchrist, A., Mills, N.J., Khan, T. (1988) Survey of head, helmet and headform sizes related to motorcycle design. Ergonomics 21 (10), 1395-1412

Got, C., Patel, A., Fayon, A., Tarriere, C., Walfisch, G. (1978) Results of experimental head inpacts on cadavers: The various data obtained and their relations to some measured physical parameters. Society of Automotive Engineers, Technical Paper 780887, 57-99

Hodgson, V.R. (1975) National operating committee on standards for athletic equipment football helmet certification program. Medicine and Science in Sports 7 (3), 225-232

Hodgson, V.R., Thomas, L.M. (1971) Comparison of head acceleration injury indices in cadaver skull fracture. In: Proceedings of the Proceedings of the 15th Stapp Car Crash Conference.

Hodgson, V.R., Thomas, L.M. (1977) Breaking strength of the human skull versus impact surface curvature. Department of Transportation HS-801-002.

Hope, P.D., Chinn, B.P. (1990) The correlation of damage to crash helmets with injury and the implications for injury tolerance criteria. In: Proceedings of the International IRCOBI Conference on the Biomechanics of Impact, Bron, France, pp. 319-331.

Hubbard, R., Mcleod, D. (1974) Definition and development of a crash dummy head. Society of Automotive Engineers, Technical paper 741193, 95-109

Hubbard, R.P., Mcleod, D.G. (1972) A basis for crash dummy skull and head geometry. In: Proceedings of the Proceedings of the Symposium on Human Impact Response, General Motors Research Laboratories, Warren, MI.

Hui, S.K., Yu, T.X. (2002) Modeling of the effectiveness of bicycle helmets under impact. International Journal of Mechanical Sciences 22, 1081-1100

Hurt, H.H., Ouellet, J.V. (1976) Analysis of accident involved motorcycle safety helmets. In: Proceedings of the 20th Annual Proceedings of the Association for the Advancement of Automotive Medicine, pp. 187-197.

Hurt, H.H., Ouellet, J.V., Thom, D.R. (1981) Motorcycle accident cause factors and identification of countermeasures, volume 1: Technical report. DOT HS-5-01160

Hurt, H.H., Thom, D.R., Ouellet, J.V. (1998) Testing the positional stability of motorcycle helmets. In: Proceedings of the 16th International Technical Conference on the Enhanced Safety of Vehicles, Windsor, Canada.

International Standards Organization (1983) Headforms for use in the testing of protective helmets. ISO-DIS-6220. Geneva, Switzerland.

Kang, H.-S., Willilnger, R., Diaw, B.M. (1997) Validation of a 3d anatomic human head model and replication of head impact in motorcycle accident by finite element modeling. 41st Stapp Car Crash Conference.

Kang, Y.-S., Moorhouse, K., Bolte, I.V.J.H. (2011) Measurement of six degrees of freedom head kinematics in impact conditions employing six accelerometers and three angular rate sensors (6aω configuration). Journal of Biomechanical Engineering 133 (11), 111007-1-111007-11

Kostopoulos, V., Markopoulos, Y.P., Giannopoulos, G., Vlachos, D.E. (2002) Finite element analysis of impact damage response of composite motorcycle safety helmets. Composites Part B (33), 99-107

Kroeker, S.G., Bonin, S.J., Demarco, A.L., Good, C.A. (2014) Does age affect the impact properties of helmet foam liners? In: Proceedings of the World Congress of Biomechanics, Boston, MA.

Kroeker, S.G., Bonin, S.J., Demarco, A.L., Good, C.A., Siegmund, G.P. (2016) Age does not affect the material properties of expanded polystyrene liners in field-used bicycle helmets. Journal of Biomechanical Engineering 138. 041005-1-041005-9

Lawrence, B.A., Max, W., Miller, T.R. (2002) Costs of injuries resulting from motorcycle crashes: A literature review. DOT HS-809-242.

Lissner, H.R., Lebow, M., Evans, F.G. (1960) Experimental studies on the relation between acceleration intracranial pressure changes in man. Surgery, Gynecology and Obstetrics 111, 329-338

Liu, B., Ivers, R., Norton, R., Boufous, S., Blows, S., Lo, S. (2008) Helmets for preventing injury in motorcycle riders. The Cochrane Collaboration, 1-37

Loftis, K.L., Moreno, D.P., Tan, J., Gabler, H.C., Stitzel, J.D. (2011) Utilizing computed tomography scans for analysis of motorcycle helmets in real-world crashes. In: Proceedings of the 48th Annual Rocky Mountain Bioengineering Symposium & 48th International ISA Biomedical Sciences Instrumentation Symposium, Denver, Colorado, USA, pp. 234-239.

Lorensen, W.E., Cline, H.E. (1987) Marching cubes: A high resolution 3D surface construction algorithm. Computer Graphics 21 (4), 163-169

Loyd, A.M., Nightingale, R.W., Song, Y., Luck, J.F., Cutcliffe, H., Myers, B.S., Bass, C. (2014) The response of the adult and atd heads to impacts onto a rigid surface. Accid Anal Prev 72, 219-29

Martin, P.G., Hall, G.W., Crandall, J.R., Pilkey, W.D. (1998) Measuring the acceleration of a rigid body. Shock & Vibration 5 (4), 211-224

Max, W., Stark, B., Root, S. (1998) Putting a lid on injury costs: The economic impact of the california motorcycle helmet law. Journal of Trauma, Injury, Infection, and Critical Care 45 (3), 550-556

Mcintosh, A.S., Patton, D.A. (2012) Impact reconstruction from damage to pedal and motorcycle helmets. Journal of Sports Engineering and Technology 226 (3/4), 274-281

Mertz, H.J., Irwin, L.I. (2003) Biomechanical and scaling bases for frontal and side impact injury assessment reference values. Stapp Car Crash Journal 47, 155-188

Mills, N.J., Gilchrist, A. (1991) The effectiveness of foams in bicycle and motorcycle helmets. Accident Analysis & Prevention 23 (2/3), 153-163

Mills, N.J., Gilchrist, A. (2008) Finite-element analysis of bicycle helmet oblique impacts. International Journal of Impact Engineering 35, 1087-1101

Mills, N.J., Wilkes, S., Derler, S., Flisch, A. (2009) Fea of oblique impact tests on a motorcycle helmet. International Journal of Impact Engineering 36, 913-925

Murdock, M.A., Waxman, K. (1991) Helmet use improves outcomes after motorcycle accidents. Western Journal of Medicine 155 (4), 370-372

National Highway Traffic Safety Administration (1996) Report to congress: Benefits of safety belts and motorcycle helmets. U.S. Department of Transportation.

National Highway Traffic Safety Administration (1997) Code of federal regulations. In: Transportation, T. ed.

National Operating Committee on Standards for Athletic Equipment (2013) Standard test method and equipment used in evaluating the performance characteristics of protective headgear/equipment. NOCSAE DOC ND 001-11M13.

Nauhm, A.M., Smith, R., Ward, C.C. (1977) Intracranial pressure dynamics during head impact, paper no. 770922. In: Proceedings of the Proceedings of the 21st Stapp Car Crash Conference, pp. 339-366.

Nelson, D., Sklar, D., Skipper, B., Mcfeeley, P.J. (1992) Motorcycle fatalities in new mexico: The association of helmet nonuse with alcohol intoxication. Annals of Emergency Medicine 21 (3), 279-283

Newman, J.A., Beusenberg, M.C., Shewchenko, N., Withnall, C., Fournier, E. (2005) Verification of biomechanical methods employed in a comprehensive study of mild traumatic brain injury and the effectiveness of american football helmets. J Biomech 38 (7), 1469-81

Nusholtz, G.S., Lux, P., Kaiker, P., Janicki, M.A. (1984) Head impact response - skull deformation and angular accelerations. Society of Automotive Engineering, Technical paper 847657

Offner, P.J., Rivara, F.P., Maier, R.V. (1992) The impact of motorcycle helmet use. Journal of Trauma 32 (5), 636-642

Oliver, M. (1990) Charles lombard; revolutionized crash helmets for pilots, cyclists. Los Angeles Times.

Orsay, E., Holden, J.A., Williams, J., Lumpkin, J.R. (1995) Motorcycle trauma in the state of illinois: Analysis of the illinois department of public health trauma registry. Annals of Emergency Medicine 26 (4), 455-460

Ouellet, S., Cronin, D., Worswick, M. (2006) Compressive response of polymeric foams under quasi-static, medium and high strain rate conditions. Polymer Testing 25, 731-743

Patton, D.A., Mcintosh, A.S., Kleiven, S. (2013) The biomechanical determinants of concussion: Finite element solutions to investigate brain tissue deformations during sproting impacts to the unprotected head. Journal of Applied Biomechanics 29, 721-730

Peek-Asa, C., Mcarthur, D.L., Kraus, J.F. (1999) The prevalence of non-standard helmet use and head injuries among motorcycle riders. Accident Analysis & Prevention 31 (3), 229-233

Pinnoji, P.K., Mahajan, P., Bourdet, N., Deck, C., Willinger, R. (2010) Impact dynamice of metal foam shells for motorcycle helmets: Experiments and numerical modeling. International Journal of Impact Engineering 37, 274-284

Prasad, P., Mertz, H.J. (1985) The position of the united states delegation to the iso working group 6 on the use of hic in the automotive environment. Society of Automotive Engineers, Technical paper 851246

Rivara, F.P., Astley, S.J., Clarren, S.K., Thompson, D.C., Thompson, R.S. (1999) Fit of bicycle safety helmets and risk of head injuries in children. Injury Prevention 5, 194-197

Rowlands, J., Rivara, F., Salzberg, P., Soderberg, R., Maier, R., Koespell, T. (1996) Motorcycle helmet use and injury outcome and hospitalization costs from crashes in Washington state. American Journal of Public Health 86 (1), 41-45

Schuller, E., Konig, W., Beier, G., (1993) Criteria for head impact protection by motorcycle helmets. In: Proceedings of the International IRCOBI Conference on the Biomechanics of Impact., Bron, France, pp. 283-294.

Siegmund, G.P., Guskiewicz, K.M., Marshall, S.W., Demarco, A.L., Bonin, S.J. (2014) A headform for testing helmet and mouthguard sensors that measure head impact severity in football players. Ann Biomed Eng 42 (9), 1834-45

Smith, T.A., Tees, D., Thom, D.R., Hurt, H.H. (1994) Evaluation and replication of impact damage to bicycle helmets. Accid Anal Prev 26 (6), 795-802

Snell Memorial Foundation (2010) Shell helmet certification program.

Snell Memorial Foundation (2015) M2015 standard for protective headgear for use with motorcycles and other motorized vehicles.

Suh, K.W., Skochdopole, R.E. (1980) Encyclopedia of chemical technology, 3rd edition Kirk-Othmer.

Tarriere, C., Walfisch, G., Fayon, A., Got, C., Guillon, F., Patel, A., Bureau, J. (1982) Acceleration, jerk and neck flexion angle: Their respective influences on the occurance of brain injury. 133-152

Thai, K.T., Mcintosh, A.S., Pang, T.Y. (2015a) Factors affecting motorcycle helmet use: Size, selection, stability, and position. Traffic Injury Prevention. 16 (3), 276-282

Thai, K.T., Mcintosh, A.S., Pang, T.Y. (2015b) Bicycle helmet size, adjustment, and stability. Traffic Injury Prevention. 16 (3), 268-275

Thom, D.R., Hurt, H.H., Smith, T.A., Year. Motorcycle helmet test headform and test apparatus comparison. In: Proceedings of the Proceedings on the 16th ESV.

U.S. Department of Transportation (1966) Highway safety act of 1966, 23, Chapter 4.

U.S. Department of Transportation (2004) Motorcycle helmet effectiveness revisited: Technical report. National Highway Traffic Safety Administration DOT HS 809-715

U.S. Department of Transportation (2006) FMVSS No. 218 National Highway Traffic Safety Administration Laboratory Test Procedure.

U.S. Department of Transportation (2010) Motorcycle helmet use in 2011 – overall results. National Highway Administration DOT HS 811 610.

U.S. Department of Transportation (2012) Frequently asked questions - quick facts 2010. National Highway Traffic Safety Administration.

U.S. Department of Transportation (2013) Motorcycle helmet use in 2013 - overall results. Traffic Safety Facts: Research Note DOT HS 812 010.

United Nations Economic Commission for Europe (2002) Regulation No. 22.4: Uniform provision concerning the approval of protective helmets and their visors for drivers and passengers of motorcycles and mopeds.

Williams, M. (1991) The protective performance of bicyclists' helmets in accidents. Accident Analysis & Prevention 23 (2/3), 119-131

Willinger, R., Baumbartner, D., Guimerteau, T. (2000) Dynamic characterization of motorcycle helmets: Modeling and coupling with the human head. Journal of Sound and Vibration 235 (4), 611-625

Wobrock, J., Smith, T., Kasantikul, V., Whiting, W. (2003) Effectiveness of collision-involved motorcycle helmets in thailand. 47th Annual Proceedings of the Association for the Advancement of Automotive Medicine, 443-461

Young, J. (1993) Head and face anthropometry of adult us civilians. In: Office of Aviation Medicine, DOT/FAA/AM-93/10.

Zhang, J., Kikuchi, N., Li, V., Yee, A., Nusholtz, G. (1998) Constitutive modeling of polymeric foam material subjected to dynamic crash loading. International Journal of Impact Engineering 21 (5), 369-386

Appendix A

X, Y, Z, and resultant acceleration (g), angular velocity (rad/s), and angular acceleration (rad/s^2) for the cadaver head impacts in Experiment A. Resultant values were transformed to the cadaver head's center of gravity and force data are overlaid on the resultant data. The raw data are red (first column) and the filtered data are blue. Vertical dashed lines indicate initial contact of the helmet onto the force plate. Vertical solid lines indicate time of maximum resultant acceleration. Force (N) data are plotted in the bottom row. Maximum values are summarized in the lower table.

Cadaver 1, 75 J

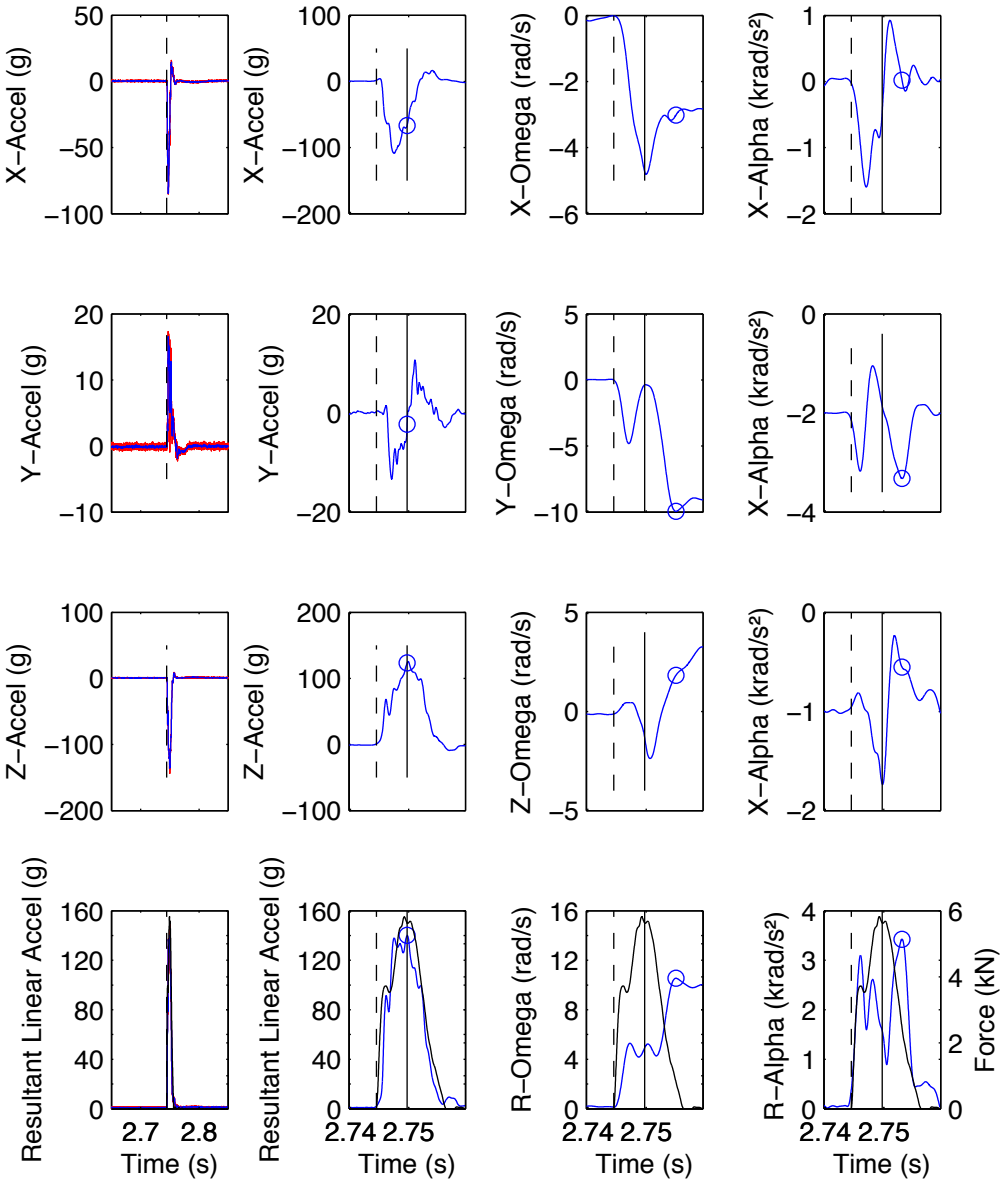

Max Resultant (g)	140.18	Max Alpha (rad/s²)	3423.83
Xg Max	–66.48	Xa Max	19.71
Yg Max	–2.27	Ya Max	–3305.38
Zg Max	123.39	Za Max	892.61
Max Omega (rad/s)	10.55	Force (N)	5818.98
Xo Max	–3.02	HIC	961.38
Yo Max	–9.94		
Zo Max	1.82		

Cadaver 1, 150 J

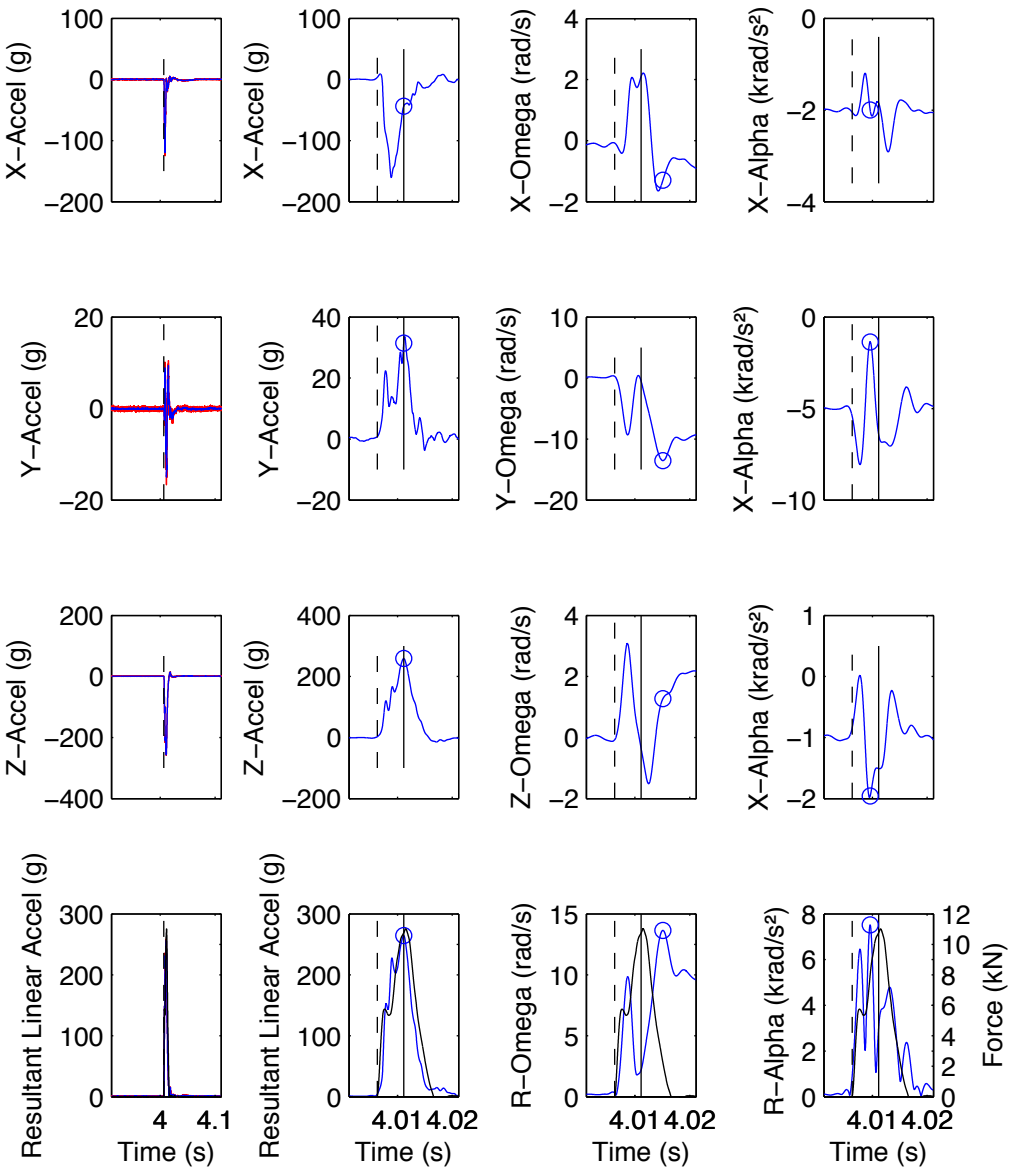

Max Resultant (g)	264.43	Max Alpha (rad/s²)	7516.73
Xg Max	–43.45	Xa Max	1.23
Yg Max	31.41	Ya Max	7268.16
Zg Max	258.94	Za Max	–1917.05
Max Omega (rad/s)	13.65	Force (N)	11017.69
Xo Max	–1.29	HIC	3120.51
Yo Max	–13.53		
Zo Max	1.27		

Cadaver 1, 195 J

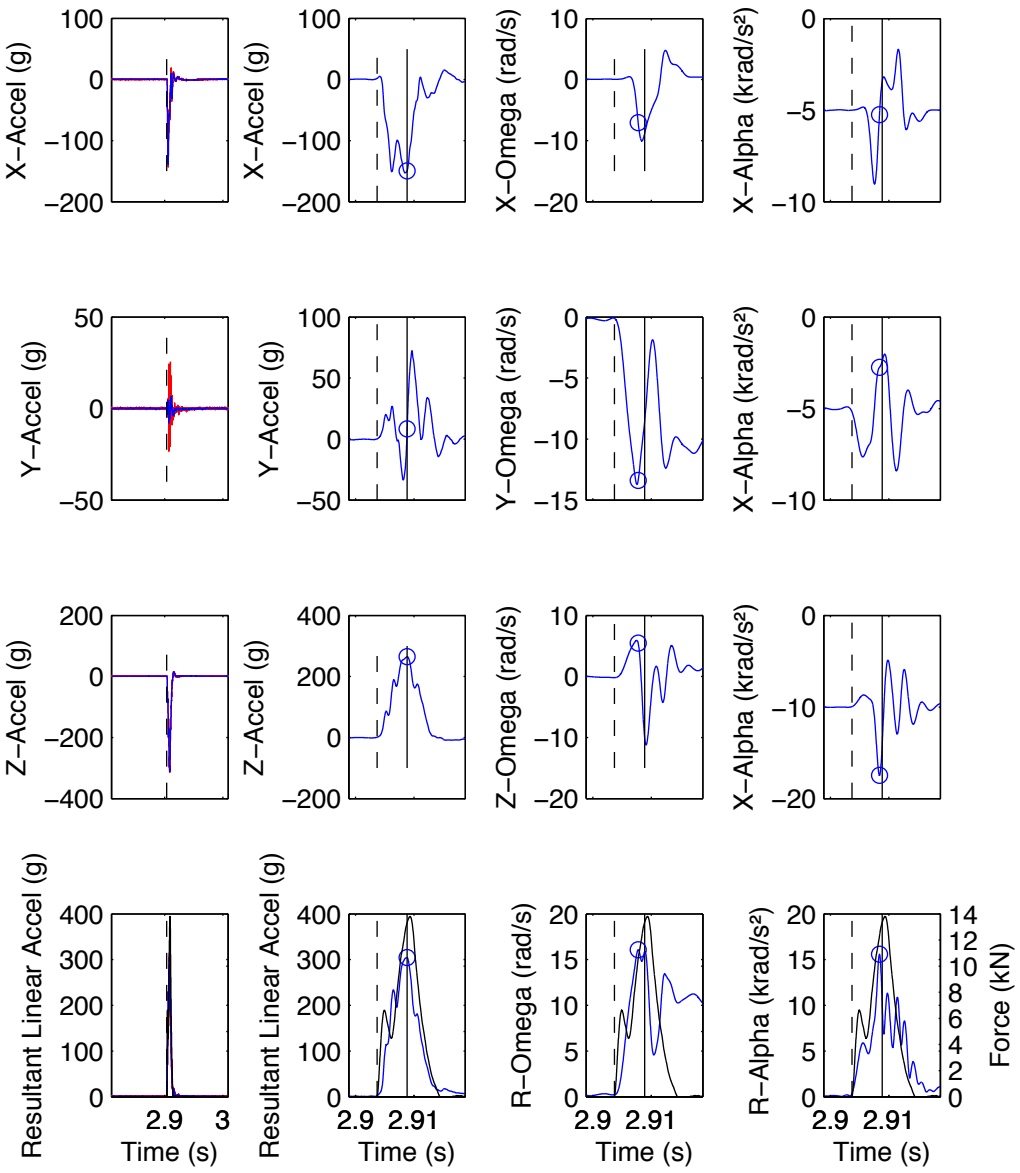

Max Resultant (g)	304.50	Max Alpha (rad/s²)	15593.02
Xg Max	–149.49	Xa Max	–488.76
Yg Max	8.40	Ya Max	4504.71
Zg Max	265.15	Za Max	–14920.16
Max Omega (rad/s)	16.09	Force (N)	13812.74
Xo Max	–7.04	HIC	4330.35
Yo Max	–13.40		
Zo Max	5.45		

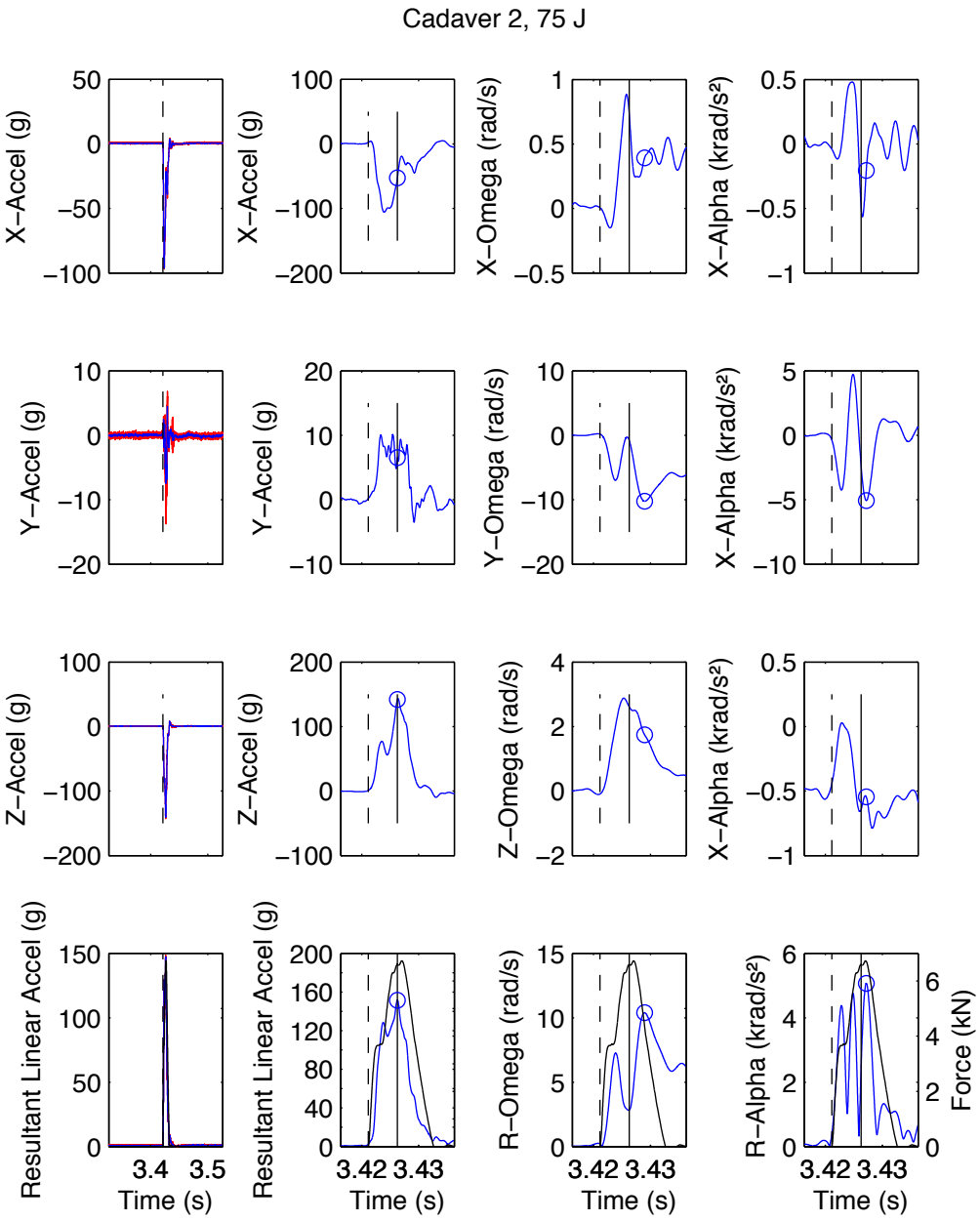

Max Resultant (g)	151.50	Max Alpha (rad/s²)	5068.25
Xg Max	–52.60	Xa Max	–205.27
Yg Max	6.53	Ya Max	–5063.29
Zg Max	141.93	Za Max	–90.50
Max Omega (rad/s)	10.39	Force (N)	6731.82
Xo Max	0.39	HIC	887.83
Yo Max	–10.24		
Zo Max	1.74		

Cadaver 2, 150 J

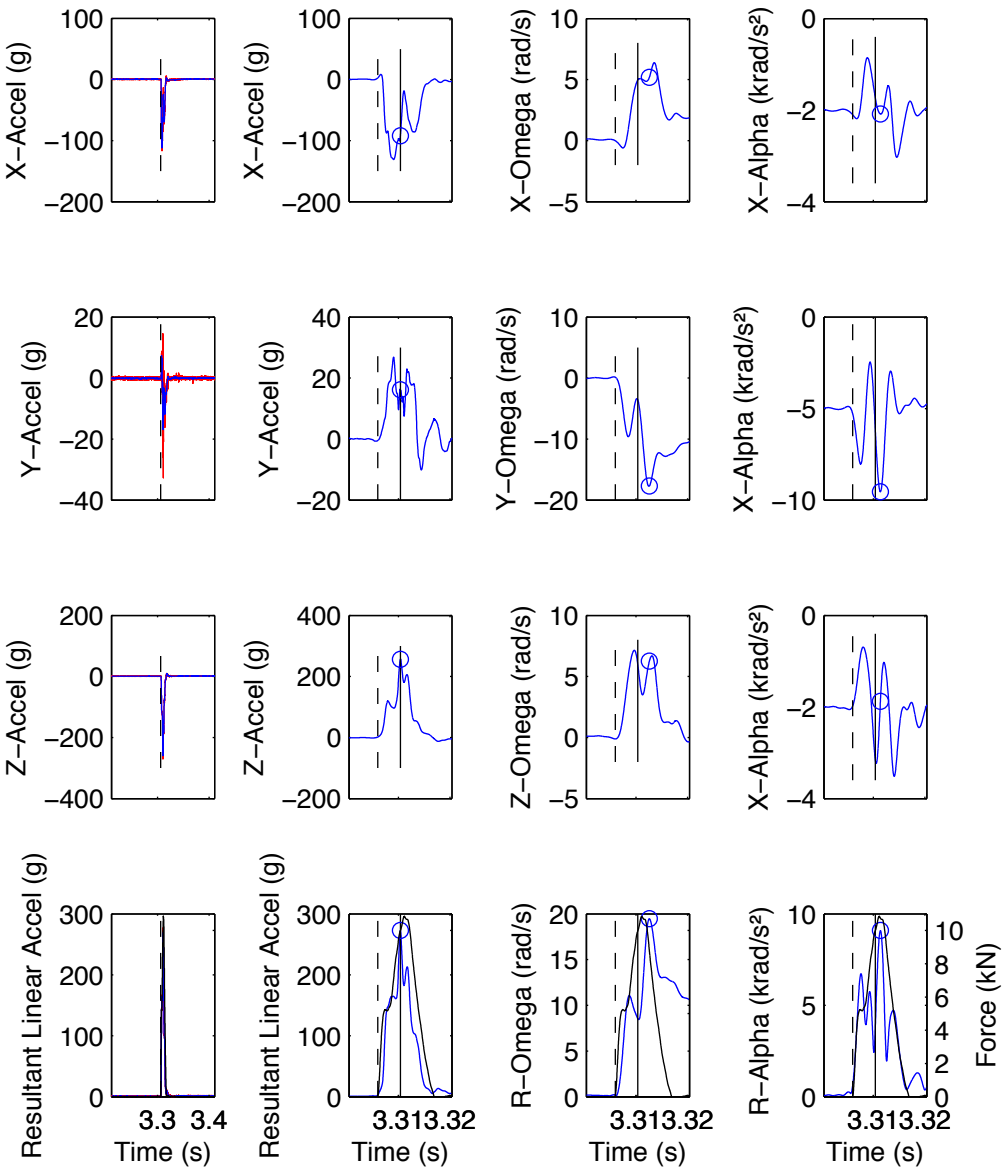

Max Resultant (g)	272.90	Max Alpha (rad/s²)	9090.37
Xg Max	–92.04	Xa Max	–216.34
Yg Max	16.16	Ya Max	–9082.36
Zg Max	256.40	Za Max	314.16
Max Omega (rad/s)	19.47	Force (N)	10853.09
Xo Max	5.19	HIC	2268.36
Yo Max	–17.69		
Zo Max	6.26		

Cadaver 2, 195 J

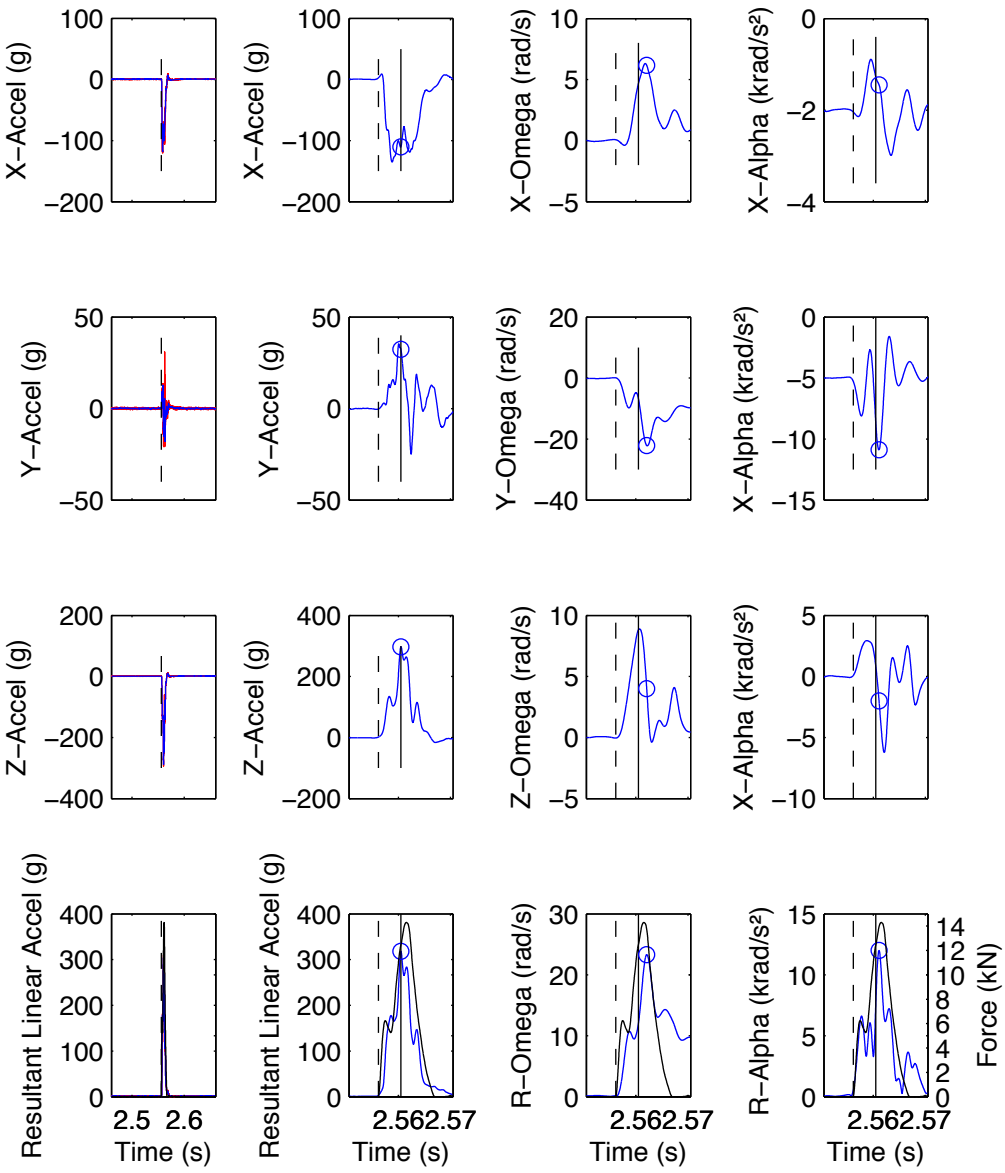

Max Resultant (g)	318.19	Max Alpha (rad/s²)	11996.93
Xg Max	–110.10	Xa Max	1378.23
Yg Max	32.29	Ya Max	–11748.05
Zg Max	296.78	Za Max	–2002.51
Max Omega (rad/s)	23.32	Force (N)	14292.58
Xo Max	6.17	HIC	3422.05
Yo Max	–22.14		
Zo Max	4.00		

Cadaver 3, 75 J

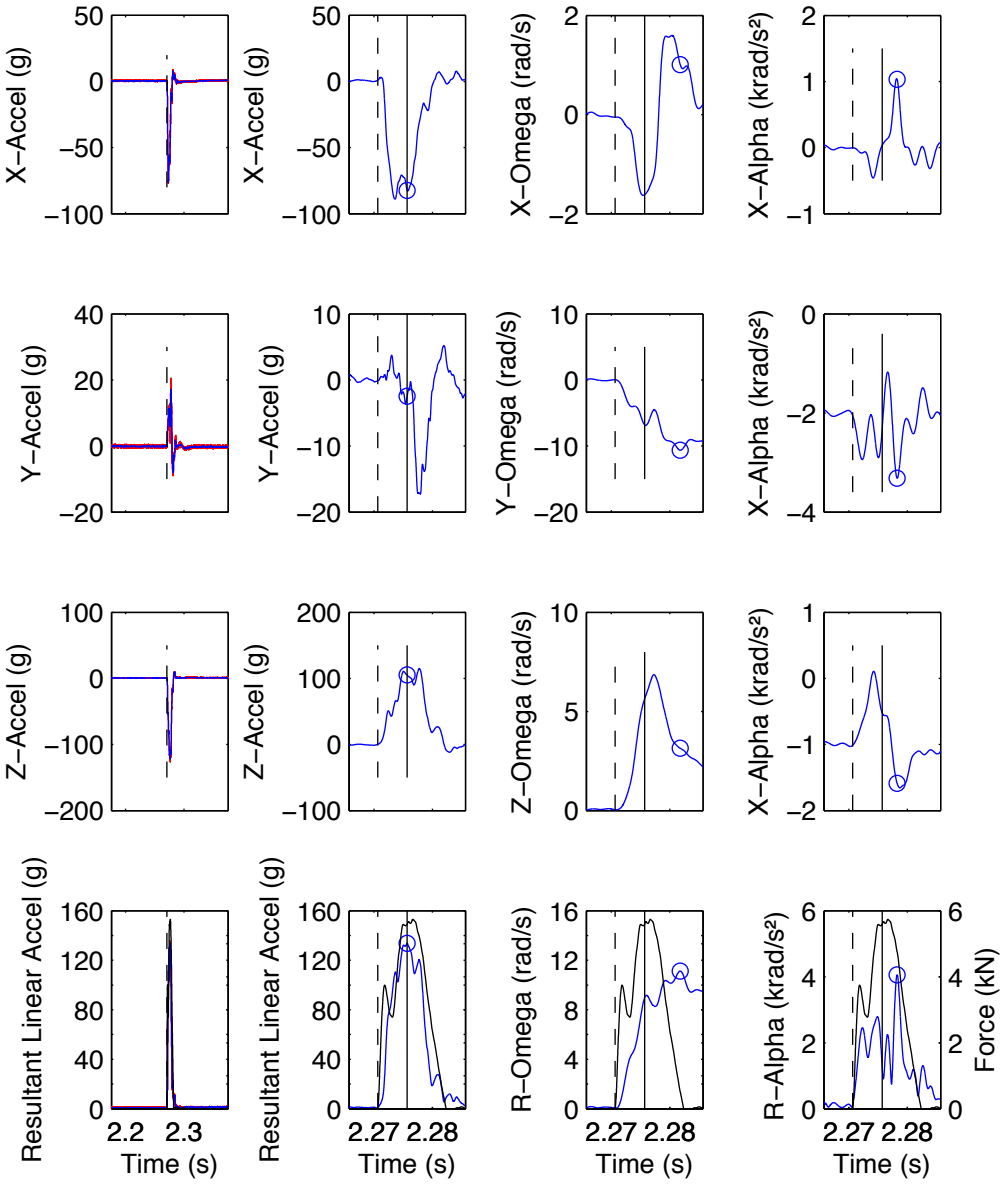

Max Resultant (g)	133.72	Max Alpha (rad/s²)	4057.13
Xg Max	–82.50	Xa Max	2067.80
Yg Max	–2.45	Ya Max	–3287.10
Zg Max	105.21	Za Max	–1174.52
Max Omega (rad/s)	11.13	Force (N)	5737.90
Xo Max	1.01	HIC	829.79
Yo Max	–10.63		
Zo Max	3.14		

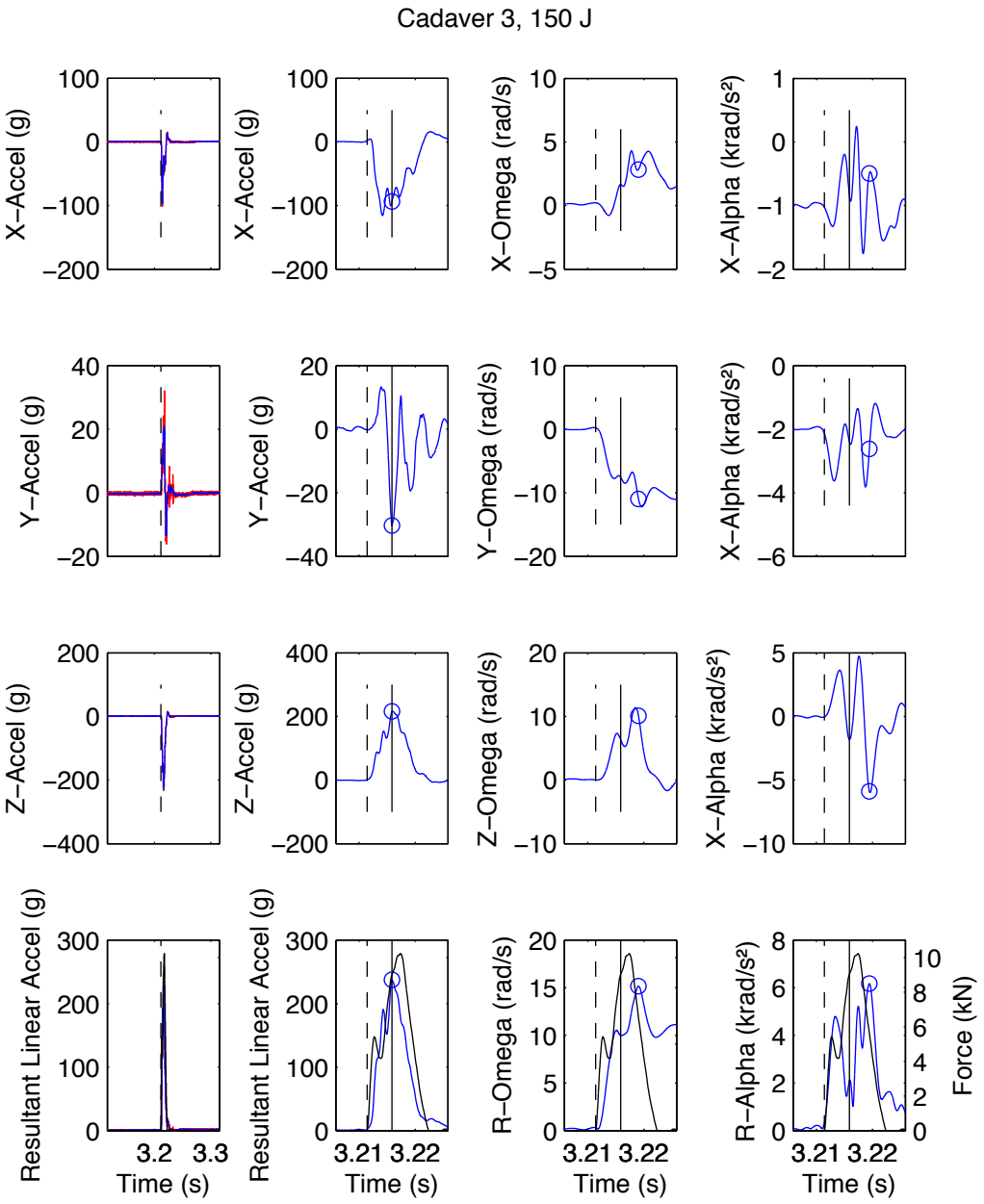

Max Resultant (g)	237.64	Max Alpha (rad/s²)	6171.50
Xg Max	–93.59	Xa Max	1011.49
Yg Max	–30.31	Ya Max	–1542.56
Zg Max	216.32	Za Max	–5889.38
Max Omega (rad/s)	15.17	Force (N)	10218.13
Xo Max	2.83	HIC	2320.73
Yo Max	–10.97		
Zo Max	10.08		

Cadaver 3, 195 J

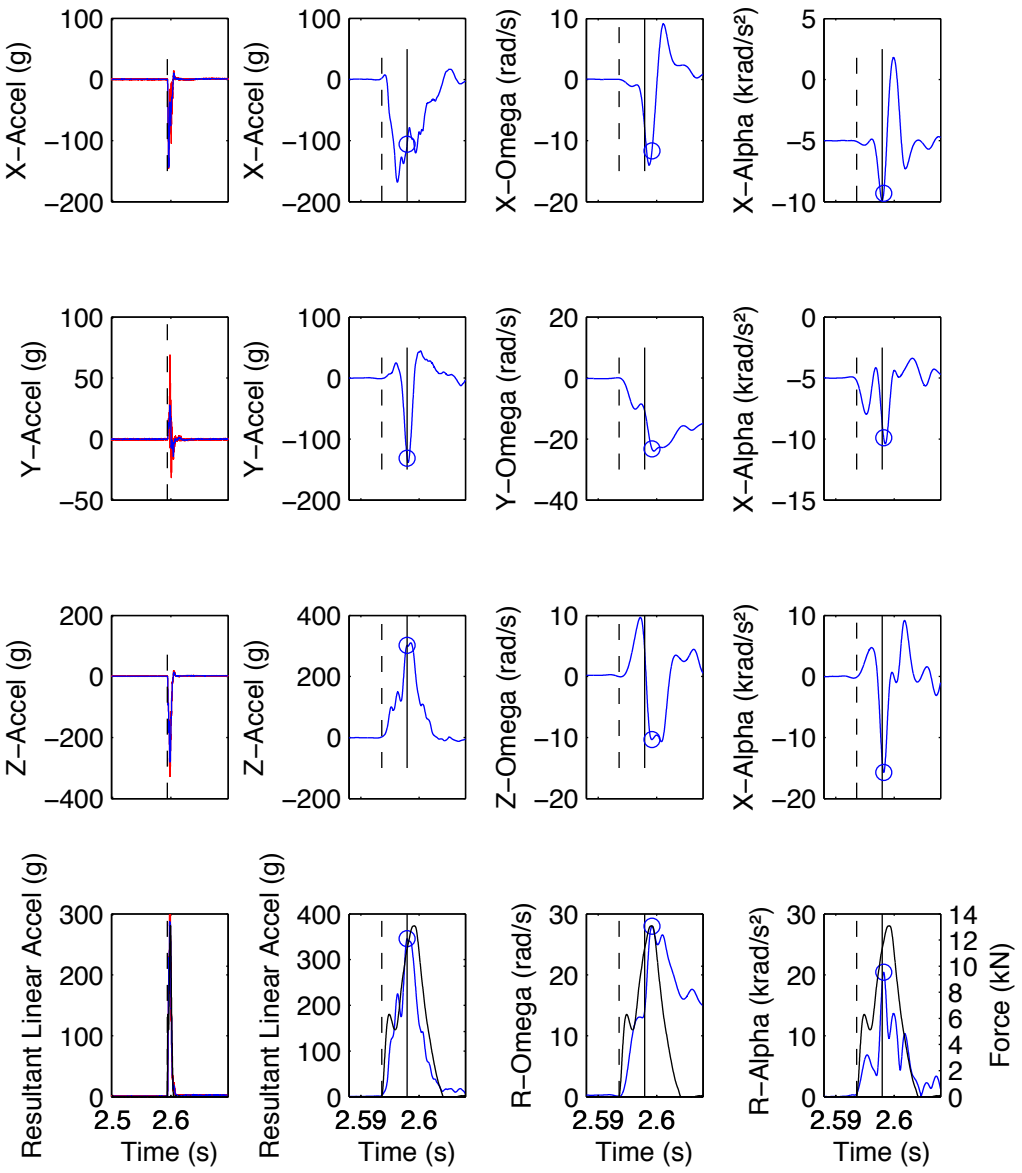

Max Resultant (g)	345.71	Max Alpha (rad/s²)	20423.94
Xg Max	–105.99	Xa Max	–8627.93
Yg Max	–131.35	Ya Max	–9793.91
Zg Max	301.71	Za Max	–15709.09
Max Omega (rad/s)	27.97	Force (N)	13083.03
Xo Max	–11.67	HIC	4403.01
Yo Max	–23.21		
Zo Max	–10.35		

Cadaver 4, 75 J

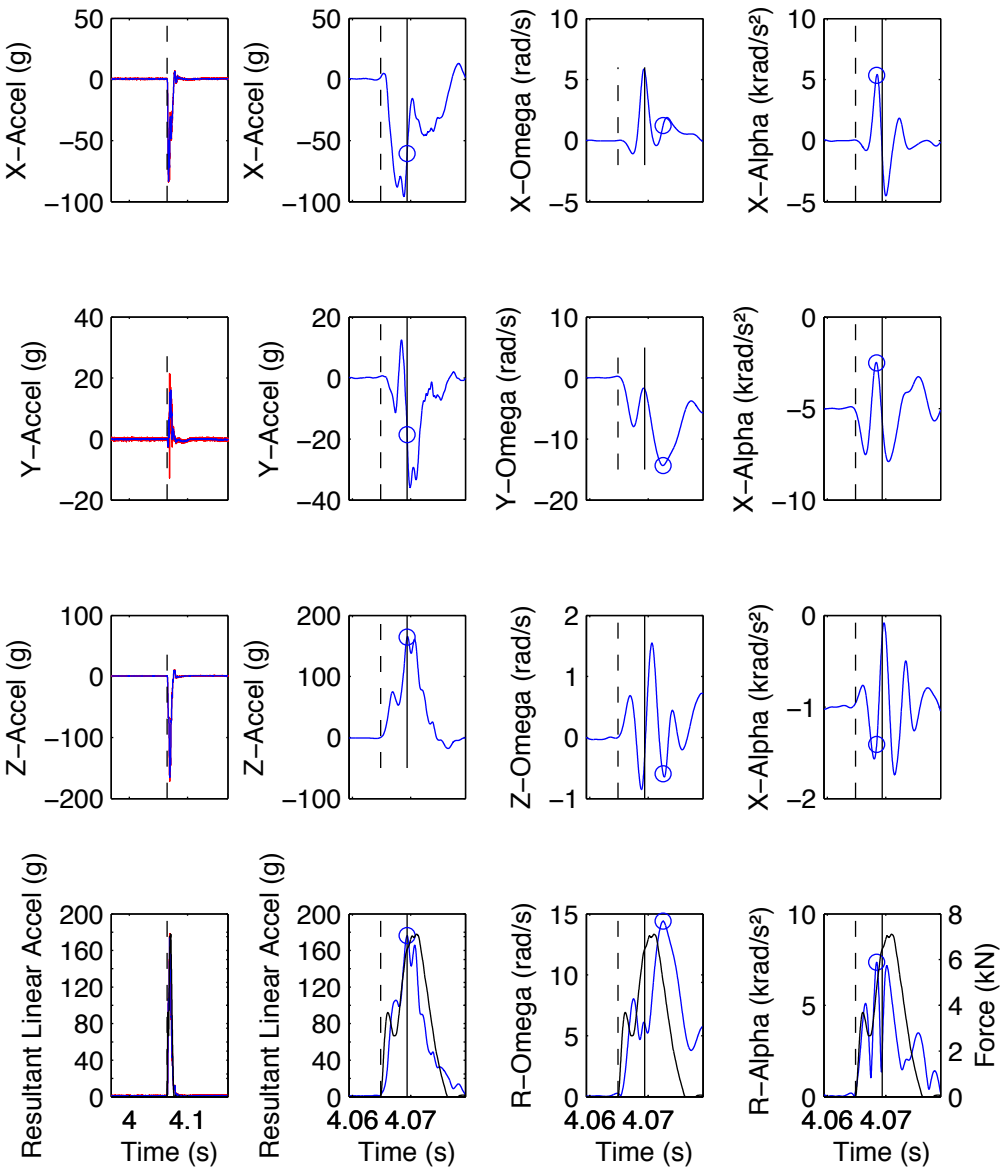

Max Resultant (g)	176.21	Max Alpha (rad/s²)	7354.51
Xg Max	–60.54	Xa Max	5345.96
Yg Max	–18.58	Ya Max	4984.24
Zg Max	164.43	Za Max	–816.60
Max Omega (rad/s)	14.40	Force (N)	7113.72
Xo Max	1.24	HIC	1019.58
Yo Max	–14.33		
Zo Max	–0.59		

Cadaver 4, 150 J

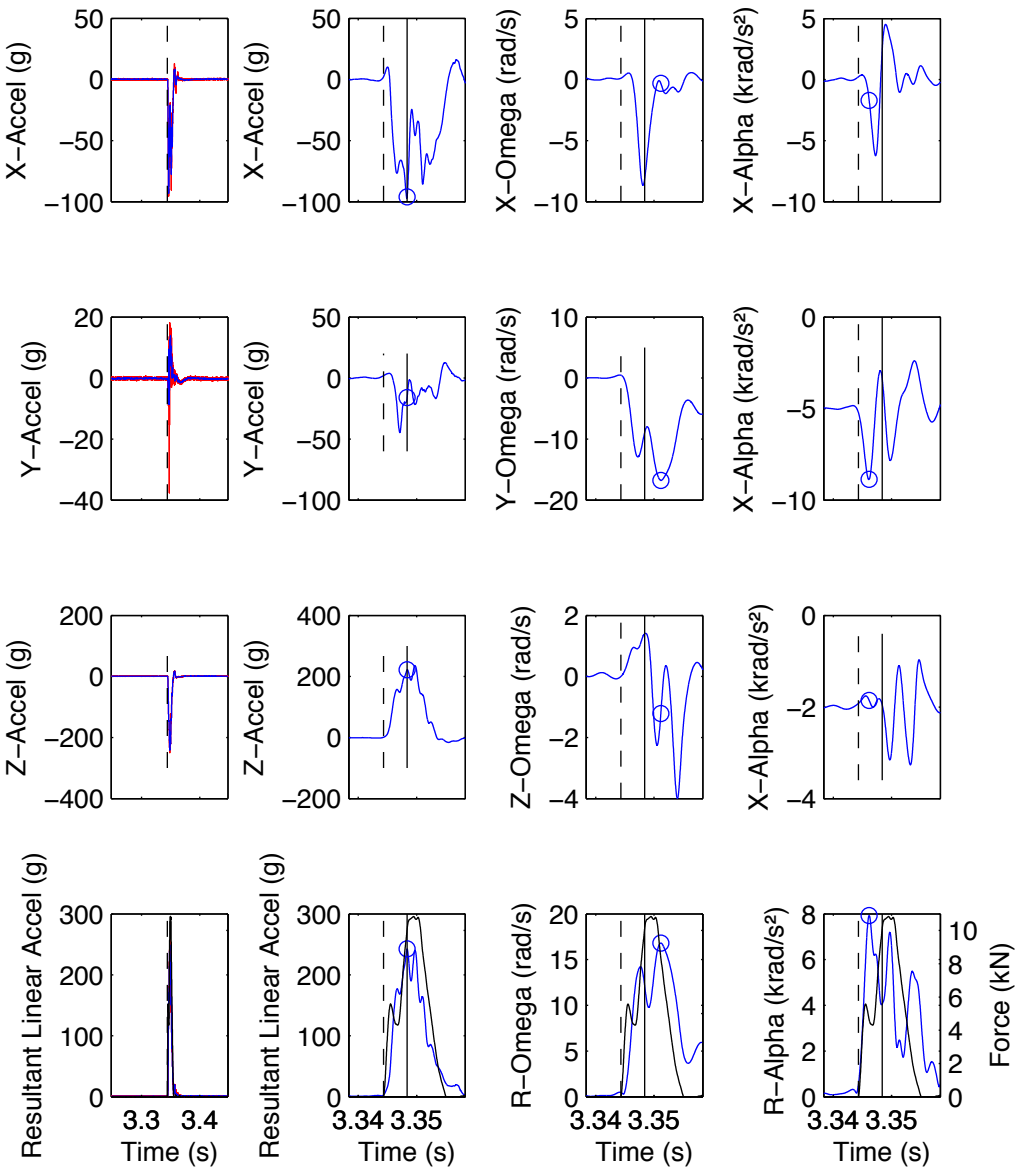

Max Resultant (g)	242.53	Max Alpha (rad/s²)	7928.06
Xg Max	–96.08	Xa Max	–1705.01
Yg Max	–15.93	Ya Max	–7734.23
Zg Max	222.12	Za Max	359.00
Max Omega (rad/s)	16.81	Force (N)	10840.63
Xo Max	–0.31	HIC	2731.35
Yo Max	–16.77		
Zo Max	–1.21		

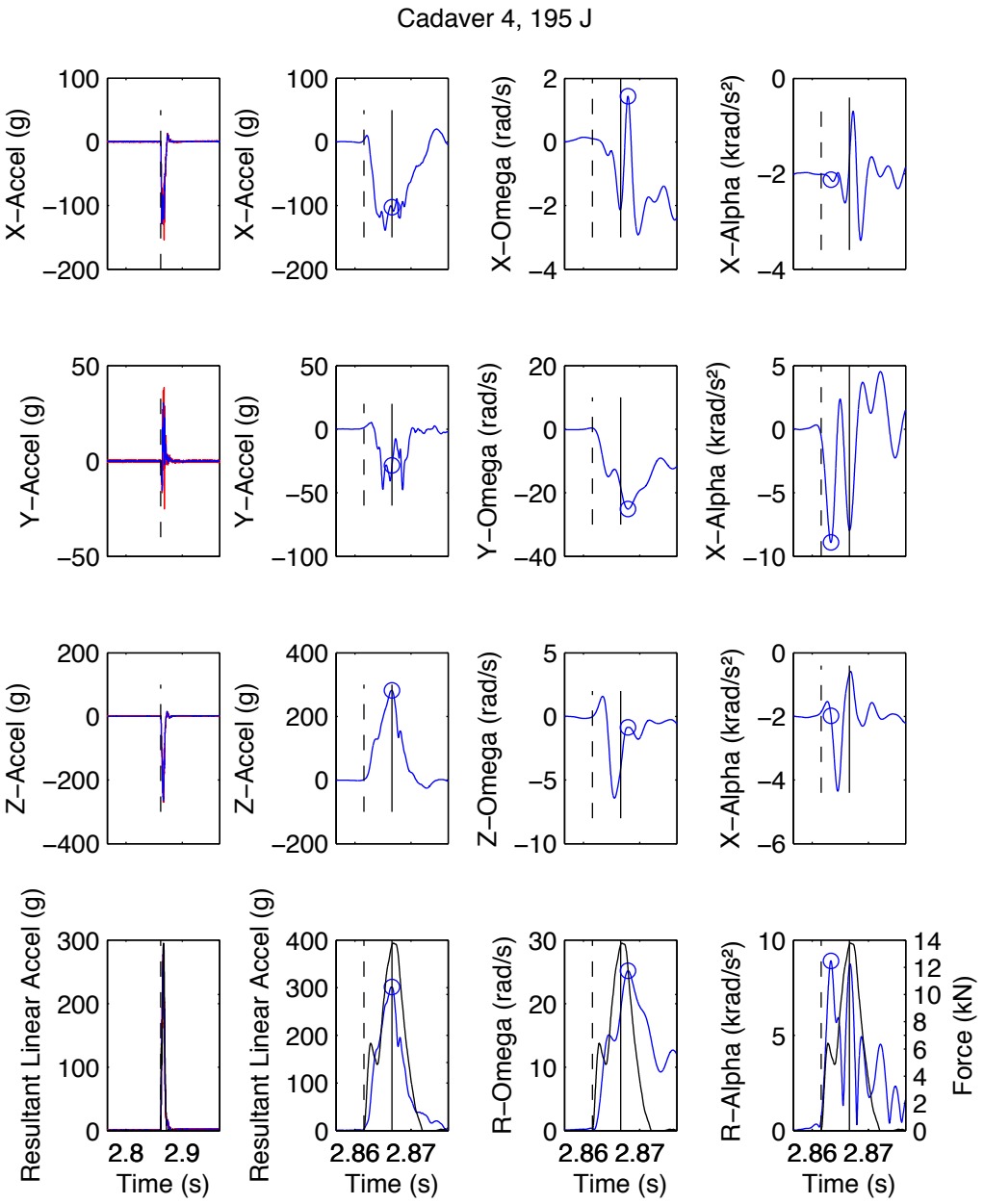

Max Resultant (g)	301.26	Max Alpha (rad/s²)	8904.98
Xg Max	–102.65	Xa Max	–306.79
Yg Max	–28.41	Ya Max	–8899.54
Zg Max	281.80	Za Max	51.90
Max Omega (rad/s)	25.17	Force (N)	13773.25
Xo Max	1.44	HIC	3988.82
Yo Max	–25.11		
Zo Max	–0.86		

Appendix B

Anterosuperior views of the residual foam liner deformation averaged over 5° x 5° elements for all cadaver head impacts in Experiment A. The circled point represents the maximum crush depth.

Cadaver 1, 75 J

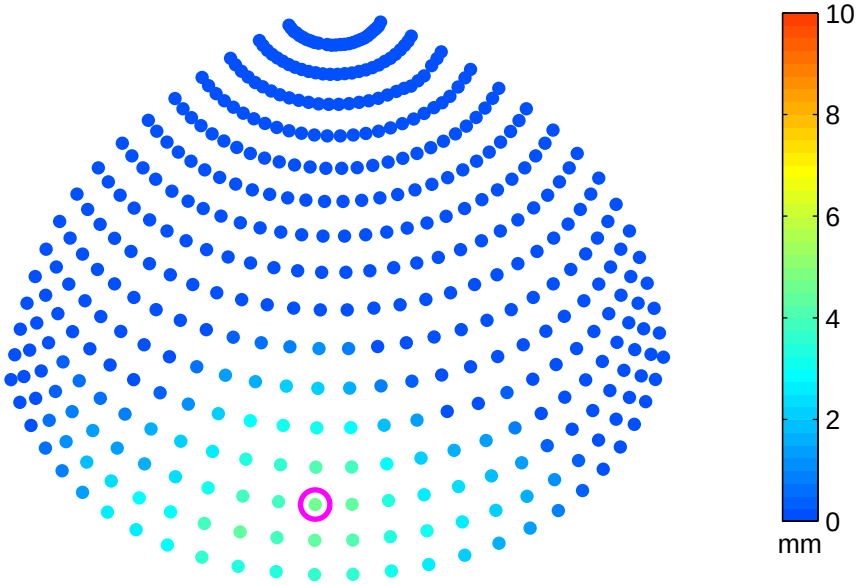

Max Residual Crush Depth (mm) 4.51 Max Crush Volume (cm³) 9.11

Cadaver 2, 75 J

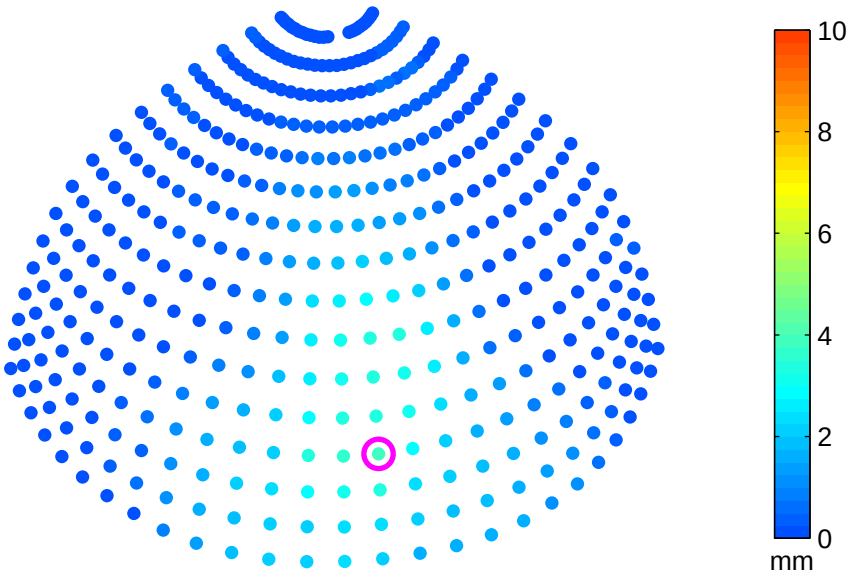

Max Residual Crush Depth (mm) 4.51 Max Crush Volume (cm³) 9.11

Cadaver 3, 75 J

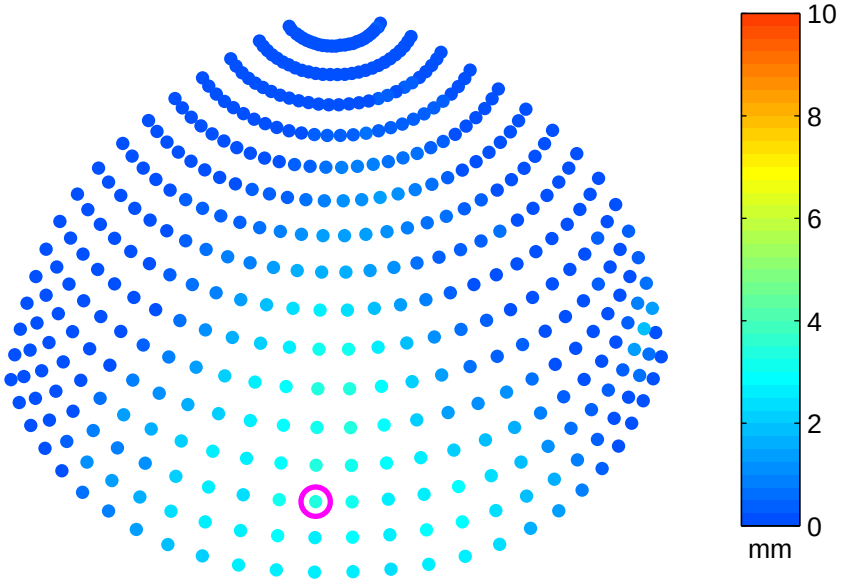

Max Residual Crush Depth (mm) 4.51

Max Crush Volume (cm³) 9.11

Cadaver 4, 75 J

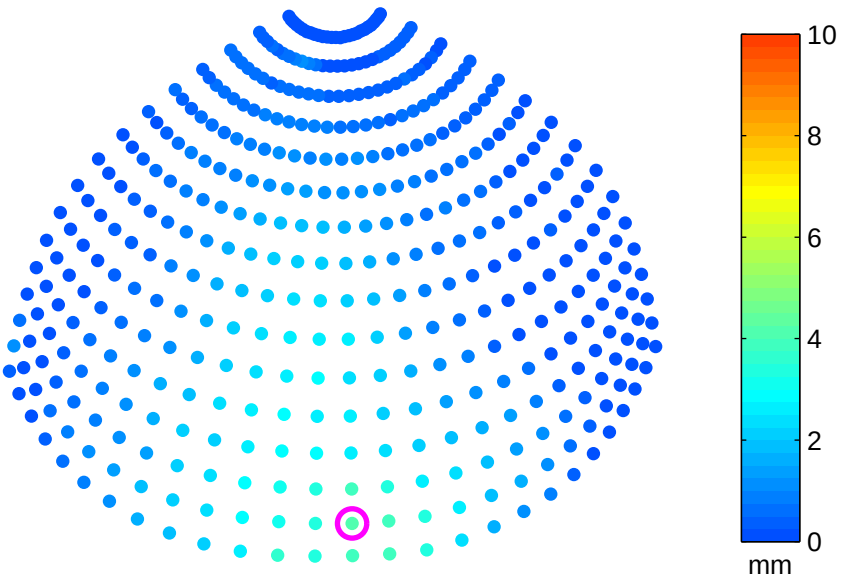

Max Residual Crush Depth (mm) 4.51

Max Crush Volume (cm³) 9.11

Cadaver 1, 150 J

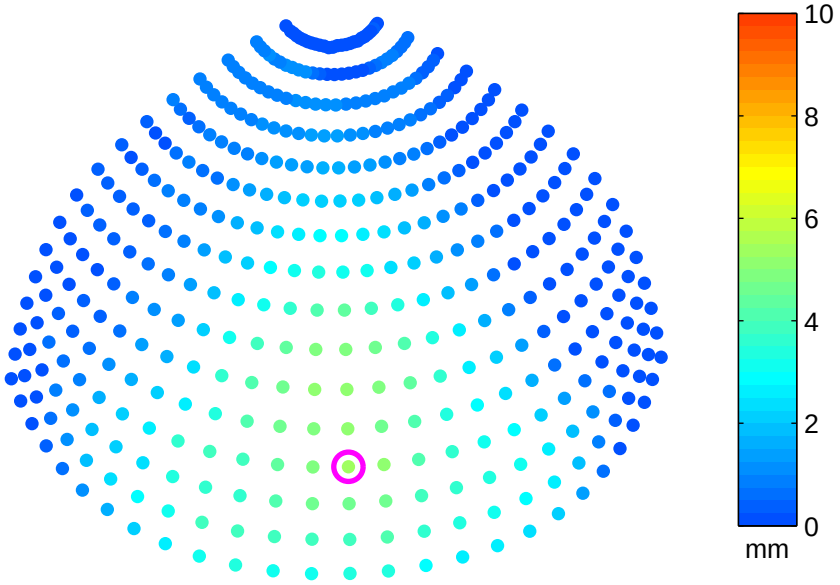

Max Residual Crush Depth (mm) 4.51 Max Crush Volume (cm³) 9.11

Cadaver 2, 150 J

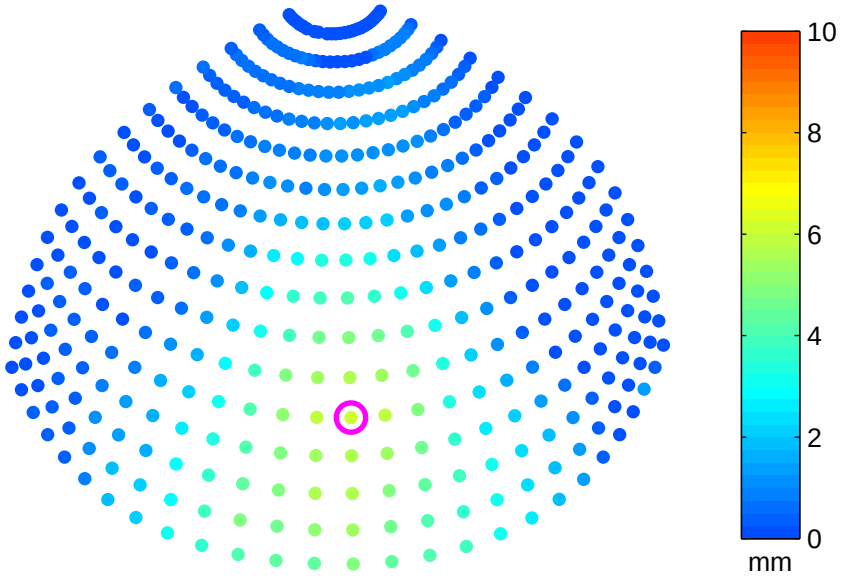

Max Residual Crush Depth (mm) 4.51 Max Crush Volume (cm³) 9.11

Cadaver 3, 150 J

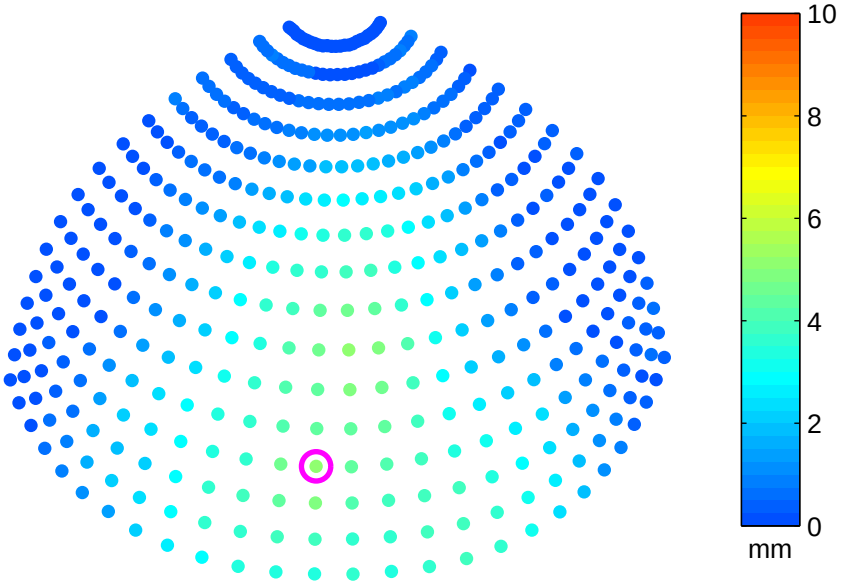

Max Residual Crush Depth (mm) 4.51

Max Crush Volume (cm³) 9.11

Cadaver 4, 150 J

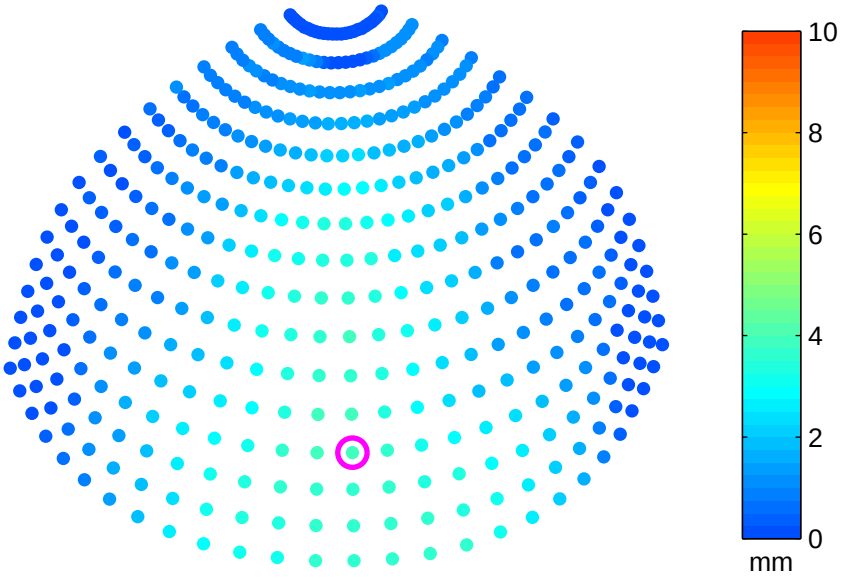

Max Residual Crush Depth (mm) 4.51

Max Crush Volume (cm³) 9.11

Cadaver 1, 195 J

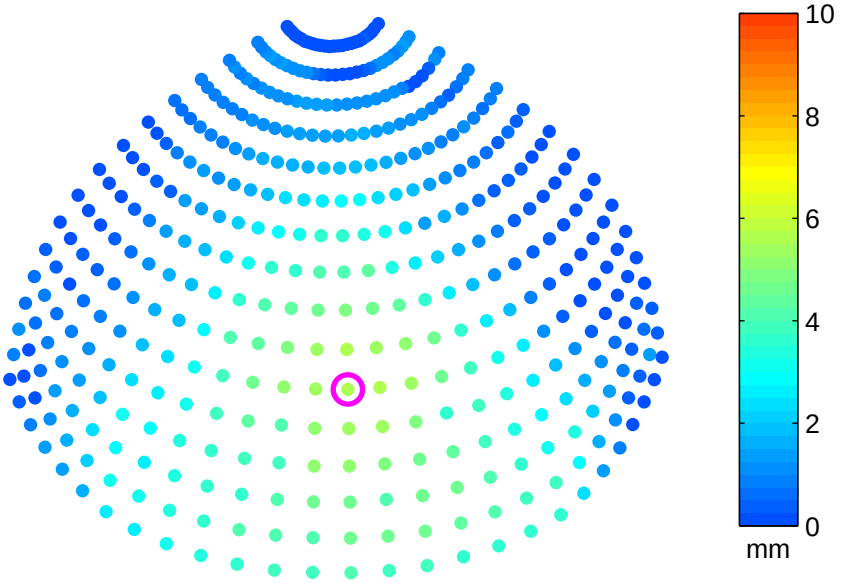

Max Residual Crush Depth (mm) 4.51 Max Crush Volume (cm³) 9.11

Cadaver 2, 195 J

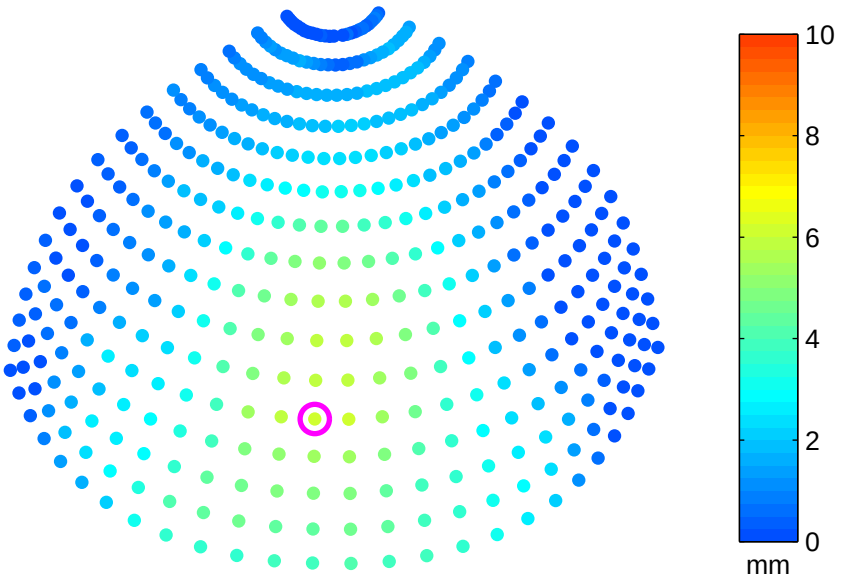

Max Residual Crush Depth (mm) 4.51 Max Crush Volume (cm³) 9.11

Cadaver 3, 195 J

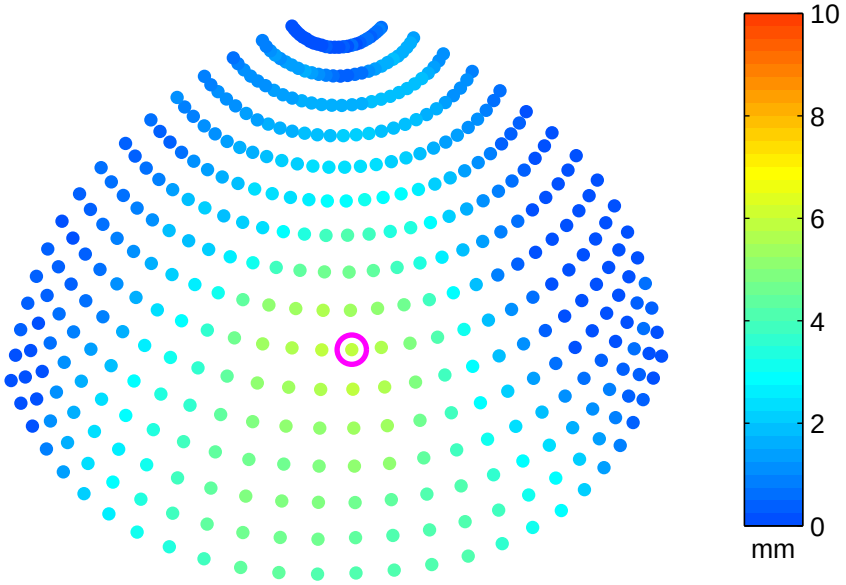

Max Residual Crush Depth (mm) 4.51

Max Crush Volume (cm³) 9.11

Cadaver 4, 195 J

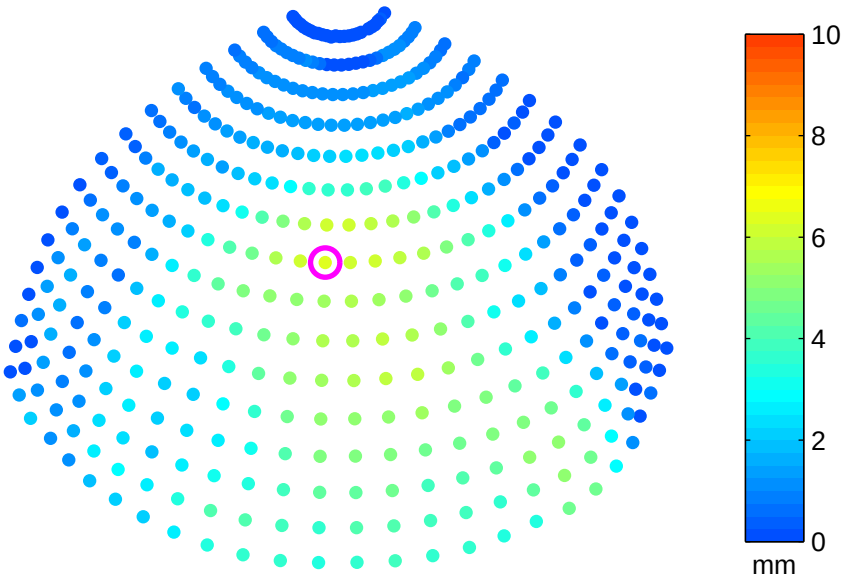

Max Residual Crush Depth (mm) 4.51

Max Crush Volume (cm³) 9.11

Appendix C

X, Y, Z, and resultant acceleration (g) for Hybrid III, DOT, and ISO headform impacts in Experiment A. Raw data are red, filtered data are blue. Vertical dashed lines indicate initial contact of the helmet onto the force plate. Force (N) data are plotted with the resultant linear acceleration data. Vertical solid lines indicate time of maximum resultant acceleration. Also shown is the anterosuperior views of the residual foam liner deformation averaged over 5° x 5° elements for all cadaver impacts. The circled point represents the maximum crush depth. Maximum values are summarized in the lower table. Figure titles include headform tested (H3 = Hybrid III, DT = DOT, and ISOH = ISO), impact energy level (low, medium or high), and helmet number.

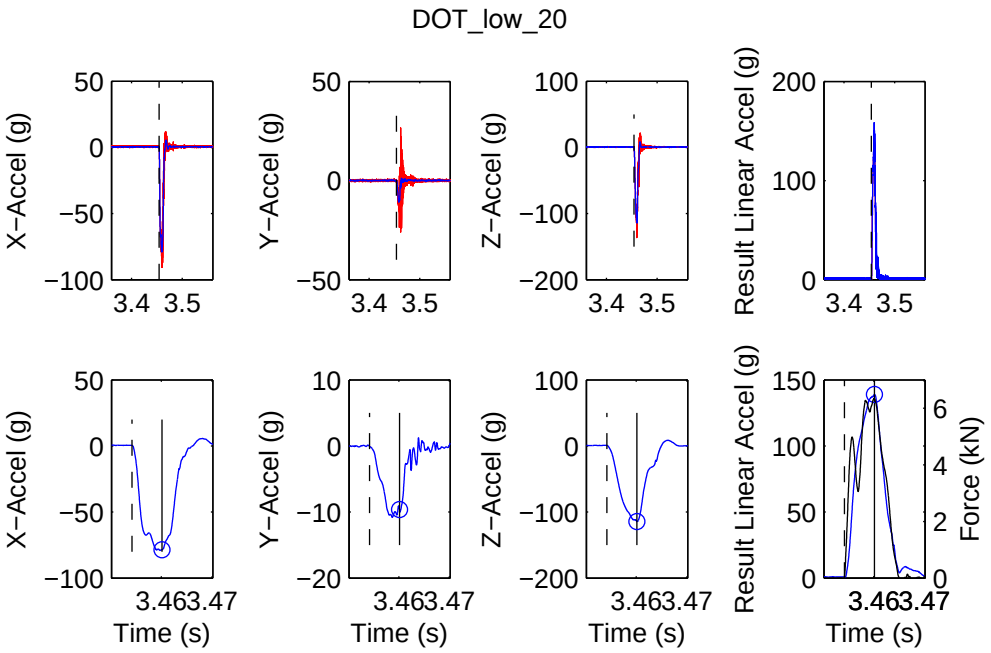

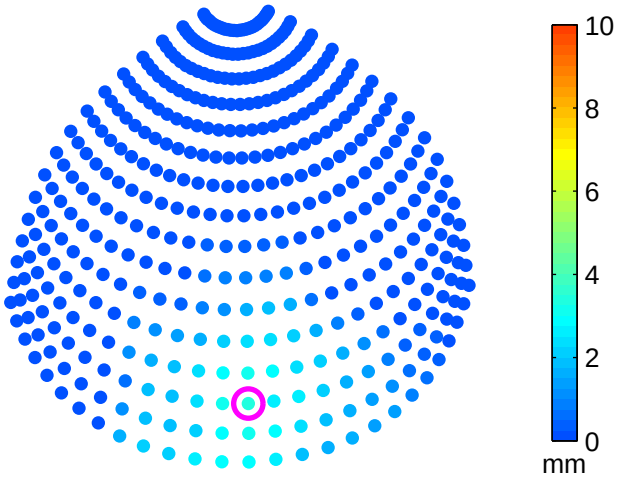

Max Resultant (g)	139.04	HIC	840.40
Xg Max	−78.51	Max Force (N)	6336.46
Yg Max	−9.62	Max Residual Crush Depth (mm)	2.68
Zg Max	−114.34	Max Crush Volume (cm³)	8.12

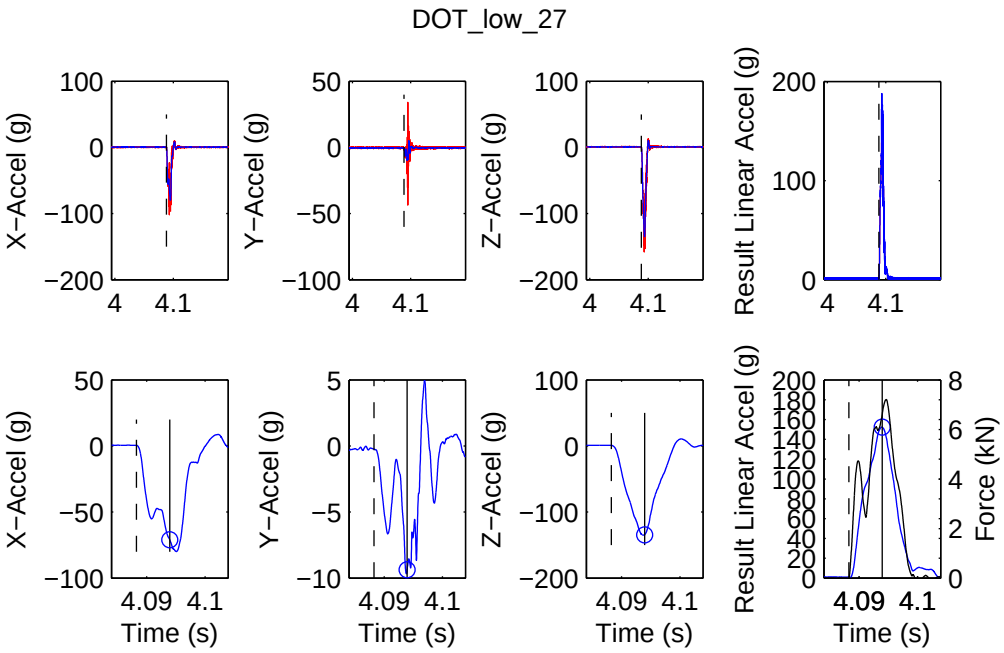

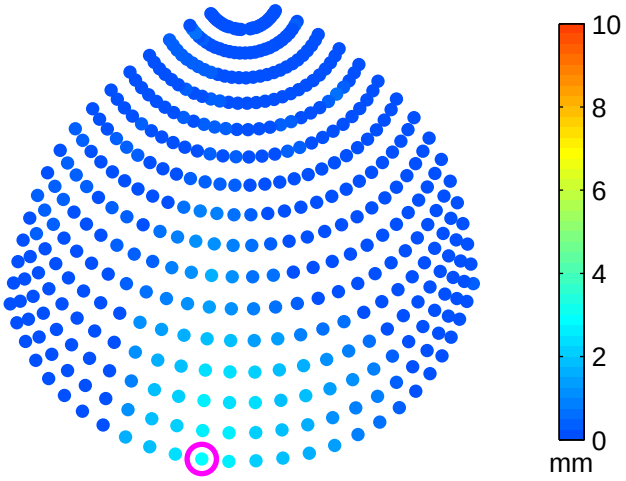

Max Resultant (g)	152.40	HIC	929.63
Xg Max	−70.91	Max Force (N)	7208.27
Yg Max	−9.37	Max Residual Crush Depth (mm)	3.24
Zg Max	−134.58	Max Crush Volume (cm³)	9.33

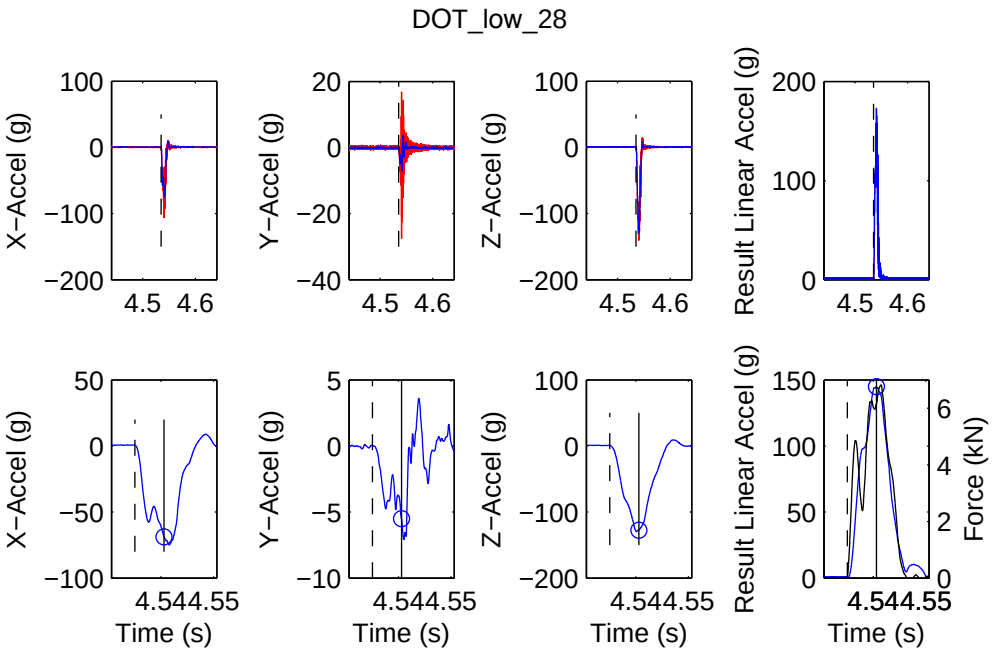

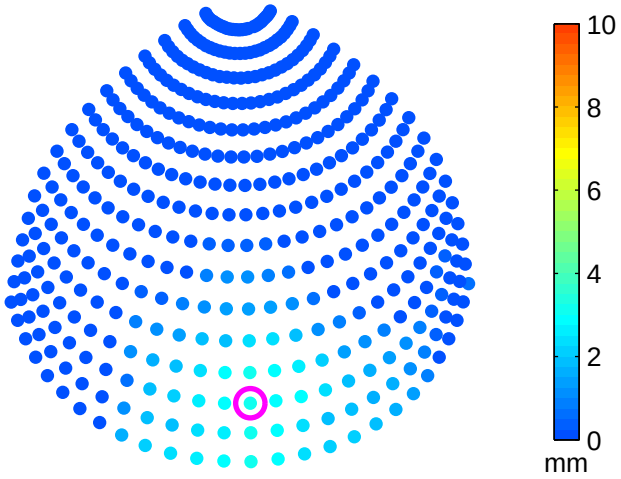

Max Resultant (g)	144.92	HIC	878.47
Xg Max	−68.82	Max Force (N)	6822.11
Yg Max	−5.49	Max Residual Crush Depth (mm)	3.36
Zg Max	−127.42	Max Crush Volume (cm³)	8.65

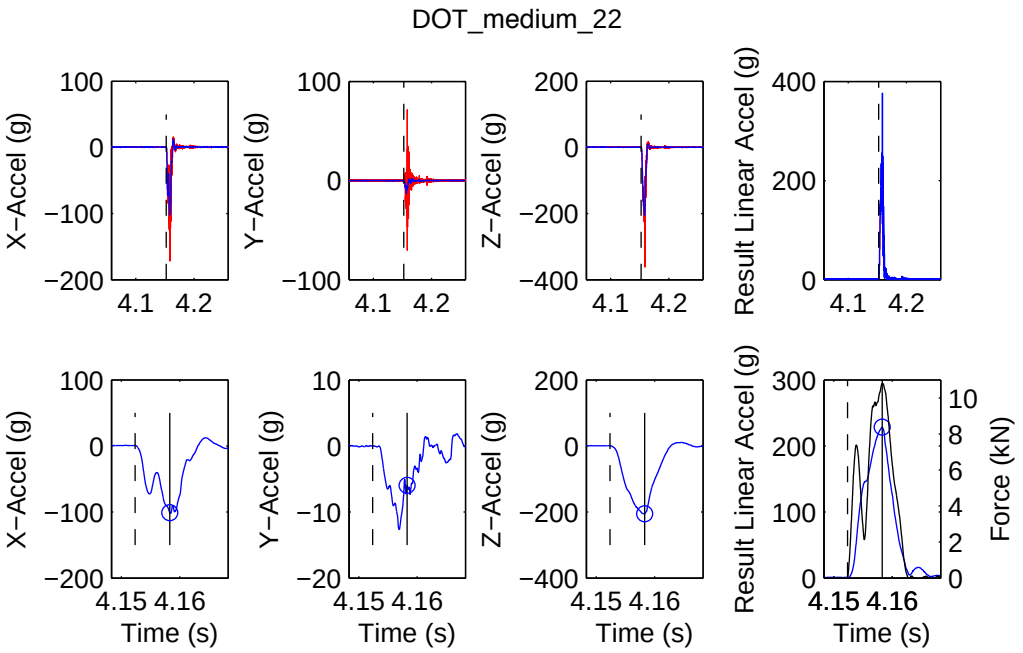

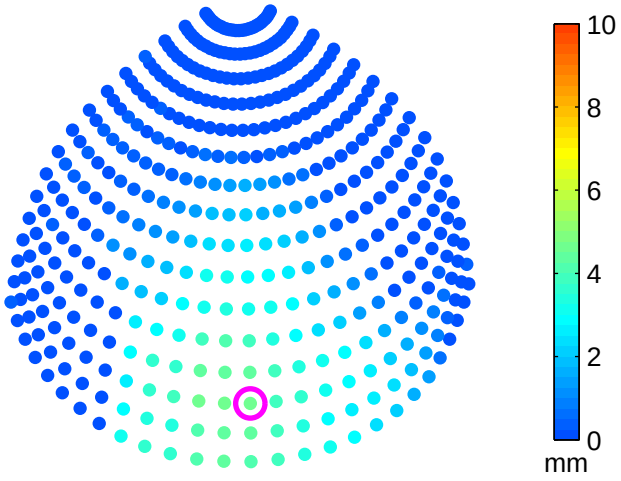

Max Resultant (g)	228.64	HIC	2363.39
Xg Max	−100.84	Max Force (N)	10802.25
Yg Max	−5.97	Max Residual Crush Depth (mm)	4.67
Zg Max	−205.11	Max Crush Volume (cm³)	20.83

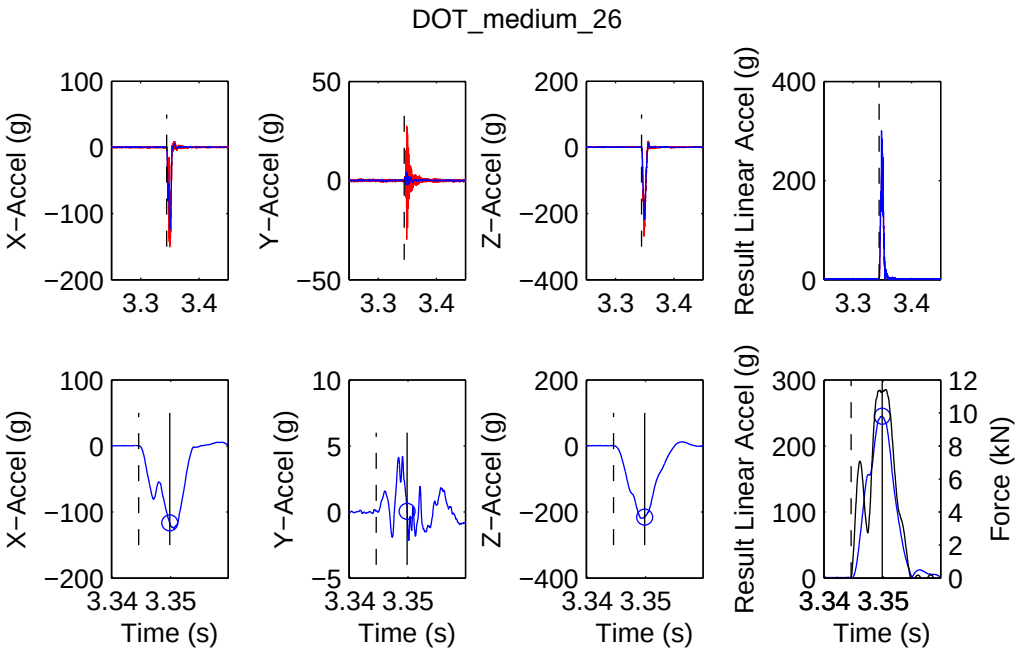

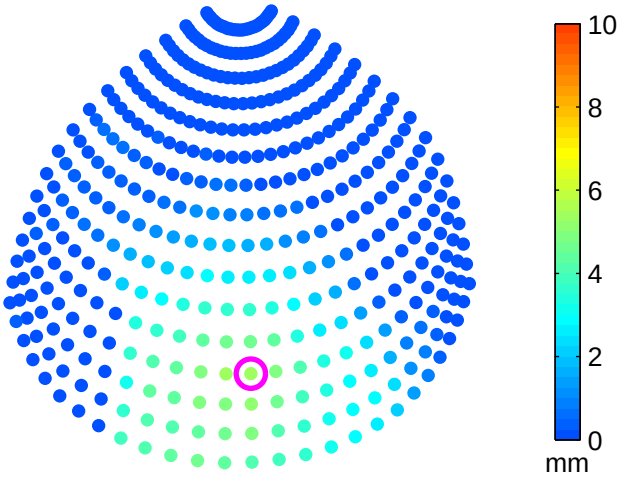

Max Resultant (g)	244.93	HIC	2794.17
Xg Max	−116.29	Max Force (N)	11408.28
Yg Max	0.05	Max Residual Crush Depth (mm)	5.28
Zg Max	−215.56	Max Crush Volume (cm³)	19.73

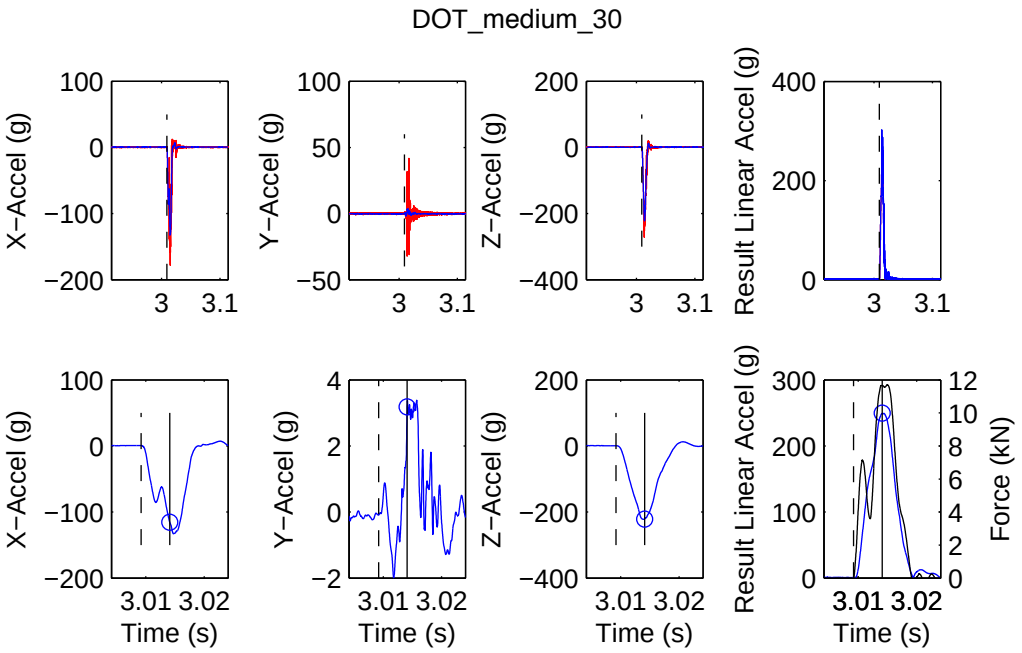

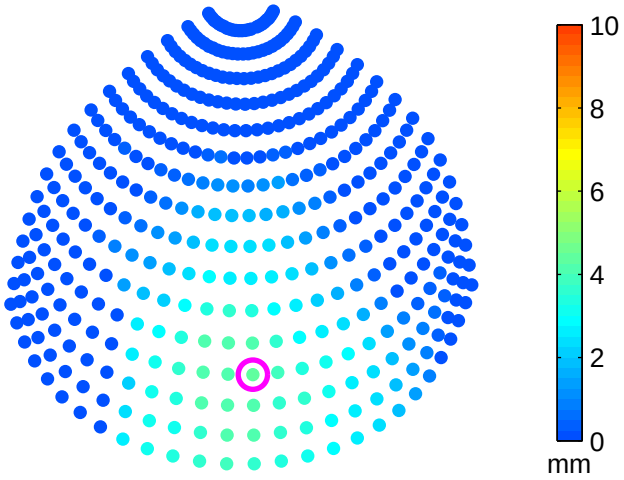

Max Resultant (g)	249.57	HIC	2891.39
Xg Max	−115.32	Max Force (N)	11708.94
Yg Max	3.19	Max Residual Crush Depth (mm)	4.25
Zg Max	−221.31	Max Crush Volume (cm³)	18.78

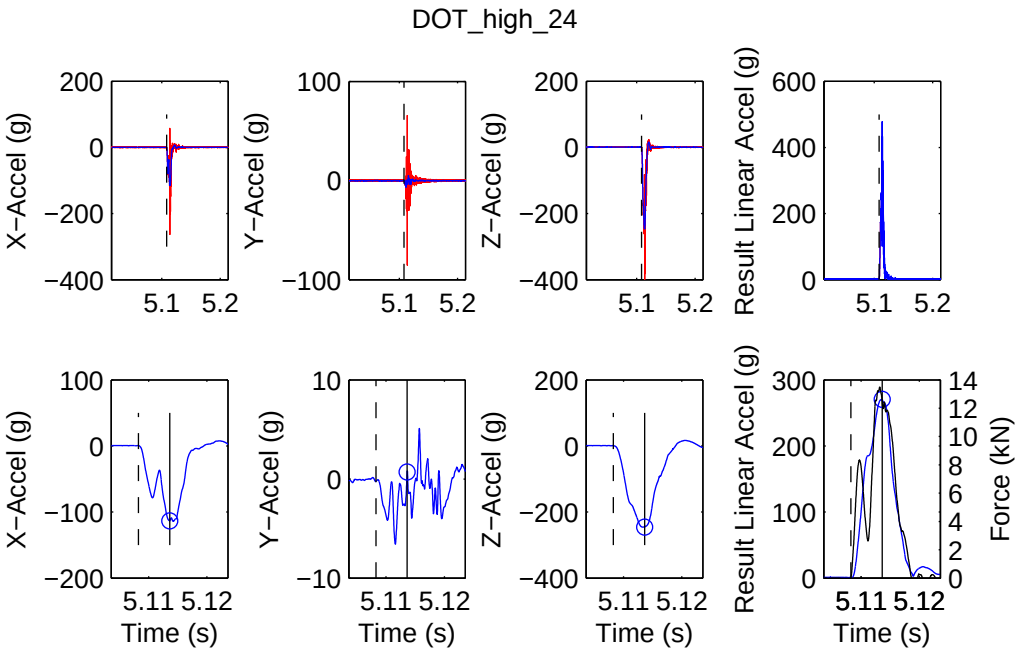

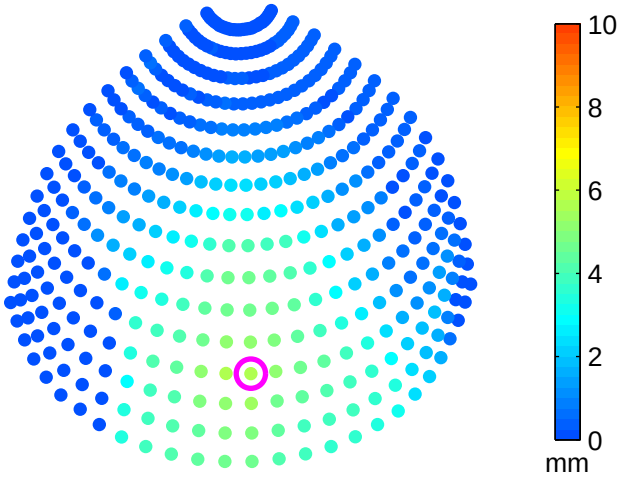

Max Resultant (g)	270.66	HIC	3702.48
Xg Max	−113.47	Max Force (N)	13494.76
Yg Max	0.71	Max Residual Crush Depth (mm)	4.77
Zg Max	−245.73	Max Crush Volume (cm³)	28.62

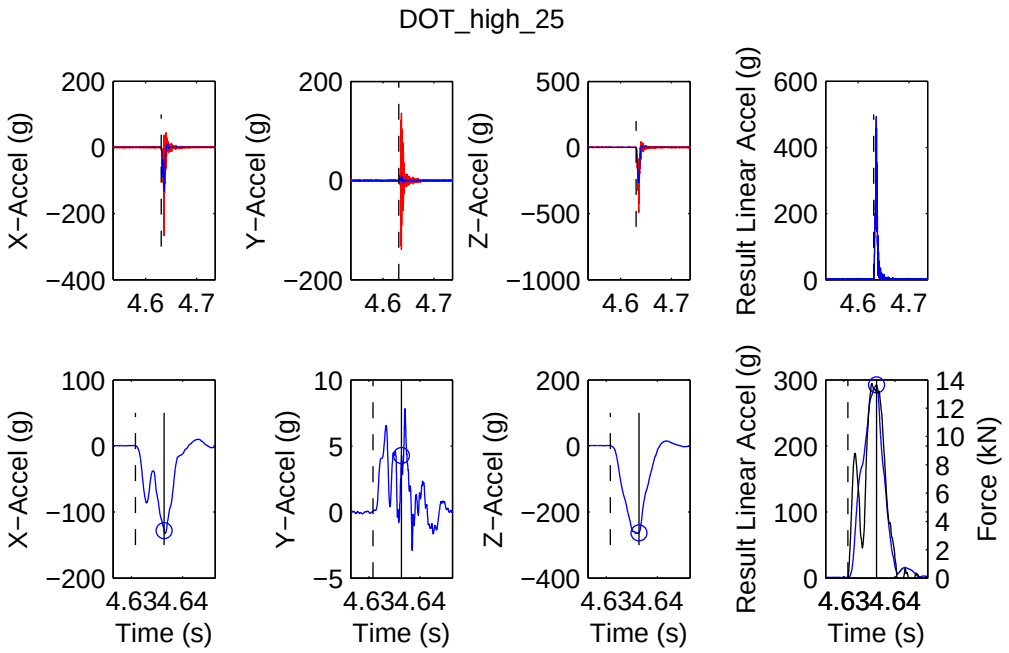

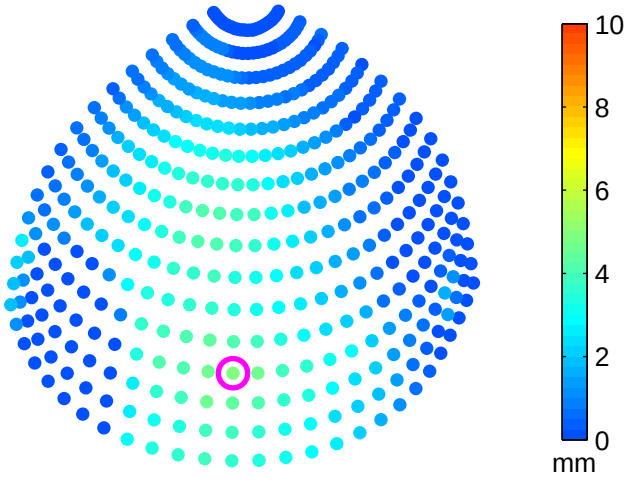

Max Resultant (g)	292.57	HIC	3942.69
Xg Max	−128.13	Max Force (N)	13748.95
Yg Max	4.27	Max Residual Crush Depth (mm)	5.70
Zg Max	−262.99	Max Crush Volume (cm³)	31.44

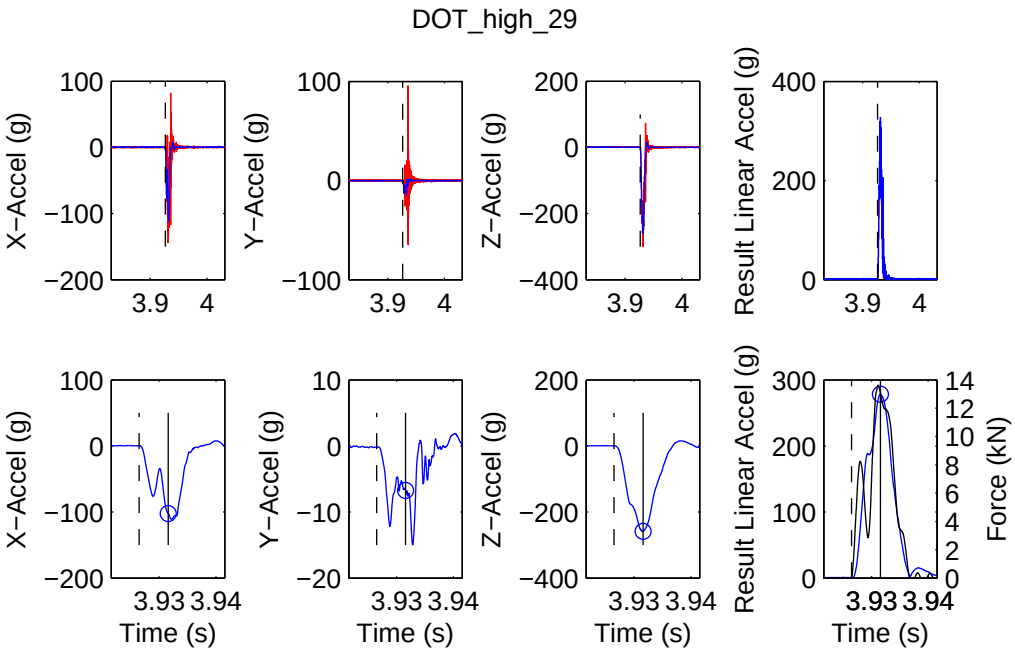

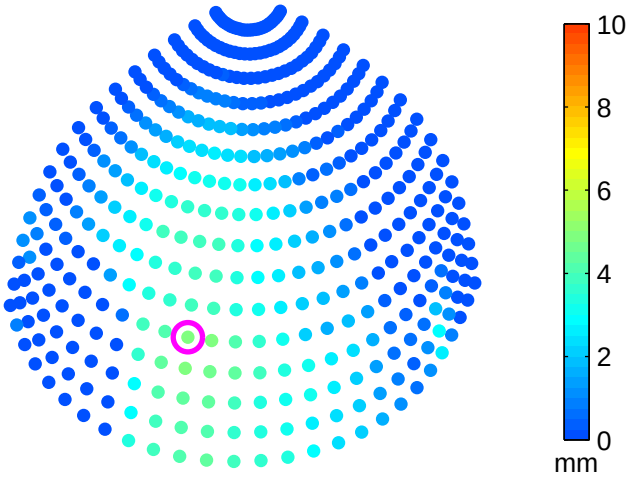

Max Resultant (g)	278.15	HIC	3771.38
Xg Max	−102.15	Max Force (N)	13617.49
Yg Max	−6.73	Max Residual Crush Depth (mm)	4.54
Zg Max	−258.63	Max Crush Volume (cm³)	26.80

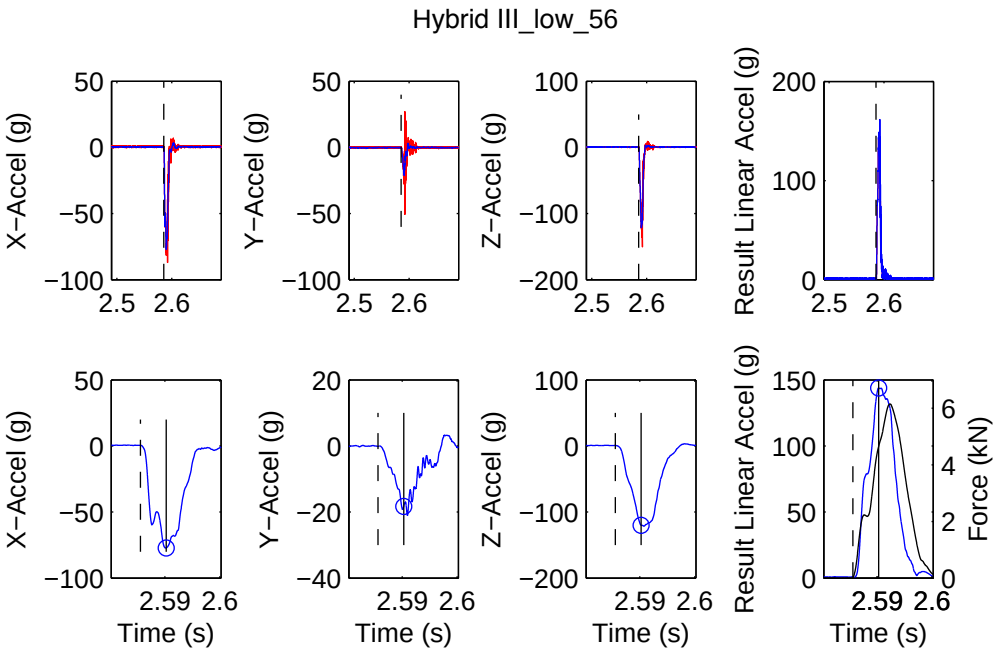

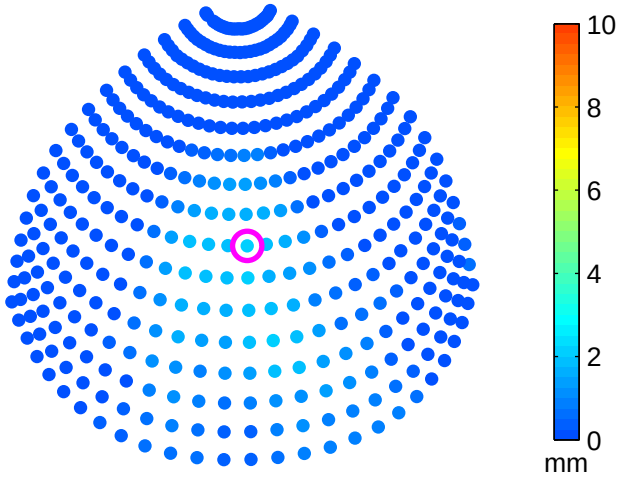

Max Resultant (g)	143.94	HIC	835.66
Xg Max	−77.22	Max Force (N)	6146.48
Yg Max	−18.30	Max Residual Crush Depth (mm)	2.11
Zg Max	−120.09	Max Crush Volume (cm³)	7.71

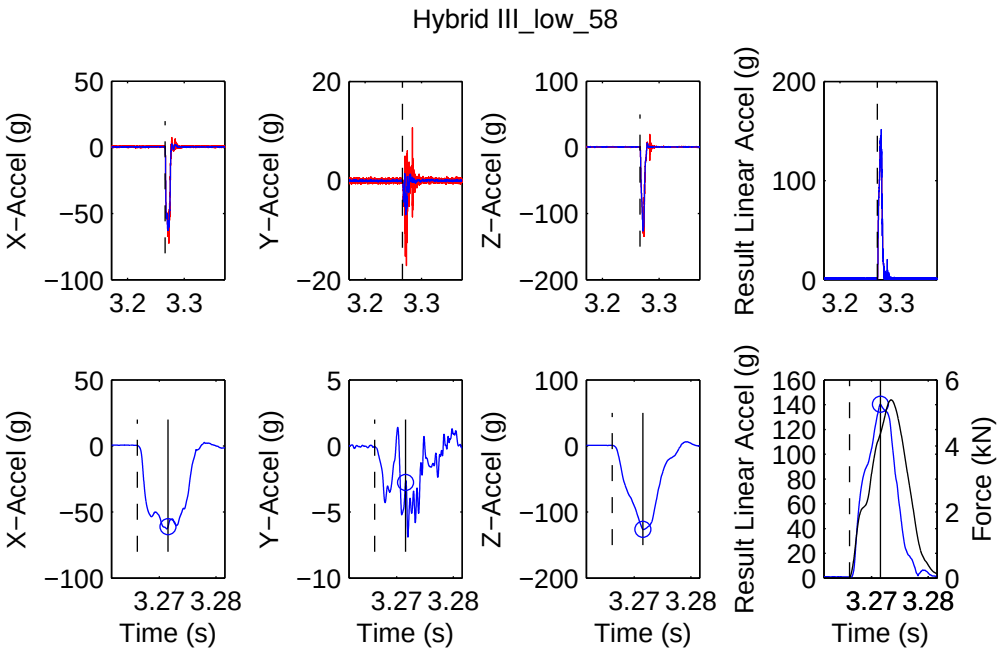

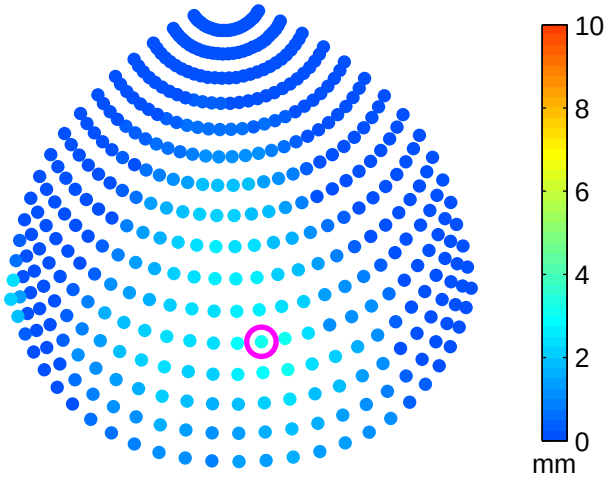

Max Resultant (g)	140.33	HIC	847.50
Xg Max	−61.12	Max Force (N)	5395.56
Yg Max	−2.77	Max Residual Crush Depth (mm)	3.24
Zg Max	−126.29	Max Crush Volume (cm³)	14.88

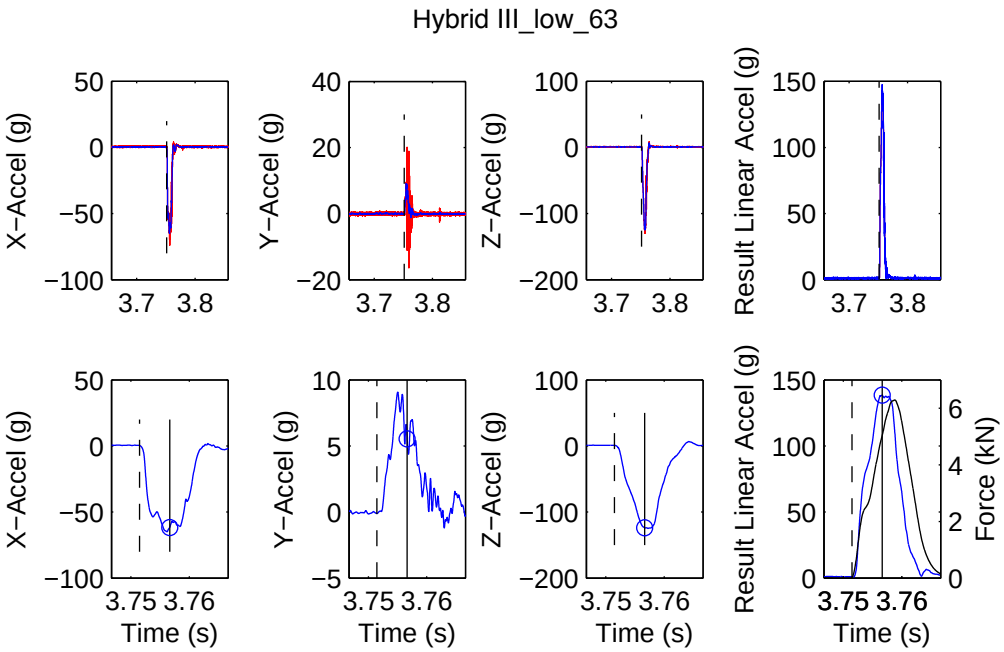

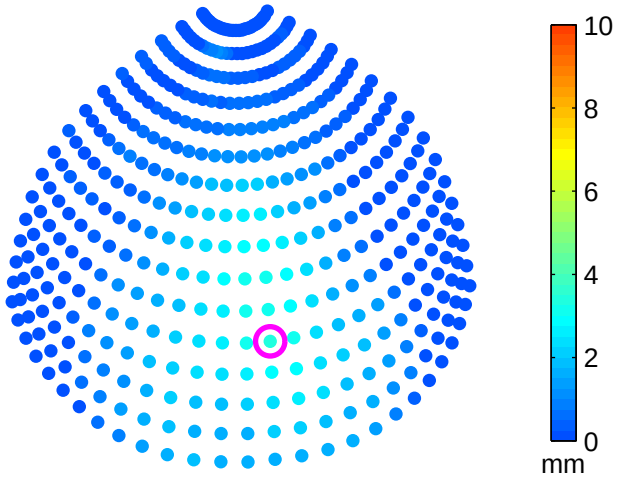

Max Resultant (g)	138.54	HIC	867.10
Xg Max	−61.66	Max Force (N)	6288.48
Yg Max	5.54	Max Residual Crush Depth (mm)	3.32
Zg Max	−123.93	Max Crush Volume (cm³)	16.84

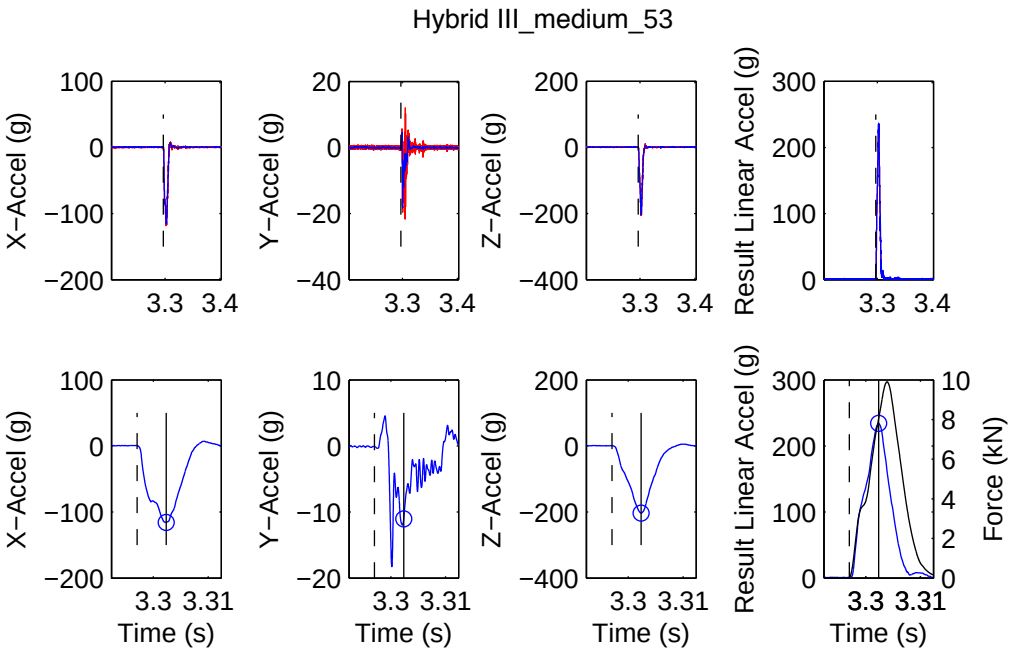

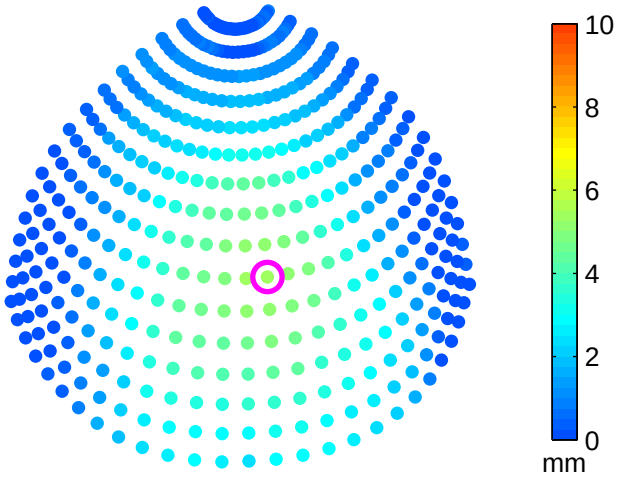

Max Resultant (g)	234.13	HIC	2325.39
Xg Max	−115.65	Max Force (N)	9903.98
Yg Max	−11.03	Max Residual Crush Depth (mm)	5.30
Zg Max	−203.27	Max Crush Volume (cm³)	35.77

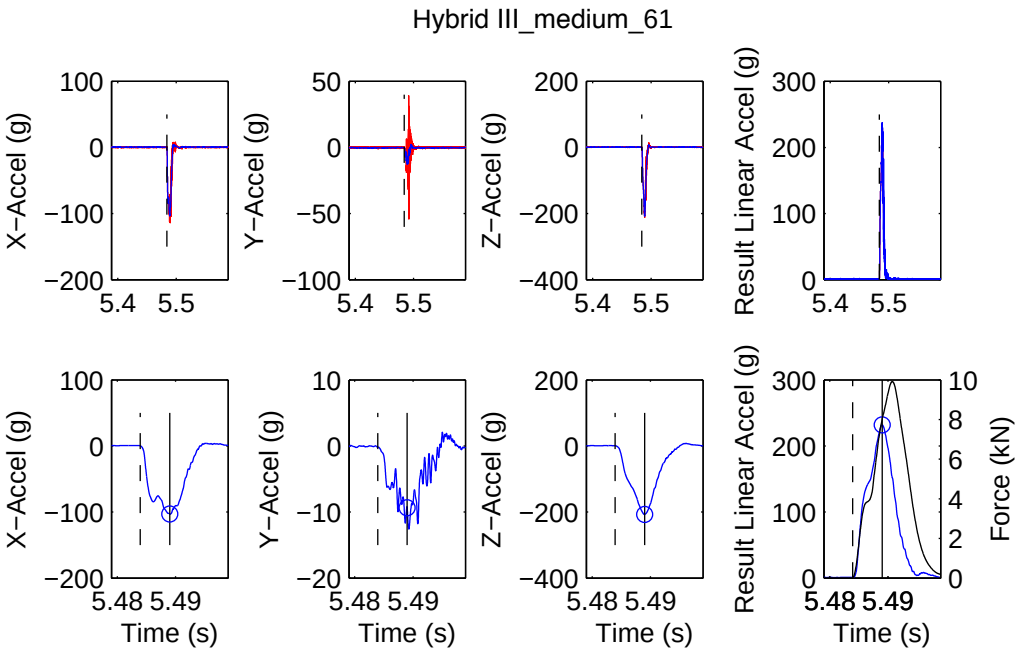

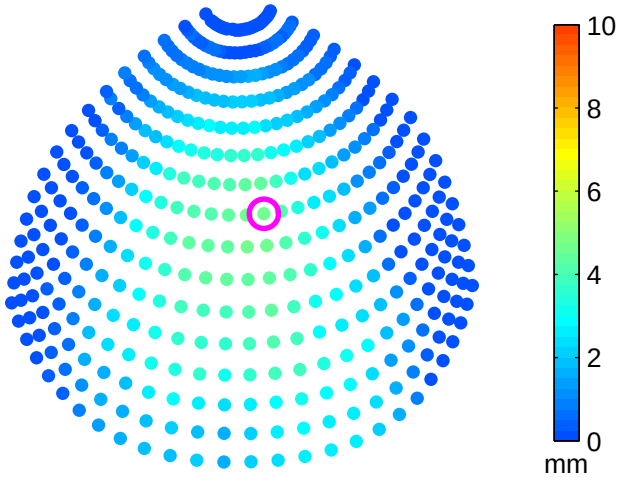

Max Resultant (g)	231.97	HIC	2343.24
Xg Max	−103.12	Max Force (N)	9914.30
Yg Max	−9.36	Max Residual Crush Depth (mm)	4.66
Zg Max	−207.58	Max Crush Volume (cm³)	31.15

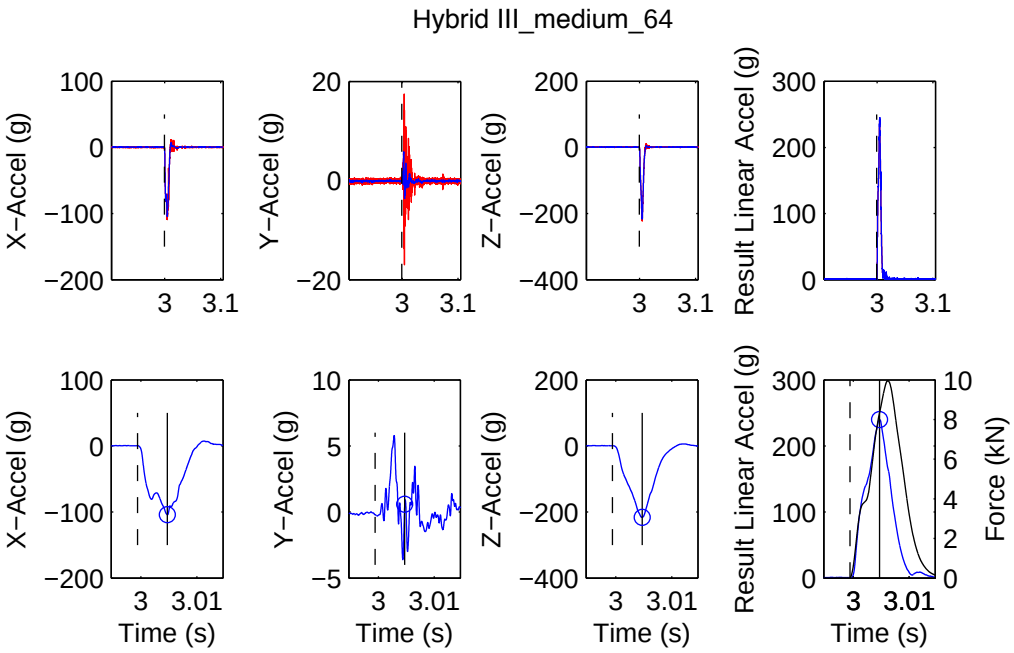

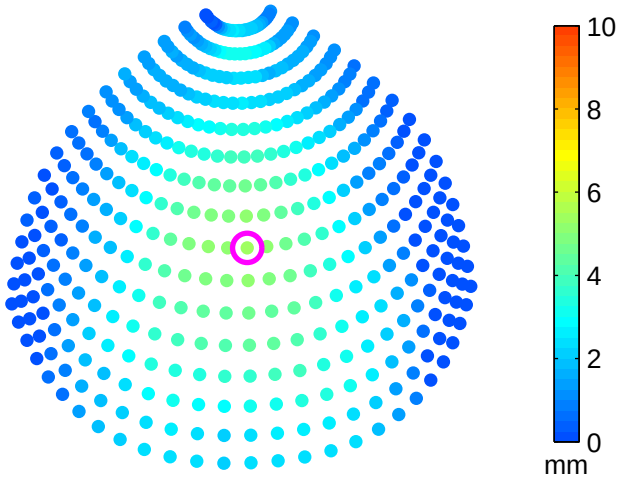

Max Resultant (g)	239.87	HIC	2397.43
Xg Max	−104.14	Max Force (N)	9962.17
Yg Max	0.59	Max Residual Crush Depth (mm)	5.28
Zg Max	−216.09	Max Crush Volume (cm³)	36.73

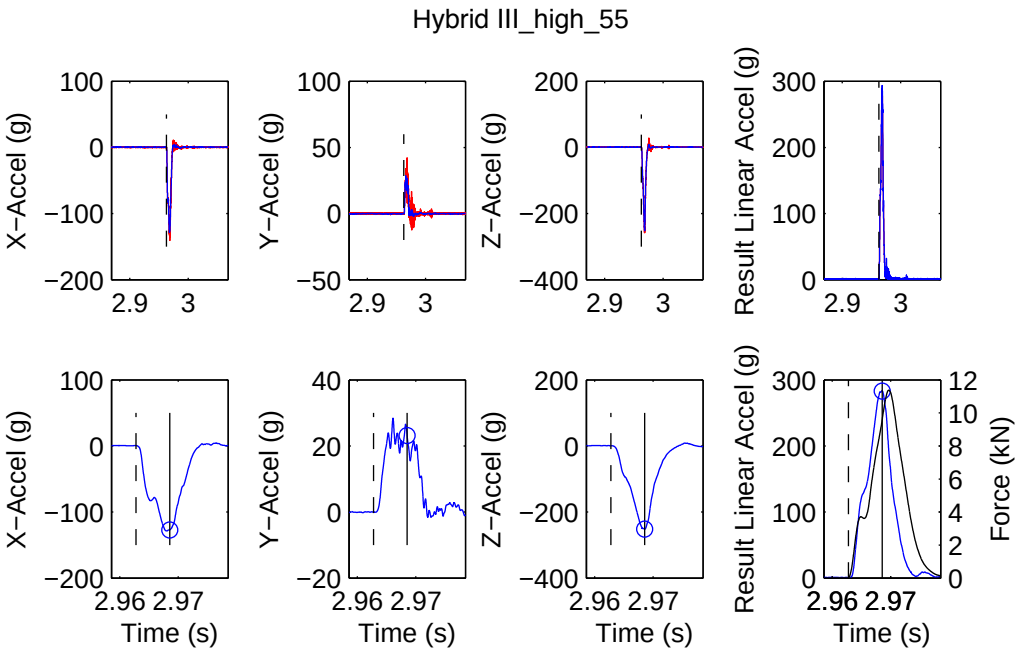

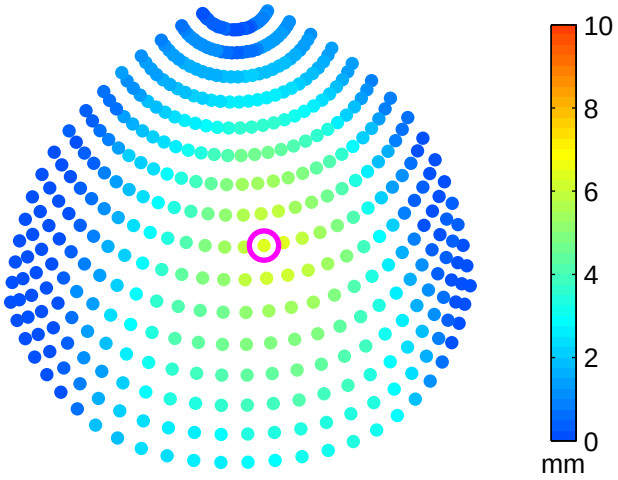

Max Resultant (g)	283.12	HIC	3278.72
Xg Max	−127.14	Max Force (N)	11376.61
Yg Max	23.15	Max Residual Crush Depth (mm)	6.29
Zg Max	−251.90	Max Crush Volume (cm³)	43.36

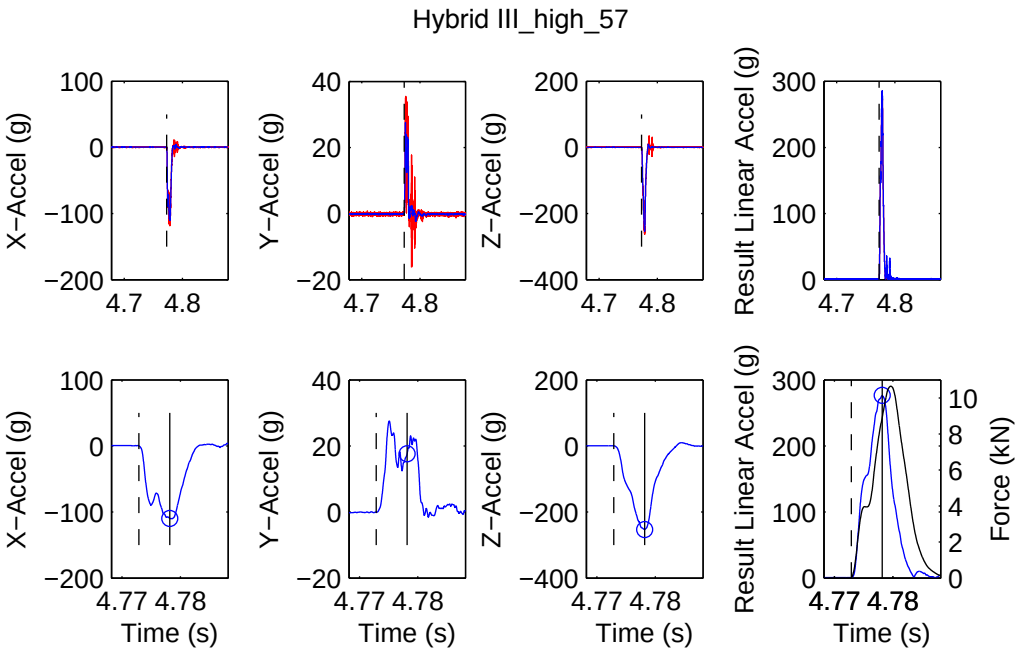

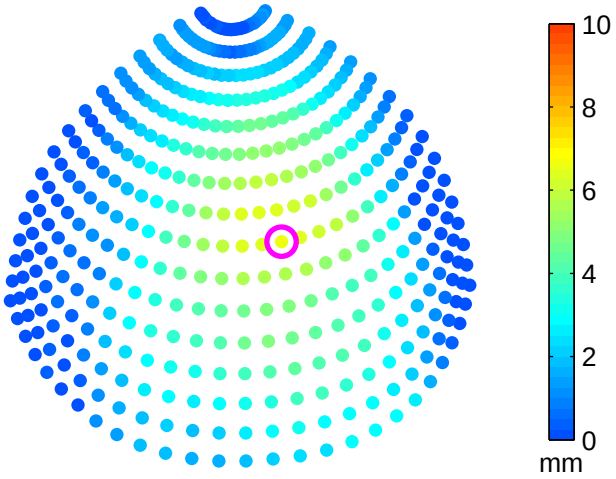

Max Resultant (g)	276.52	HIC	3417.97
Xg Max	−109.76	Max Force (N)	10648.53
Yg Max	17.66	Max Residual Crush Depth (mm)	6.61
Zg Max	−253.19	Max Crush Volume (cm³)	44.05

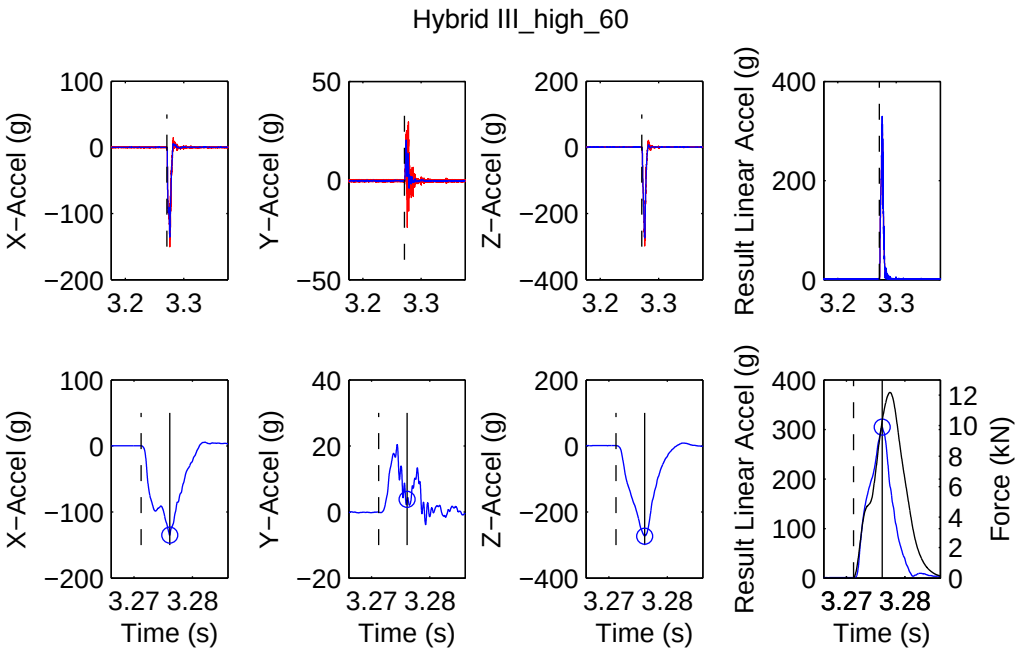

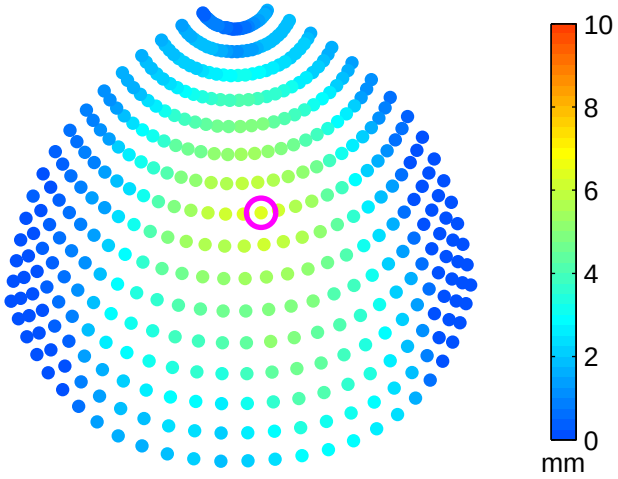

Max Resultant (g)	304.59	HIC	3735.82
Xg Max	−135.08	Max Force (N)	12173.18
Yg Max	3.86	Max Residual Crush Depth (mm)	6.18
Zg Max	−272.97	Max Crush Volume (cm³)	44.78

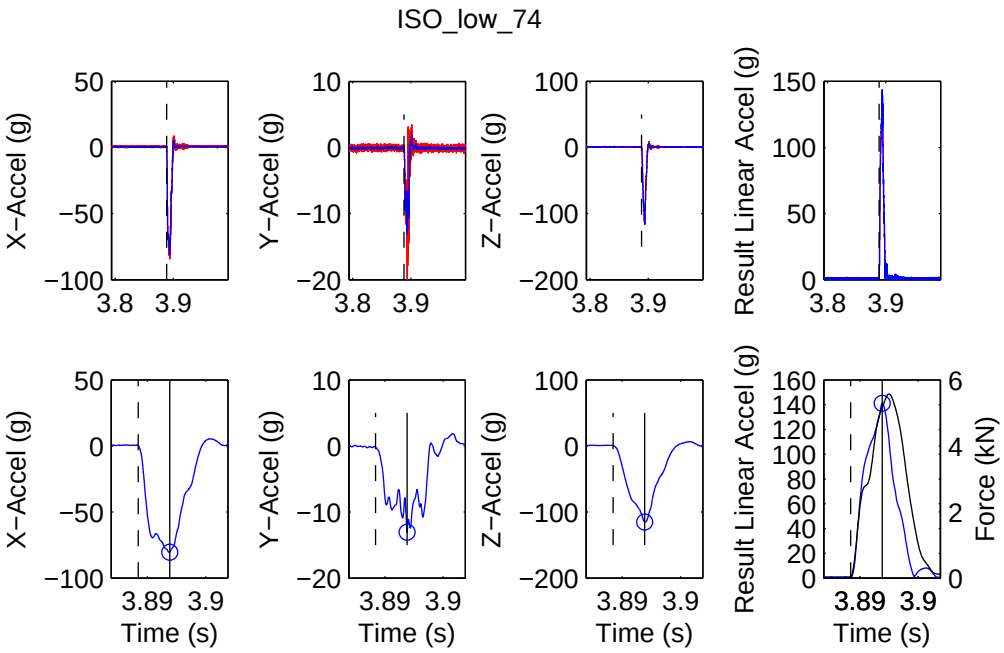

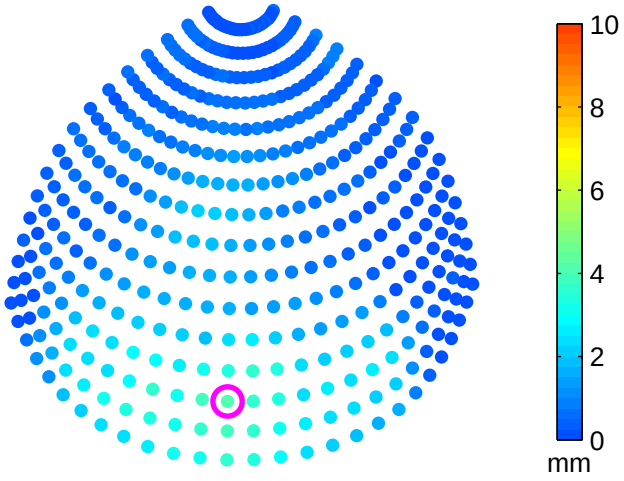

Max Resultant (g)	141.09
Xg Max	−80.45
Yg Max	−13.06
Zg Max	−115.16

HIC	744.06
Max Force (N)	5573.55
Max Residual Crush Depth (mm)	4.14
Max Crush Volume (cm³)	16.48

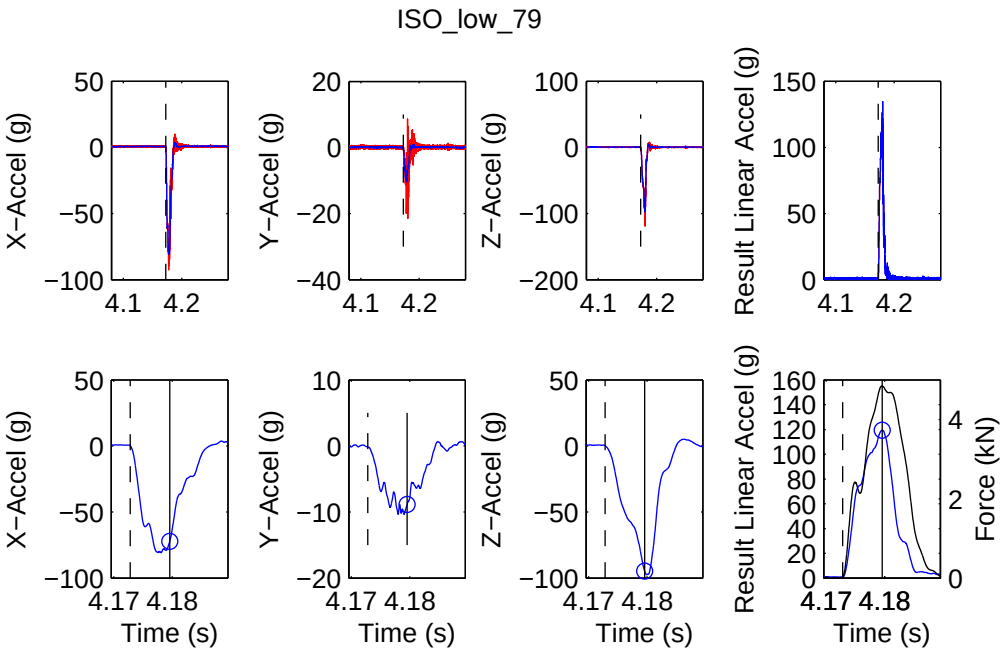

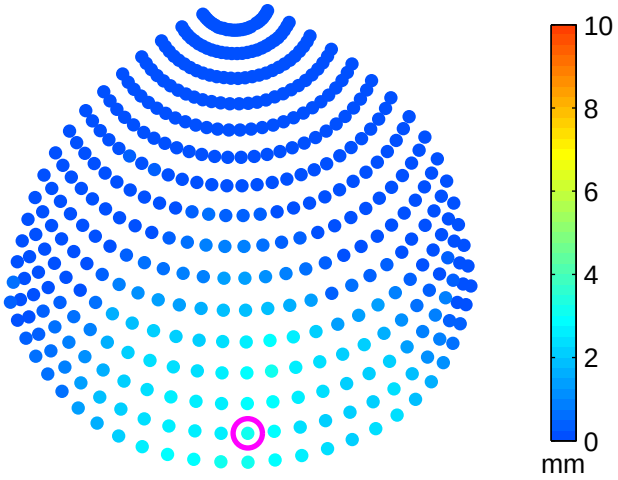

Max Resultant (g)	119.38	HIC	602.51
Xg Max	−72.23	Max Force (N)	4848.61
Yg Max	−8.85	Max Residual Crush Depth (mm)	3.05
Zg Max	−94.63	Max Crush Volume (cm³)	10.02

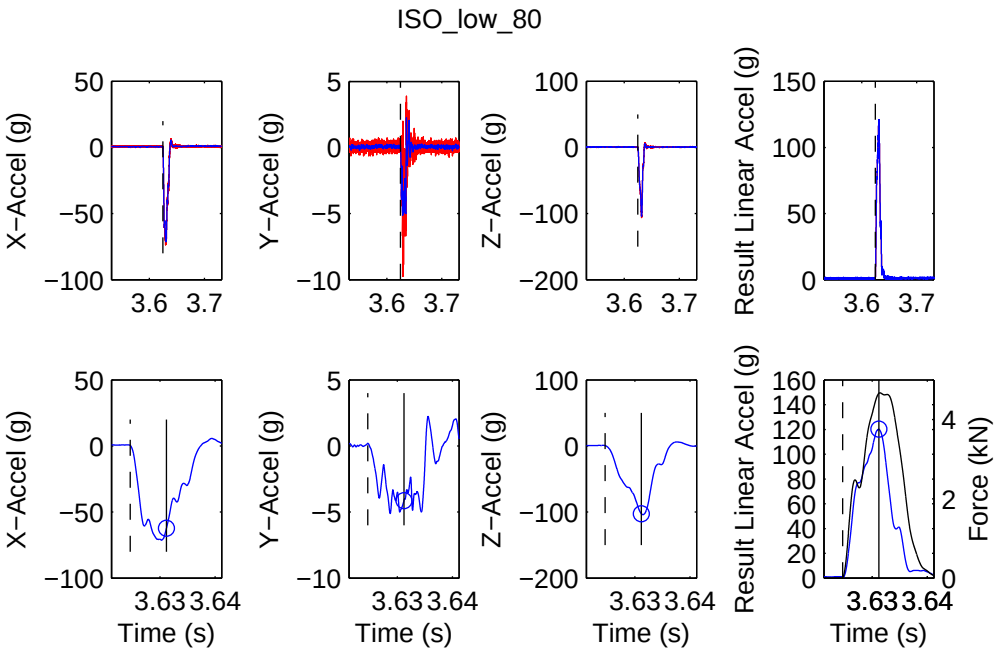

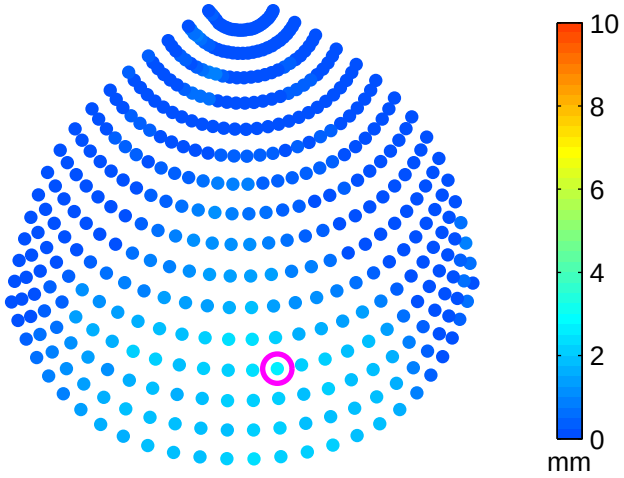

Max Resultant (g)	120.20	HIC	581.75
Xg Max	−62.17	Max Force (N)	4673.84
Yg Max	−4.14	Max Residual Crush Depth (mm)	2.55
Zg Max	−102.79	Max Crush Volume (cm³)	10.66

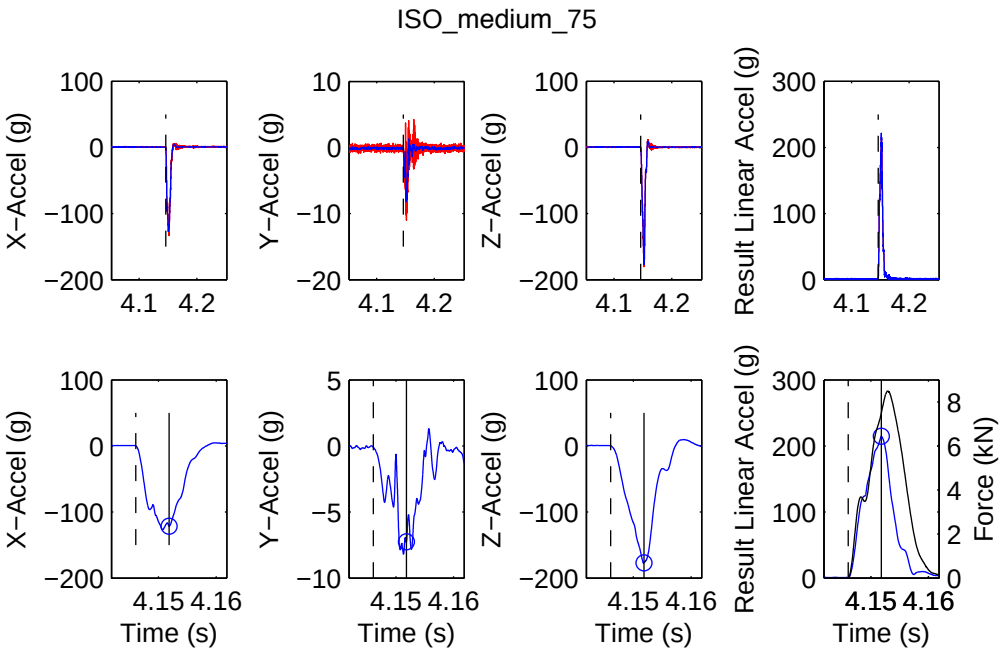

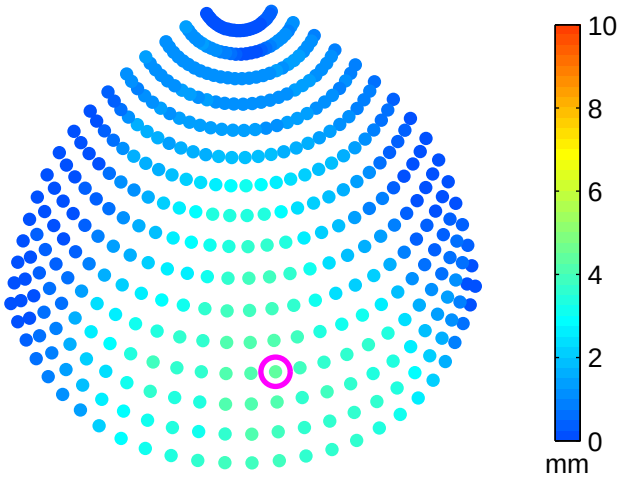

Max Resultant (g)	214.64	HIC	2008.05
Xg Max	−121.31	Max Force (N)	8492.69
Yg Max	−7.24	Max Residual Crush Depth (mm)	4.34
Zg Max	−176.93	Max Crush Volume (cm³)	29.26

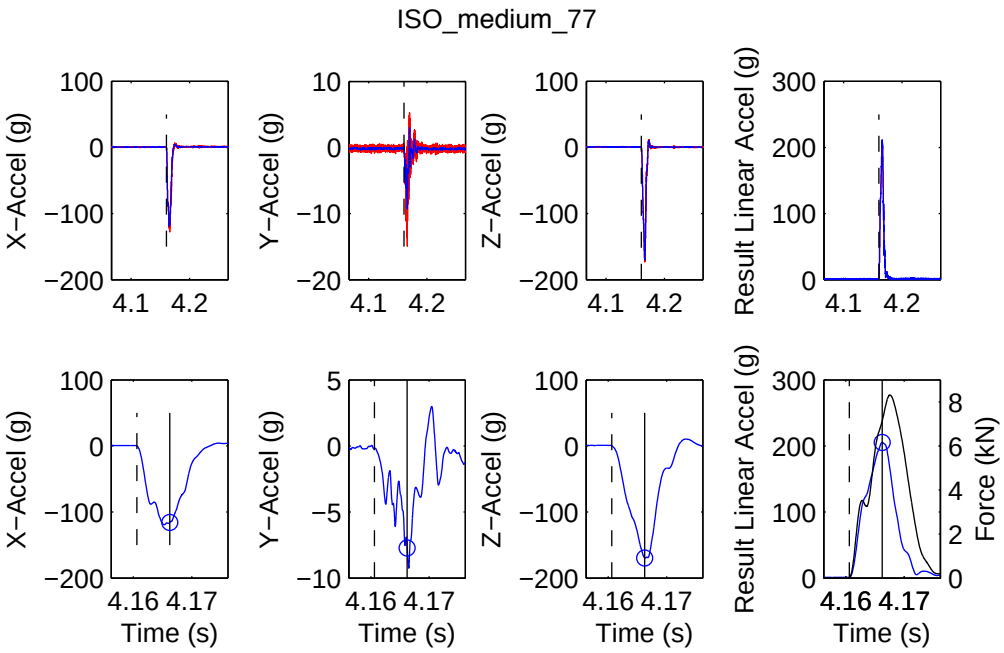

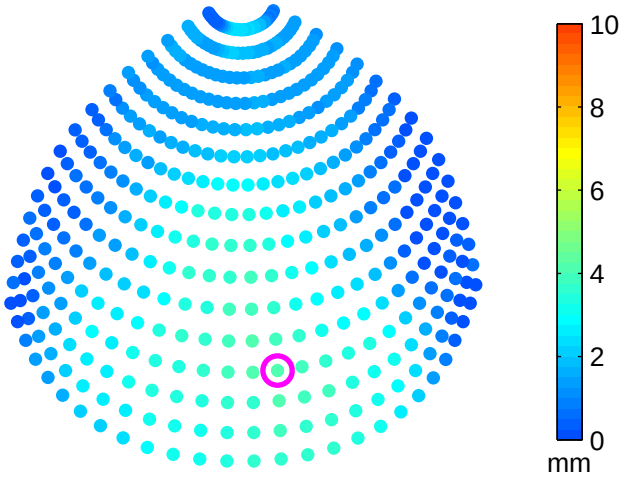

Max Resultant (g)	205.37	HIC	1946.24
Xg Max	−115.74	Max Force (N)	8311.52
Yg Max	−7.72	Max Residual Crush Depth (mm)	4.20
Zg Max	−169.47	Max Crush Volume (cm³)	30.11

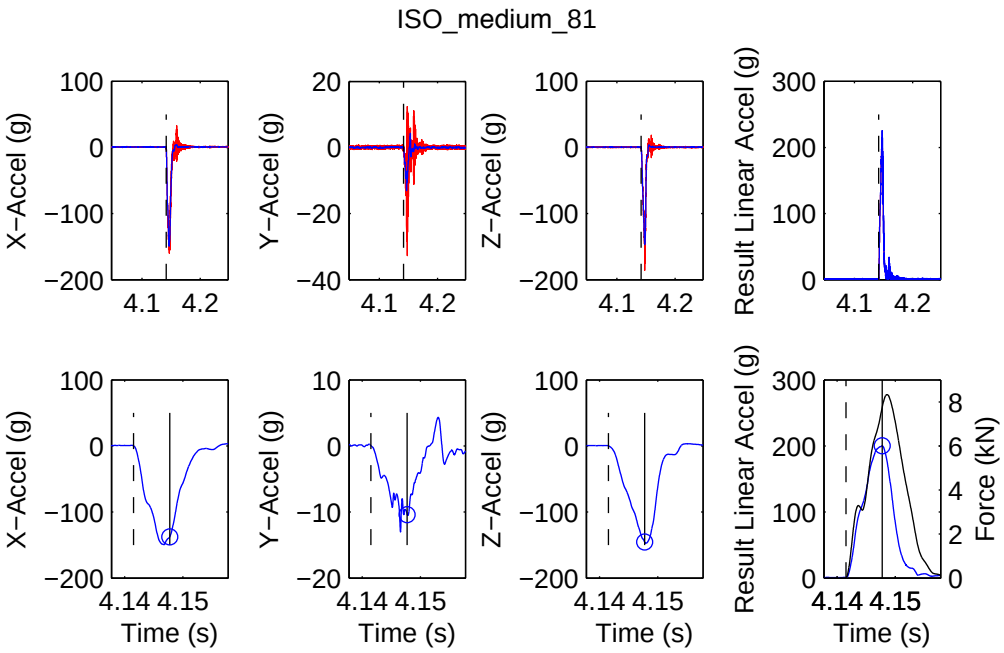

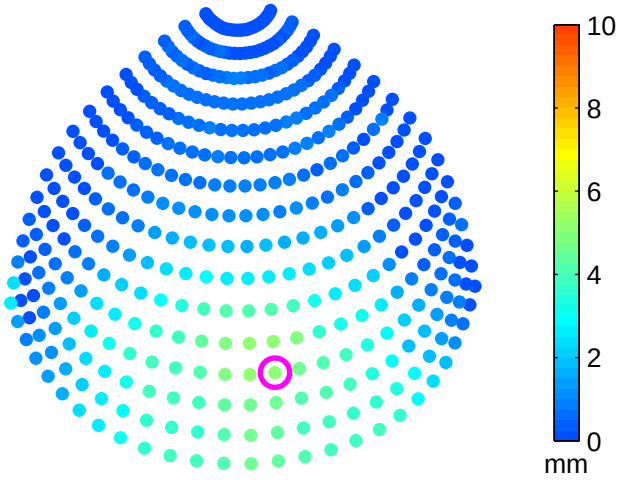

Max Resultant (g)	200.40	HIC	1933.29
Xg Max	−137.48	Max Force (N)	8331.79
Yg Max	−10.38	Max Residual Crush Depth (mm)	5.26
Zg Max	−145.44	Max Crush Volume (cm³)	23.72

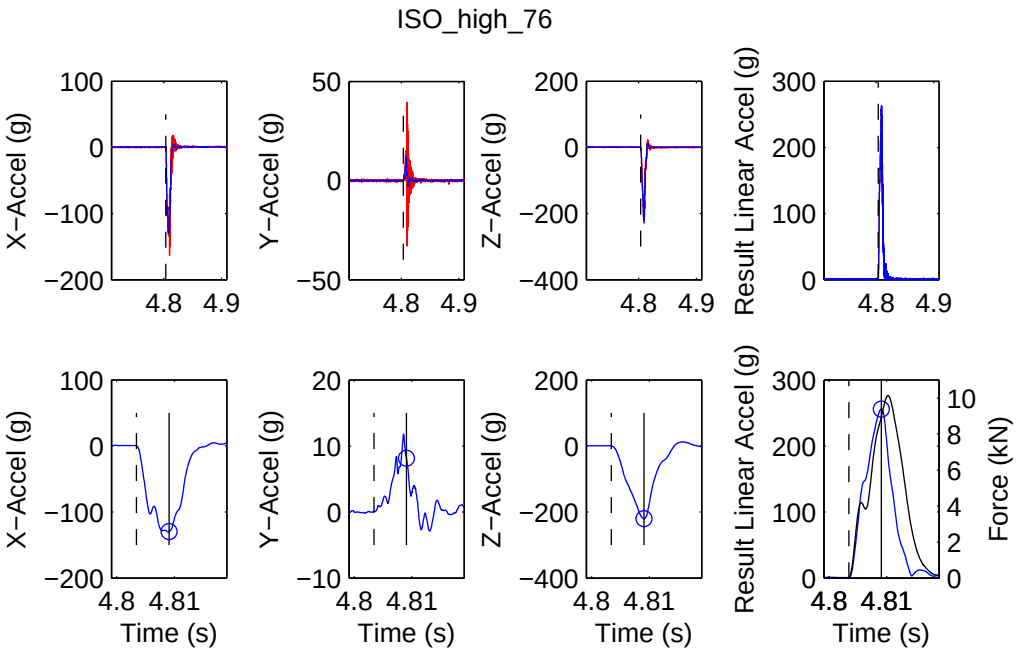

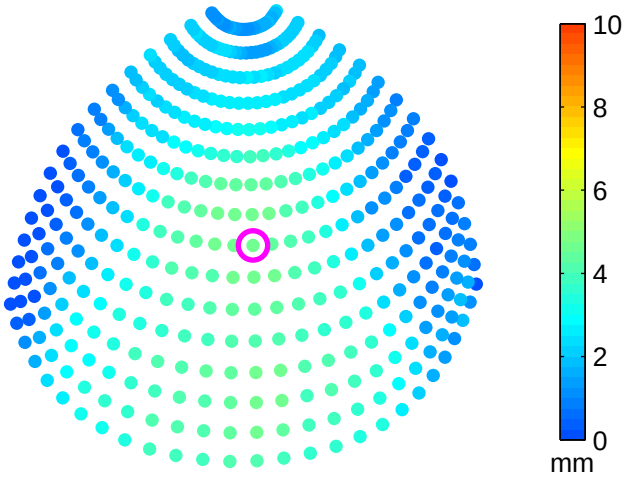

Max Resultant (g)	255.71	HIC	3004.60
Xg Max	−129.52	Max Force (N)	10129.35
Yg Max	8.16	Max Residual Crush Depth (mm)	4.70
Zg Max	−220.33	Max Crush Volume (cm³)	40.42

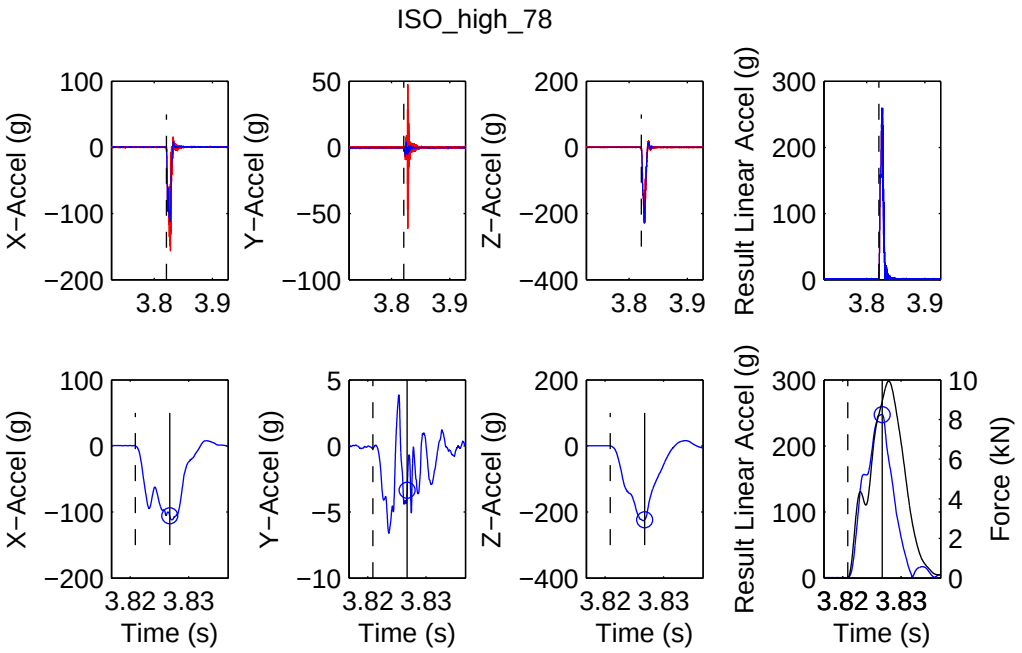

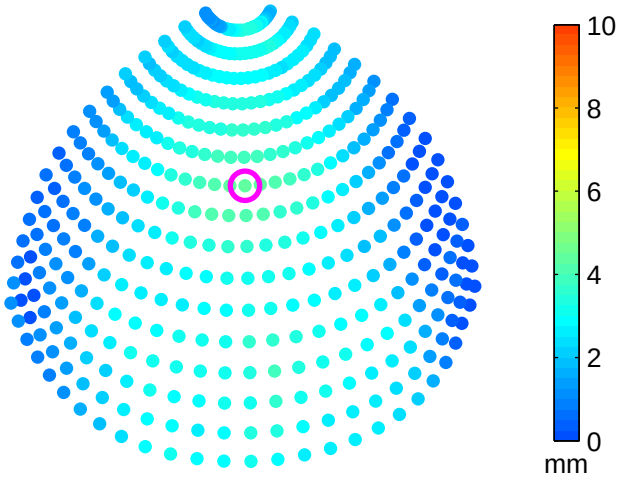

Max Resultant (g)	247.43	HIC	2990.72
Xg Max	−105.60	Max Force (N)	9938.27
Yg Max	−3.34	Max Residual Crush Depth (mm)	4.40
Zg Max	−223.73	Max Crush Volume (cm³)	35.05

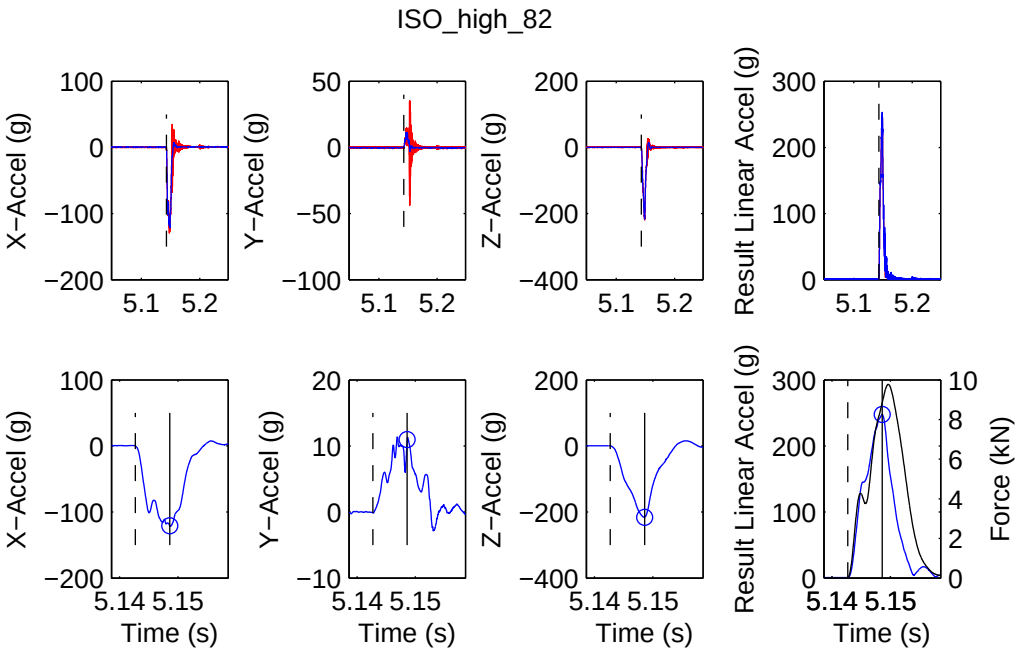

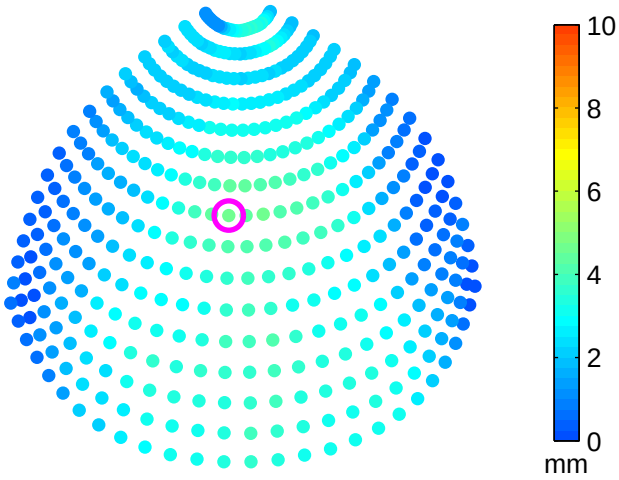

Max Resultant (g)	247.55	HIC	2839.02
Xg Max	−120.70	Max Force (N)	9775.24
Yg Max	10.97	Max Residual Crush Depth (mm)	4.50
Zg Max	−215.85	Max Crush Volume (cm³)	37.63

Appendix D

Linear acceleration and anterosuperior views of the residual foam liner deformation averaged over 5° x 5° elements for Experiment B impacts. The circled point represents the maximum crush depth. Data are summarized in the lower table. Labeling above figure specifies helmet size, headform type, test number, and impact speed.

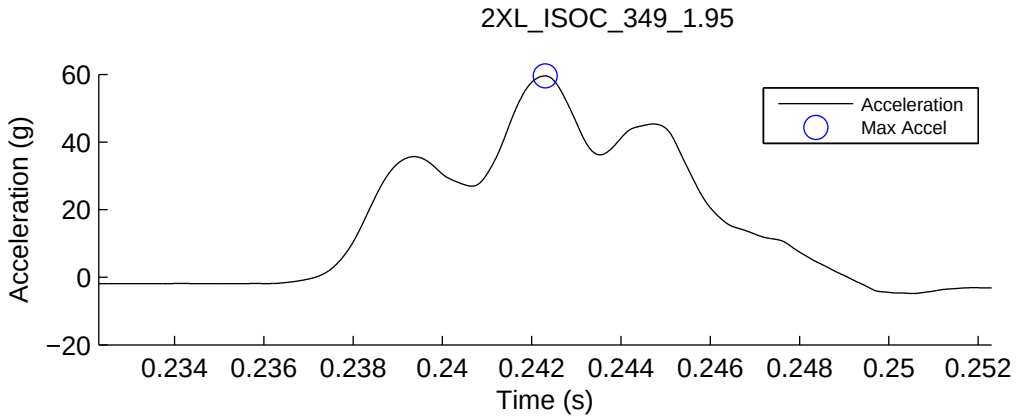

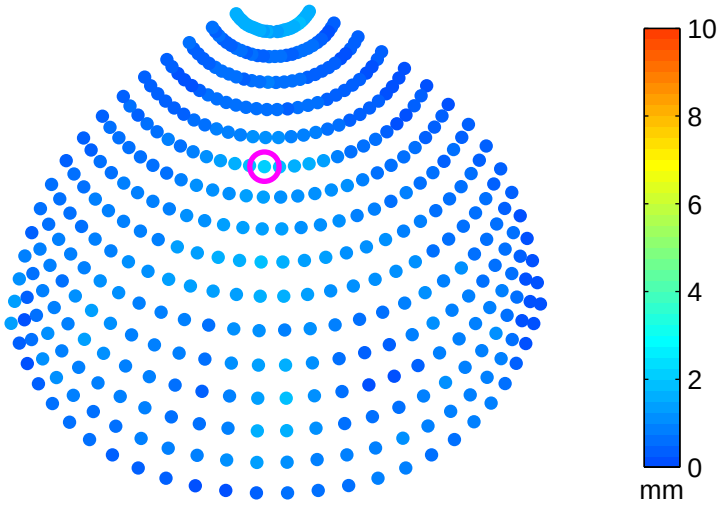

Max Resultant Accel (g)	59.57
HIC	71.83
Impact Speed (m/s)	1.95
Impact Energy (J)	9.43
Maximum Crush (mm)	2.07
Crush Volume (cm³)	17.05
Mismatch (cm)	10.25

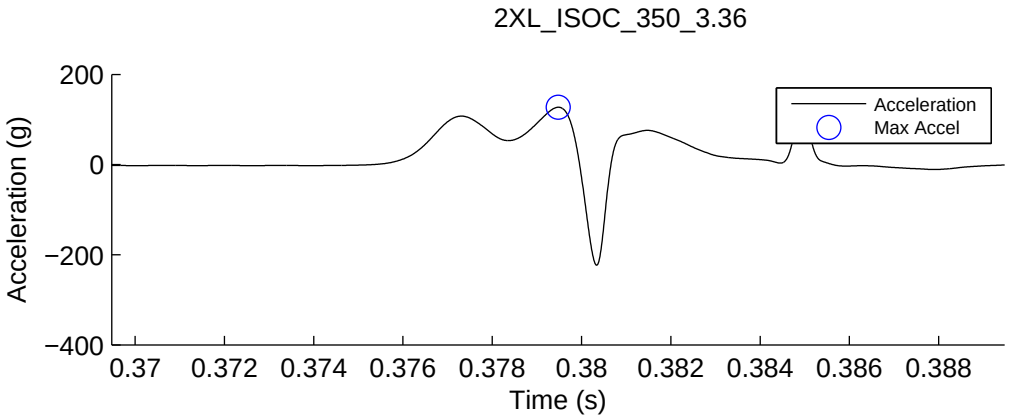

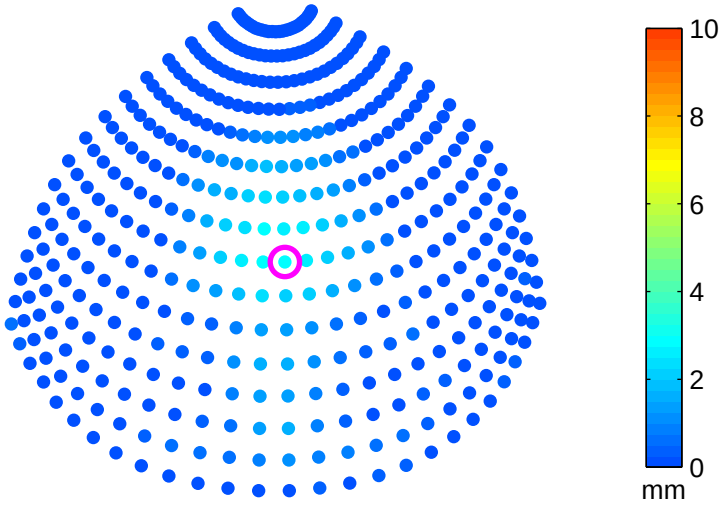

Max Resultant Accel (g)	127.25
HIC	231.49
Impact Speed (m/s)	3.36
Impact Energy (J)	28.07
Maximum Crush (mm)	2.87
Crush Volume (cm³)	8.28
Mismatch (cm)	10.25

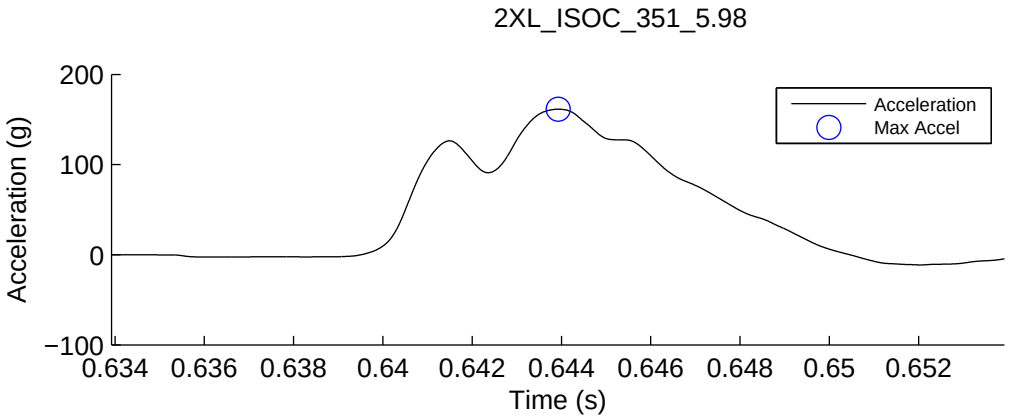

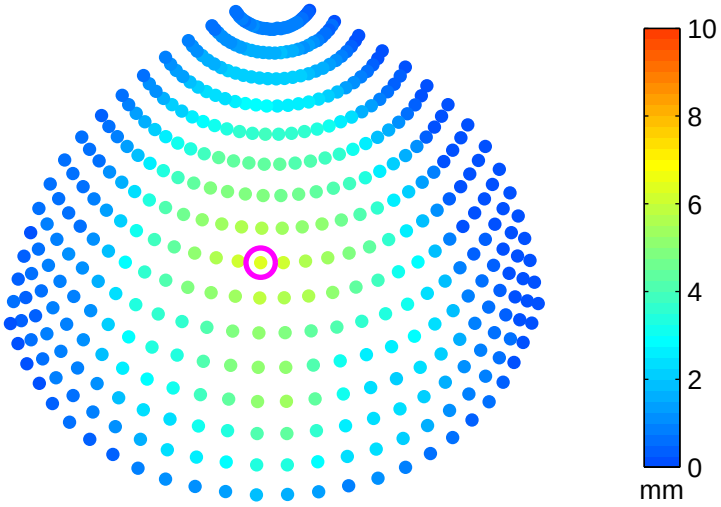

Max Resultant Accel (g)	161.46
HIC	1006.99
Impact Speed (m/s)	5.98
Impact Energy (J)	89.17
Maximum Crush (mm)	6.29
Crush Volume (cm³)	48.17
Mismatch (cm)	10.25

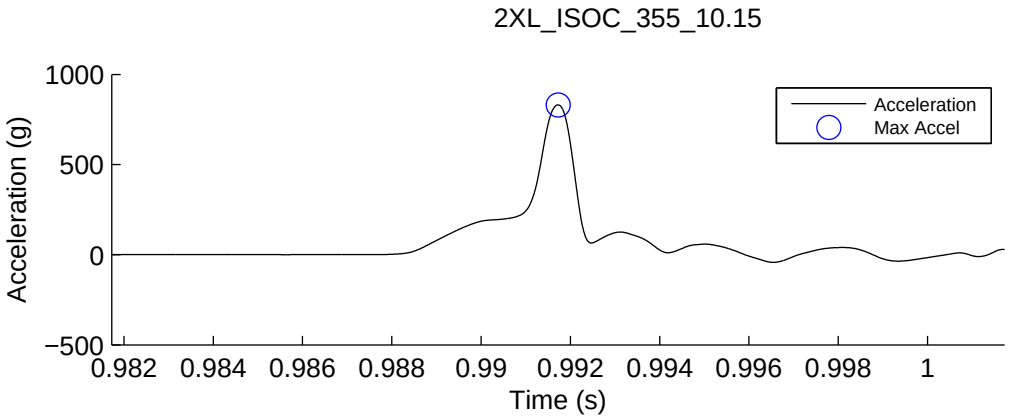

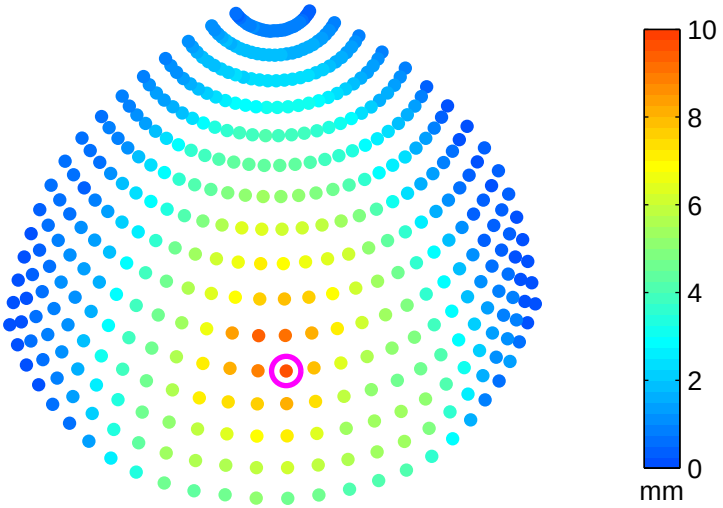

Max Resultant Accel (g)	831.12
HIC	10476.81
Impact Speed (m/s)	10.15
Impact Energy (J)	256.42
Maximum Crush (mm)	9.54
Crush Volume (cm³)	72.75
Mismatch (cm)	10.25

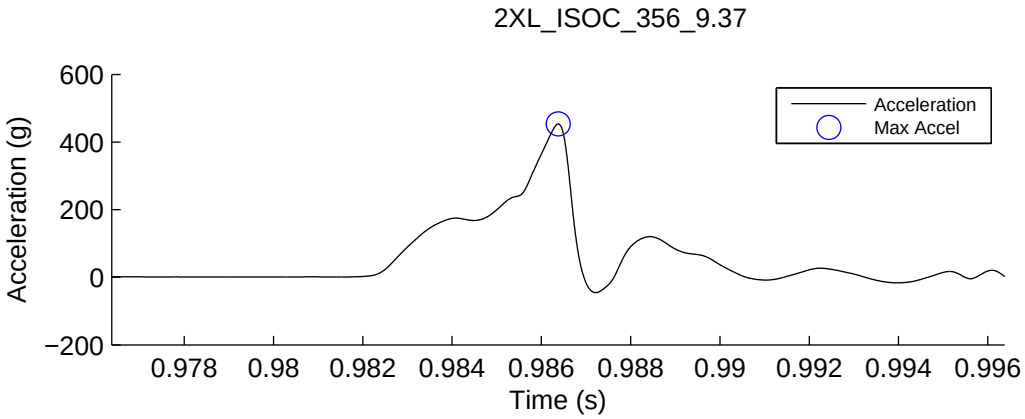

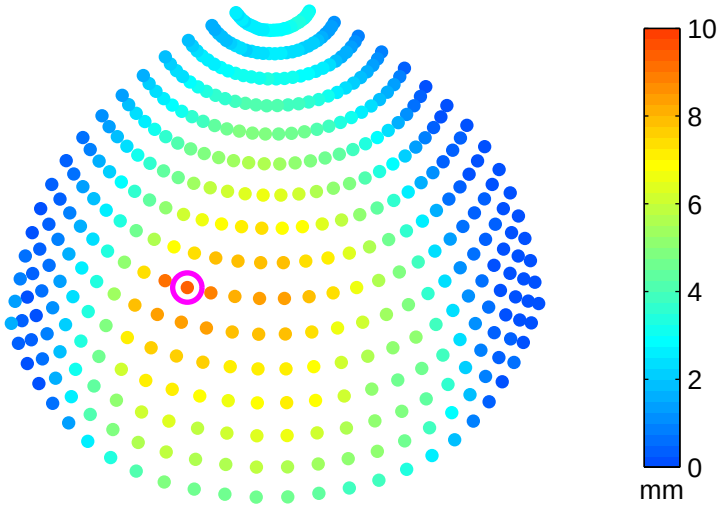

Max Resultant Accel (g)	453.45
HIC	3090.40
Impact Speed (m/s)	9.37
Impact Energy (J)	218.48
Maximum Crush (mm)	9.31
Crush Volume (cm³)	82.24
Mismatch (cm)	10.25

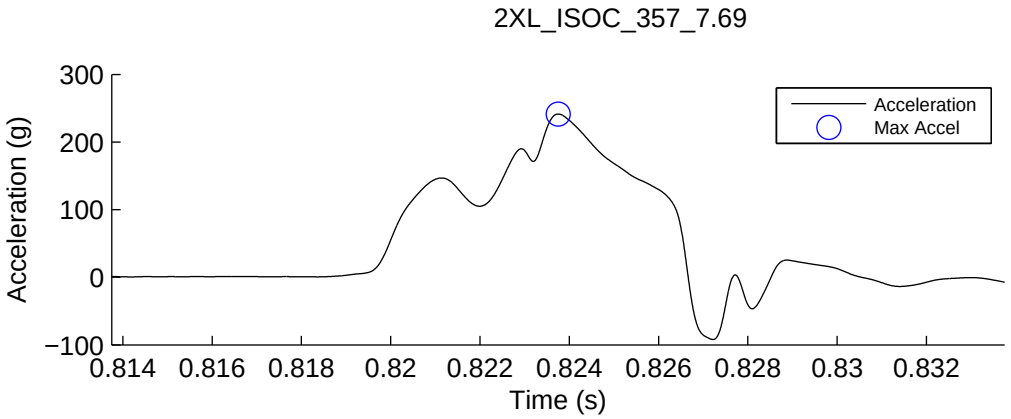

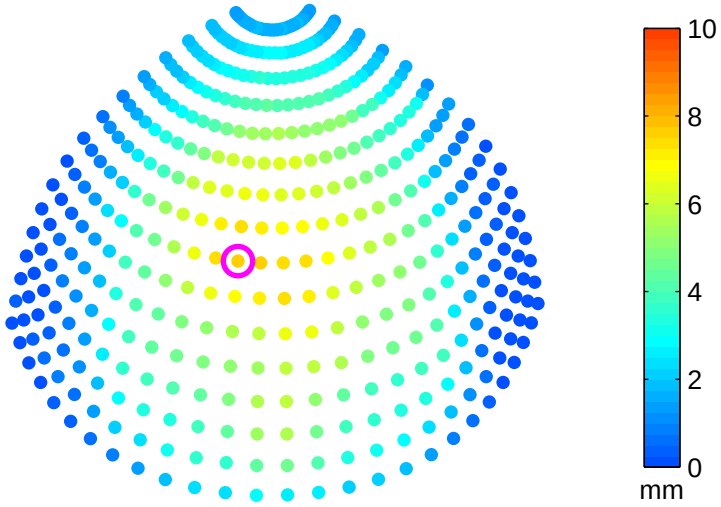

Max Resultant Accel (g)	241.49
HIC	1935.36
Impact Speed (m/s)	7.69
Impact Energy (J)	147.41
Maximum Crush (mm)	7.68
Crush Volume (cm³)	68.51
Mismatch (cm)	10.25

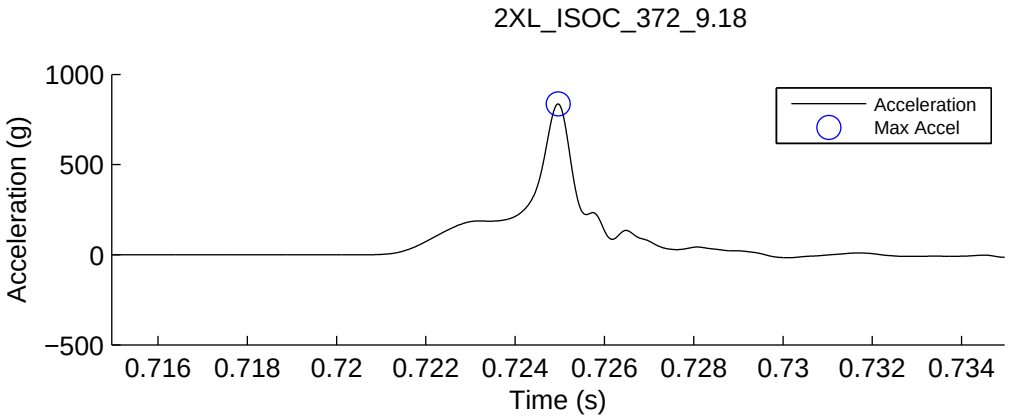

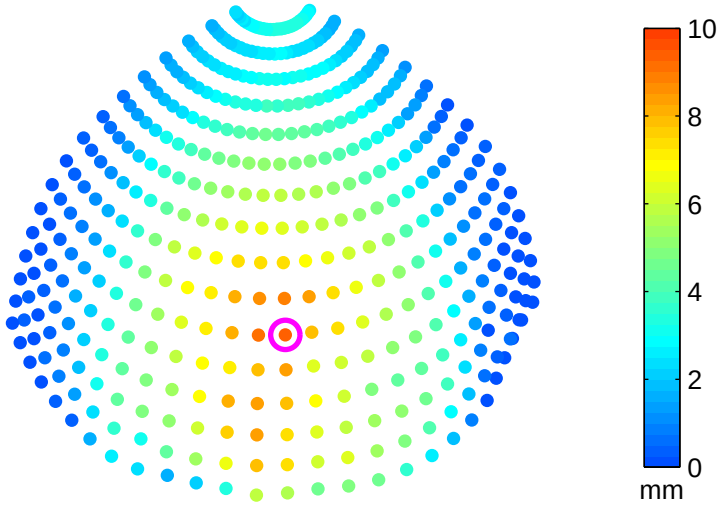

Max Resultant Accel (g)	836.46
HIC	8746.64
Impact Speed (m/s)	9.18
Impact Energy (J)	209.96
Maximum Crush (mm)	9.29
Crush Volume (cm³)	76.14
Mismatch (cm)	10.25

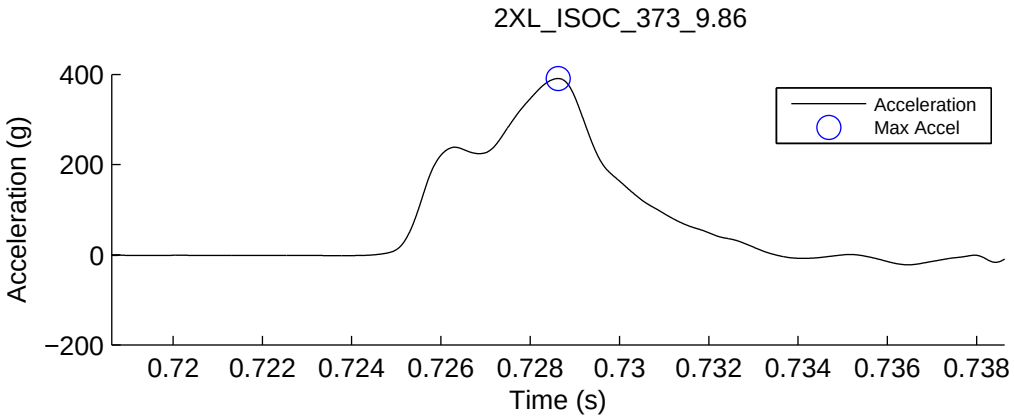

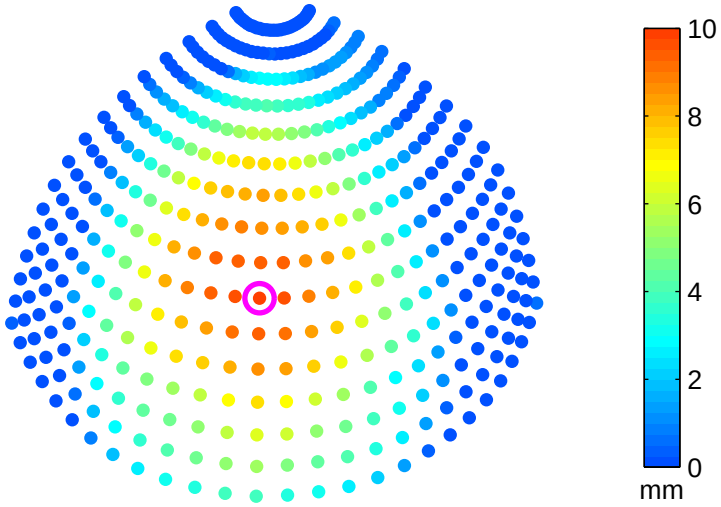

Max Resultant Accel (g)	390.92
HIC	5411.78
Impact Speed (m/s)	9.86
Impact Energy (J)	242.17
Maximum Crush (mm)	9.80
Crush Volume (cm³)	68.85
Mismatch (cm)	10.25

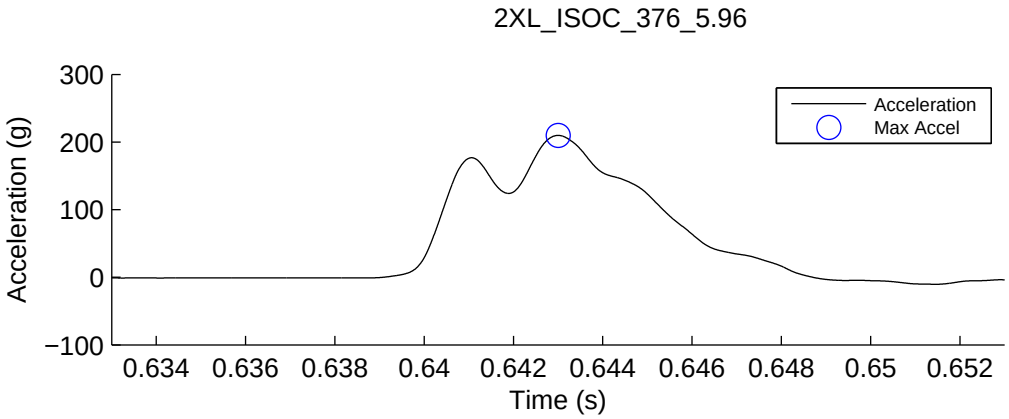

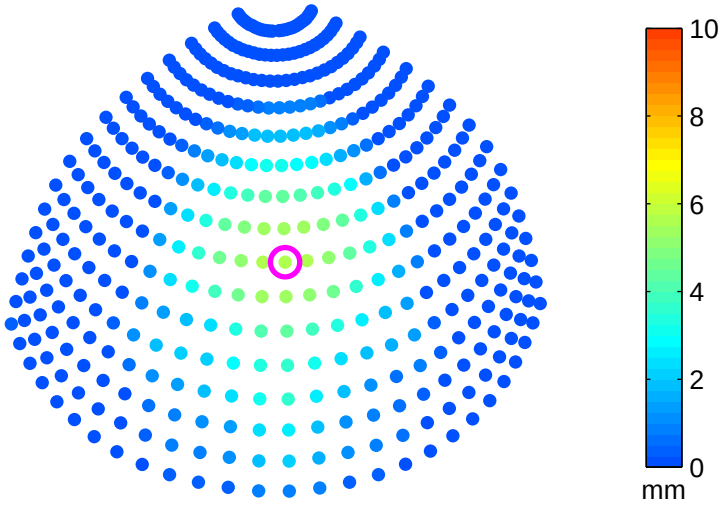

Max Resultant Accel (g)	209.82
HIC	1529.66
Impact Speed (m/s)	5.96
Impact Energy (J)	88.41
Maximum Crush (mm)	5.63
Crush Volume (cm³)	21.63
Mismatch (cm)	10.25

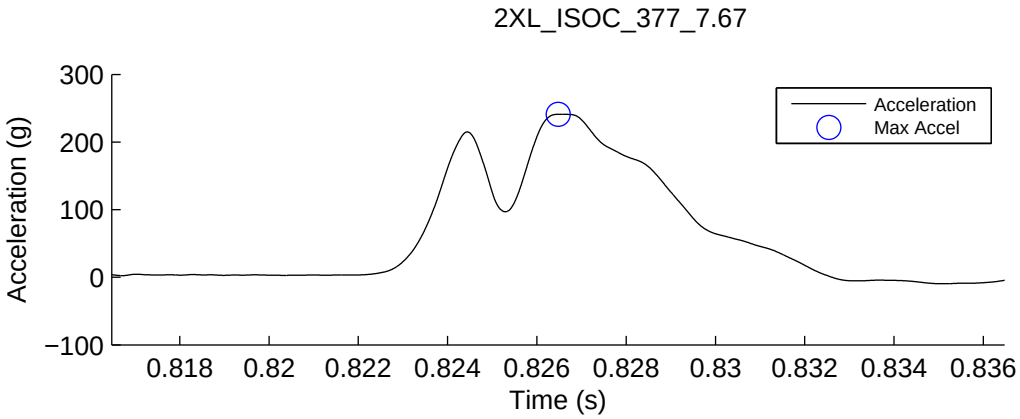

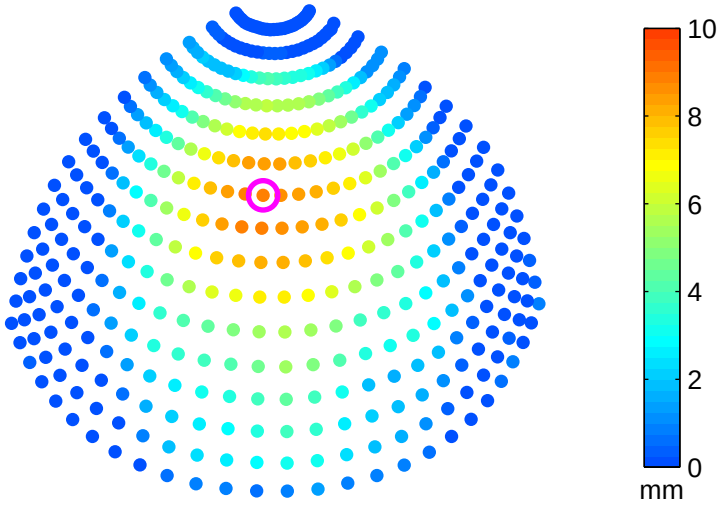

Max Resultant Accel (g)	240.95
HIC	2308.43
Impact Speed (m/s)	7.67
Impact Energy (J)	146.60
Maximum Crush (mm)	8.94
Crush Volume (cm³)	55.33
Mismatch (cm)	10.25

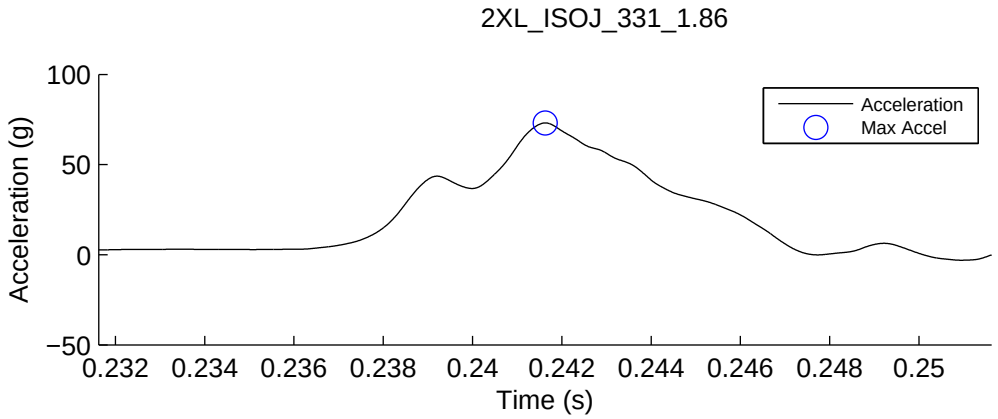

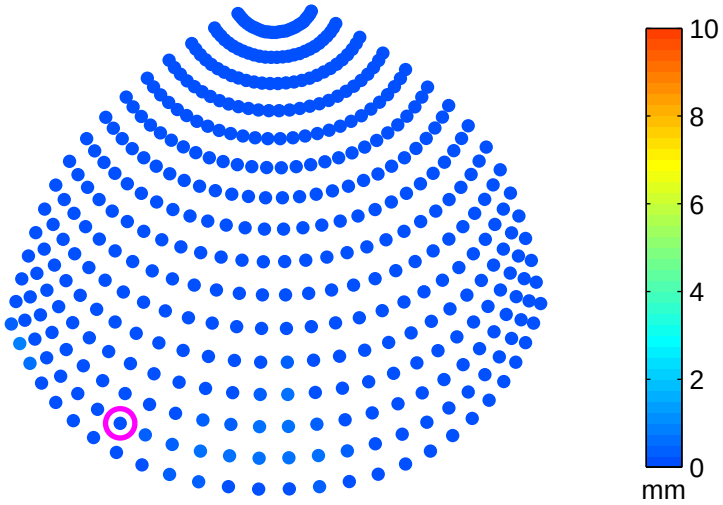

Max Resultant Accel (g)	73.11
HIC	111.31
Impact Speed (m/s)	1.86
Impact Energy (J)	8.63
Maximum Crush (mm)	0.69
Crush Volume (cm³)	0.99
Mismatch (cm)	5.25

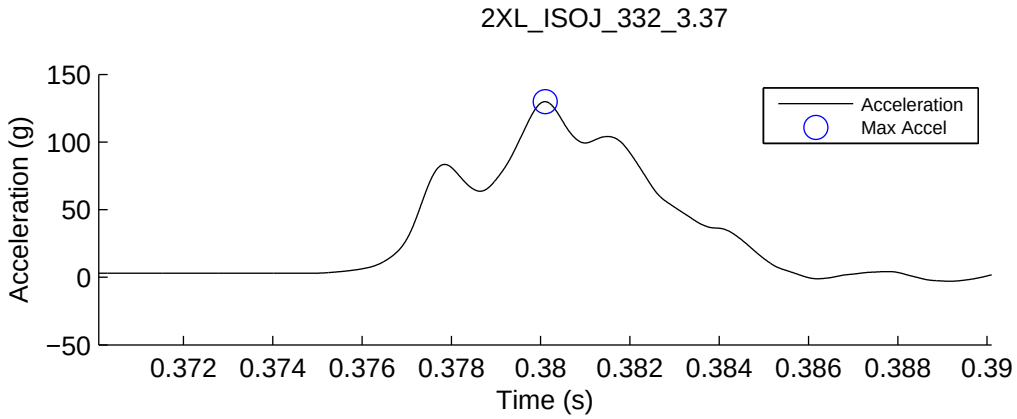

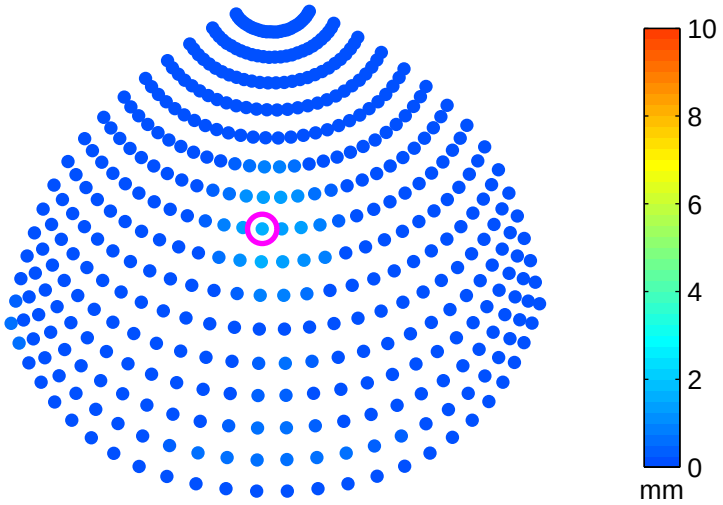

Max Resultant Accel (g)	129.87
HIC	424.76
Impact Speed (m/s)	3.37
Impact Energy (J)	28.47
Maximum Crush (mm)	1.69
Crush Volume (cm³)	2.54
Mismatch (cm)	5.25

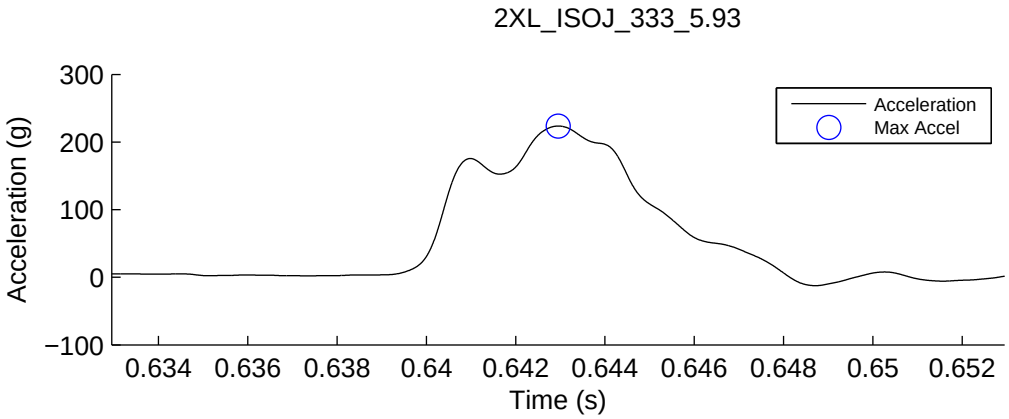

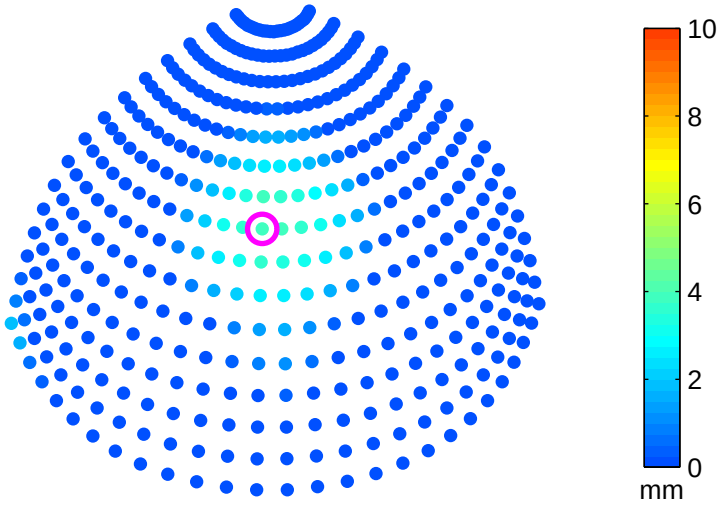

Max Resultant Accel (g)	223.71
HIC	1930.37
Impact Speed (m/s)	5.93
Impact Energy (J)	88.00
Maximum Crush (mm)	3.91
Crush Volume (cm³)	7.66
Mismatch (cm)	5.25

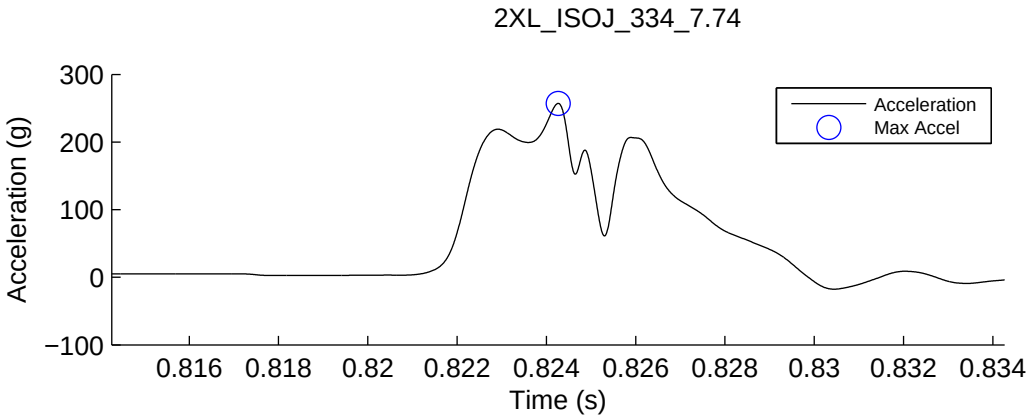

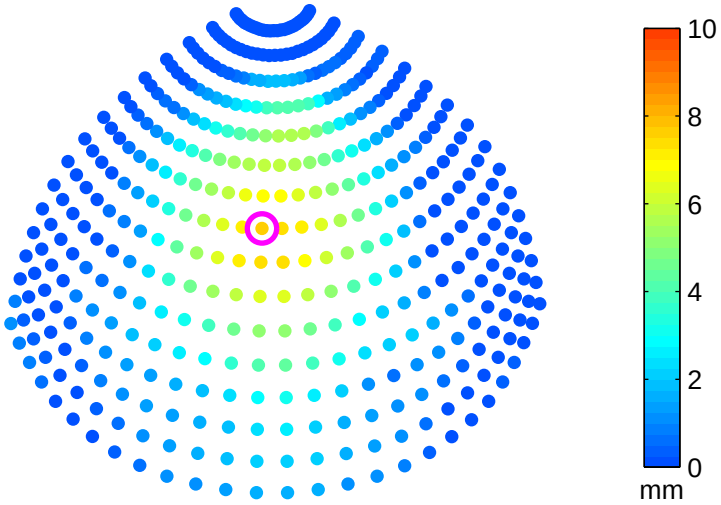

Max Resultant Accel (g)	257.17
HIC	2094.28
Impact Speed (m/s)	7.74
Impact Energy (J)	149.60
Maximum Crush (mm)	7.59
Crush Volume (cm³)	36.94
Mismatch (cm)	5.25

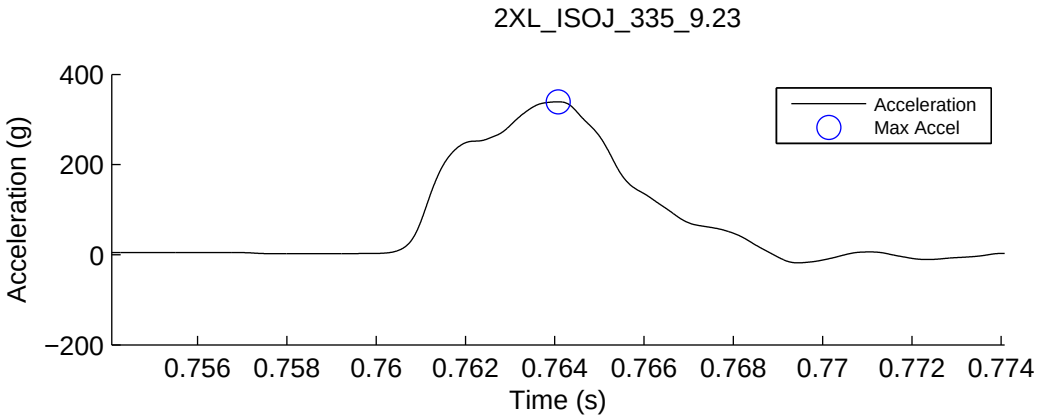

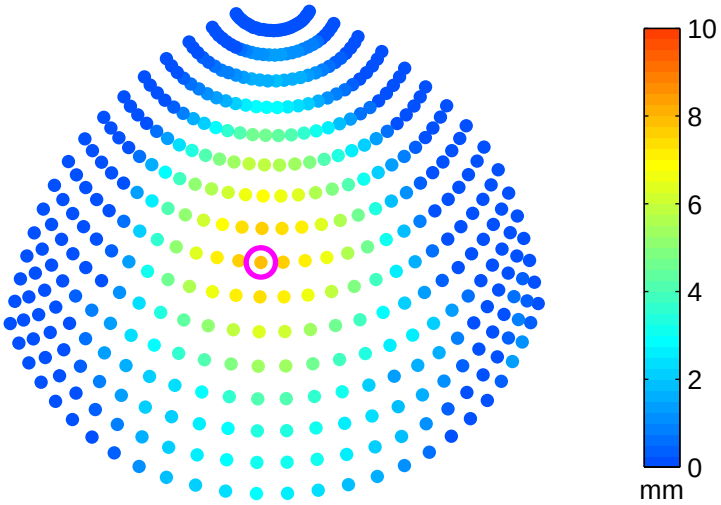

Max Resultant Accel (g)	339.29
HIC	5276.88
Impact Speed (m/s)	9.23
Impact Energy (J)	212.85
Maximum Crush (mm)	7.94
Crush Volume (cm³)	42.64
Mismatch (cm)	5.25

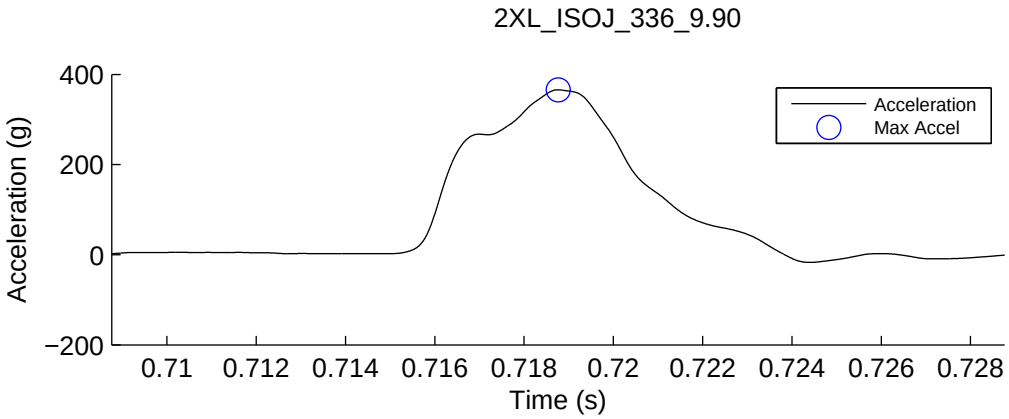

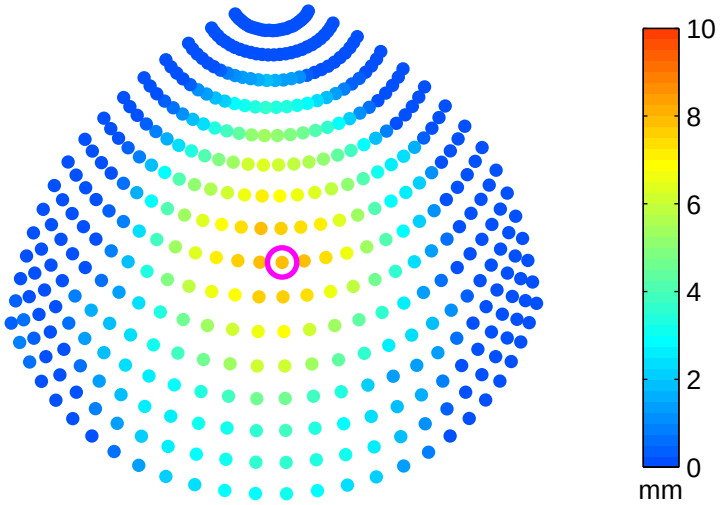

Max Resultant Accel (g)	365.93
HIC	6231.51
Impact Speed (m/s)	9.90
Impact Energy (J)	244.81
Maximum Crush (mm)	8.00
Crush Volume (cm³)	47.47
Mismatch (cm)	5.25

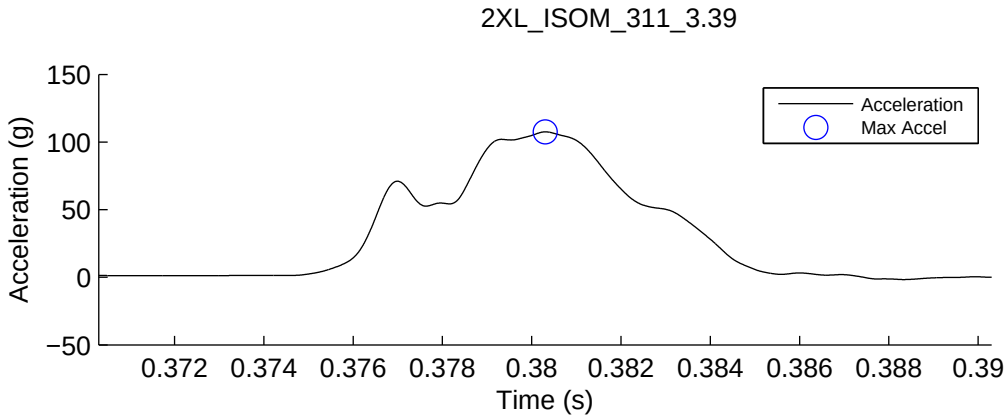

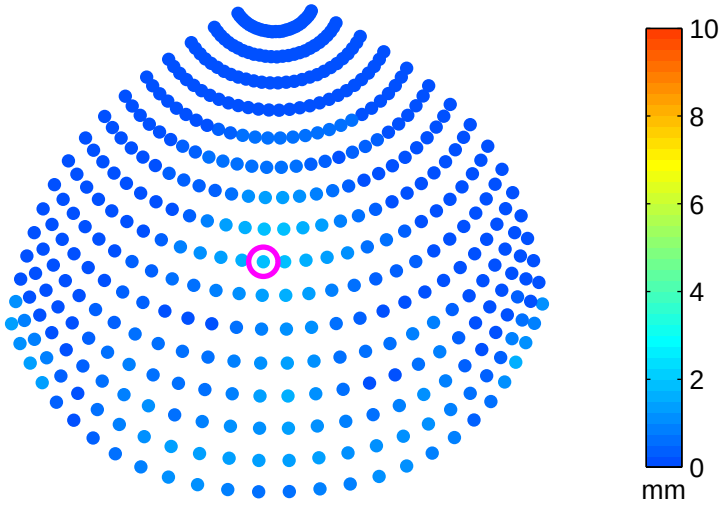

Max Resultant Accel (g)	107.54
HIC	345.91
Impact Speed (m/s)	3.39
Impact Energy (J)	28.73
Maximum Crush (mm)	1.93
Crush Volume (cm³)	10.47
Mismatch (cm)	2.25

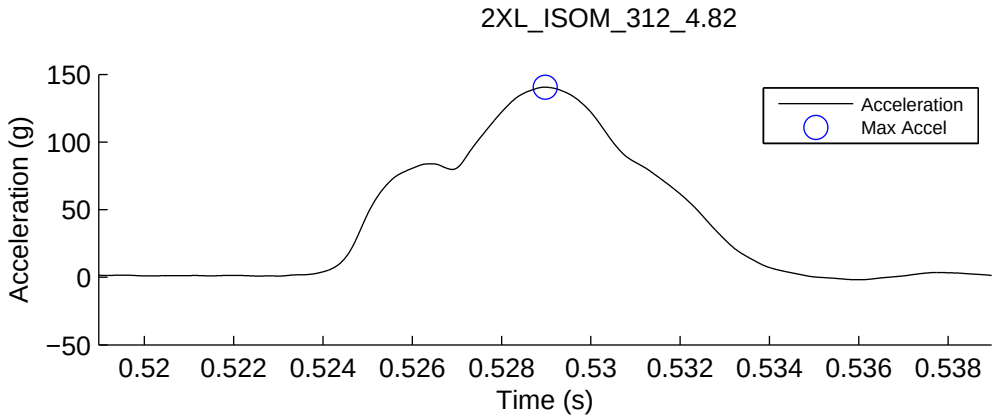

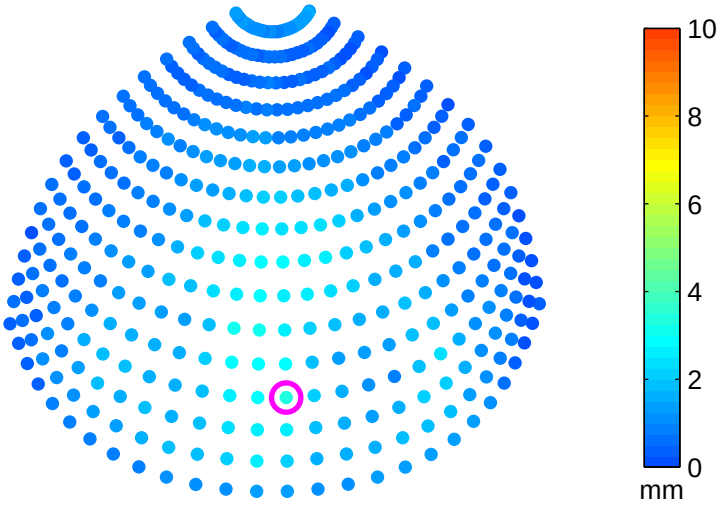

Max Resultant Accel (g)	140.61
HIC	694.79
Impact Speed (m/s)	4.82
Impact Energy (J)	58.07
Maximum Crush (mm)	3.28
Crush Volume (cm³)	26.42
Mismatch (cm)	2.25

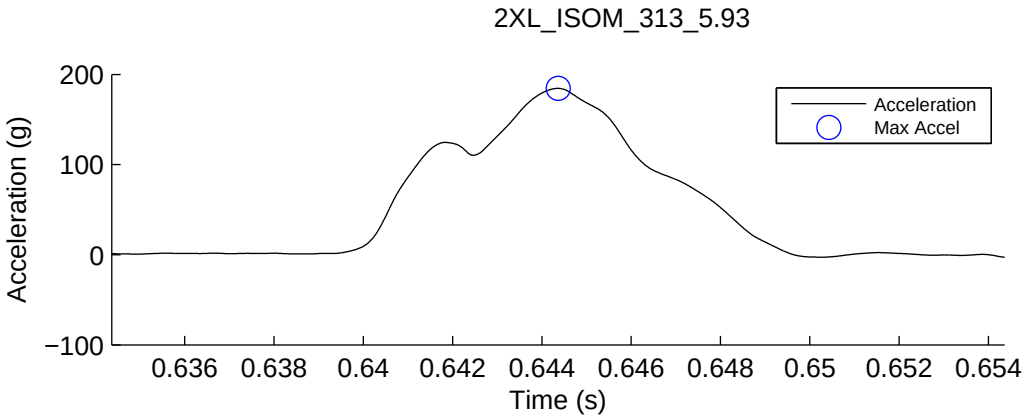

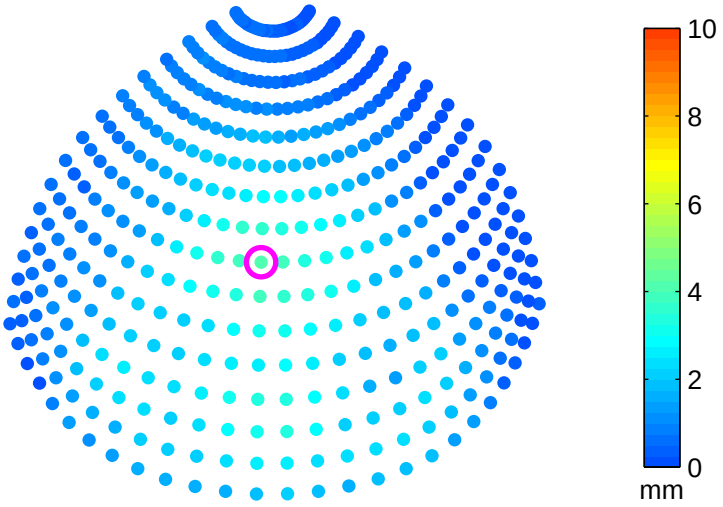

Max Resultant Accel (g)	184.54
HIC	1277.73
Impact Speed (m/s)	5.93
Impact Energy (J)	88.00
Maximum Crush (mm)	4.03
Crush Volume (cm³)	32.02
Mismatch (cm)	2.25

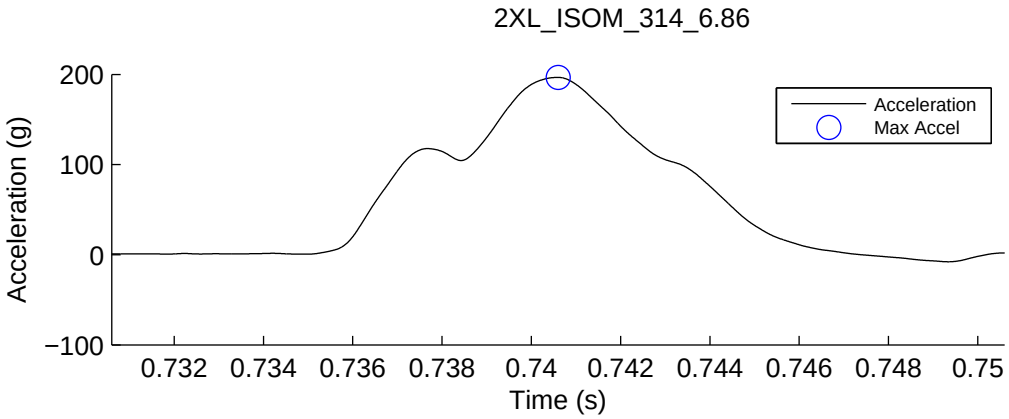

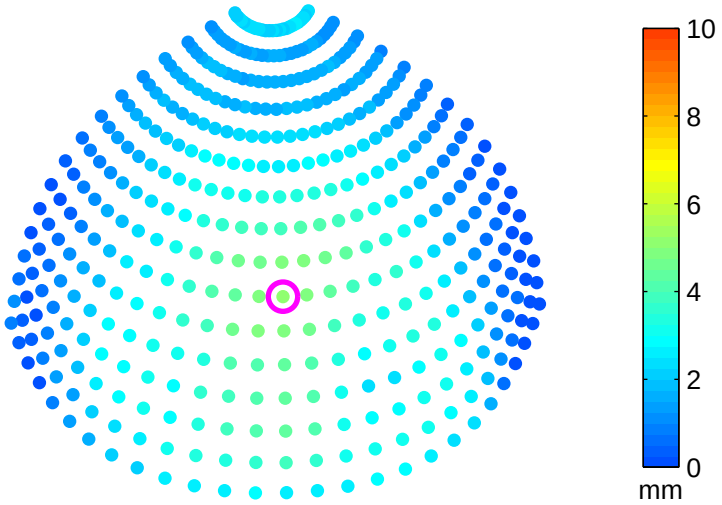

Max Resultant Accel (g)	196.74
HIC	1560.70
Impact Speed (m/s)	6.86
Impact Energy (J)	117.77
Maximum Crush (mm)	5.07
Crush Volume (cm³)	48.84
Mismatch (cm)	2.25

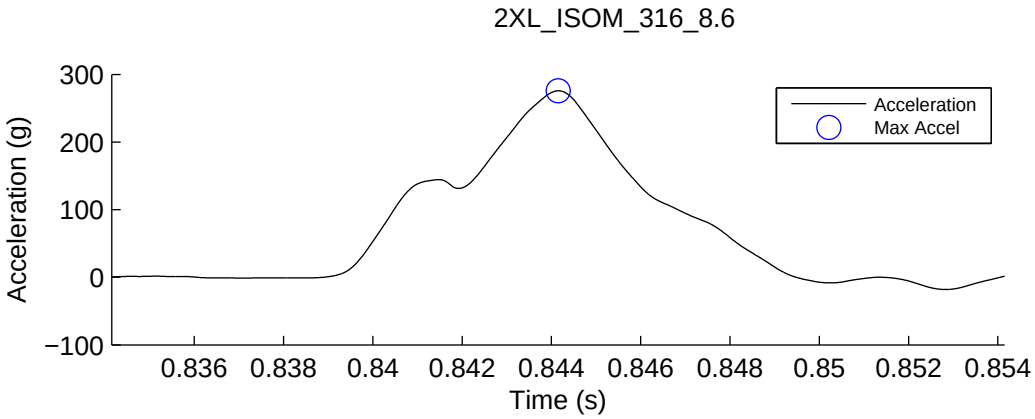

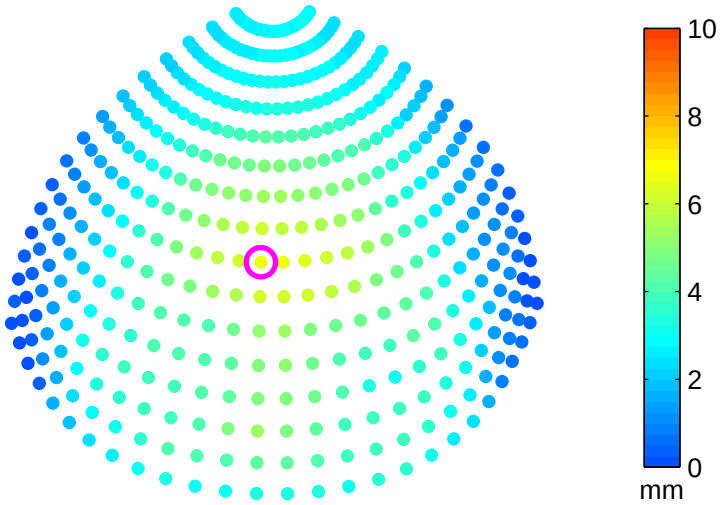

Max Resultant Accel (g)	275.83
HIC	2738.12
Impact Speed (m/s)	8.51
Impact Energy (J)	181.05
Maximum Crush (mm)	6.57
Crush Volume (cm³)	67.46
Mismatch (cm)	2.25

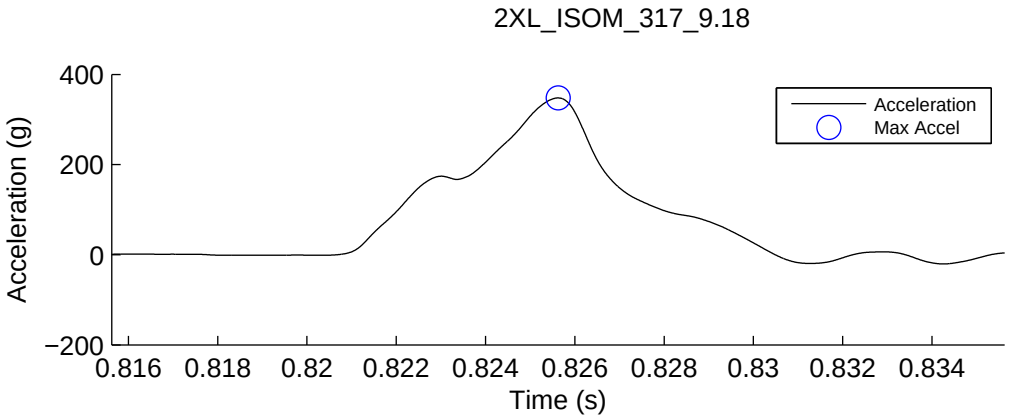

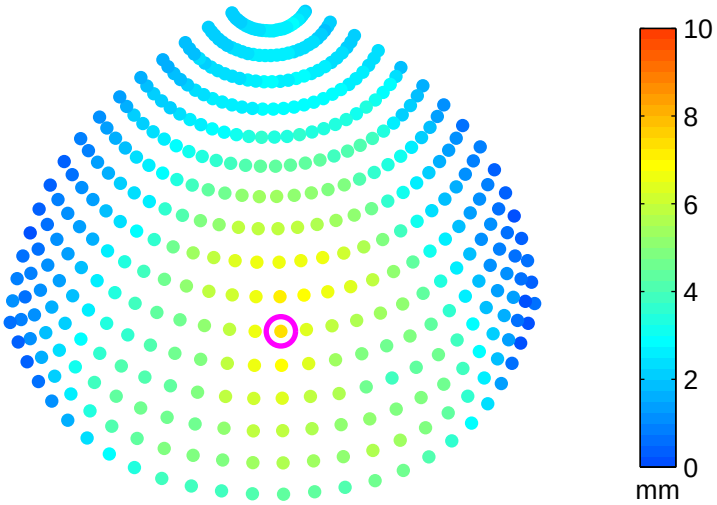

Max Resultant Accel (g)	347.83
HIC	3911.24
Impact Speed (m/s)	9.18
Impact Energy (J)	210.84
Maximum Crush (mm)	7.32
Crush Volume (cm³)	72.91
Mismatch (cm)	2.25

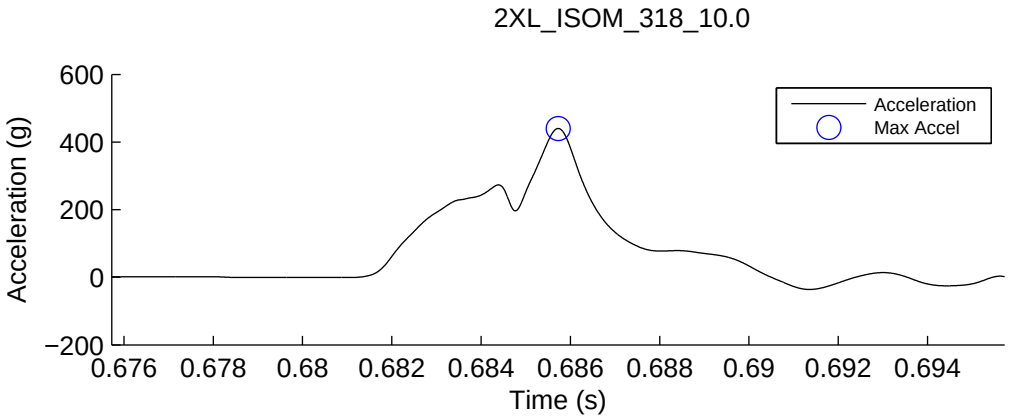

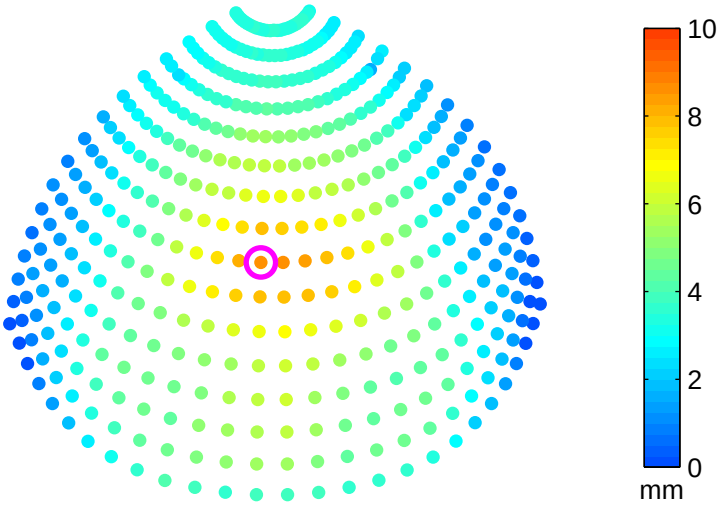

Max Resultant Accel (g)	440.21
HIC	4799.37
Impact Speed (m/s)	10.00
Impact Energy (J)	250.11
Maximum Crush (mm)	8.63
Crush Volume (cm³)	82.27
Mismatch (cm)	2.25

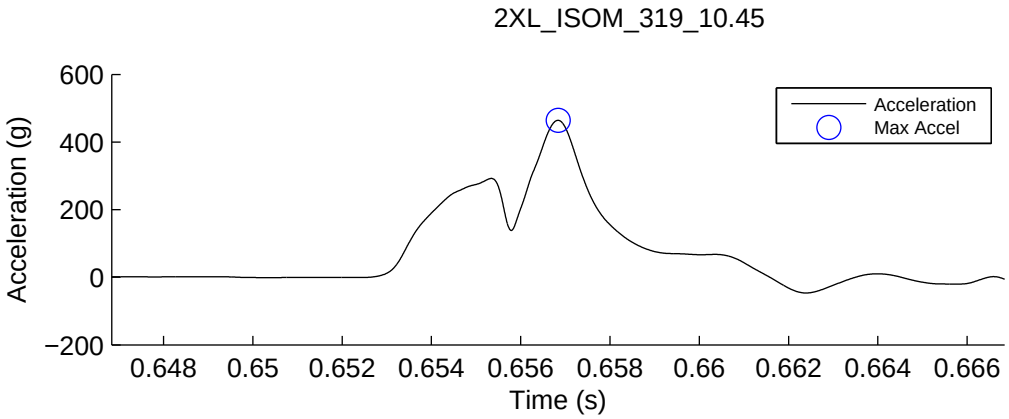

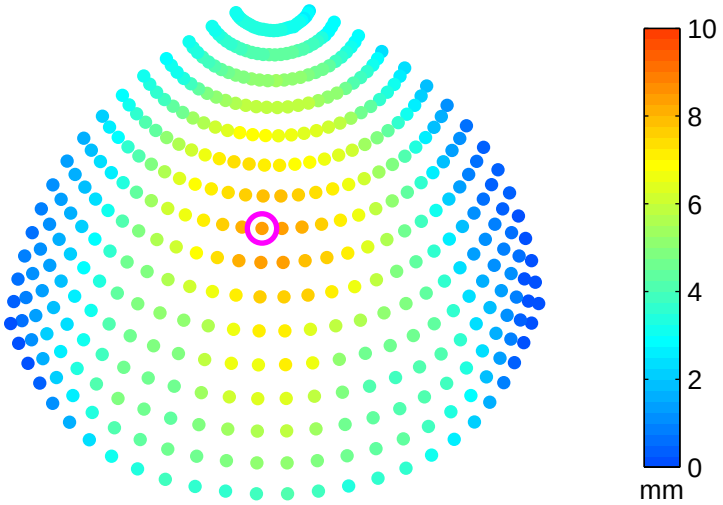

Max Resultant Accel (g)	464.31
HIC	5303.17
Impact Speed (m/s)	10.45
Impact Energy (J)	273.23
Maximum Crush (mm)	8.40
Crush Volume (cm³)	87.11
Mismatch (cm)	2.25

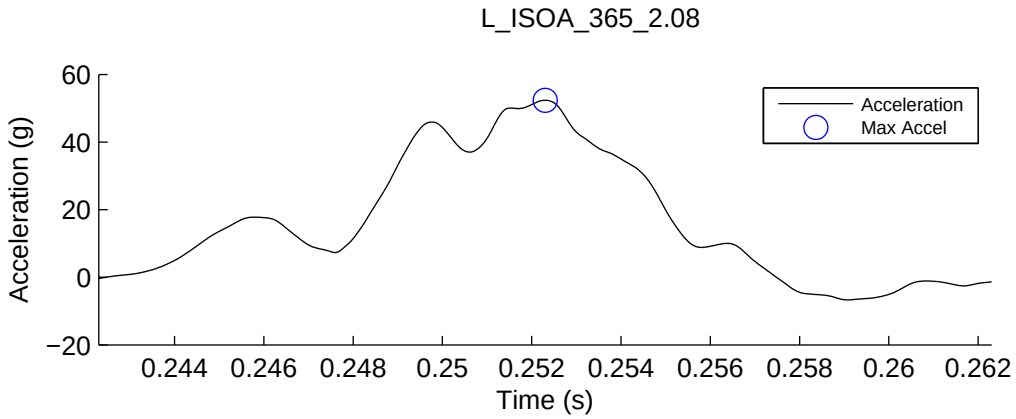

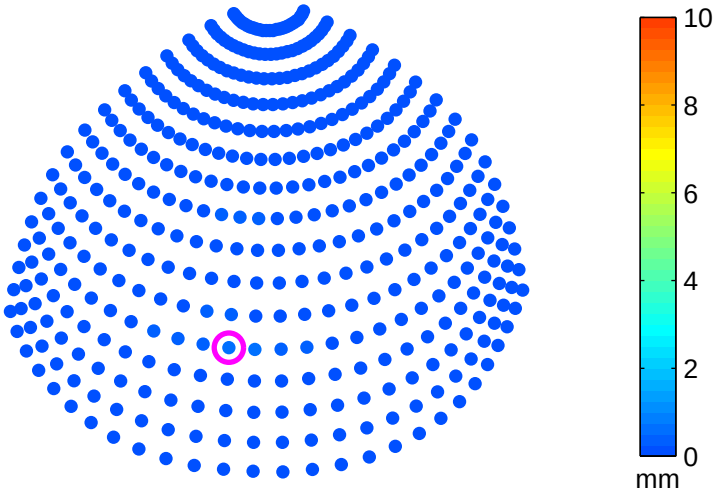

Max Resultant Accel (g)	52.37
HIC	66.77
Impact Speed (m/s)	2.08
Impact Energy (J)	10.70
Maximum Crush (mm)	0.74
Crush Volume (cm³)	0.63
Mismatch (cm)	10.25

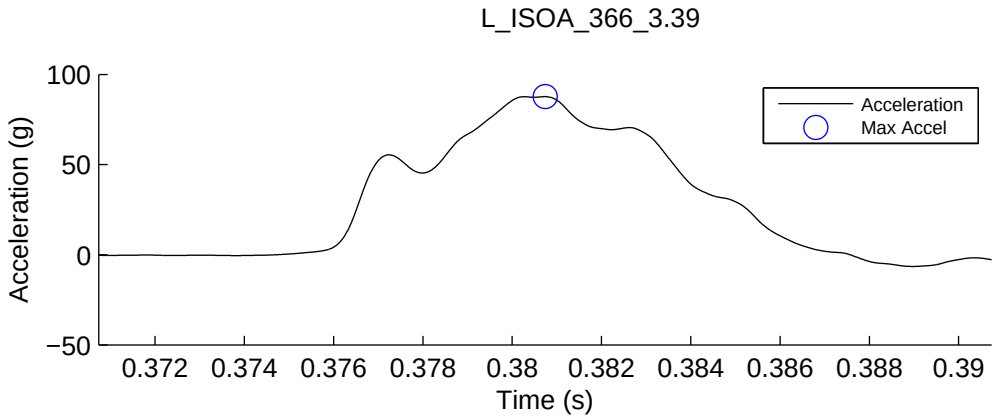

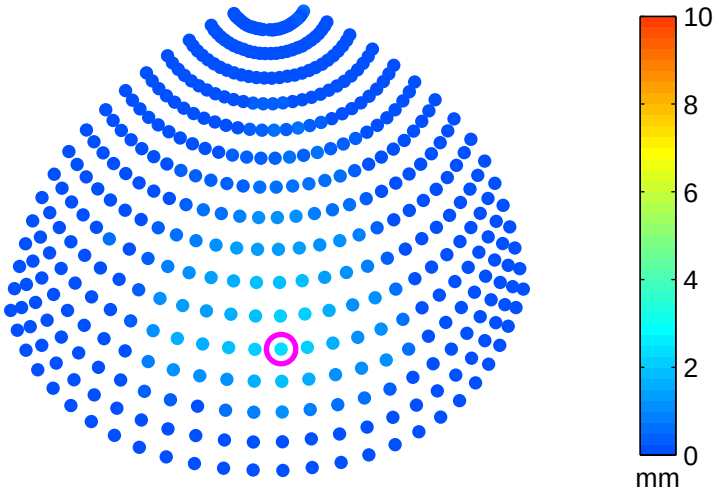

Max Resultant Accel (g)	87.69
HIC	259.03
Impact Speed (m/s)	3.39
Impact Energy (J)	28.61
Maximum Crush (mm)	2.29
Crush Volume (cm³)	6.83
Mismatch (cm)	10.25

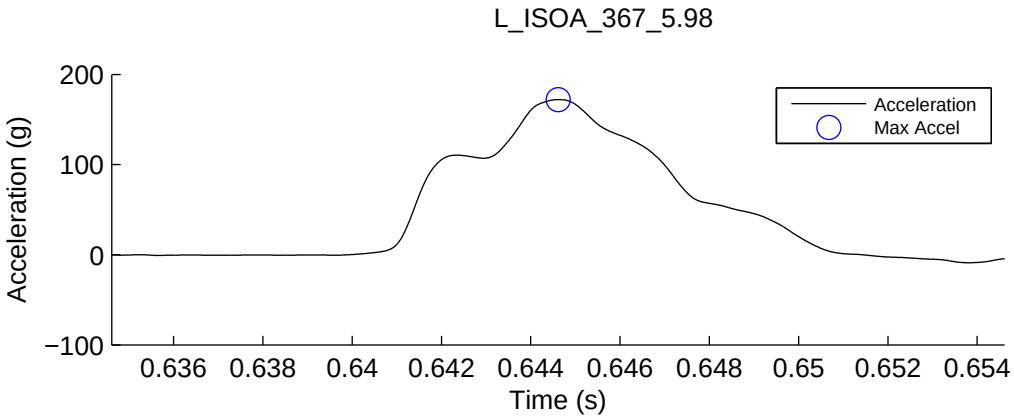

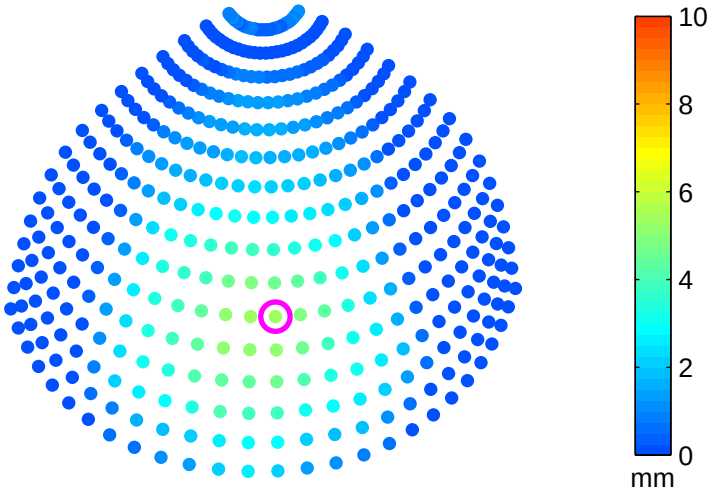

Max Resultant Accel (g)	172.14
HIC	1085.55
Impact Speed (m/s)	5.98
Impact Energy (J)	88.91
Maximum Crush (mm)	5.38
Crush Volume (cm³)	26.41
Mismatch (cm)	10.25

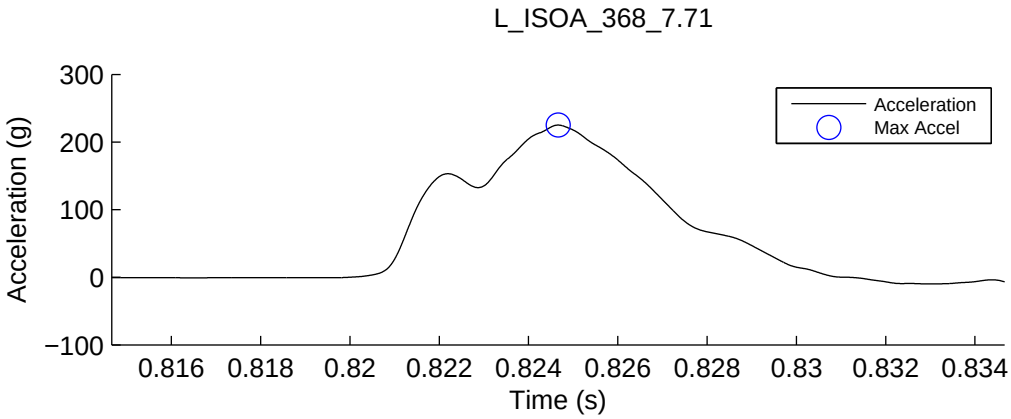

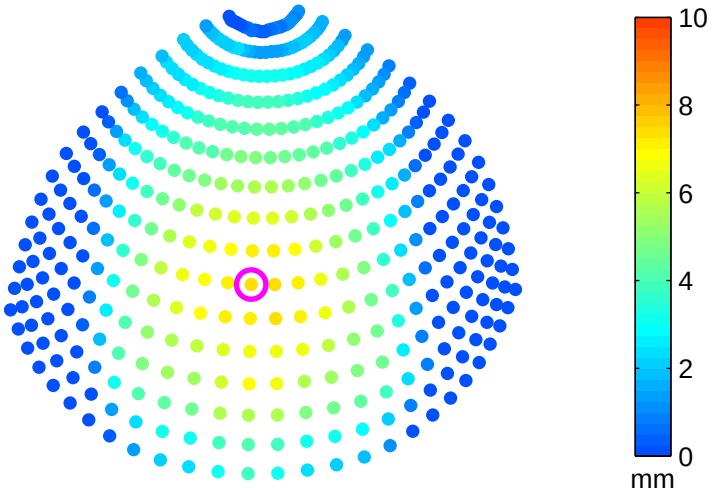

Max Resultant Accel (g)	225.09
HIC	2102.71
Impact Speed (m/s)	7.71
Impact Energy (J)	147.81
Maximum Crush (mm)	7.37
Crush Volume (cm³)	53.81
Mismatch (cm)	10.25

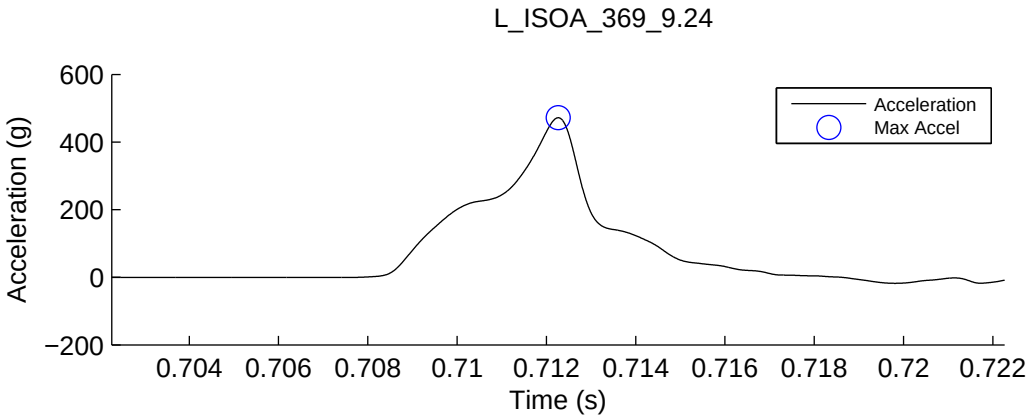

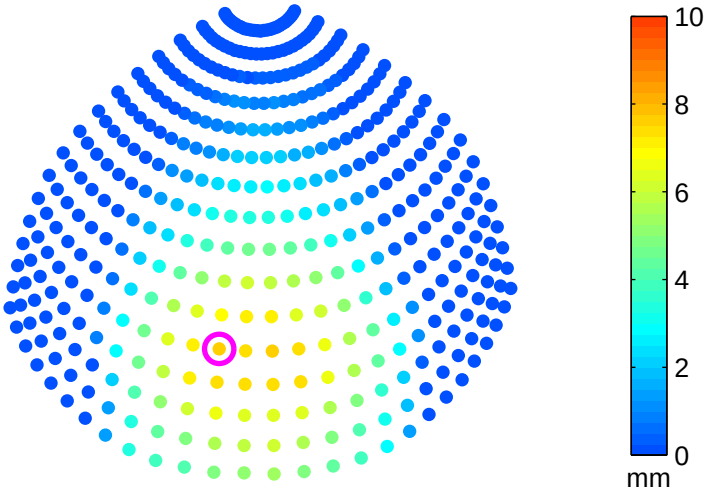

Max Resultant Accel (g)	472.00
HIC	5001.43
Impact Speed (m/s)	9.24
Impact Energy (J)	212.15
Maximum Crush (mm)	7.67
Crush Volume (cm³)	38.38
Mismatch (cm)	10.25

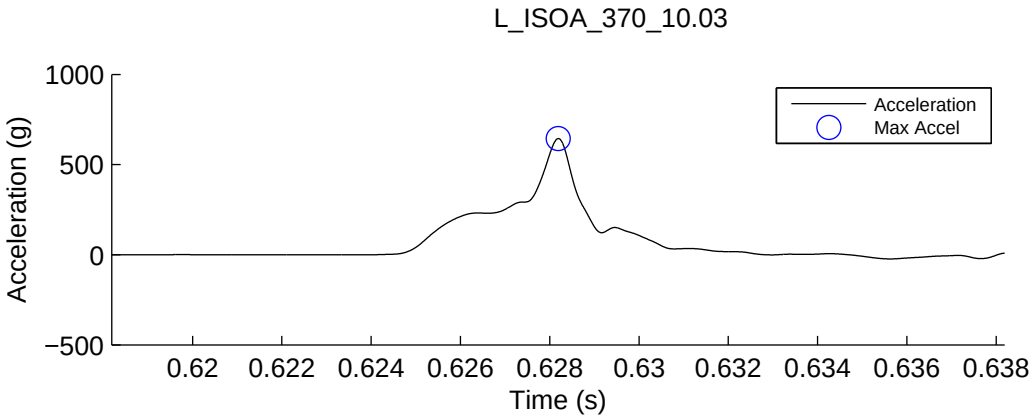

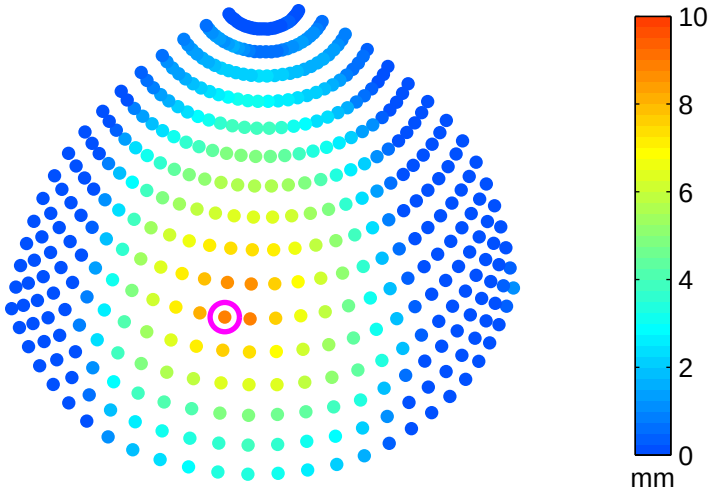

Max Resultant Accel (g)	644.26
HIC	6091.16
Impact Speed (m/s)	10.04
Impact Energy (J)	250.22
Maximum Crush (mm)	8.96
Crush Volume (cm³)	48.53
Mismatch (cm)	10.25

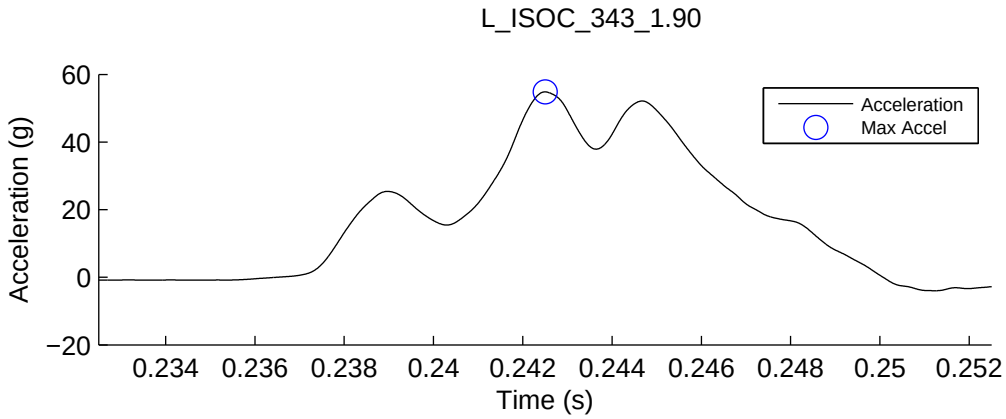

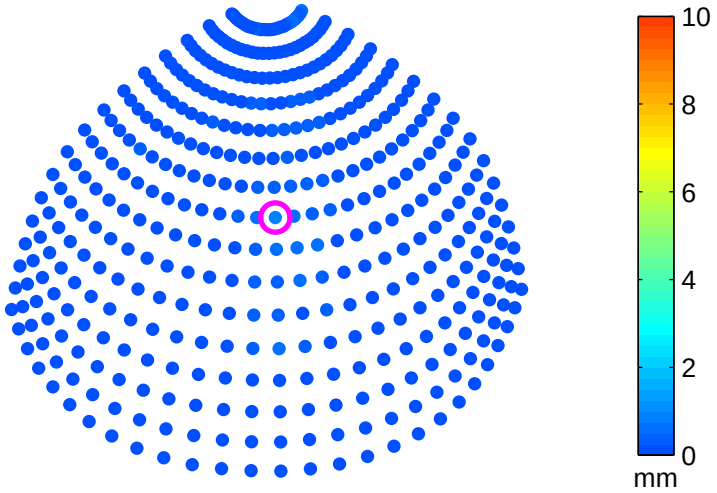

Max Resultant Accel (g)	54.83
HIC	64.02
Impact Speed (m/s)	1.90
Impact Energy (J)	9.02
Maximum Crush (mm)	0.75
Crush Volume (cm³)	1.22
Mismatch (cm)	8.25

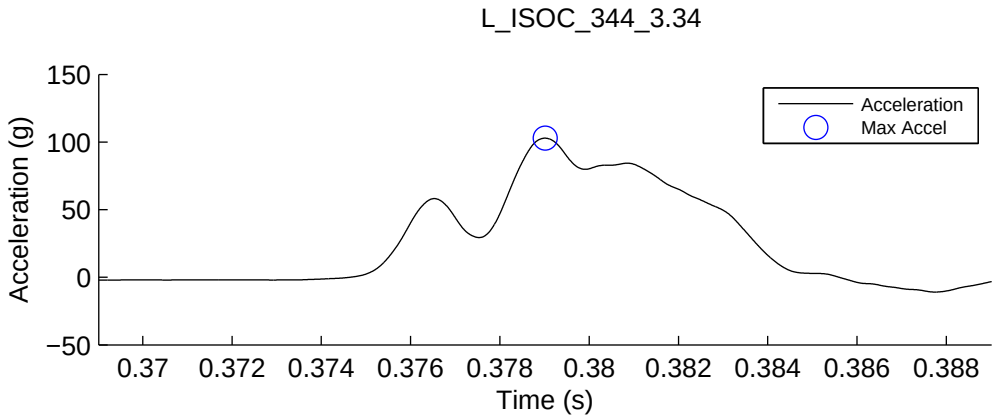

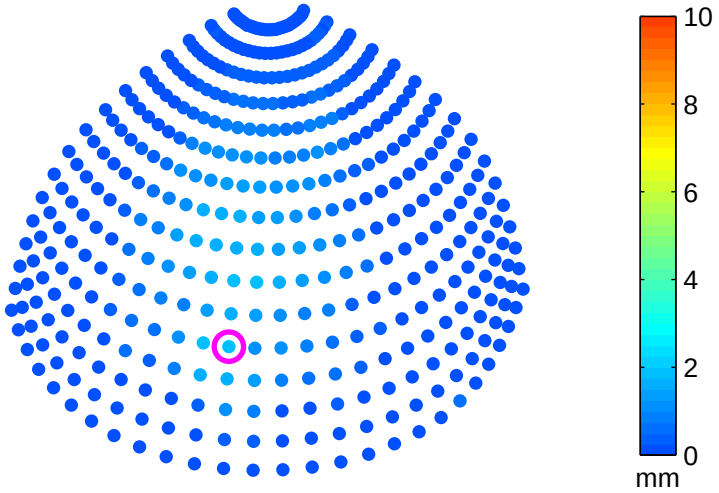

Max Resultant Accel (g)	102.87
HIC	266.11
Impact Speed (m/s)	3.34
Impact Energy (J)	27.74
Maximum Crush (mm)	1.94
Crush Volume (cm³)	7.16
Mismatch (cm)	8.25

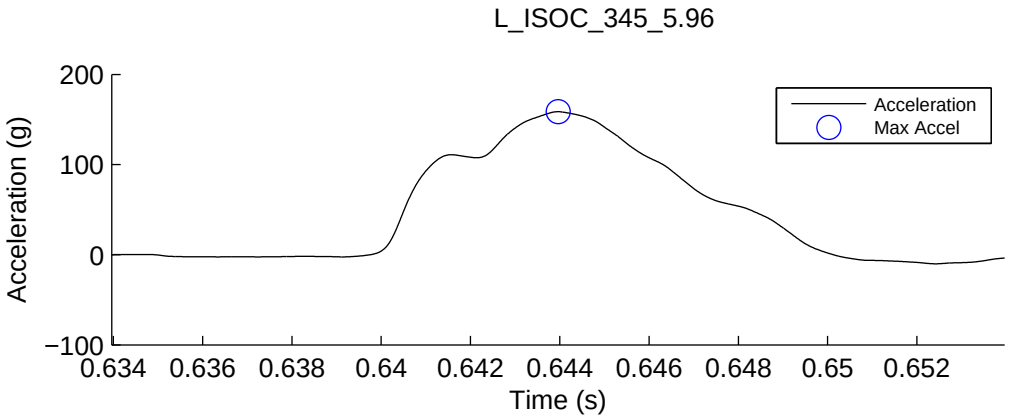

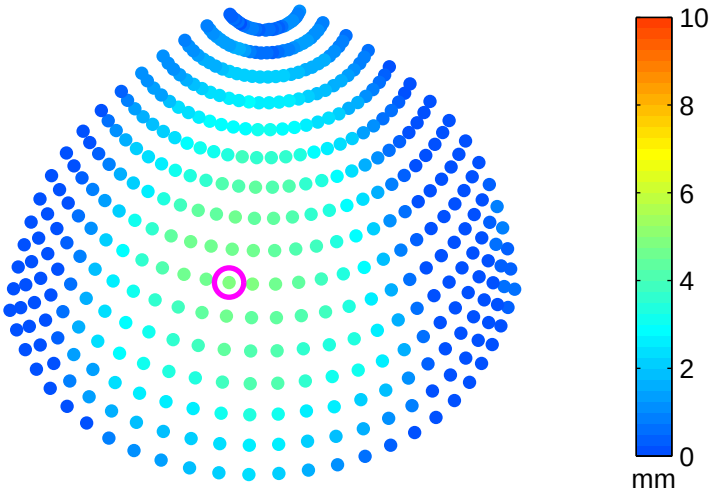

Max Resultant Accel (g)	158.66
HIC	1047.48
Impact Speed (m/s)	5.96
Impact Energy (J)	88.42
Maximum Crush (mm)	4.92
Crush Volume (cm³)	35.50
Mismatch (cm)	8.25

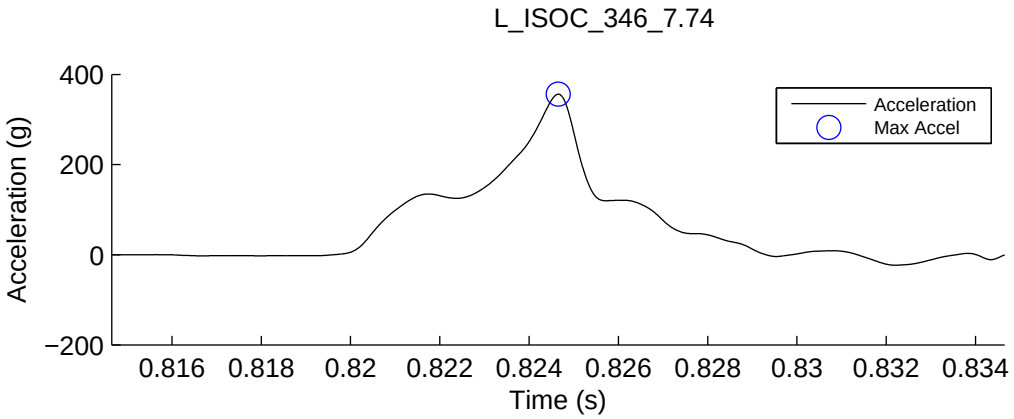

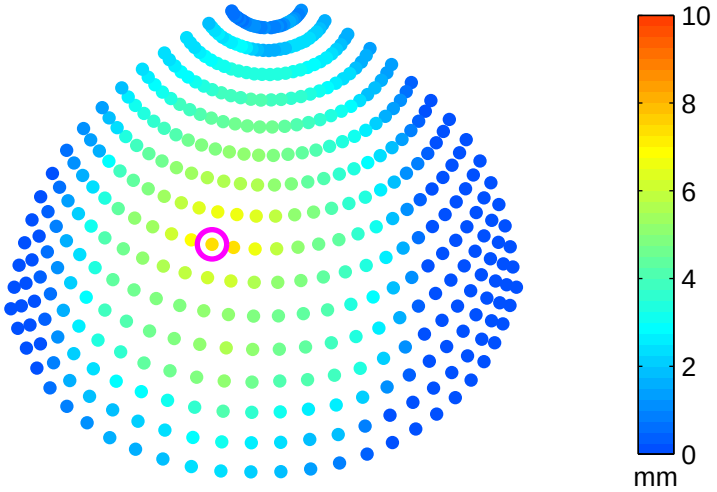

Max Resultant Accel (g)	356.19
HIC	2327.25
Impact Speed (m/s)	7.74
Impact Energy (J)	149.05
Maximum Crush (mm)	7.39
Crush Volume (cm³)	50.47
Mismatch (cm)	8.25

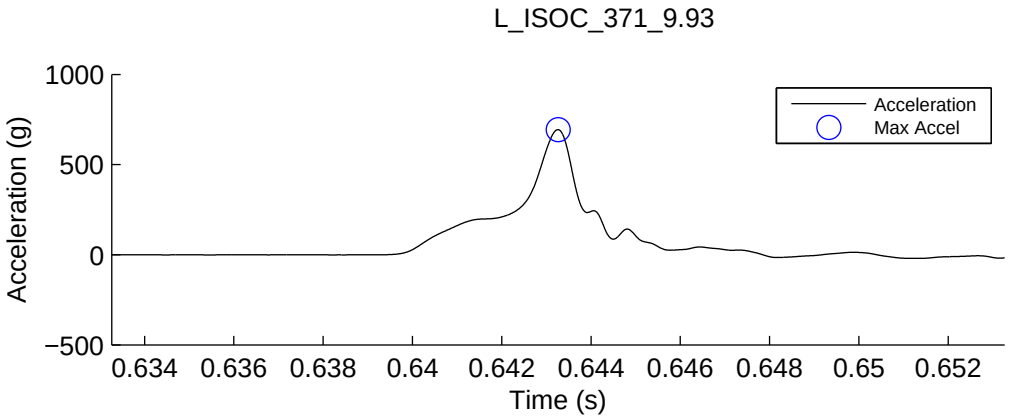

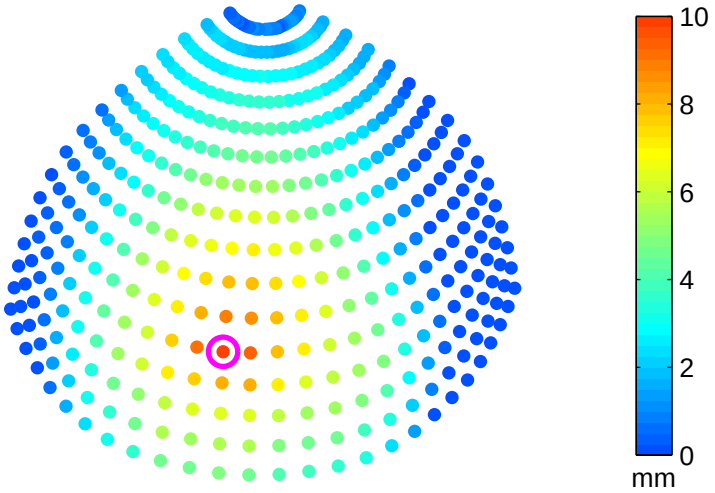

Max Resultant Accel (g)	693.74
HIC	7231.17
Impact Speed (m/s)	9.93
Impact Energy (J)	245.62
Maximum Crush (mm)	10.23
Crush Volume (cm³)	63.60
Mismatch (cm)	8.25

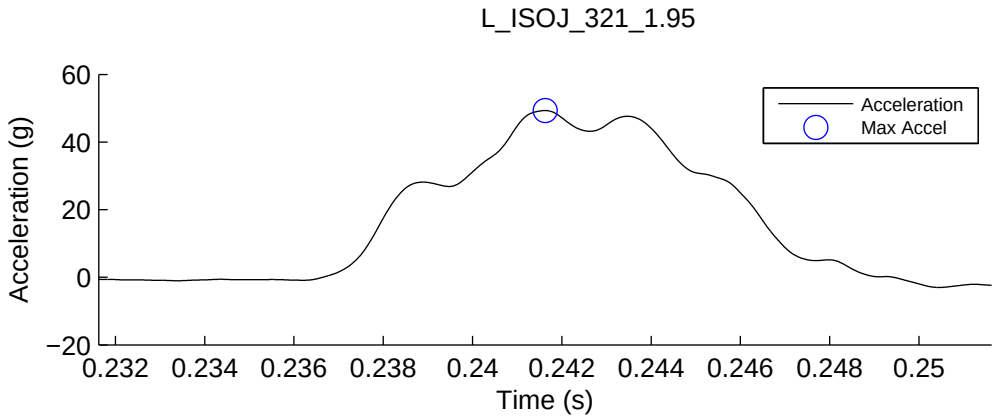

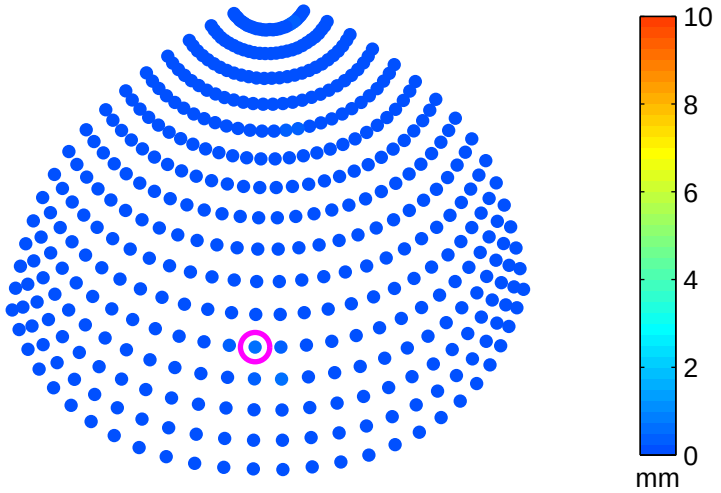

Max Resultant Accel (g)	49.32
HIC	66.38
Impact Speed (m/s)	1.95
Impact Energy (J)	9.54
Maximum Crush (mm)	0.62
Crush Volume (cm³)	0.41
Mismatch (cm)	3.25

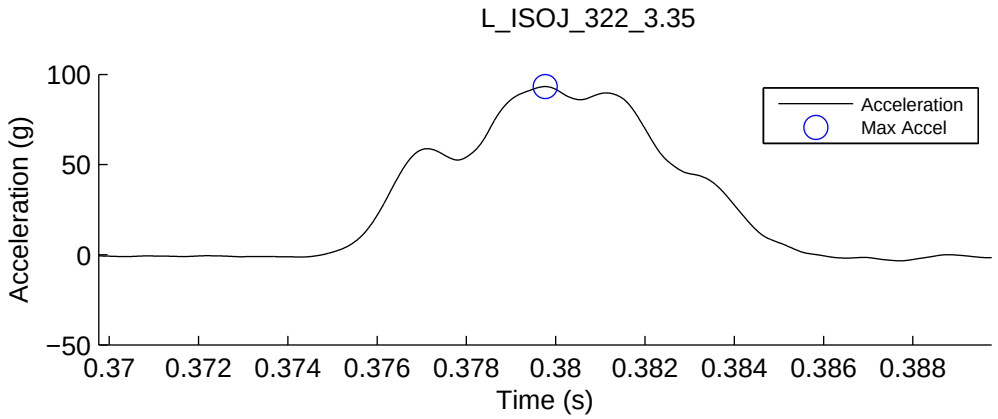

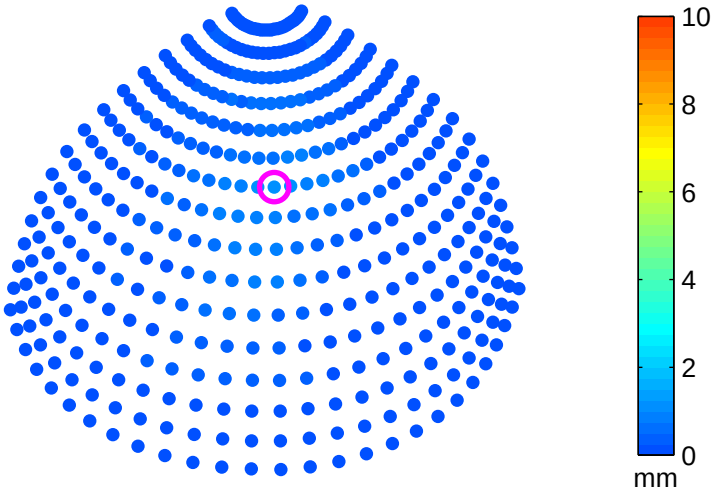

Max Resultant Accel (g)	93.28
HIC	287.28
Impact Speed (m/s)	3.35
Impact Energy (J)	28.05
Maximum Crush (mm)	1.05
Crush Volume (cm³)	3.24
Mismatch (cm)	3.25

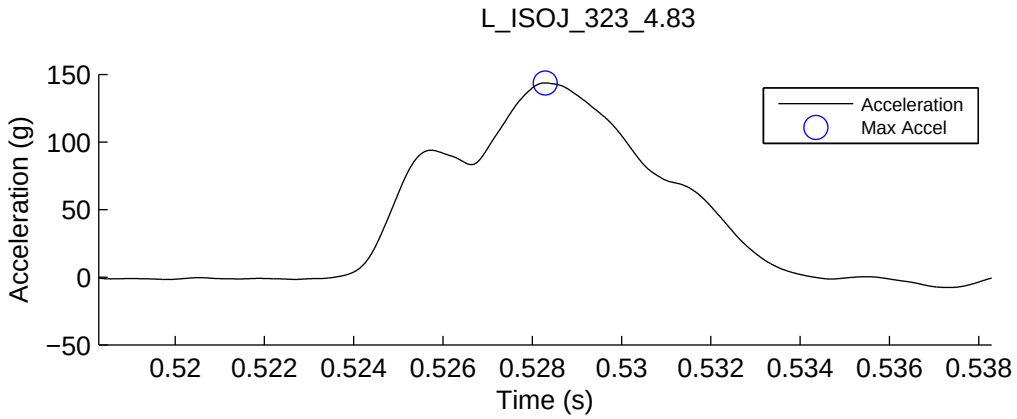

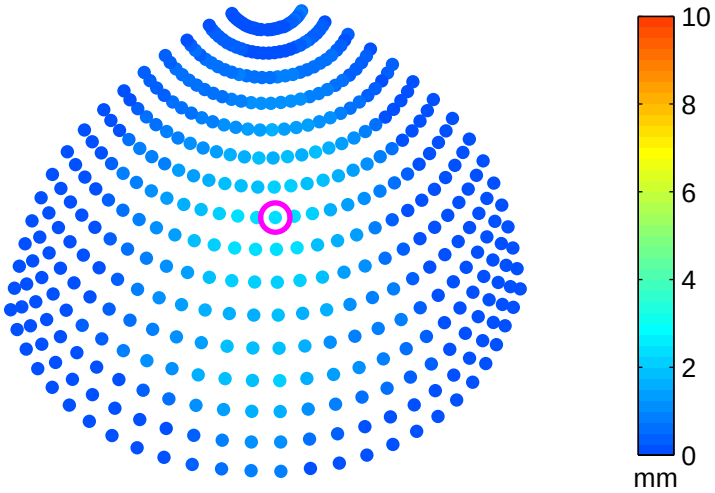

Max Resultant Accel (g)	143.75
HIC	717.33
Impact Speed (m/s)	4.83
Impact Energy (J)	58.34
Maximum Crush (mm)	2.46
Crush Volume (cm³)	12.89
Mismatch (cm)	3.25

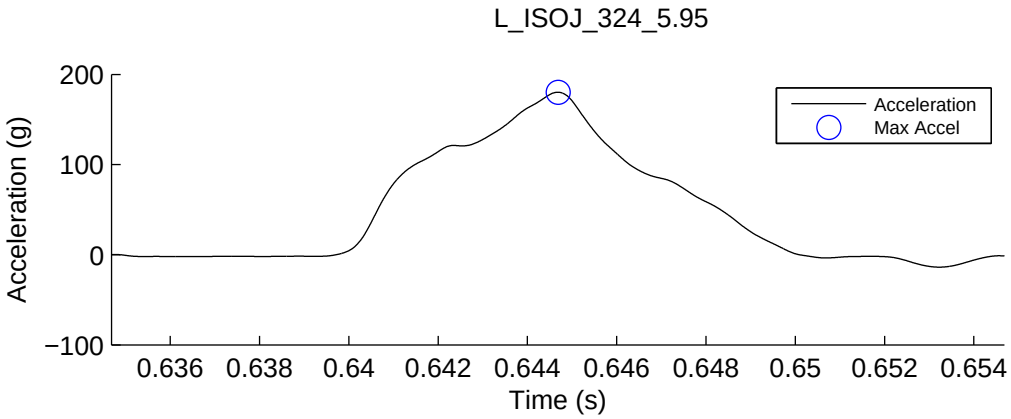

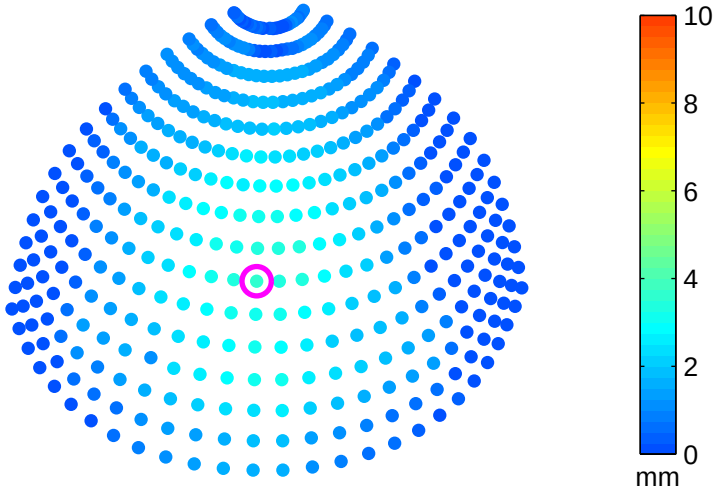

Max Resultant Accel (g)	180.27
HIC	1136.51
Impact Speed (m/s)	5.95
Impact Energy (J)	88.35
Maximum Crush (mm)	3.55
Crush Volume (cm³)	24.82
Mismatch (cm)	3.25

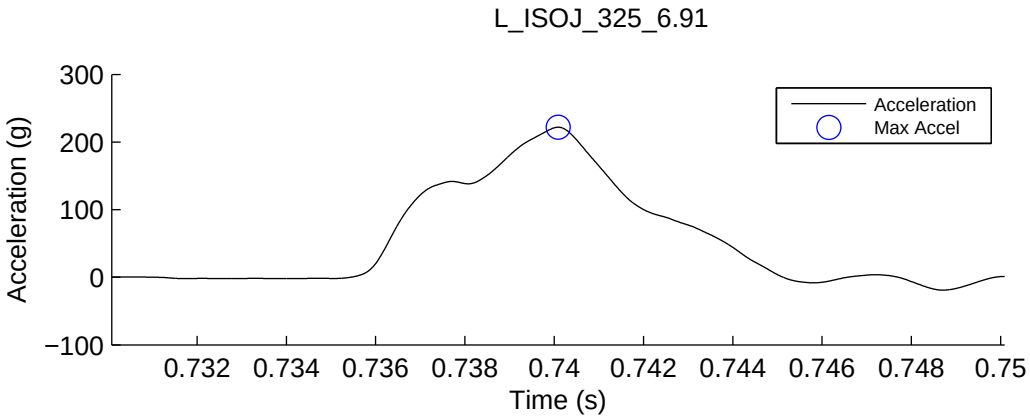

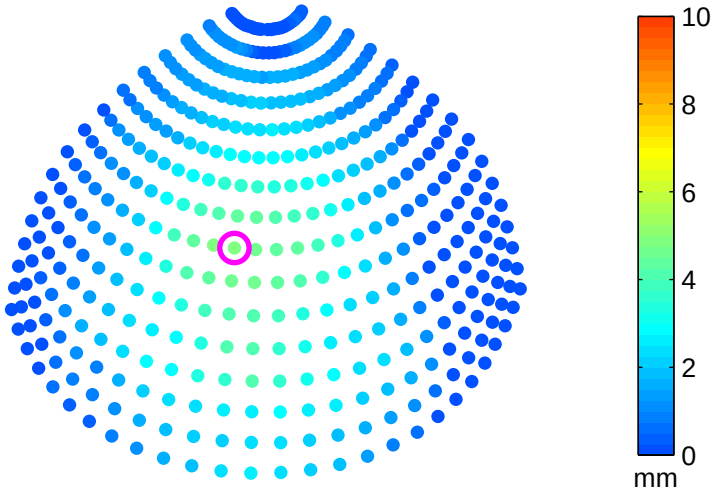

Max Resultant Accel (g)	221.96
HIC	1754.96
Impact Speed (m/s)	6.91
Impact Energy (J)	119.51
Maximum Crush (mm)	4.82
Crush Volume (cm³)	31.54
Mismatch (cm)	3.25

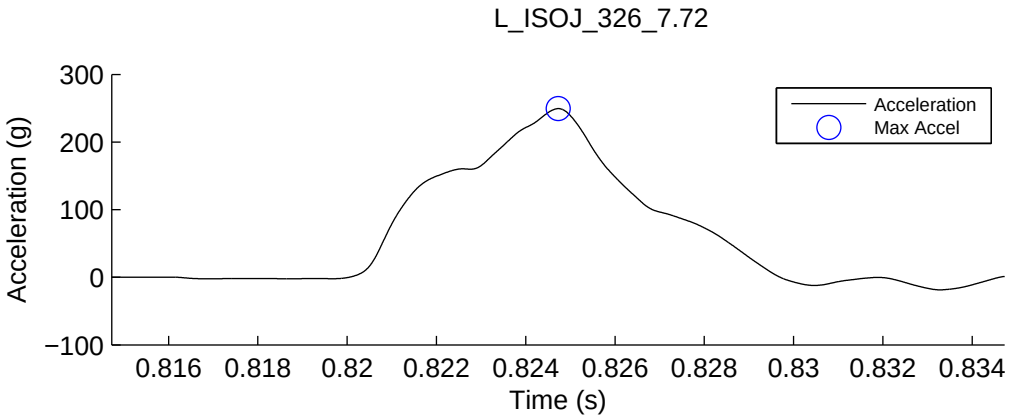

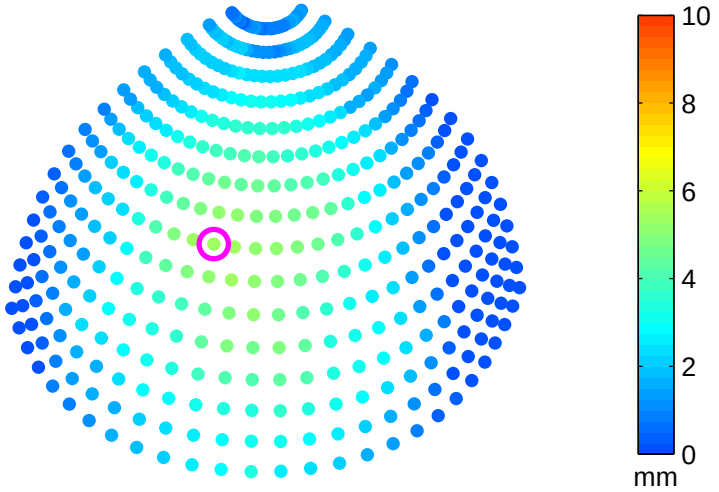

Max Resultant Accel (g)	249.46
HIC	2312.83
Impact Speed (m/s)	7.71
Impact Energy (J)	148.77
Maximum Crush (mm)	5.42
Crush Volume (cm³)	43.32
Mismatch (cm)	3.25

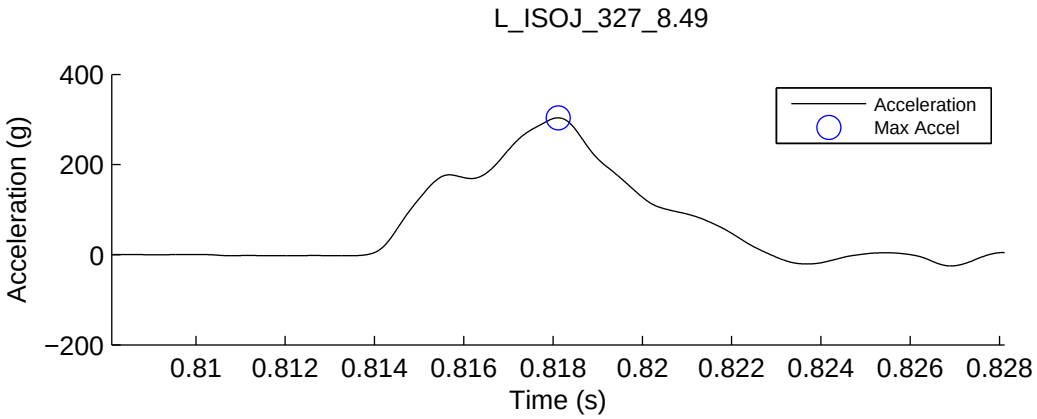

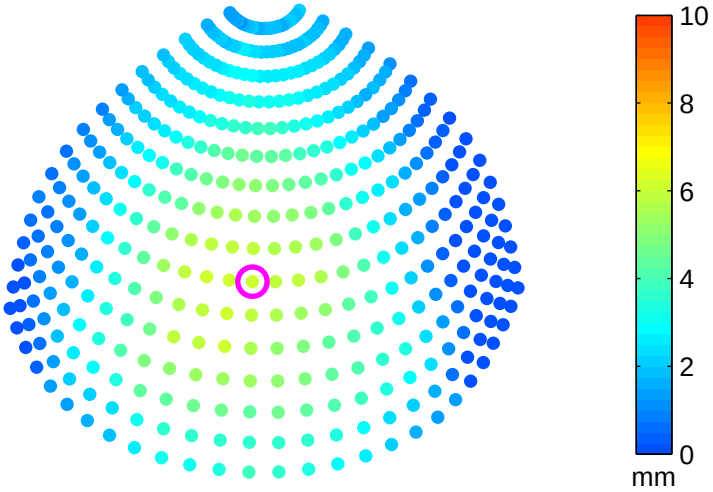

Max Resultant Accel (g)	303.70
HIC	3319.53
Impact Speed (m/s)	8.49
Impact Energy (J)	180.10
Maximum Crush (mm)	6.17
Crush Volume (cm³)	53.55
Mismatch (cm)	3.25

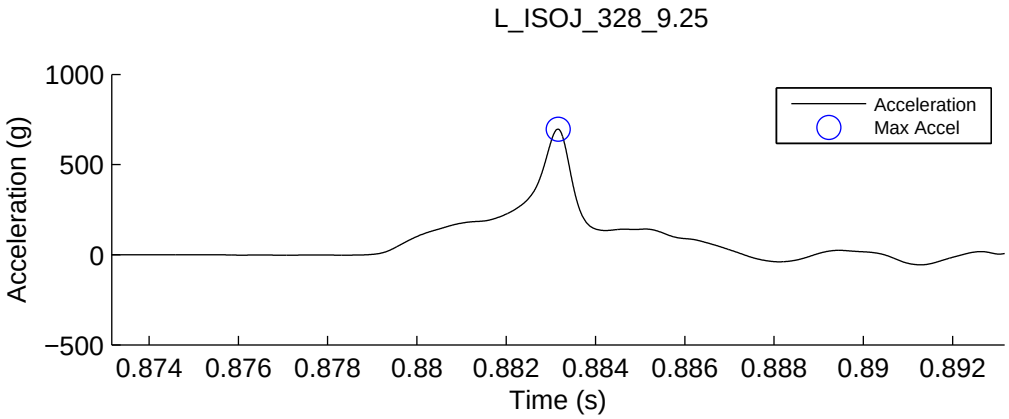

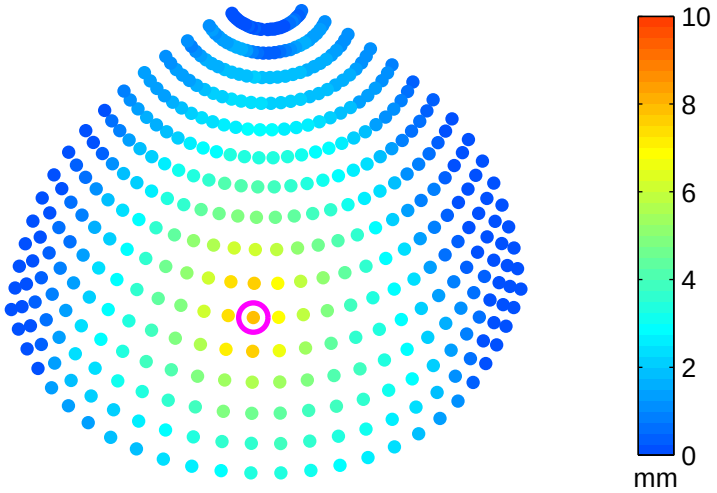

Max Resultant Accel (g)	696.69
HIC	6283.75
Impact Speed (m/s)	9.25
Impact Energy (J)	213.96
Maximum Crush (mm)	7.99
Crush Volume (cm³)	47.95
Mismatch (cm)	3.25

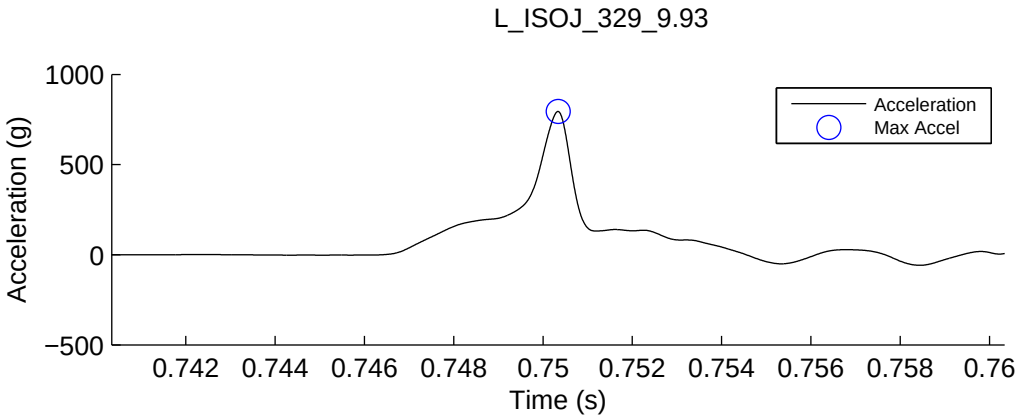

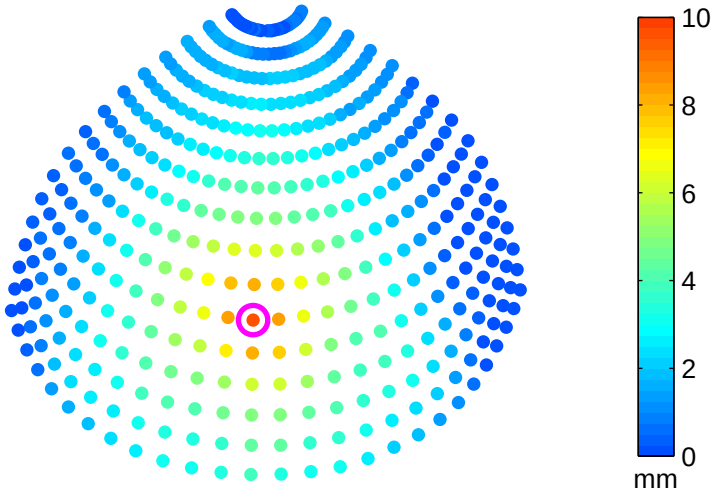

Max Resultant Accel (g)	794.50
HIC	8514.21
Impact Speed (m/s)	9.93
Impact Energy (J)	246.59
Maximum Crush (mm)	9.67
Crush Volume (cm³)	51.89
Mismatch (cm)	3.25

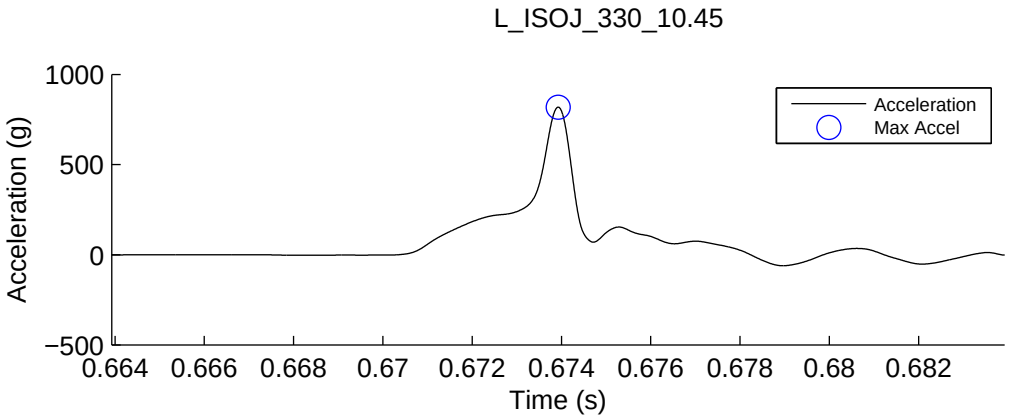

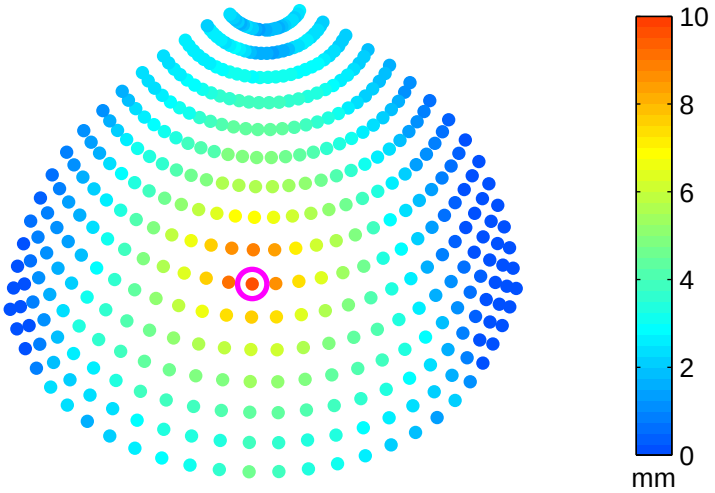

Max Resultant Accel (g)	818.55
HIC	8271.17
Impact Speed (m/s)	10.45
Impact Energy (J)	272.95
Maximum Crush (mm)	9.55
Crush Volume (cm³)	61.19
Mismatch (cm)	3.25

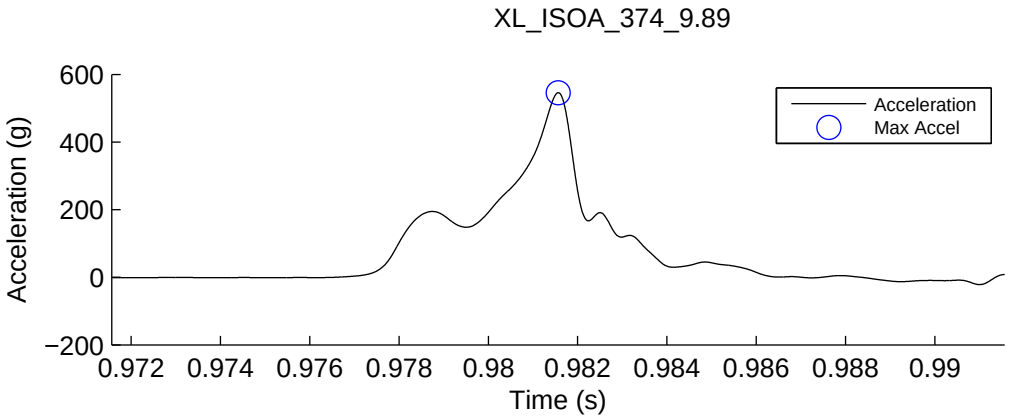

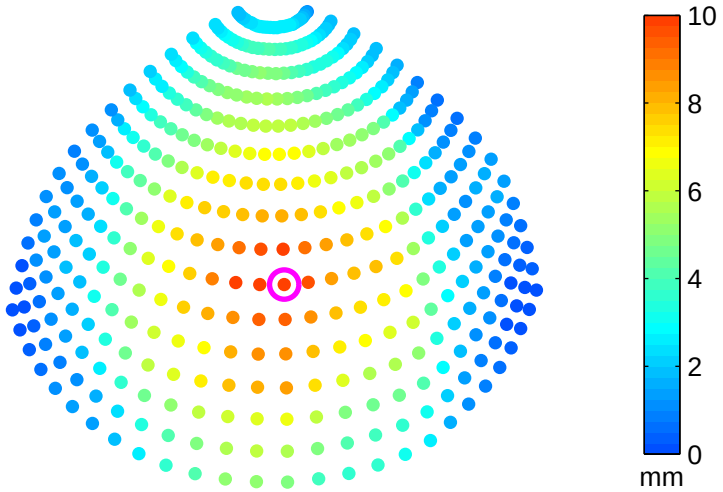

Max Resultant Accel (g)	546.05
HIC	4866.65
Impact Speed (m/s)	9.90
Impact Energy (J)	243.20
Maximum Crush (mm)	10.88
Crush Volume (cm³)	86.96
Mismatch (cm)	12.01

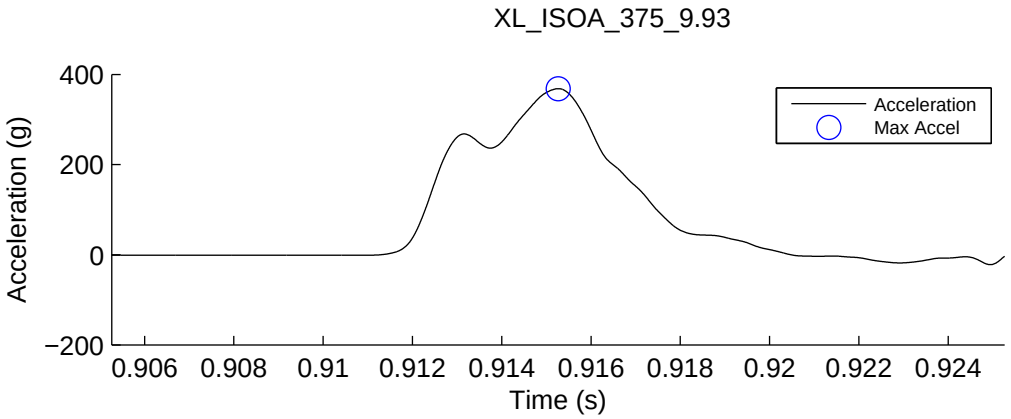

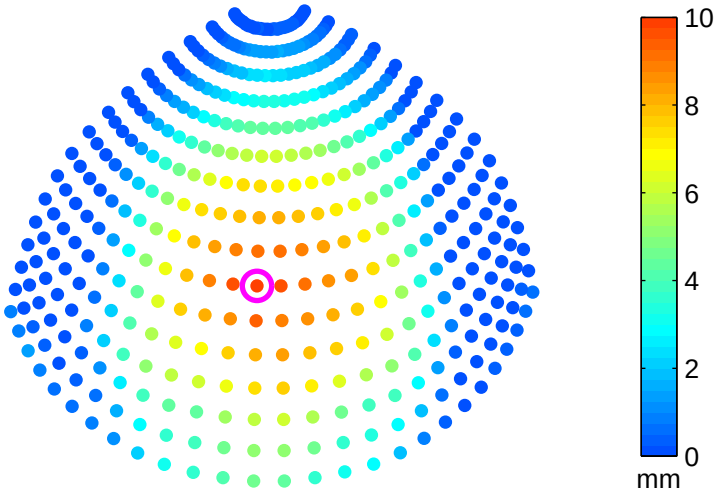

Max Resultant Accel (g)	368.45
HIC	5423.59
Impact Speed (m/s)	9.93
Impact Energy (J)	244.92
Maximum Crush (mm)	9.92
Crush Volume (cm³)	65.15
Mismatch (cm)	12.01

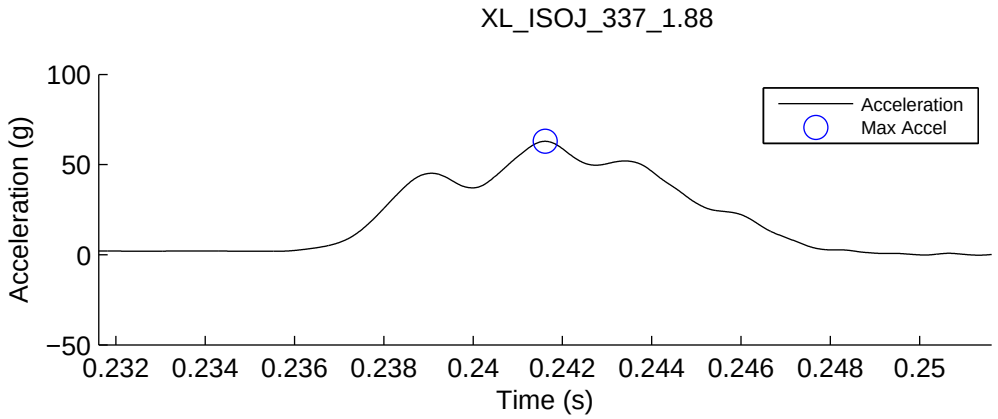

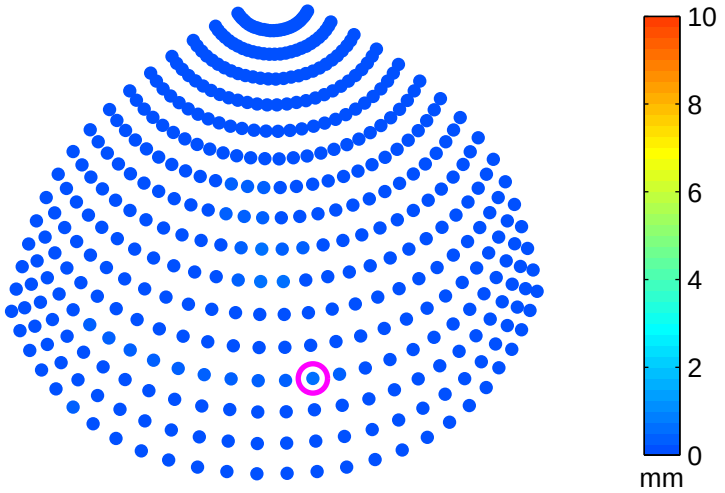

Max Resultant Accel (g)	62.91
HIC	101.76
Impact Speed (m/s)	1.88
Impact Energy (J)	8.87
Maximum Crush (mm)	0.58
Crush Volume (cm³)	0.88
Mismatch (cm)	5.01

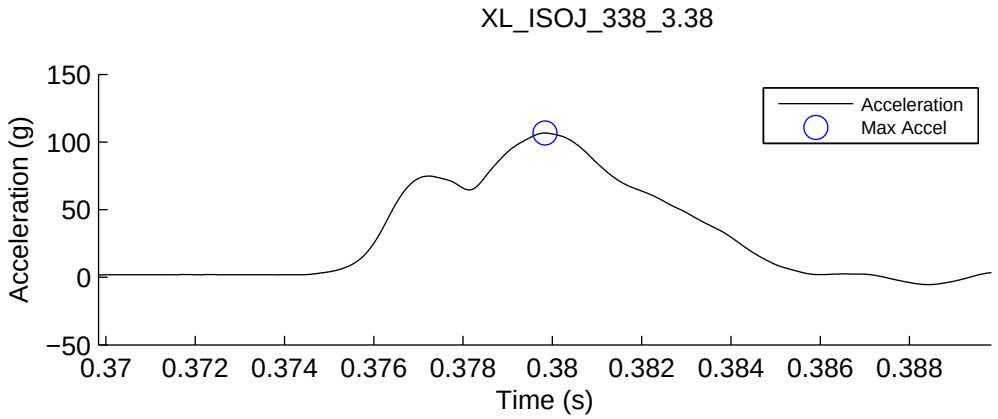

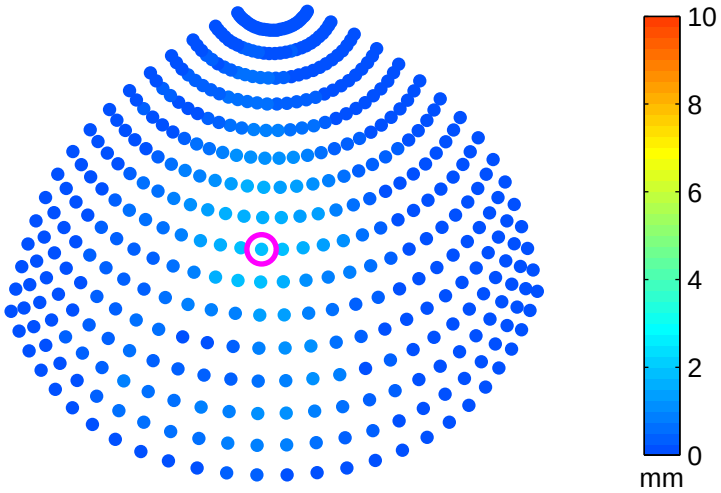

Max Resultant Accel (g)	106.65
HIC	353.90
Impact Speed (m/s)	3.38
Impact Energy (J)	28.52
Maximum Crush (mm)	1.99
Crush Volume (cm³)	7.80
Mismatch (cm)	5.01

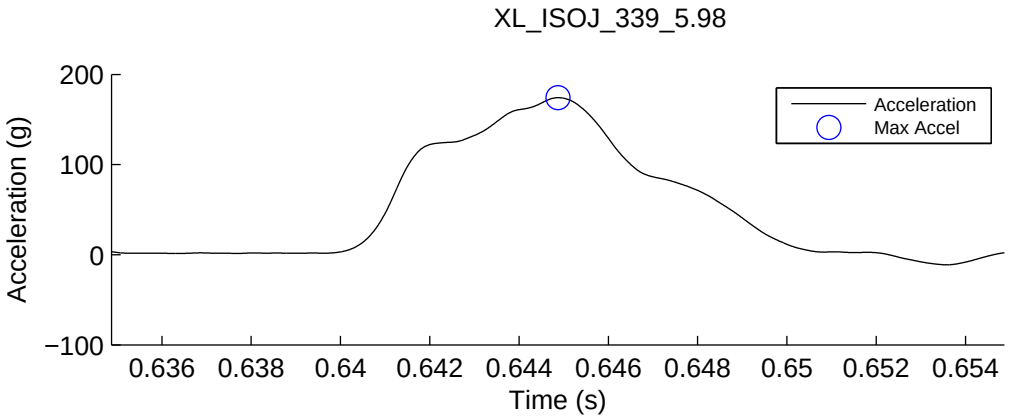

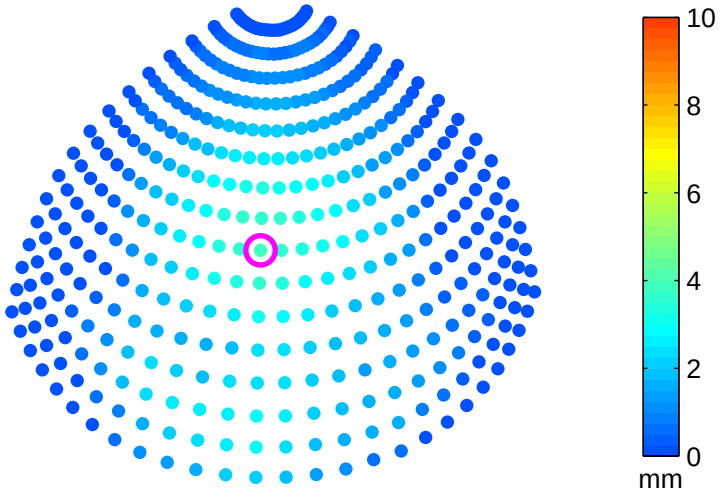

Max Resultant Accel (g)	174.22
HIC	1234.33
Impact Speed (m/s)	5.97
Impact Energy (J)	89.16
Maximum Crush (mm)	3.91
Crush Volume (cm³)	23.94
Mismatch (cm)	5.01

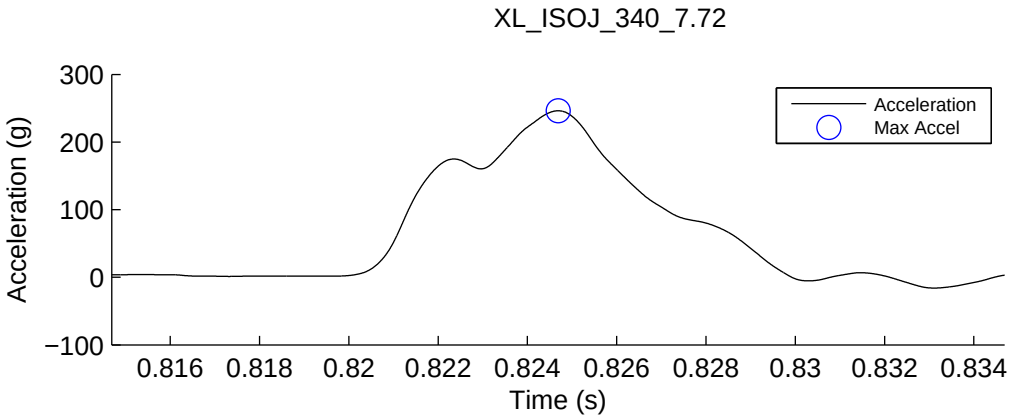

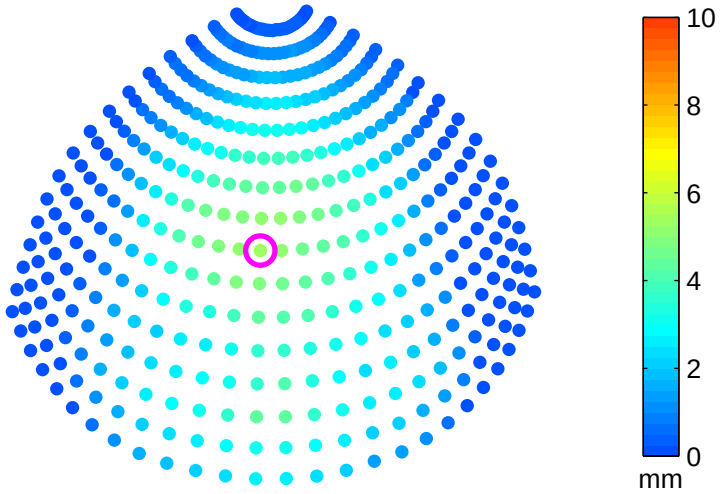

Max Resultant Accel (g)	246.22
HIC	2437.62
Impact Speed (m/s)	7.72
Impact Energy (J)	149.06
Maximum Crush (mm)	5.36
Crush Volume (cm³)	36.32
Mismatch (cm)	5.01

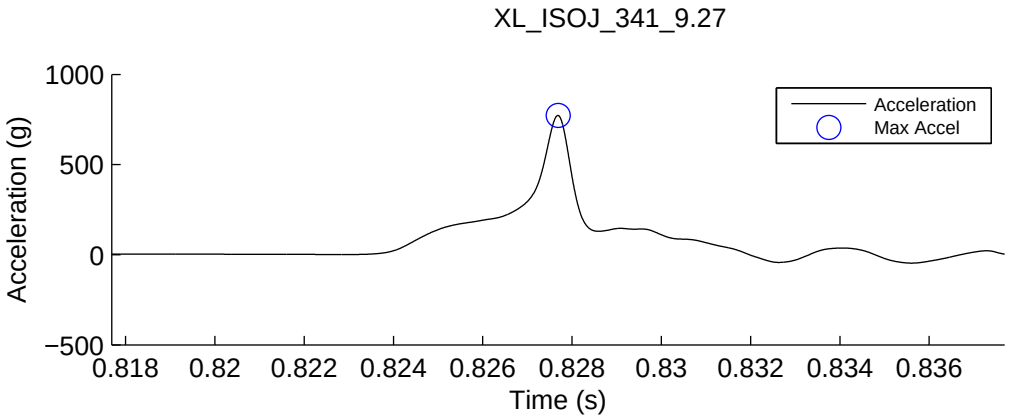

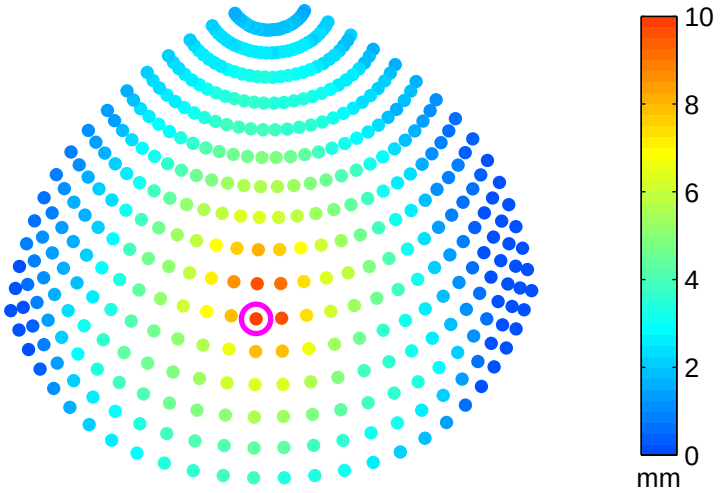

Max Resultant Accel (g)	772.43
HIC	7331.15
Impact Speed (m/s)	9.27
Impact Energy (J)	214.97
Maximum Crush (mm)	10.02
Crush Volume (cm³)	64.20
Mismatch (cm)	5.01

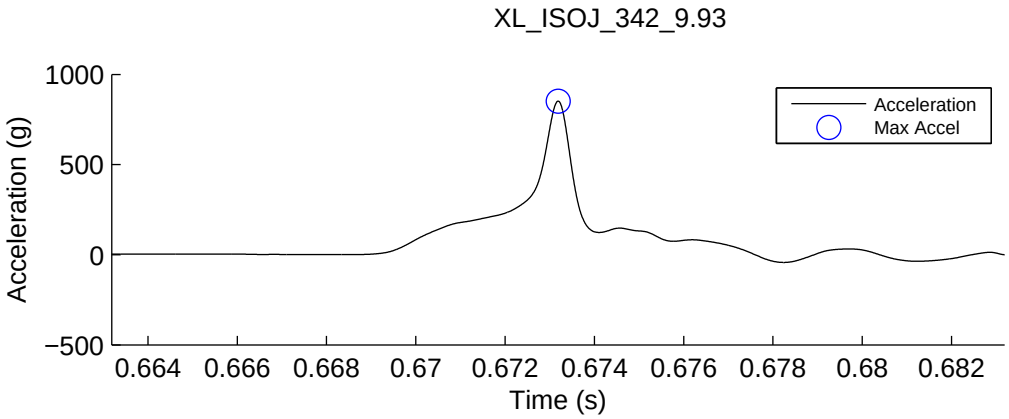

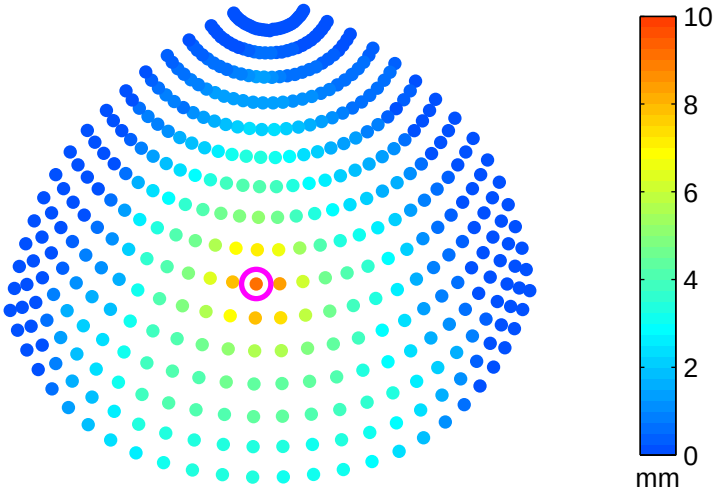

Max Resultant Accel (g)	852.05
HIC	8855.15
Impact Speed (m/s)	9.93
Impact Energy (J)	246.59
Maximum Crush (mm)	9.02
Crush Volume (cm³)	42.48
Mismatch (cm)	5.01

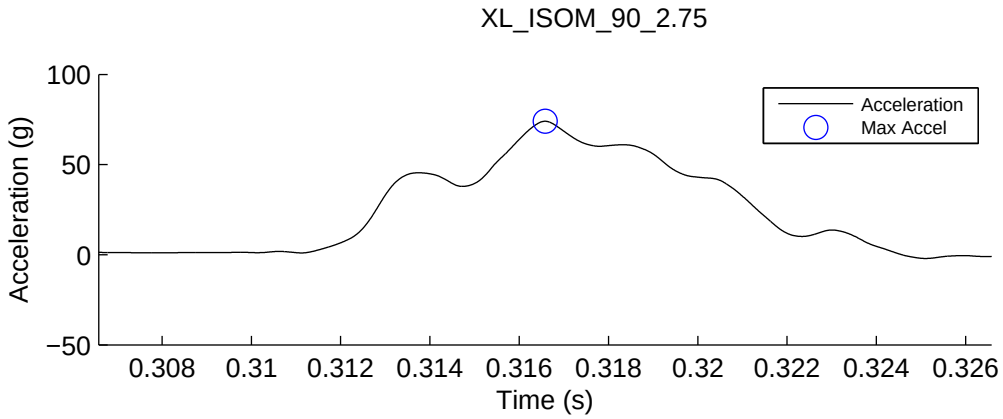

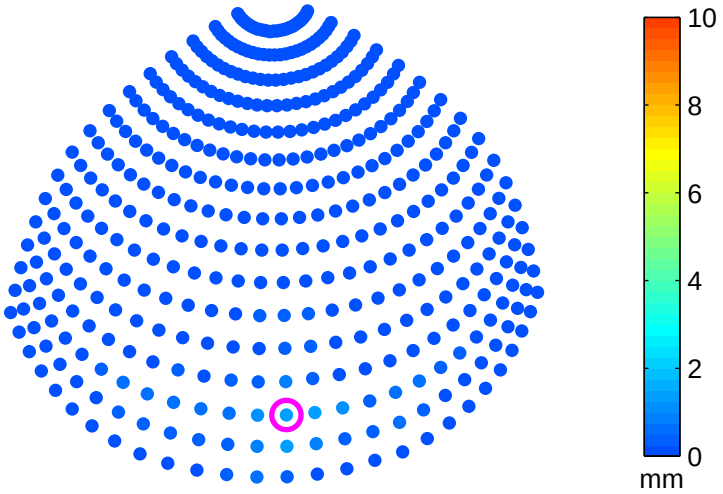

Max Resultant Accel (g)	74.03
HIC	155.19
Impact Speed (m/s)	2.75
Impact Energy (J)	18.65
Maximum Crush (mm)	1.31
Crush Volume (cm³)	2.10
Mismatch (cm)	2.01

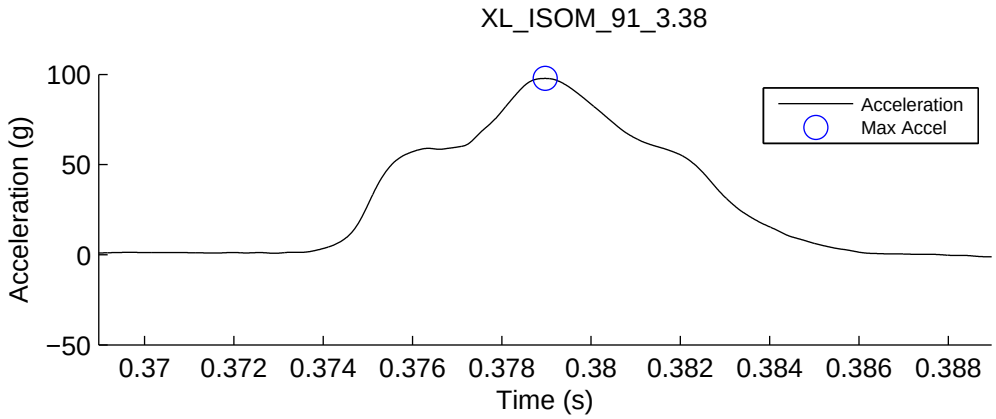

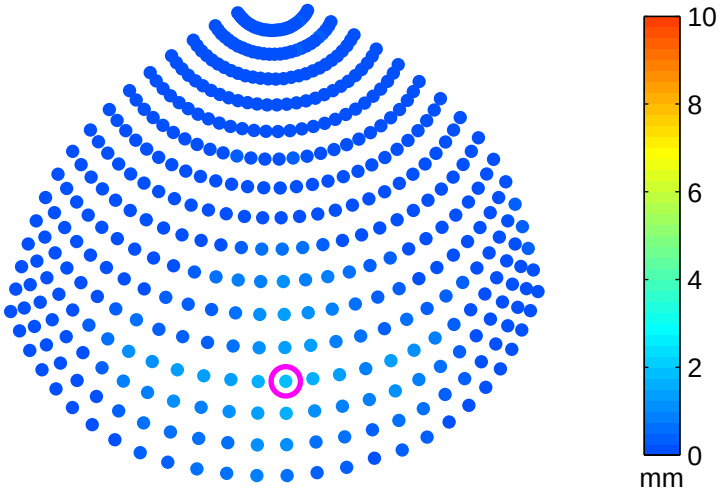

Max Resultant Accel (g)	97.78
HIC	297.74
Impact Speed (m/s)	3.38
Impact Energy (J)	28.11
Maximum Crush (mm)	1.93
Crush Volume (cm³)	6.09
Mismatch (cm)	2.01

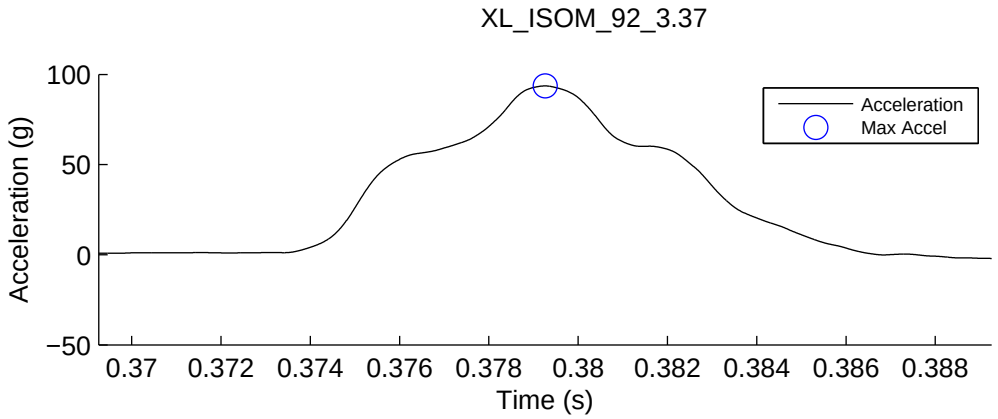

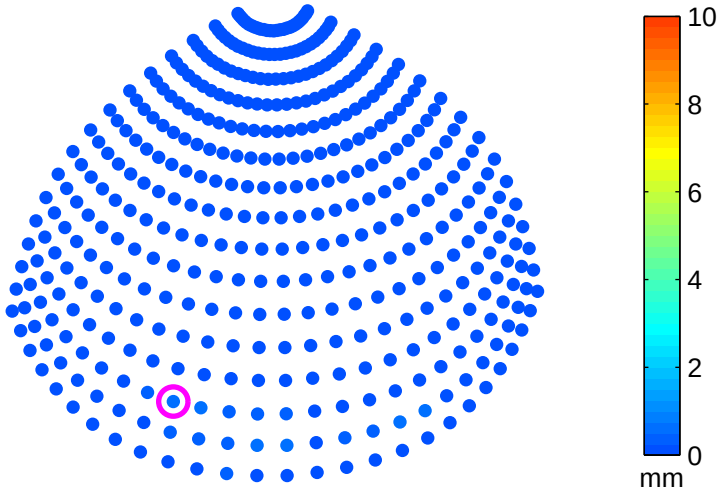

Max Resultant Accel (g)	93.63
HIC	278.59
Impact Speed (m/s)	3.37
Impact Energy (J)	27.94
Maximum Crush (mm)	0.67
Crush Volume (cm³)	0.73
Mismatch (cm)	2.01

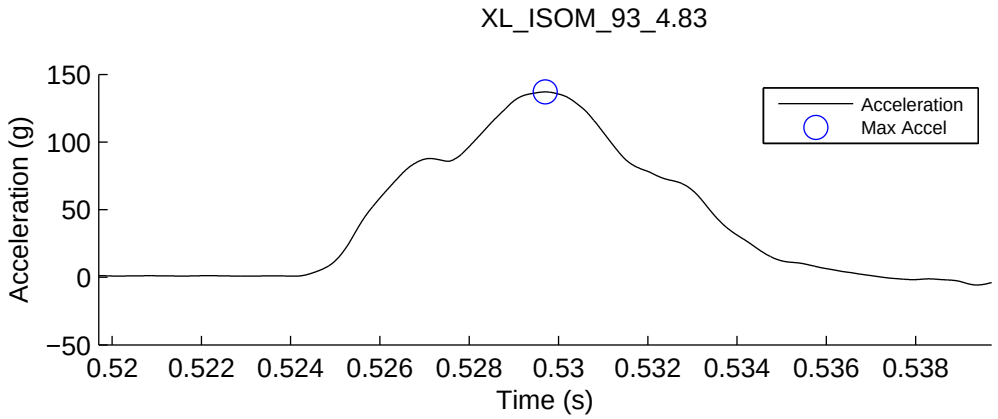

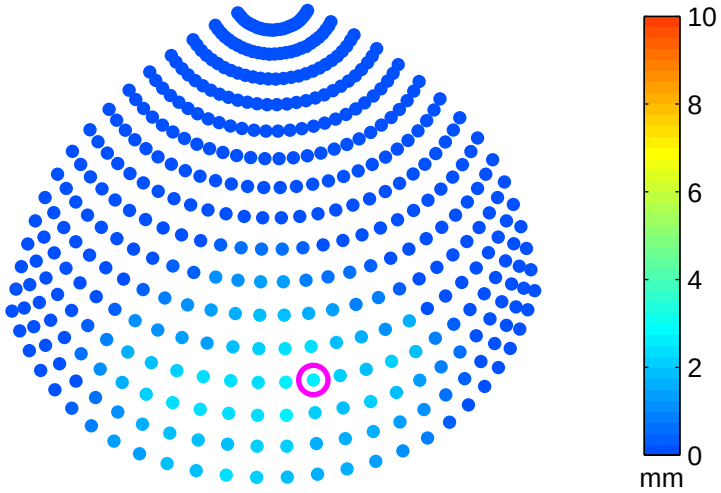

Max Resultant Accel (g)	137.06
HIC	699.01
Impact Speed (m/s)	4.83
Impact Energy (J)	57.66
Maximum Crush (mm)	2.63
Crush Volume (cm³)	11.30
Mismatch (cm)	2.01

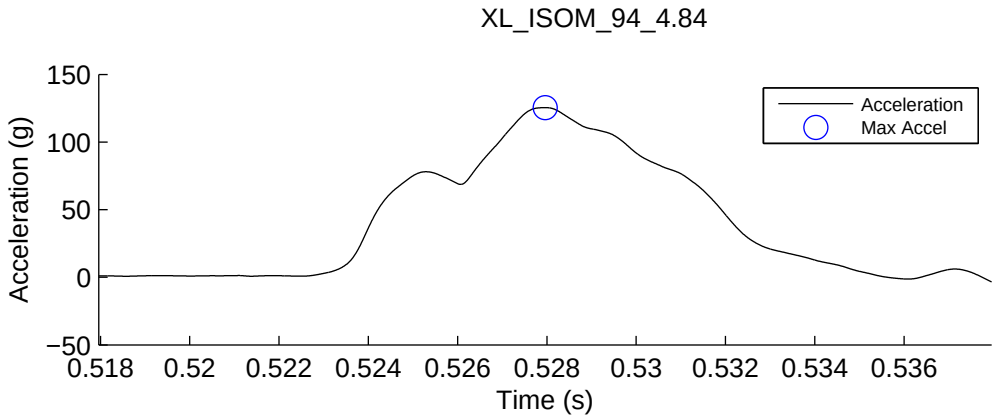

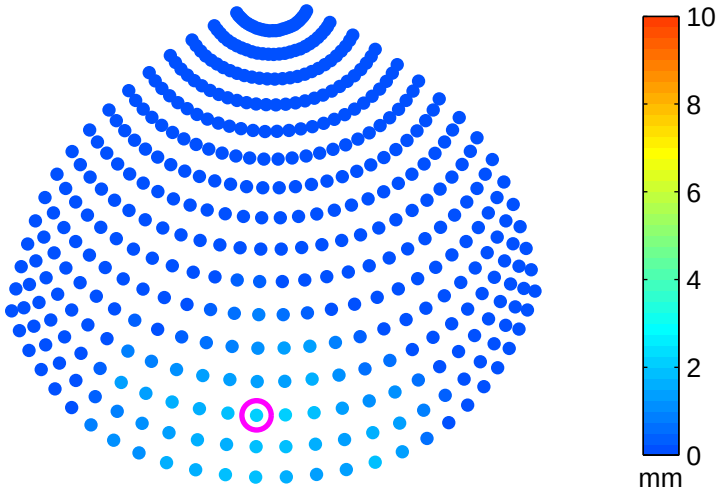

Max Resultant Accel (g)	125.48
HIC	589.81
Impact Speed (m/s)	4.84
Impact Energy (J)	57.82
Maximum Crush (mm)	2.11
Crush Volume (cm³)	6.50
Mismatch (cm)	2.01

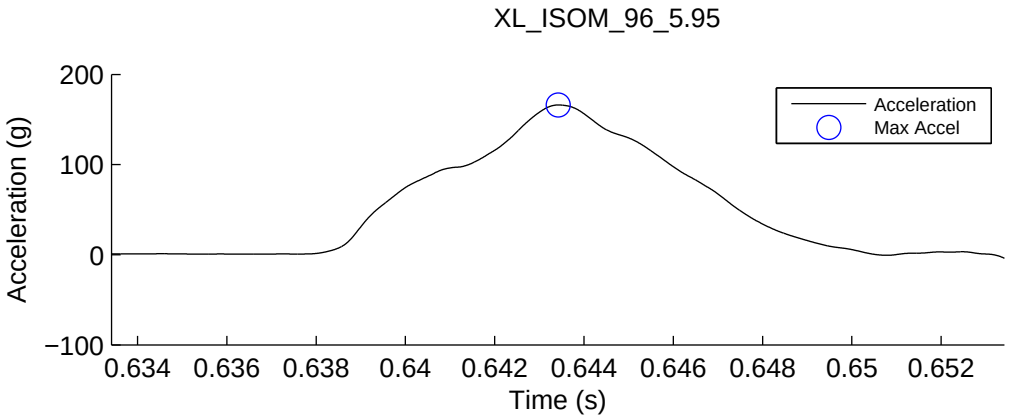

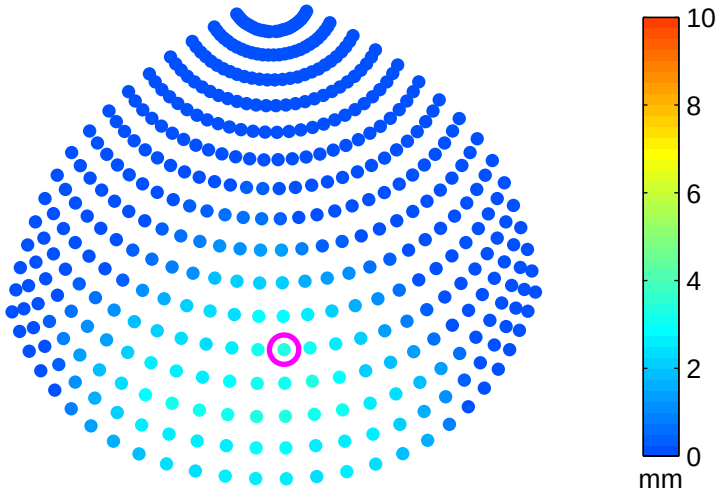

Max Resultant Accel (g)	166.15
HIC	1066.36
Impact Speed (m/s)	5.95
Impact Energy (J)	87.42
Maximum Crush (mm)	3.44
Crush Volume (cm³)	16.86
Mismatch (cm)	2.01

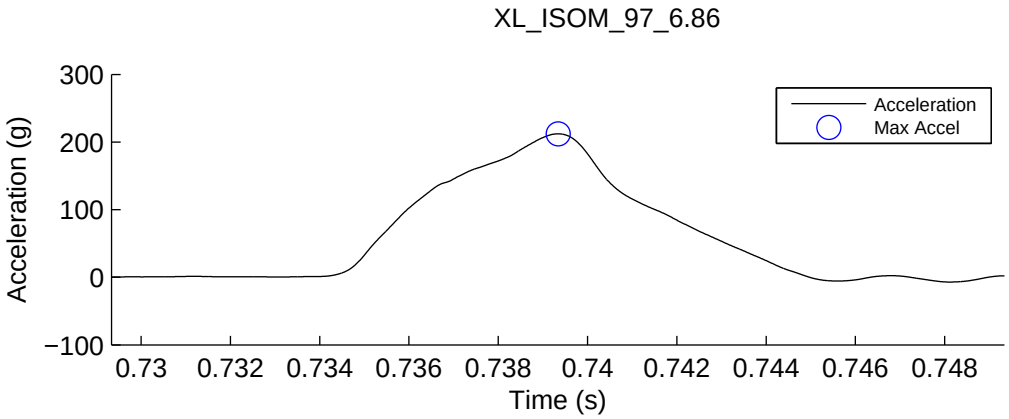

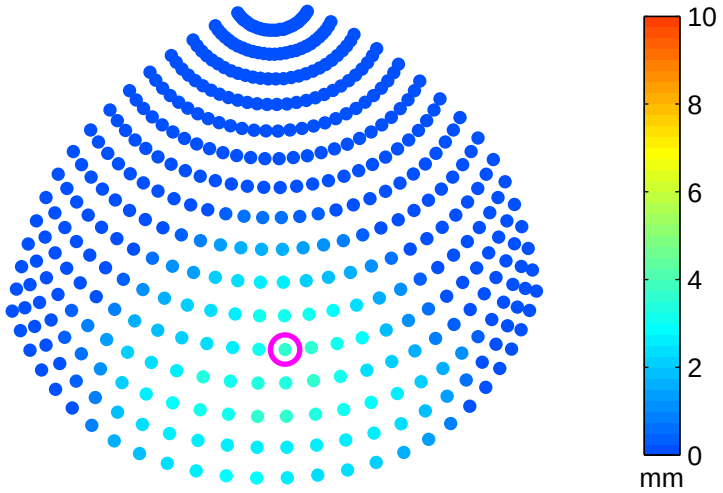

Max Resultant Accel (g)	212.16
HIC	1776.38
Impact Speed (m/s)	6.86
Impact Energy (J)	116.21
Maximum Crush (mm)	3.64
Crush Volume (cm³)	17.69
Mismatch (cm)	2.01

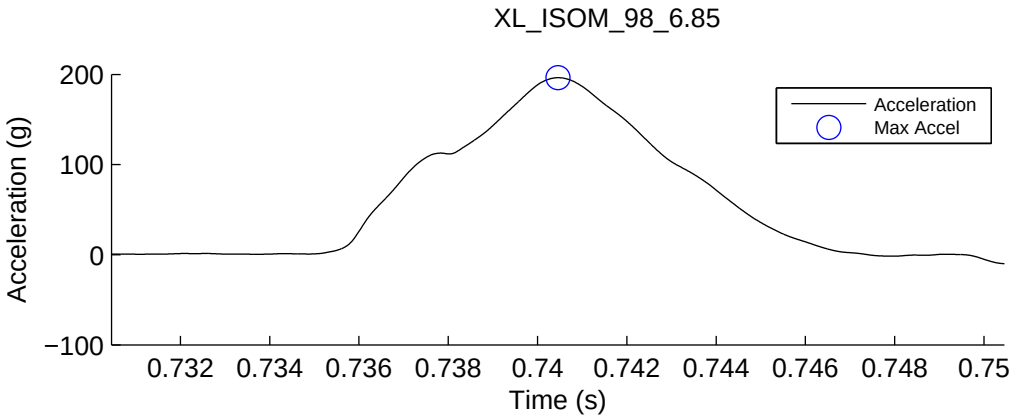

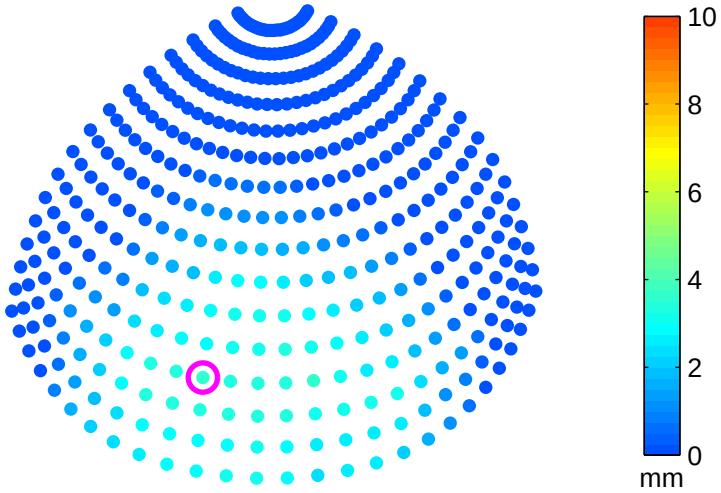

Max Resultant Accel (g)	196.39
HIC	1591.01
Impact Speed (m/s)	6.85
Impact Energy (J)	115.76
Maximum Crush (mm)	3.54
Crush Volume (cm³)	21.80
Mismatch (cm)	2.01

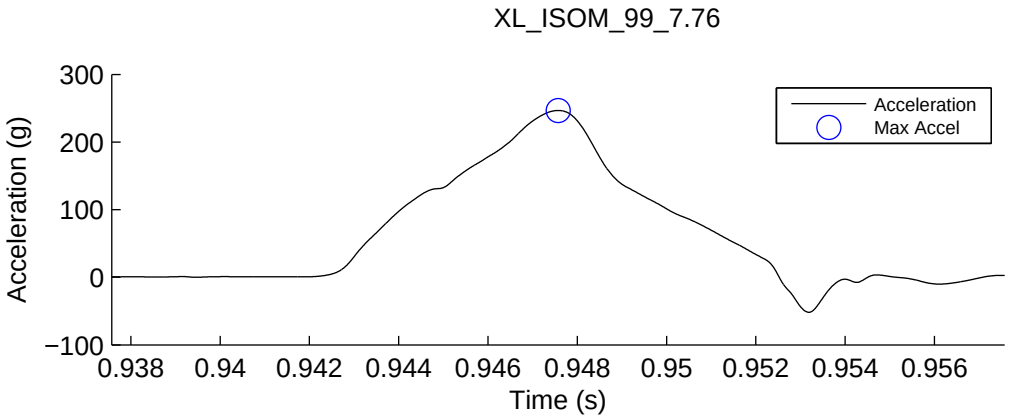

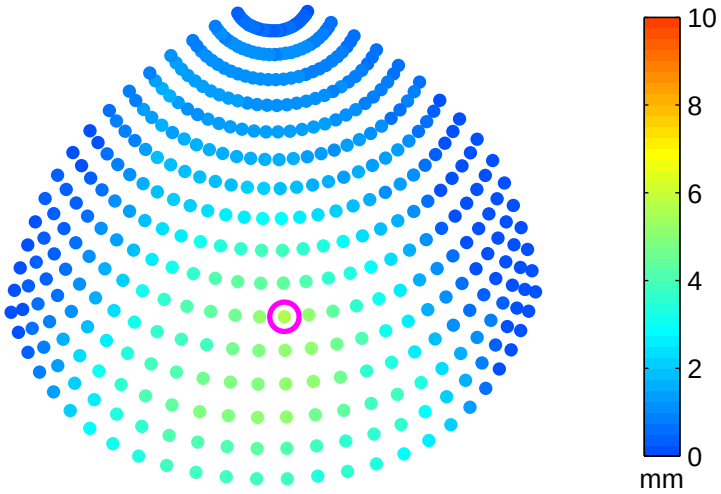

Max Resultant Accel (g)	246.68
HIC	2262.99
Impact Speed (m/s)	7.76
Impact Energy (J)	148.61
Maximum Crush (mm)	5.51
Crush Volume (cm³)	41.21
Mismatch (cm)	2.01

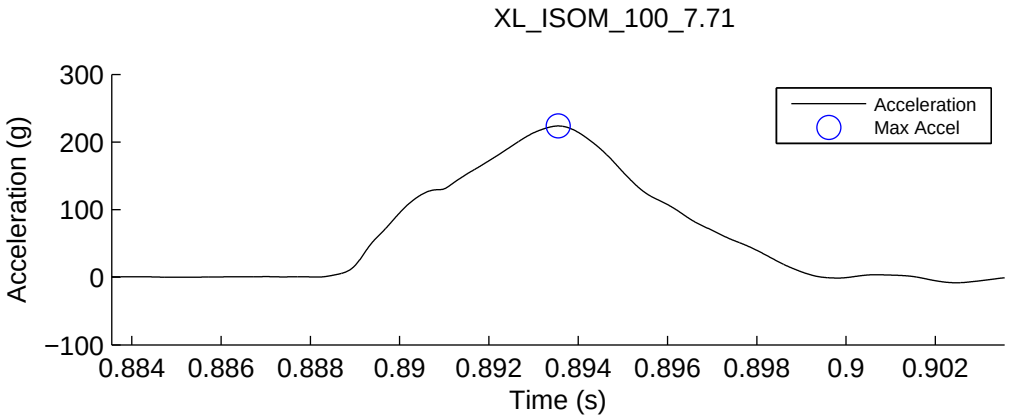

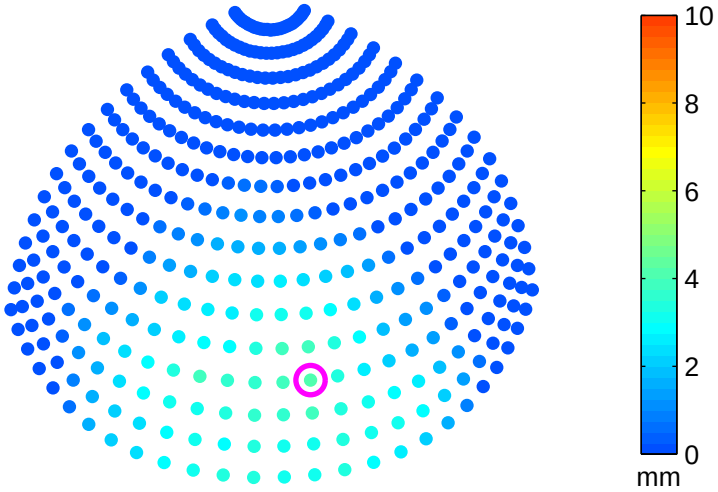

Max Resultant Accel (g)	223.78
HIC	2160.18
Impact Speed (m/s)	7.71
Impact Energy (J)	146.65
Maximum Crush (mm)	4.08
Crush Volume (cm³)	20.99
Mismatch (cm)	2.01

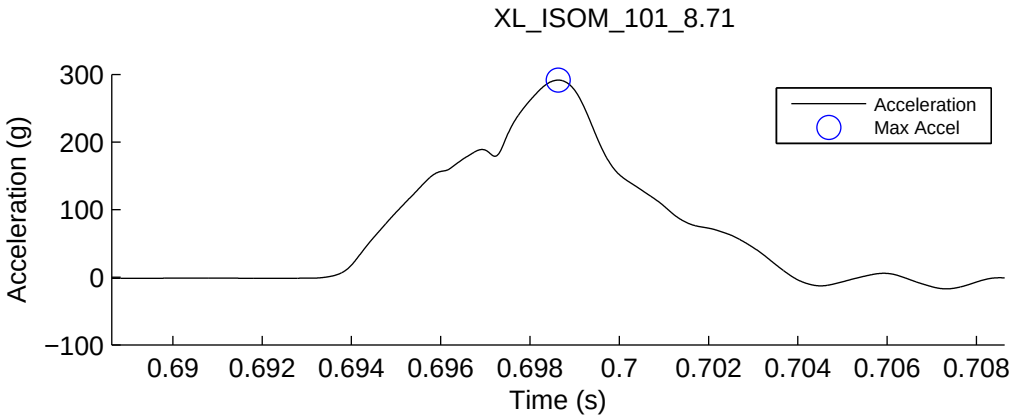

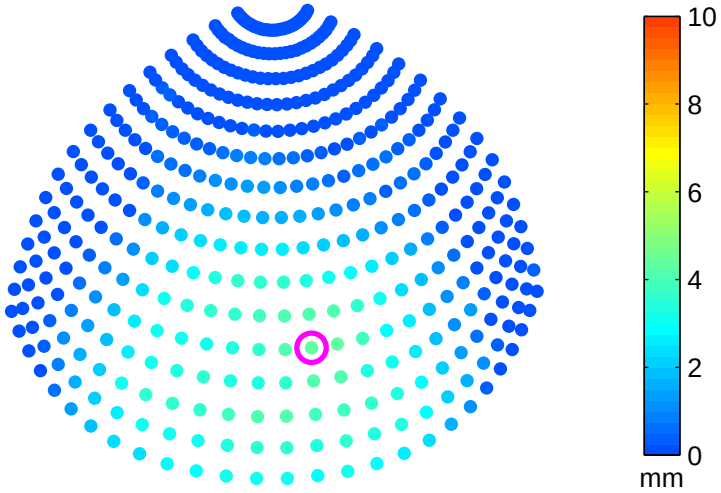

Max Resultant Accel (g)	291.60
HIC	3004.84
Impact Speed (m/s)	8.71
Impact Energy (J)	187.05
Maximum Crush (mm)	4.39
Crush Volume (cm³)	28.86
Mismatch (cm)	2.01

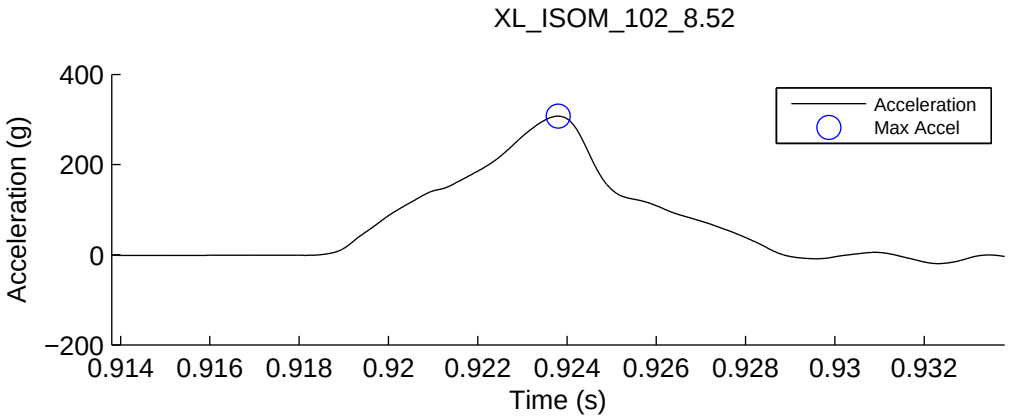

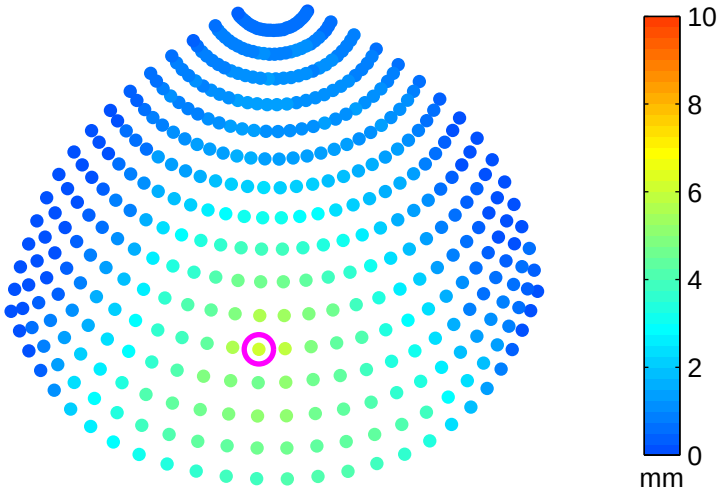

Max Resultant Accel (g)	307.42
HIC	3036.40
Impact Speed (m/s)	8.52
Impact Energy (J)	178.95
Maximum Crush (mm)	6.01
Crush Volume (cm³)	42.67
Mismatch (cm)	2.01

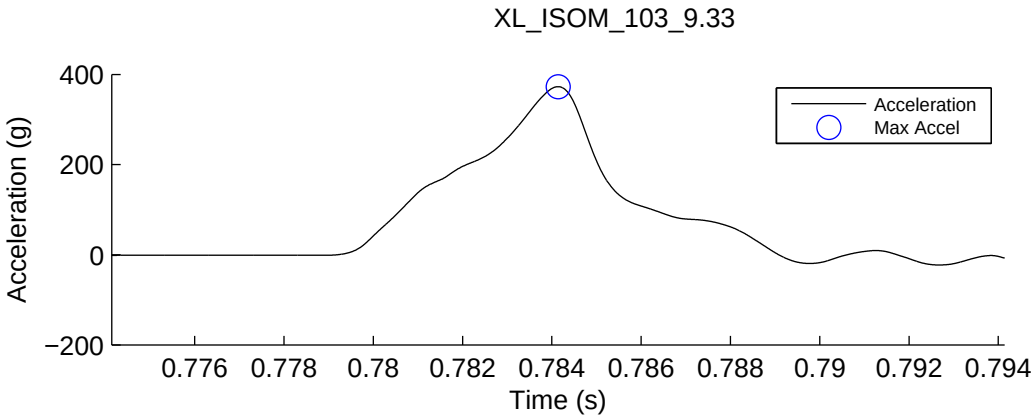

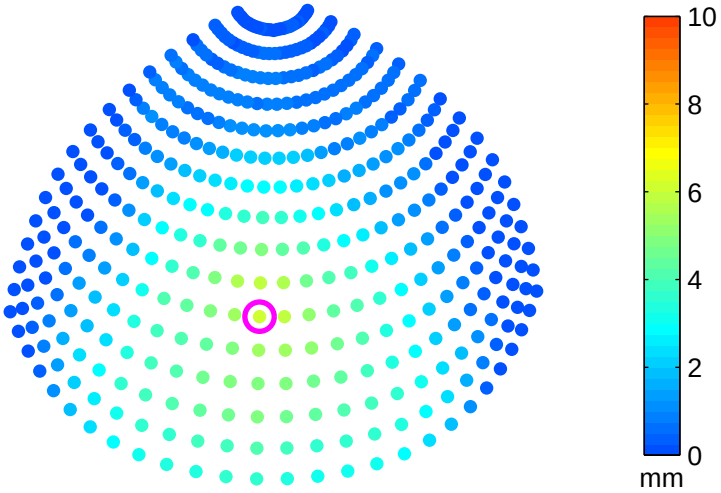

Max Resultant Accel (g)	372.88
HIC	4282.09
Impact Speed (m/s)	9.33
Impact Energy (J)	214.96
Maximum Crush (mm)	6.22
Crush Volume (cm³)	40.73
Mismatch (cm)	2.01

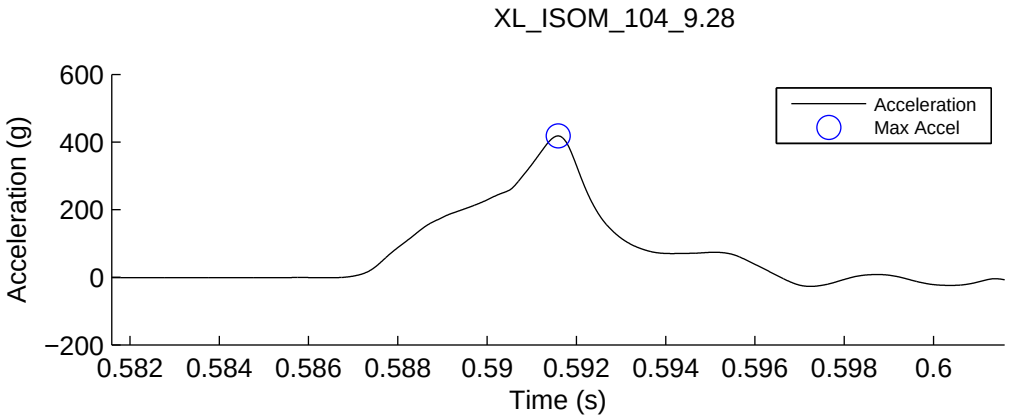

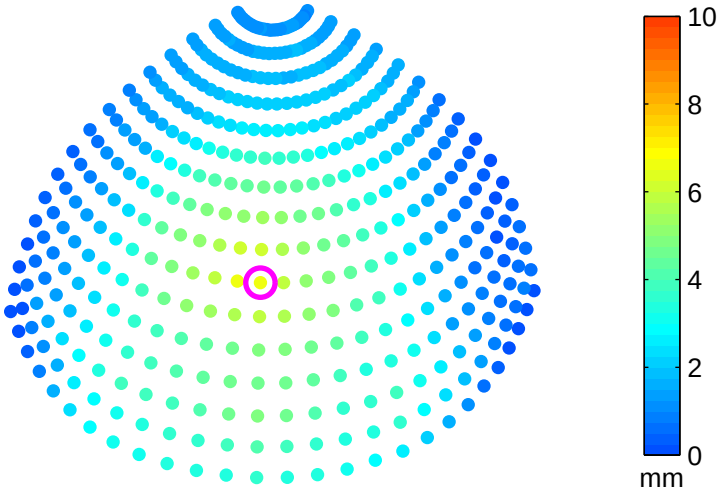

Max Resultant Accel (g)	418.01
HIC	4641.99
Impact Speed (m/s)	9.29
Impact Energy (J)	212.69
Maximum Crush (mm)	6.59
Crush Volume (cm³)	52.85
Mismatch (cm)	2.01

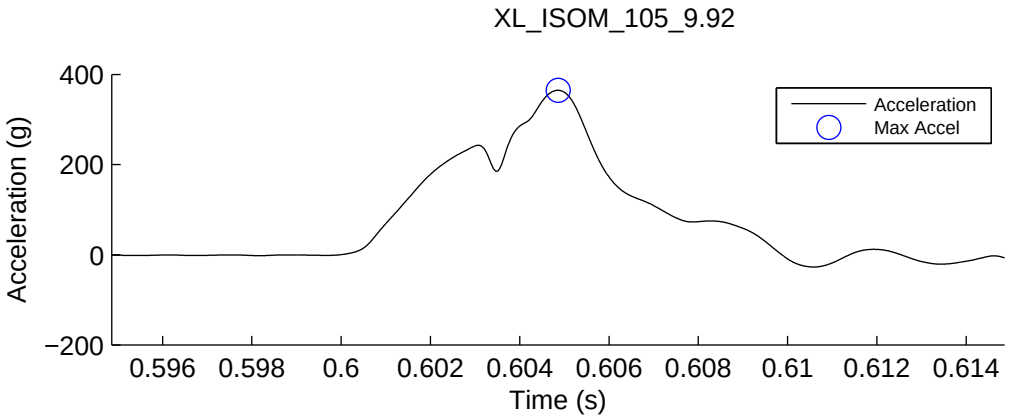

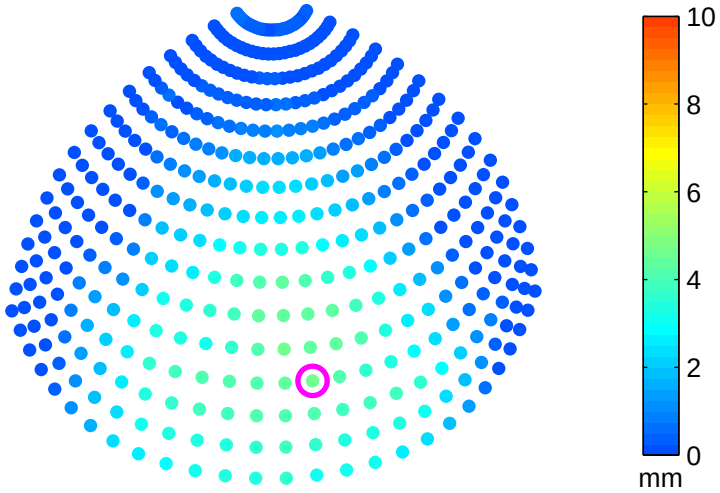

Max Resultant Accel (g)	364.87
HIC	4481.24
Impact Speed (m/s)	9.92
Impact Energy (J)	242.59
Maximum Crush (mm)	4.57
Crush Volume (cm³)	32.28
Mismatch (cm)	2.01

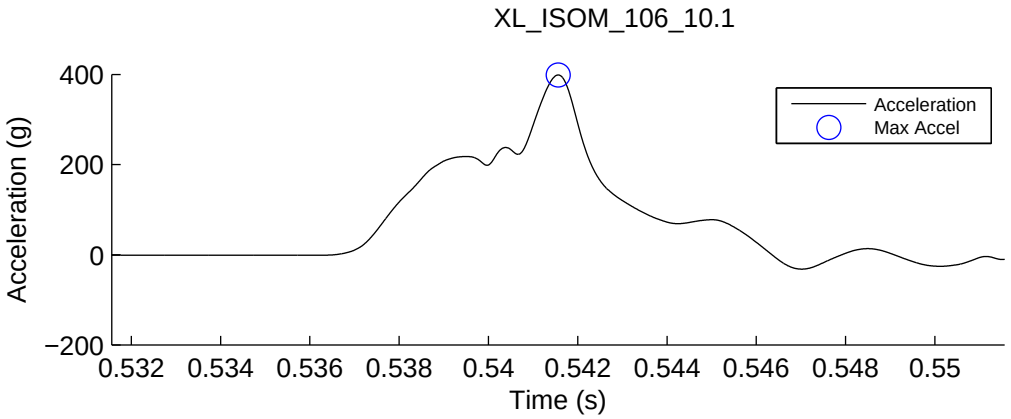

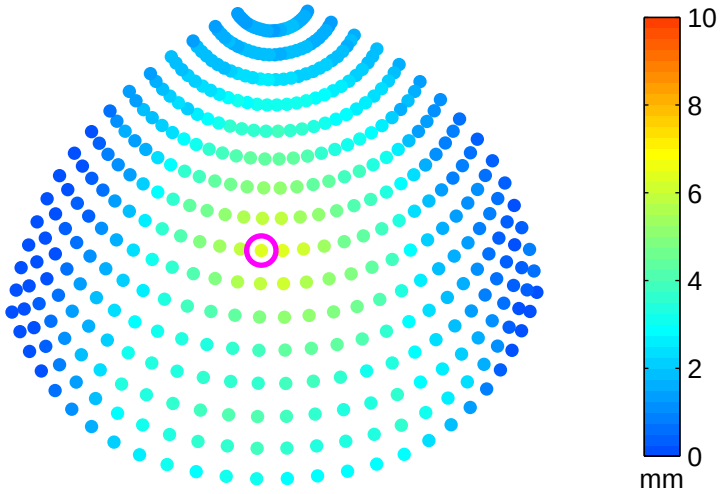

Max Resultant Accel (g)	398.83
HIC	4049.46
Impact Speed (m/s)	10.06
Impact Energy (J)	249.61
Maximum Crush (mm)	6.47
Crush Volume (cm³)	50.98
Mismatch (cm)	2.01

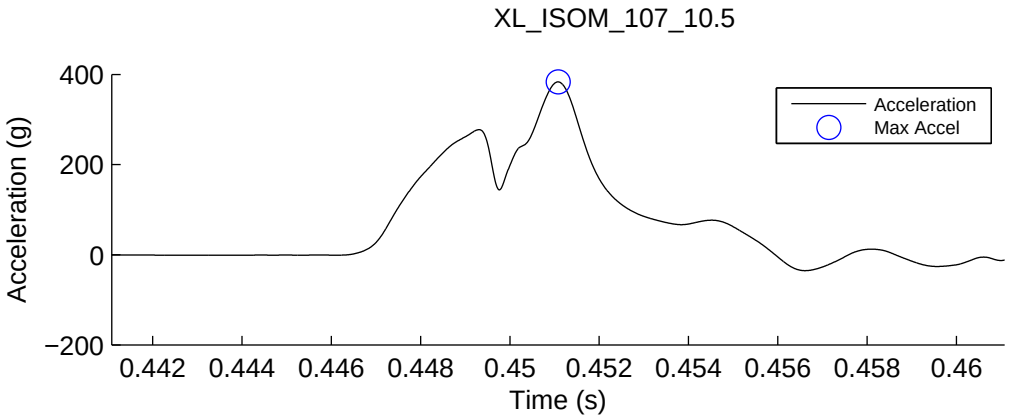

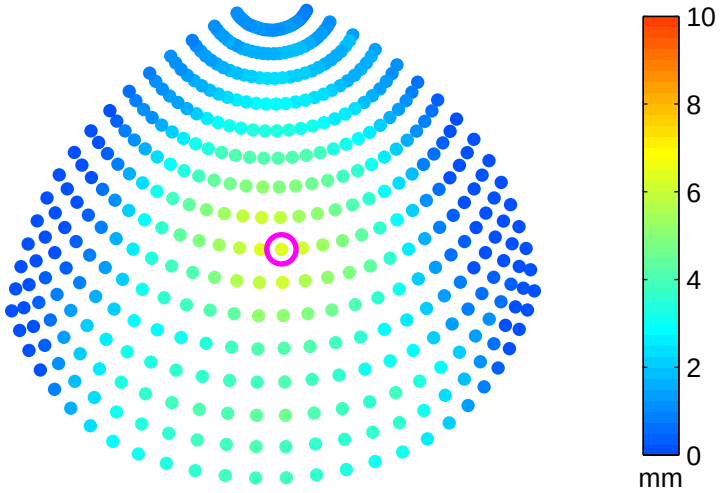

Max Resultant Accel (g)	383.41
HIC	4218.25
Impact Speed (m/s)	10.54
Impact Energy (J)	274.26
Maximum Crush (mm)	6.36
Crush Volume (cm³)	48.67
Mismatch (cm)	2.01

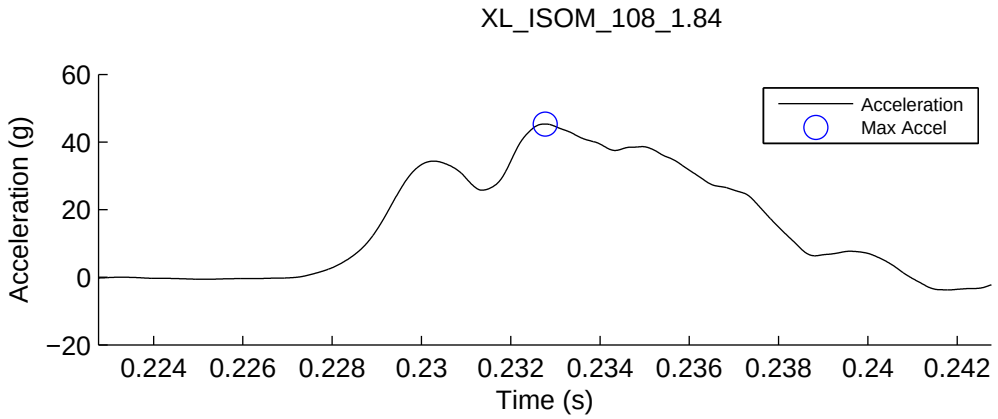

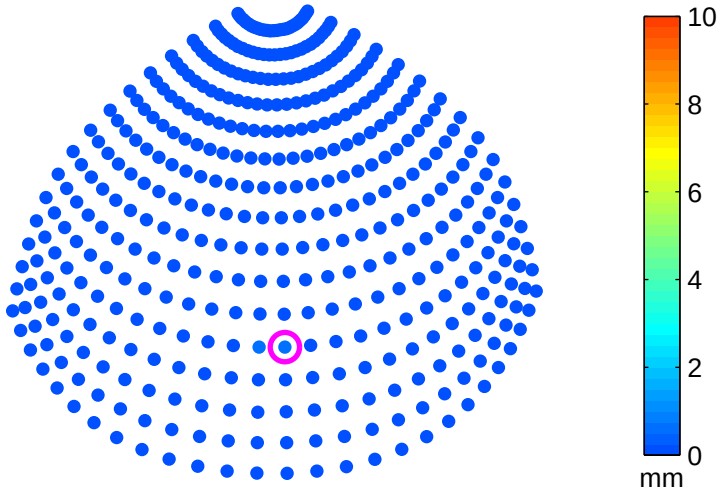

Max Resultant Accel (g)	45.34
HIC	55.47
Impact Speed (m/s)	1.84
Impact Energy (J)	8.37
Maximum Crush (mm)	0.74
Crush Volume (cm³)	0.10
Mismatch (cm)	2.01

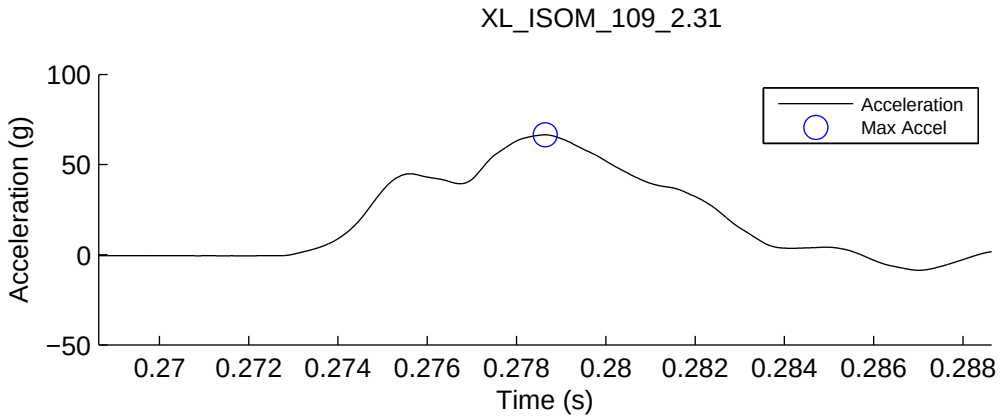

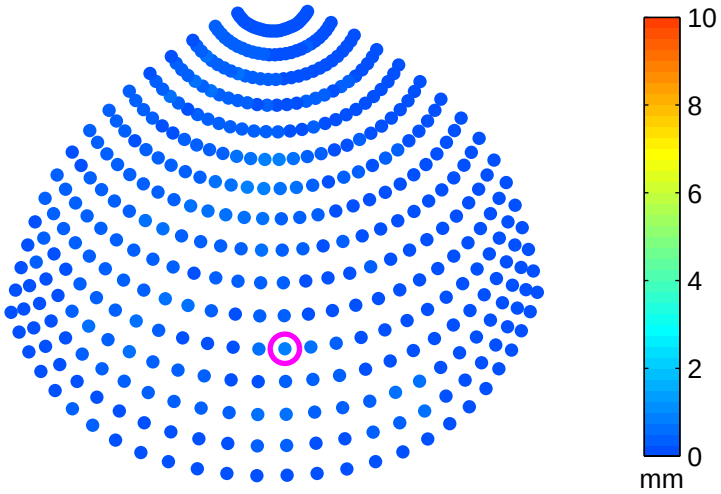

Max Resultant Accel (g)	66.49
HIC	118.94
Impact Speed (m/s)	2.31
Impact Energy (J)	13.15
Maximum Crush (mm)	0.89
Crush Volume (cm³)	4.71
Mismatch (cm)	2.01

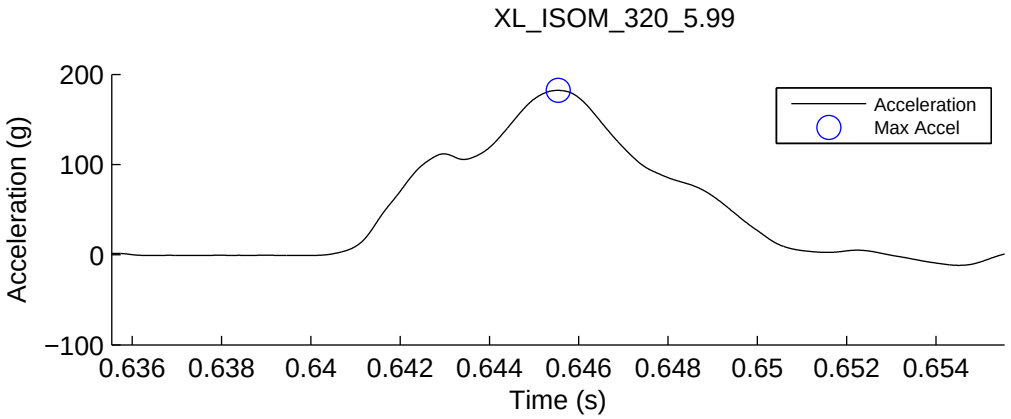

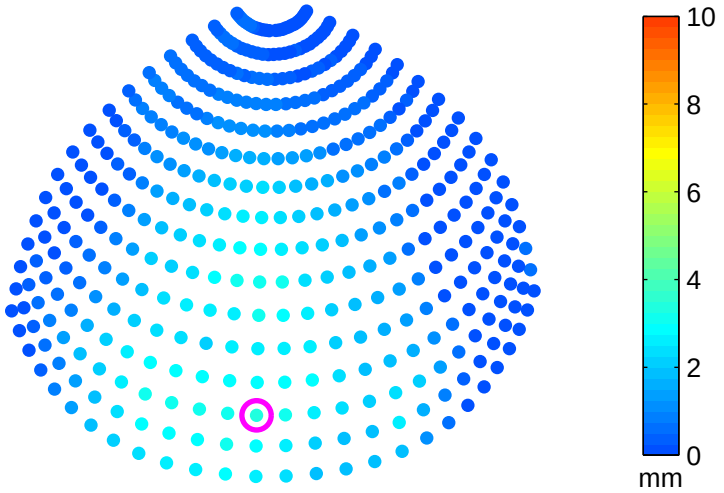

Max Resultant Accel (g)	182.34
HIC	1159.76
Impact Speed (m/s)	5.97
Impact Energy (J)	89.05
Maximum Crush (mm)	3.35
Crush Volume (cm³)	24.97
Mismatch (cm)	2.01

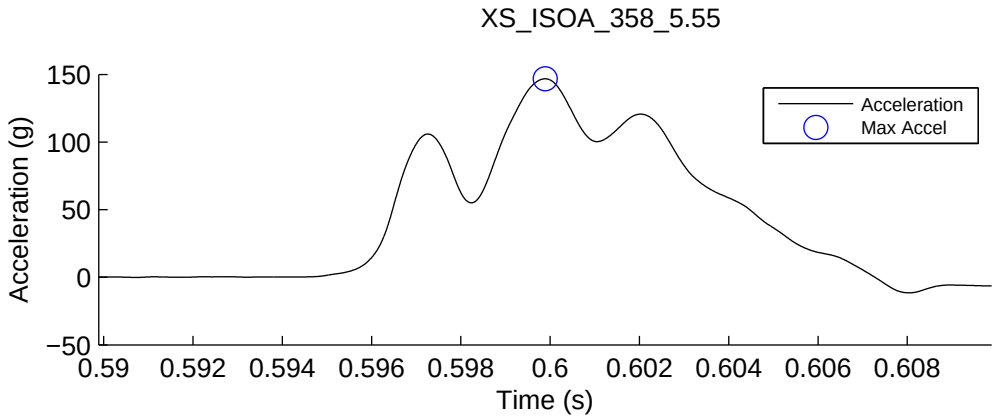

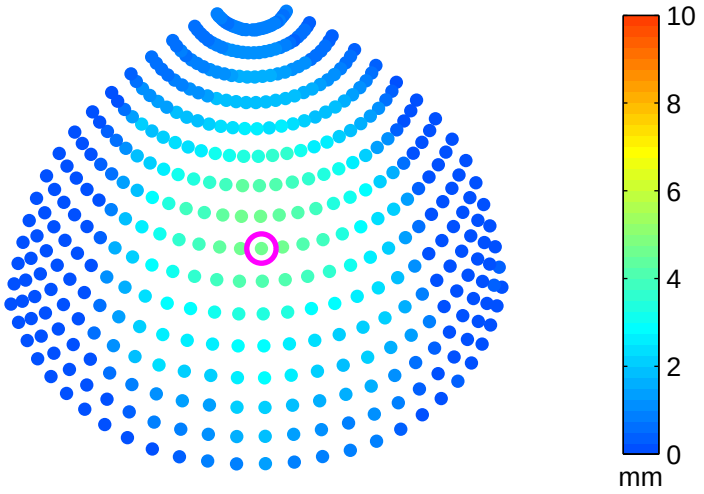

Max Resultant Accel (g)	146.77
HIC	736.45
Impact Speed (m/s)	5.55
Impact Energy (J)	76.36
Maximum Crush (mm)	4.60
Crush Volume (cm³)	26.66
Mismatch (cm)	7.60

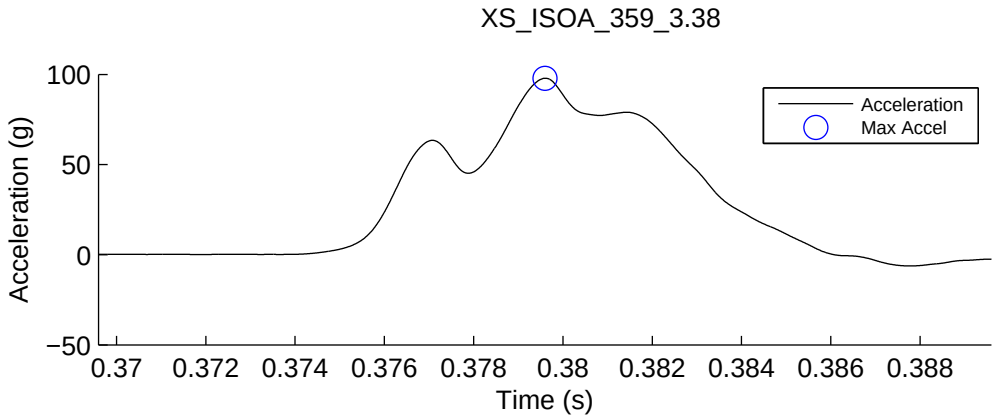

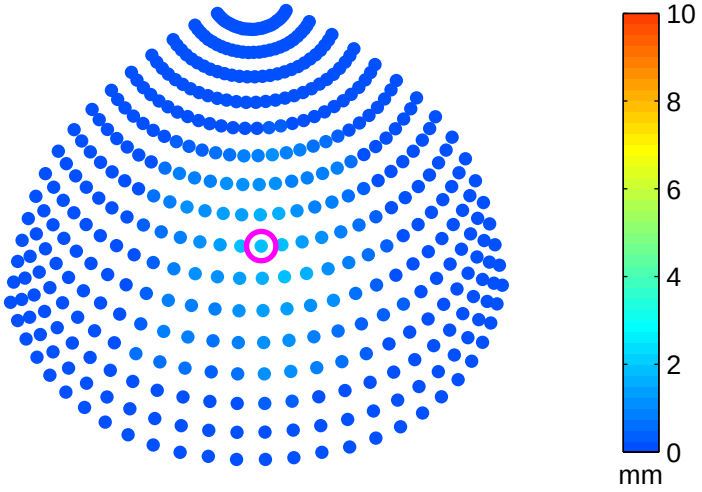

Max Resultant Accel (g)	97.90
HIC	266.99
Impact Speed (m/s)	3.38
Impact Energy (J)	28.34
Maximum Crush (mm)	1.97
Crush Volume (cm³)	4.98
Mismatch (cm)	7.60

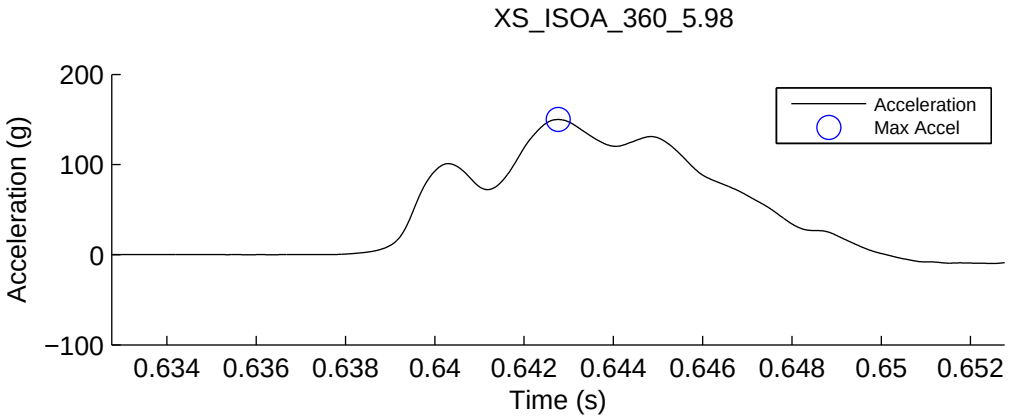

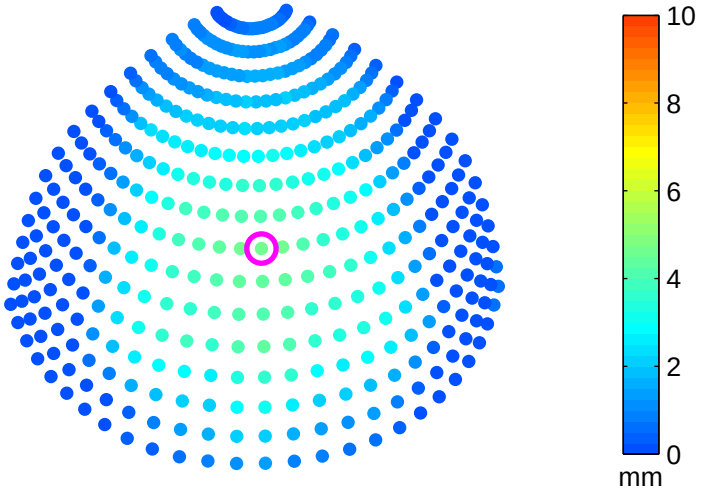

Max Resultant Accel (g)	150.02
HIC	895.59
Impact Speed (m/s)	5.98
Impact Energy (J)	88.91
Maximum Crush (mm)	4.56
Crush Volume (cm³)	30.53
Mismatch (cm)	7.60

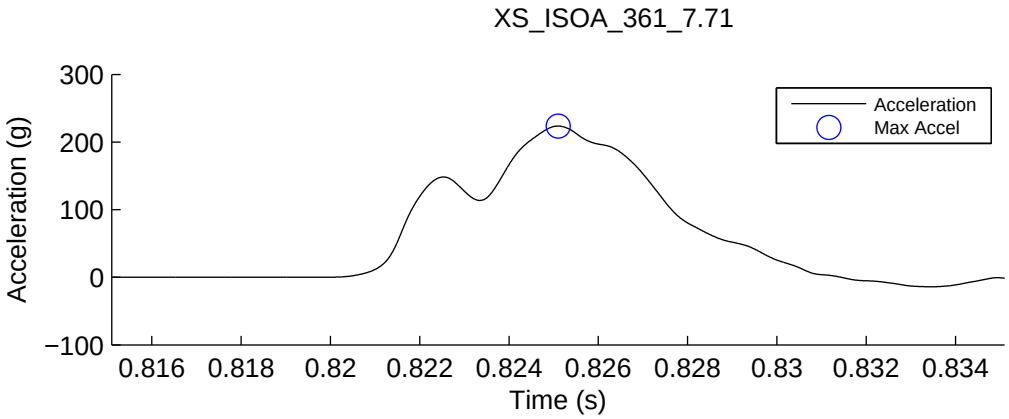

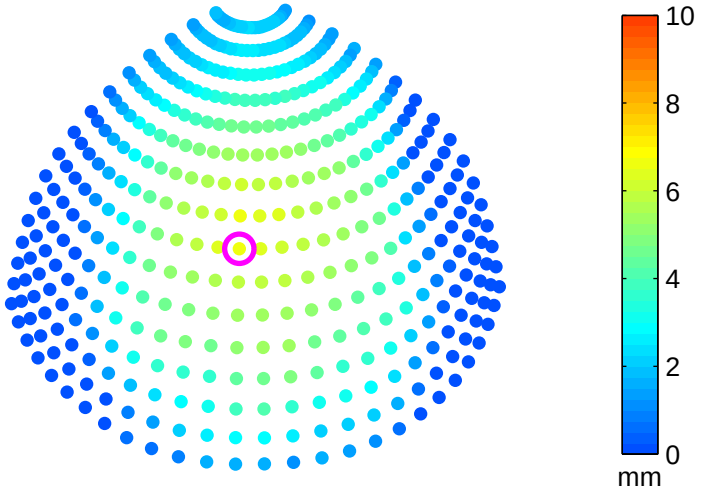

Max Resultant Accel (g)	223.67
HIC	2048.86
Impact Speed (m/s)	7.71
Impact Energy (J)	147.81
Maximum Crush (mm)	6.53
Crush Volume (cm³)	47.97
Mismatch (cm)	7.60

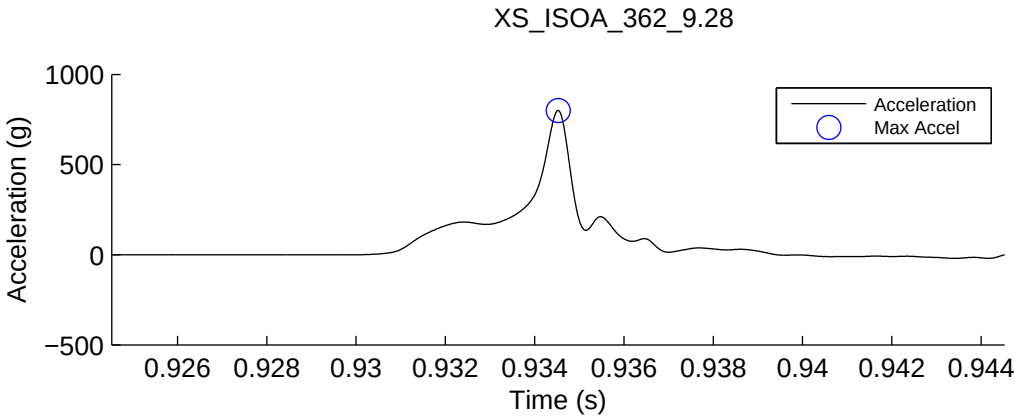

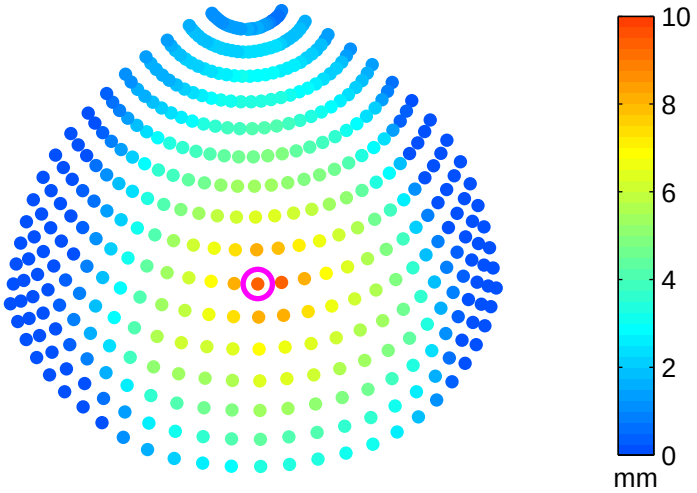

Max Resultant Accel (g)	800.21
HIC	7307.80
Impact Speed (m/s)	9.27
Impact Energy (J)	213.56
Maximum Crush (mm)	9.49
Crush Volume (cm³)	56.57
Mismatch (cm)	7.60

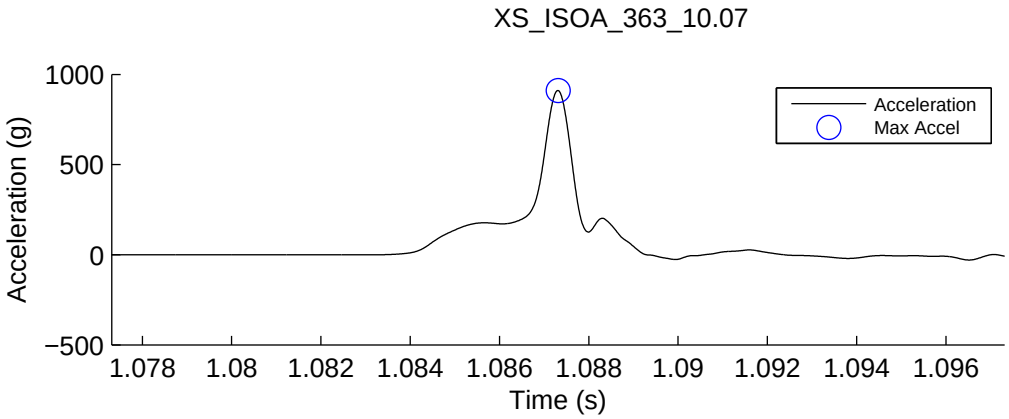

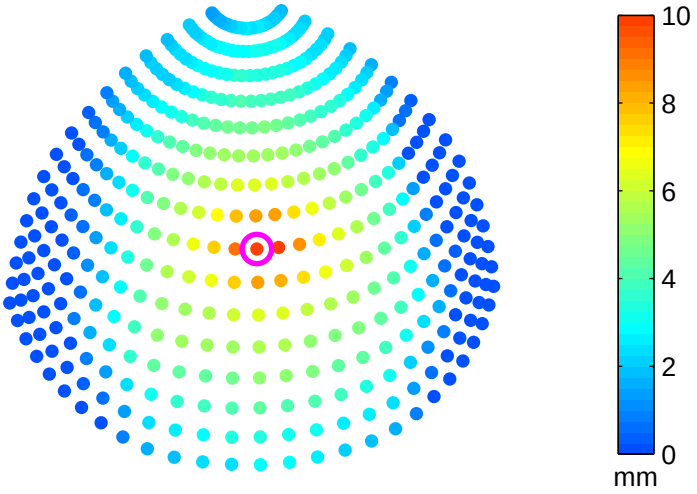

Max Resultant Accel (g)	910.79
HIC	10526.26
Impact Speed (m/s)	10.07
Impact Energy (J)	252.03
Maximum Crush (mm)	10.16
Crush Volume (cm³)	55.30
Mismatch (cm)	7.60

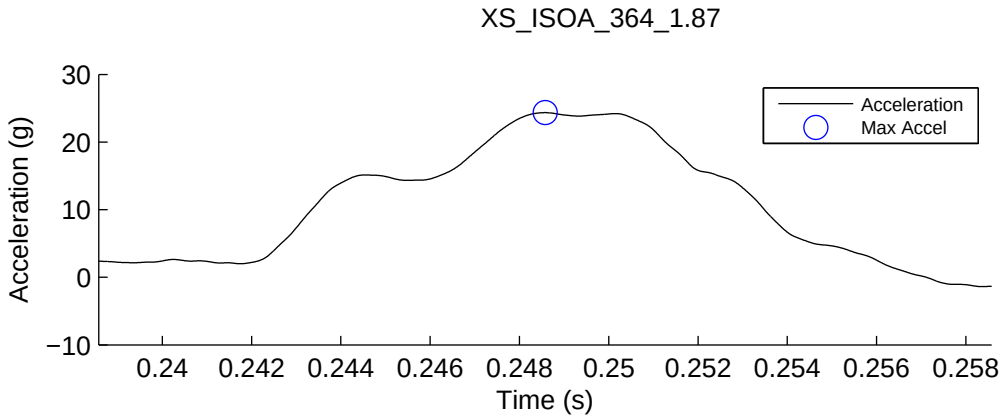

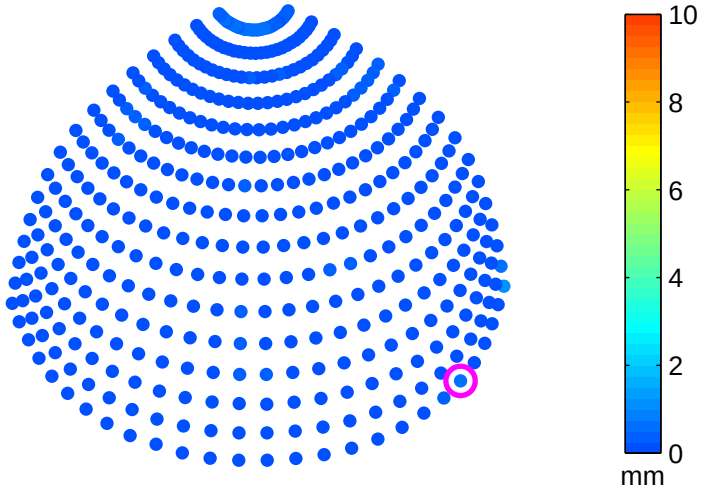

Max Resultant Accel (g)	24.35
HIC	14.53
Impact Speed (m/s)	1.87
Impact Energy (J)	8.69
Maximum Crush (mm)	0.51
Crush Volume (cm³)	0.89
Mismatch (cm)	7.60

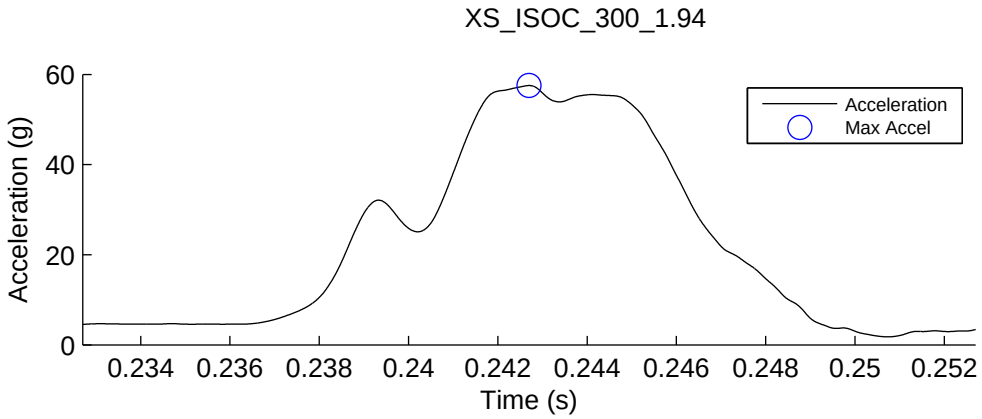

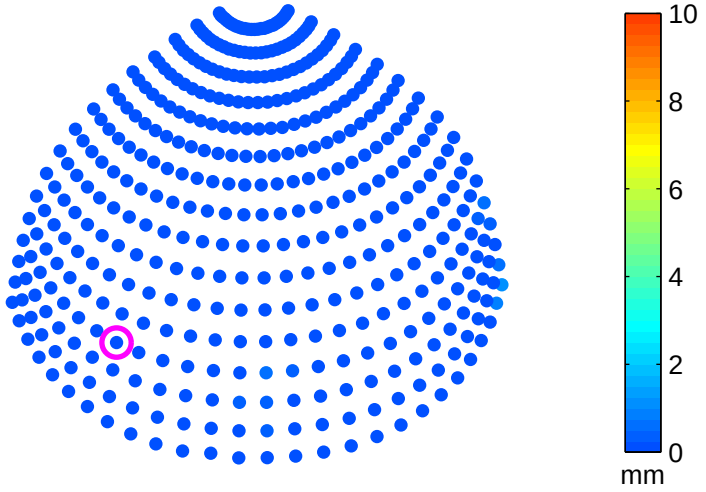

Max Resultant Accel (g)	57.54
HIC	102.11
Impact Speed (m/s)	1.94
Impact Energy (J)	9.34
Maximum Crush (mm)	0.51
Crush Volume (cm³)	0.30
Mismatch (cm)	5.60

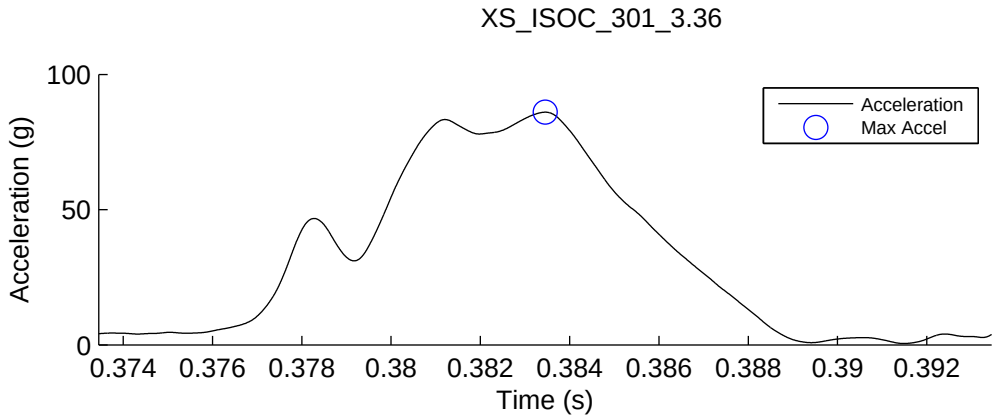

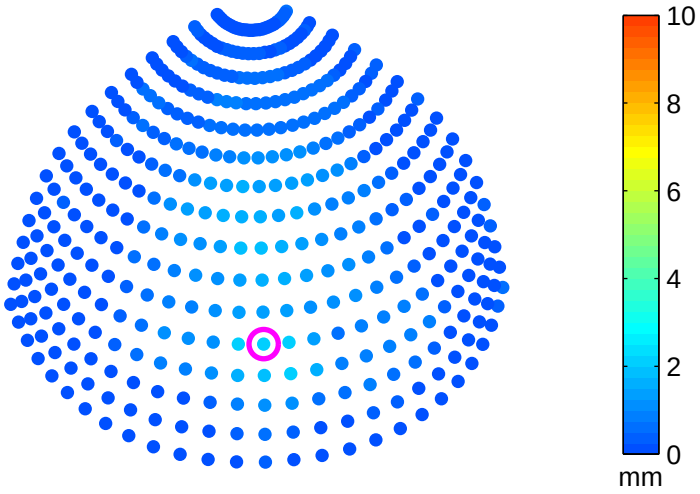

Max Resultant Accel (g)	86.04
HIC	266.78
Impact Speed (m/s)	3.36
Impact Energy (J)	28.07
Maximum Crush (mm)	2.19
Crush Volume (cm³)	8.84
Mismatch (cm)	5.60

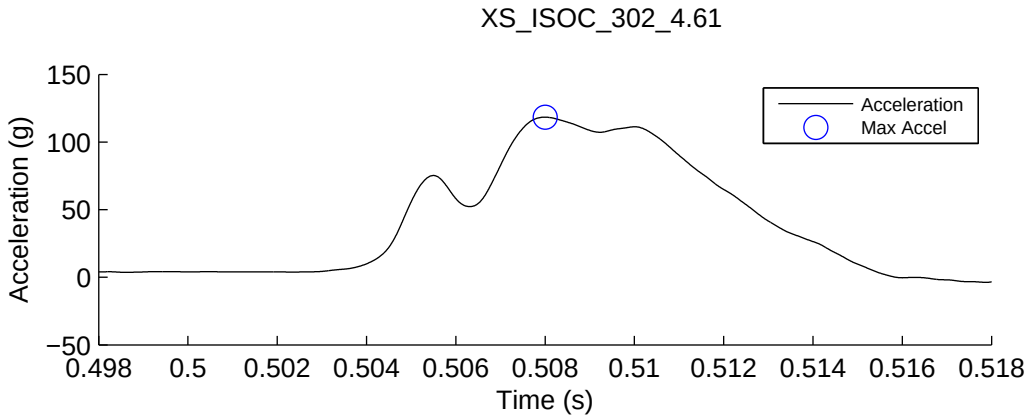

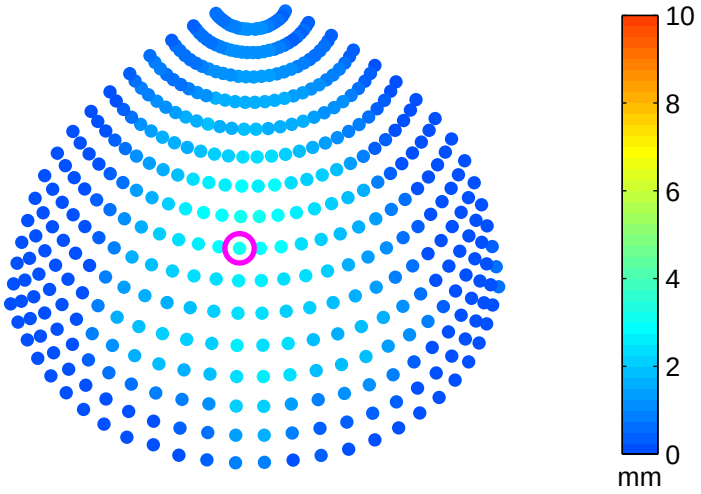

Max Resultant Accel (g)	118.43
HIC	563.50
Impact Speed (m/s)	4.61
Impact Energy (J)	53.00
Maximum Crush (mm)	3.09
Crush Volume (cm³)	17.97
Mismatch (cm)	5.60

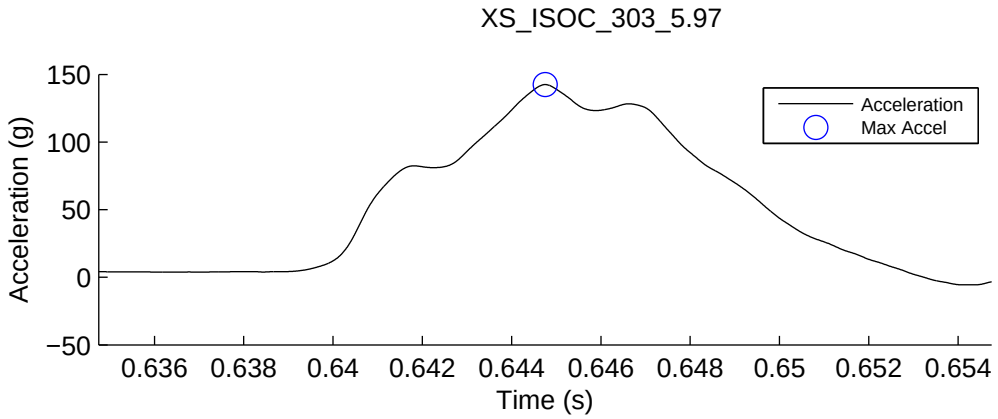

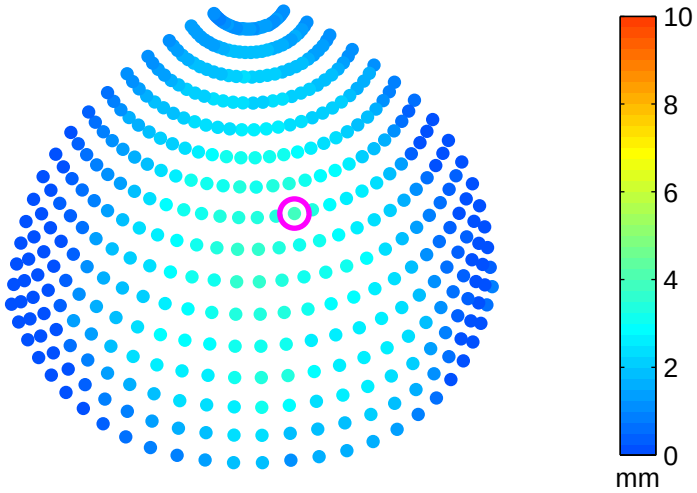

Max Resultant Accel (g)	142.49
HIC	930.79
Impact Speed (m/s)	5.97
Impact Energy (J)	88.79
Maximum Crush (mm)	3.90
Crush Volume (cm³)	31.72
Mismatch (cm)	5.60

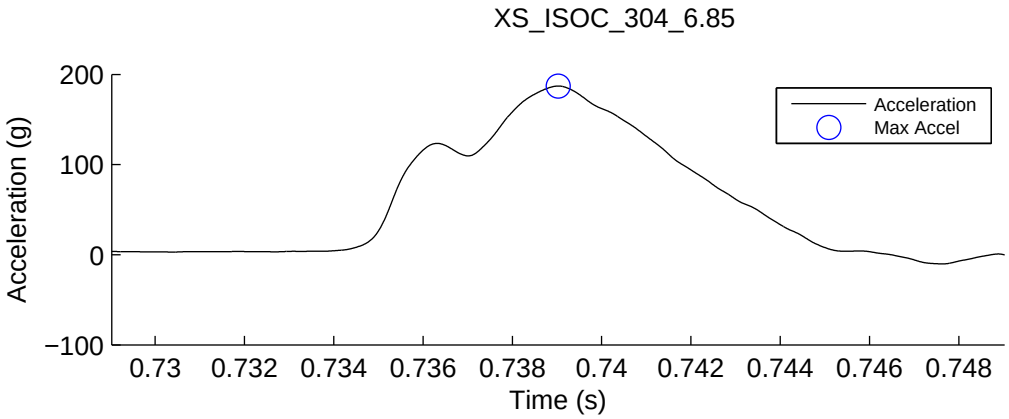

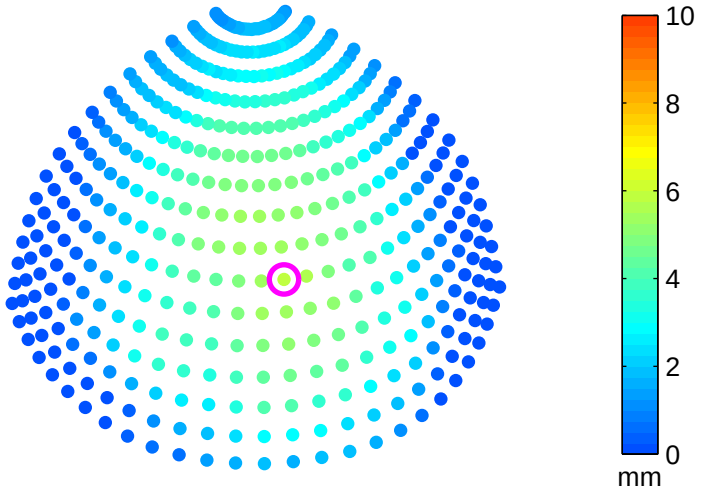

Max Resultant Accel (g)	187.17
HIC	1524.20
Impact Speed (m/s)	6.85
Impact Energy (J)	116.75
Maximum Crush (mm)	5.83
Crush Volume (cm³)	42.25
Mismatch (cm)	5.60

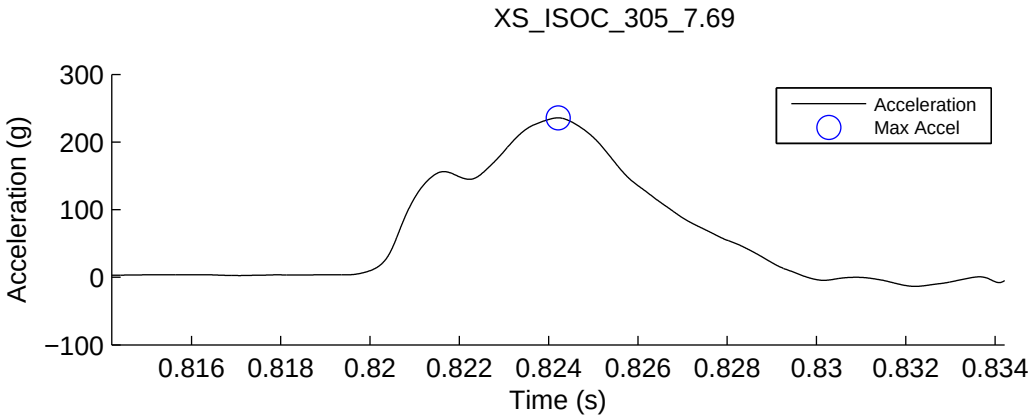

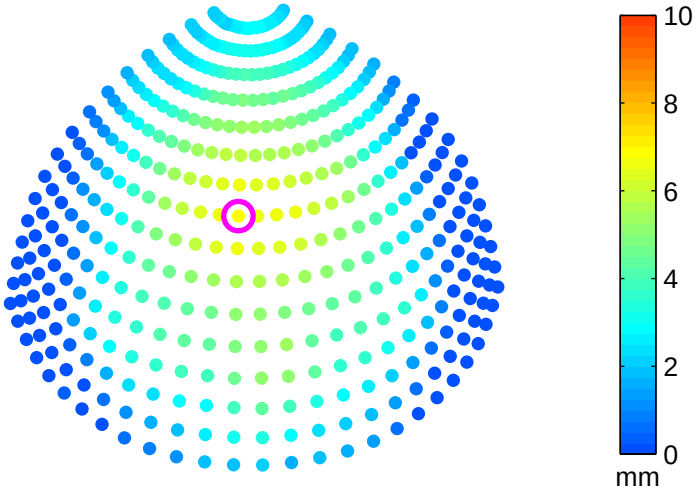

Max Resultant Accel (g)	235.77
HIC	2325.72
Impact Speed (m/s)	7.69
Impact Energy (J)	147.41
Maximum Crush (mm)	6.81
Crush Volume (cm³)	50.55
Mismatch (cm)	5.60

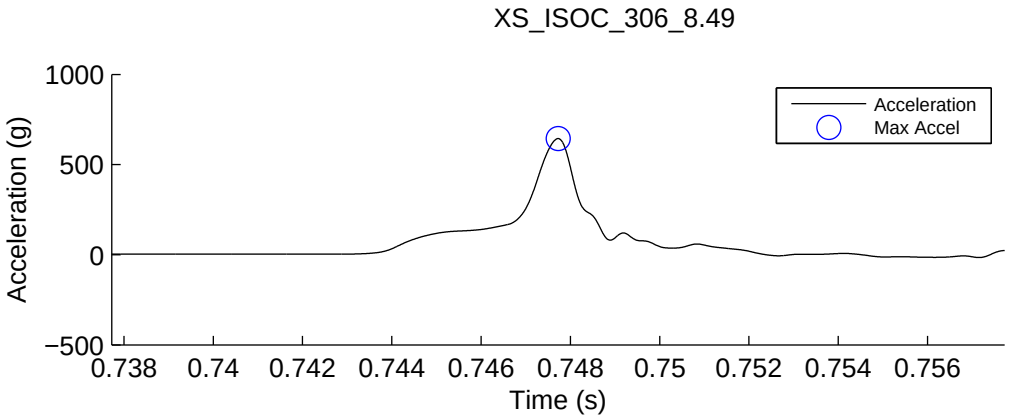

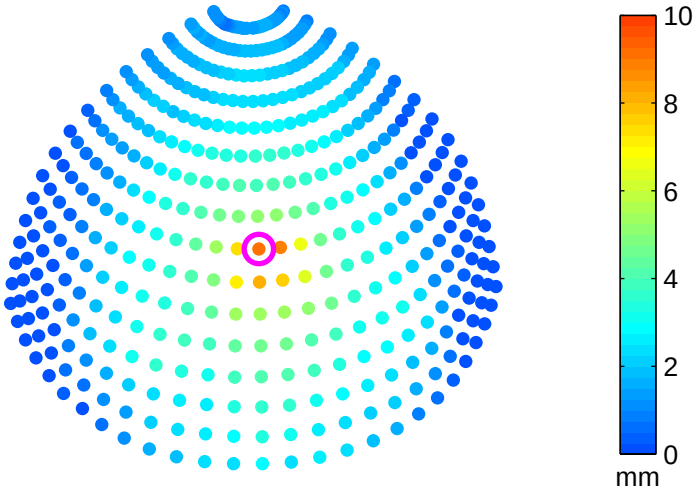

Max Resultant Accel (g)	644.13
HIC	6335.46
Impact Speed (m/s)	8.49
Impact Energy (J)	179.35
Maximum Crush (mm)	9.15
Crush Volume (cm³)	41.35
Mismatch (cm)	5.60

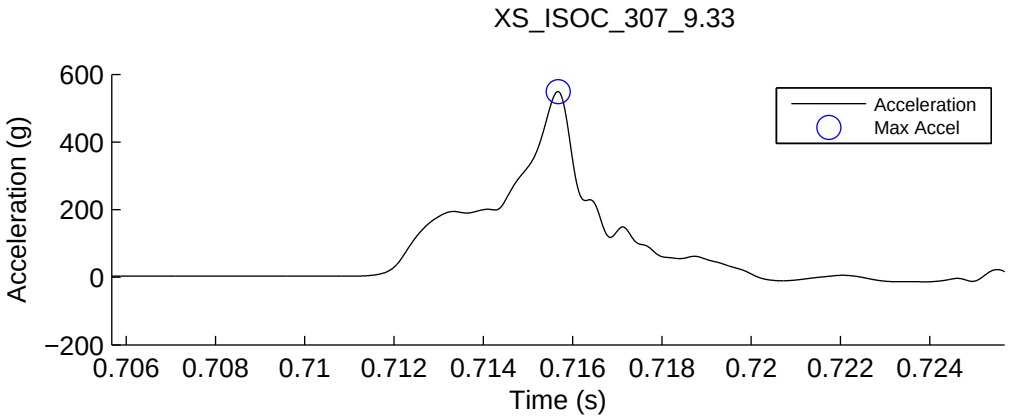

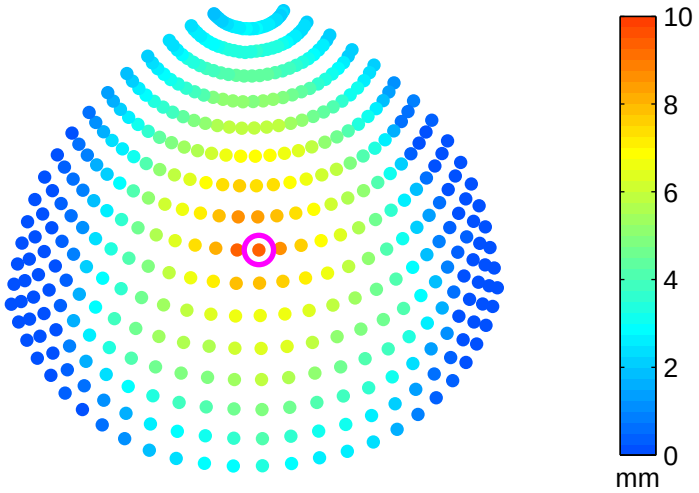

Max Resultant Accel (g)	549.27
HIC	4961.72
Impact Speed (m/s)	9.33
Impact Energy (J)	217.02
Maximum Crush (mm)	9.36
Crush Volume (cm³)	62.47
Mismatch (cm)	5.60

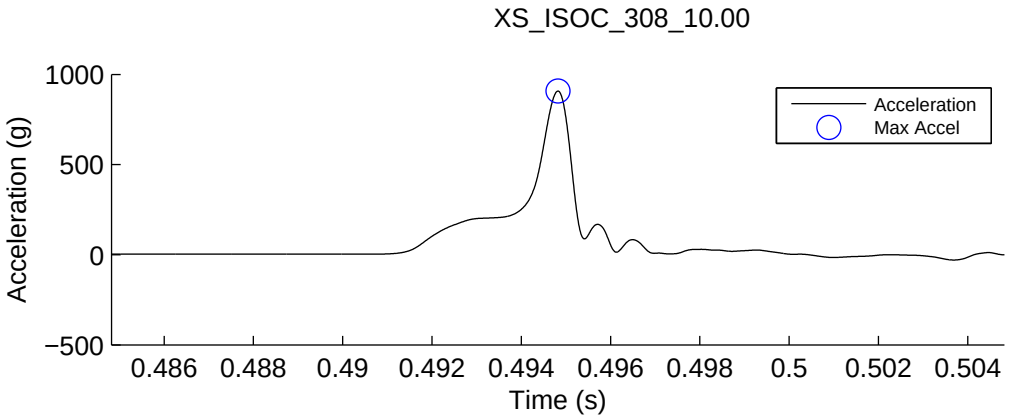

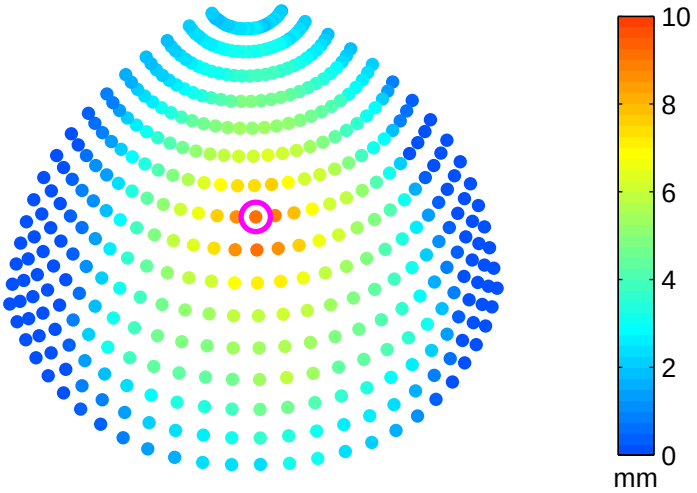

Max Resultant Accel (g)	907.62
HIC	11117.42
Impact Speed (m/s)	10.00
Impact Energy (J)	249.14
Maximum Crush (mm)	9.11
Crush Volume (cm³)	57.07
Mismatch (cm)	5.60

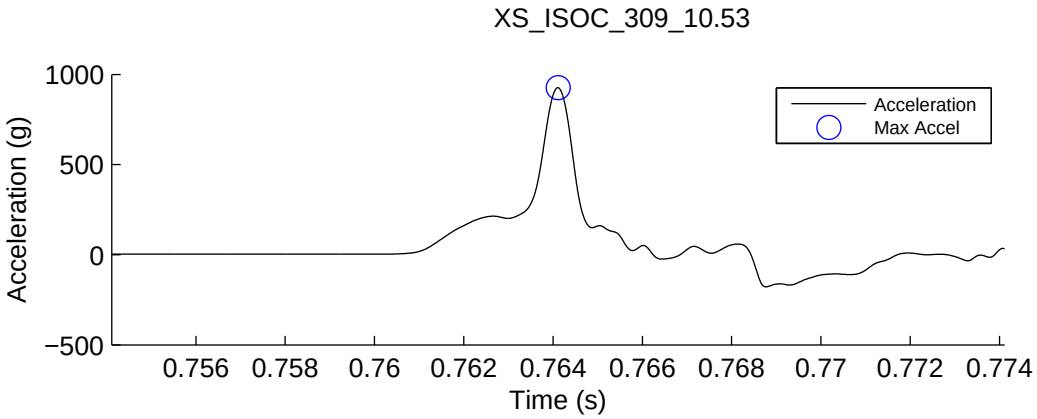

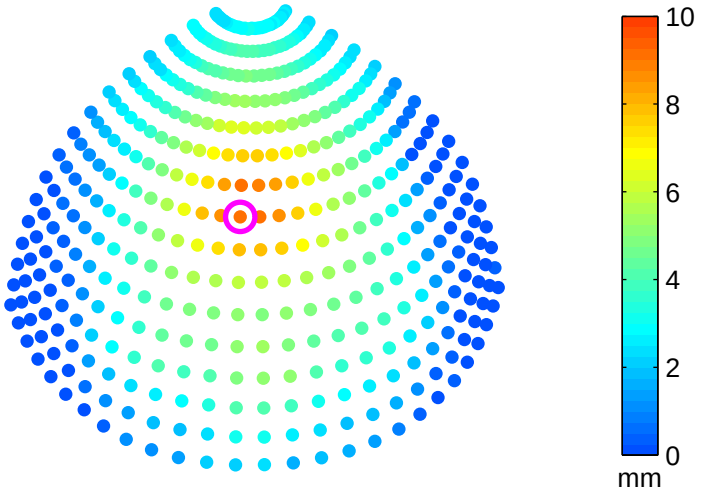

Max Resultant Accel (g)	926.31
HIC	12292.98
Impact Speed (m/s)	10.53
Impact Energy (J)	276.06
Maximum Crush (mm)	9.22
Crush Volume (cm³)	55.87
Mismatch (cm)	5.60

Appendix E

Appendix E1-E6 plots either peak acceleration (g), HIC, or impact speed (m/s) against either maximum crush depth (mm) or crush volume (cm^3). E7 plots peak acceleration (g) against impact speed (m/s) for Experiment B impacts. The headform size tested is indicated on the left side of each row and the helmet size tested is indicated at the top of each column. The right column includes data from each corresponding row and the bottom row includes data from each corresponding column. All data are included in the bottom right sub-plot. The difference between helmet and headform size (Δ) is indicated by the number in the upper left corner of the sub-plots. Dots indicate impacts that produced less than either 7.9 mm of maximum residual crush depth or 40 cm^3 of crush volume and x-marks indicated impacts that produced more than 7.9 mm of maximum residual crush depth or 40 cm^3 of crush volume. Dots and x-marks are separated by a vertical red line in the bottom right sub-plot. Crush levels are not distinguished in E7.

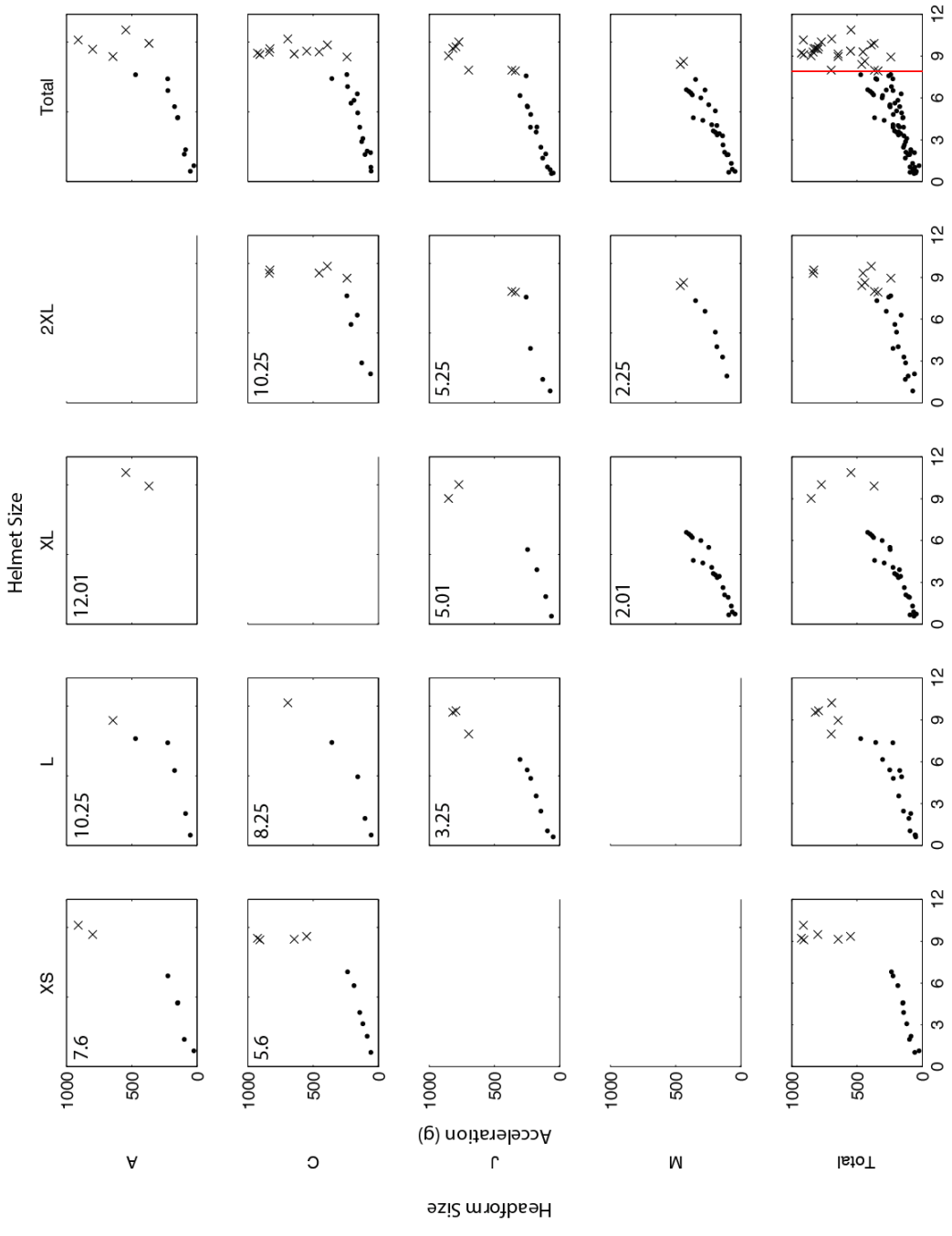

E1: Peak acceleration (g) vs. maximum crush (mm)

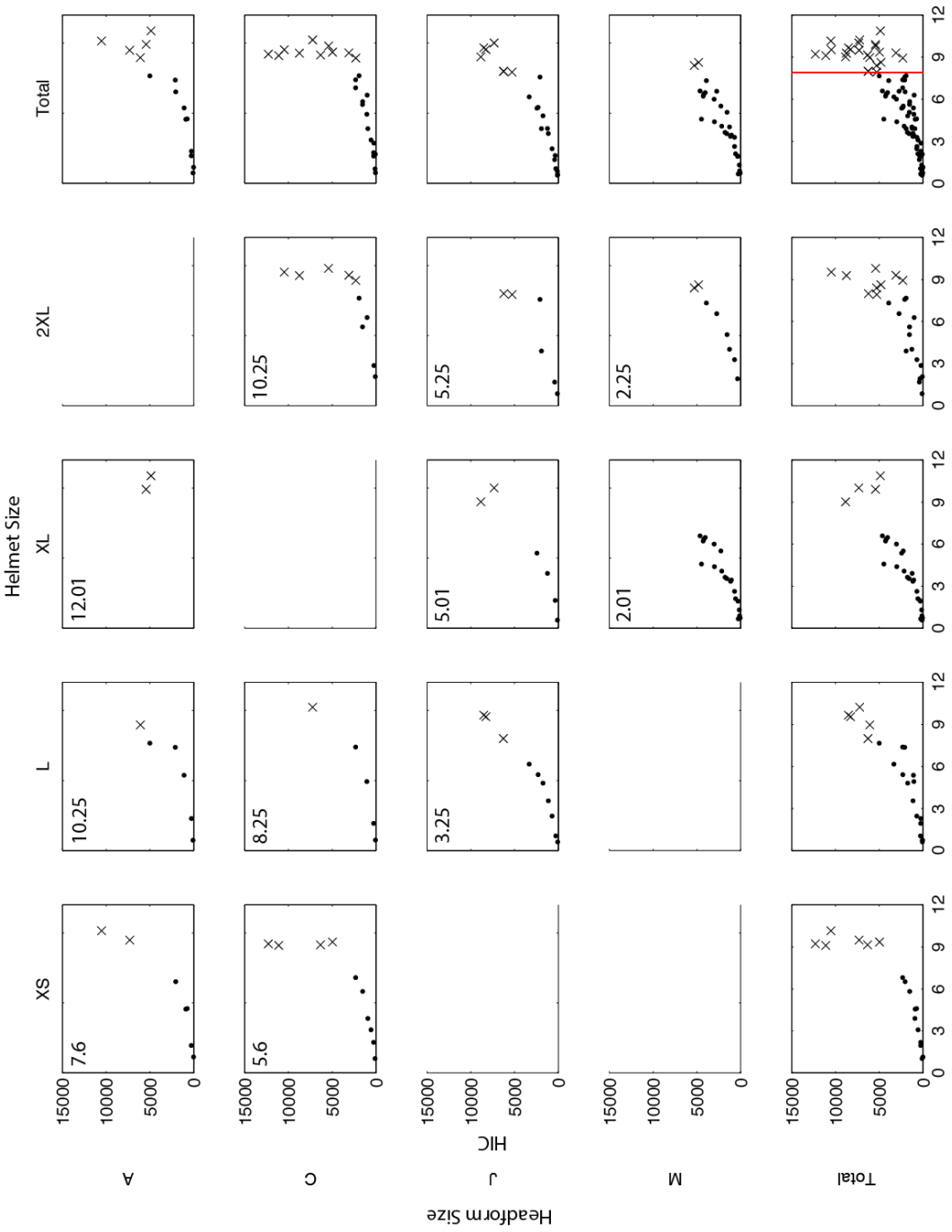

E2: HIC vs. maximum crush (mm)

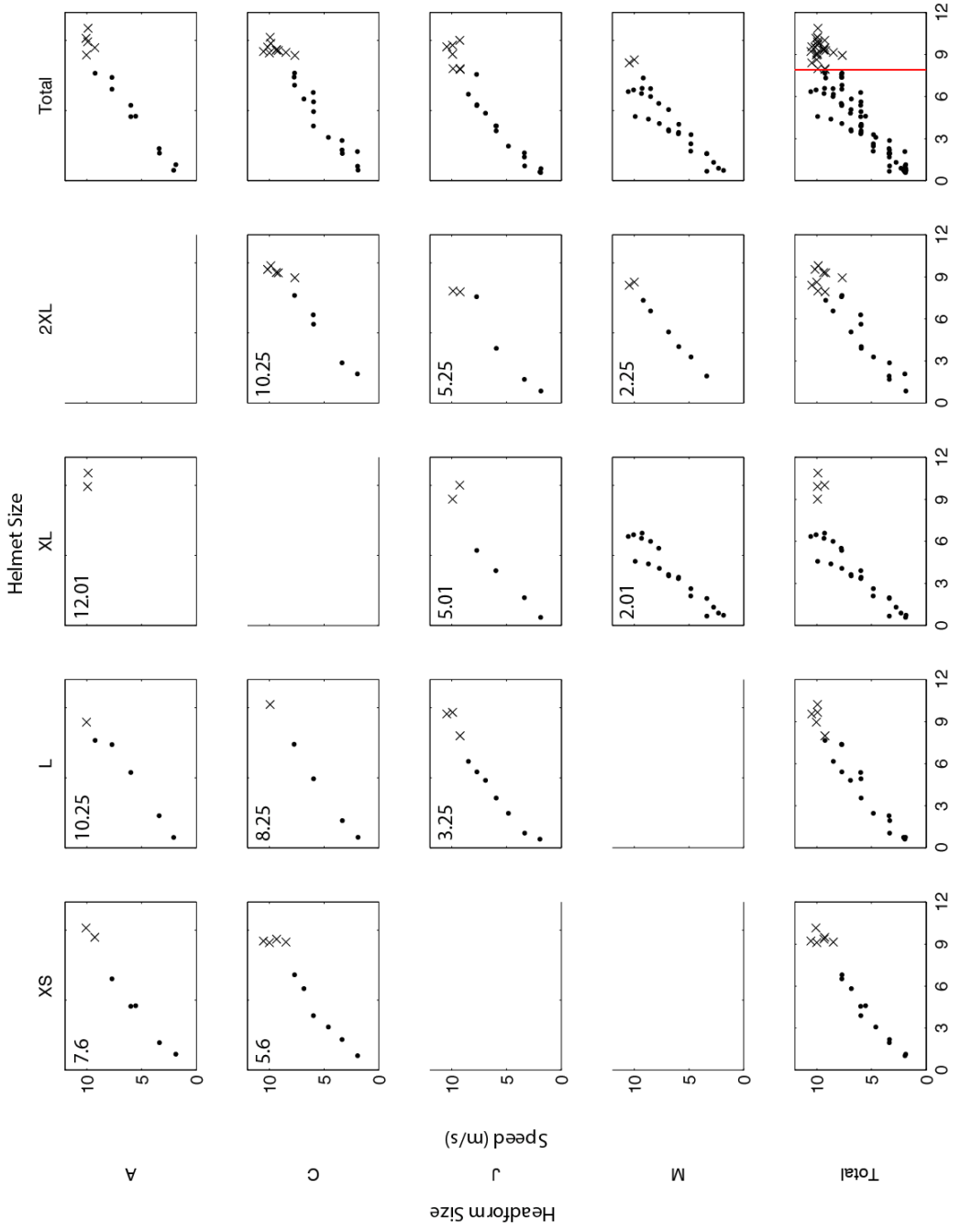

E3: Speed (m/s) vs. maximum crush (mm)

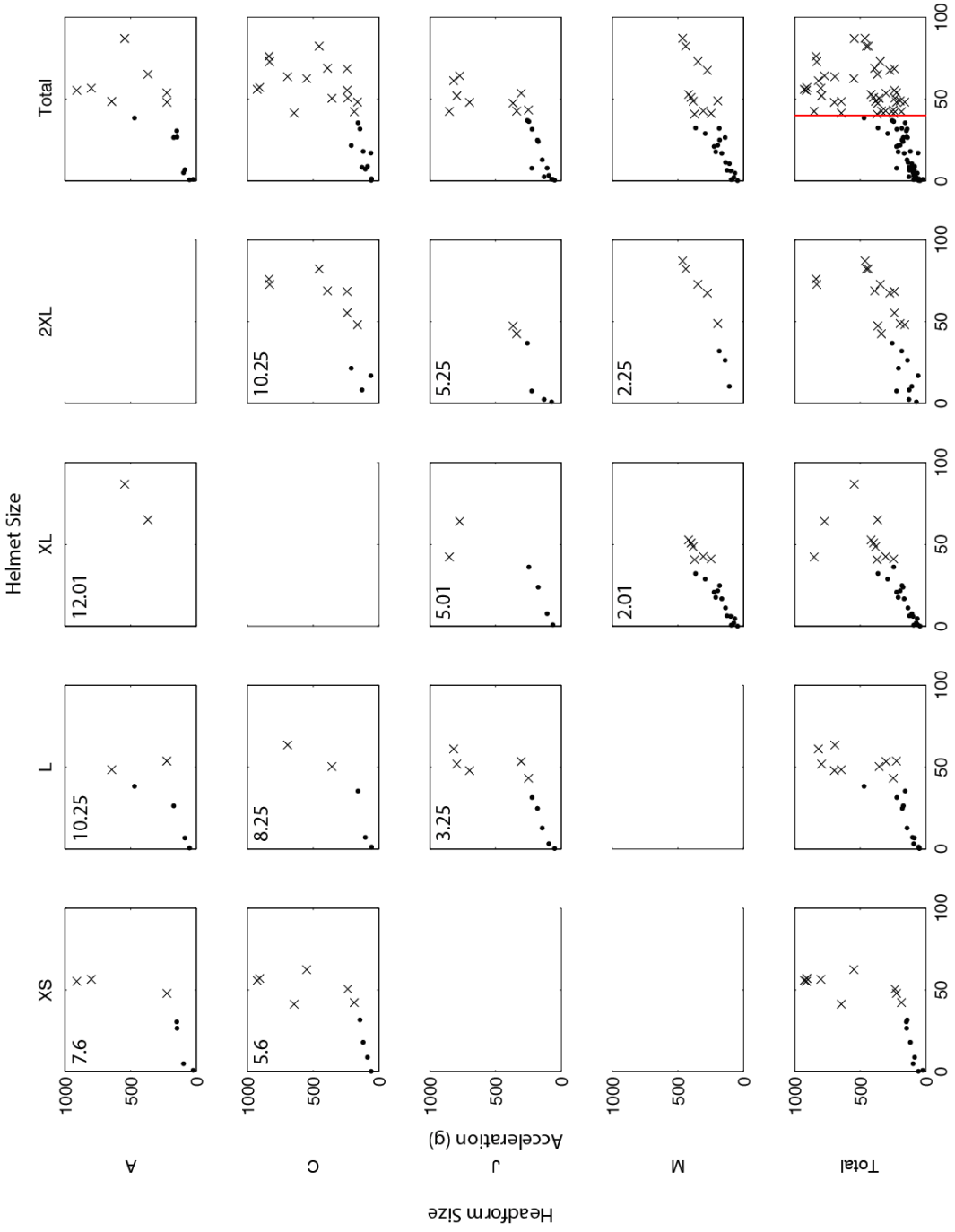

E4: Peak acceleration (g) vs. crush volume (cm^3)

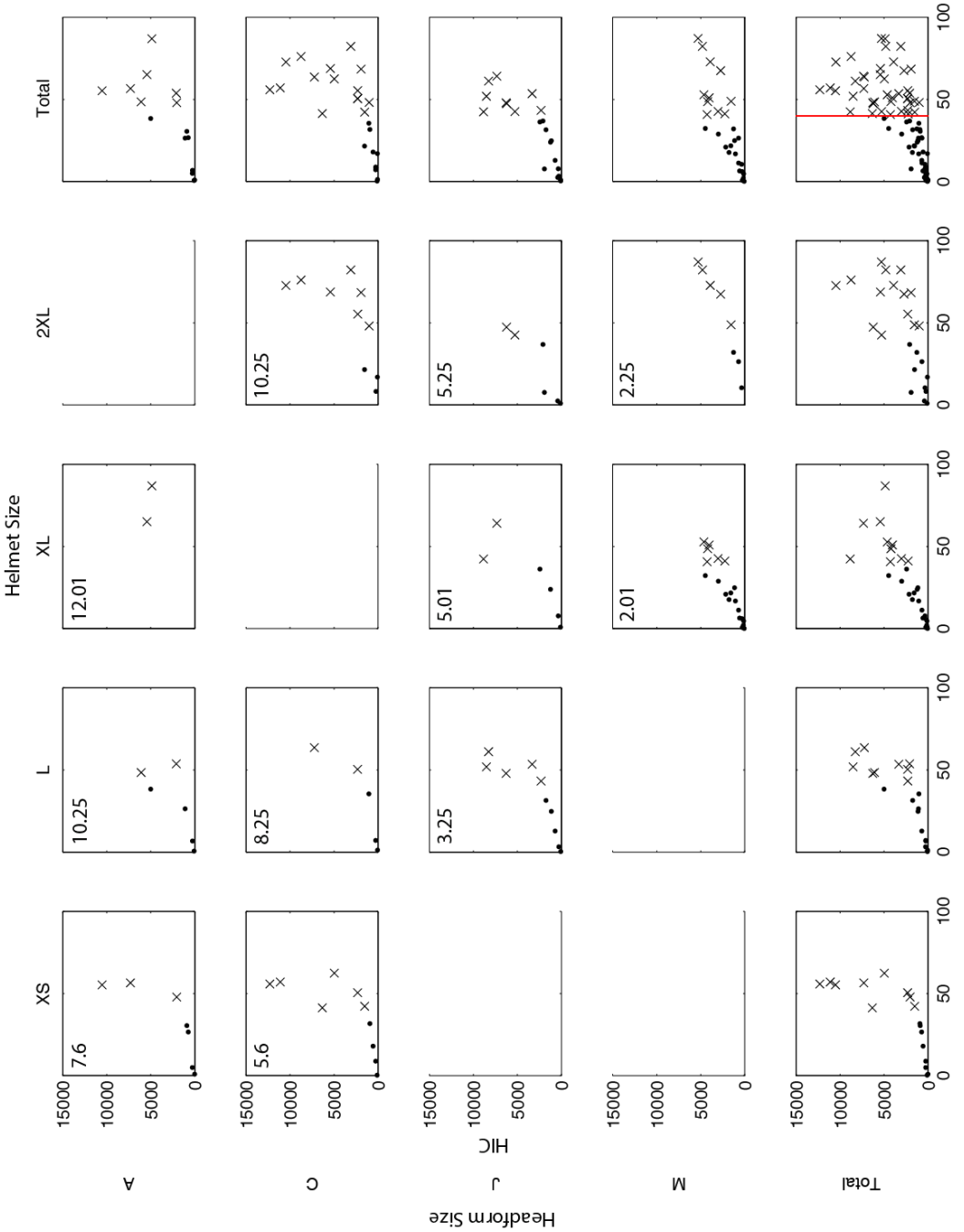

E5: HIC vs. crush volume (cm^3)

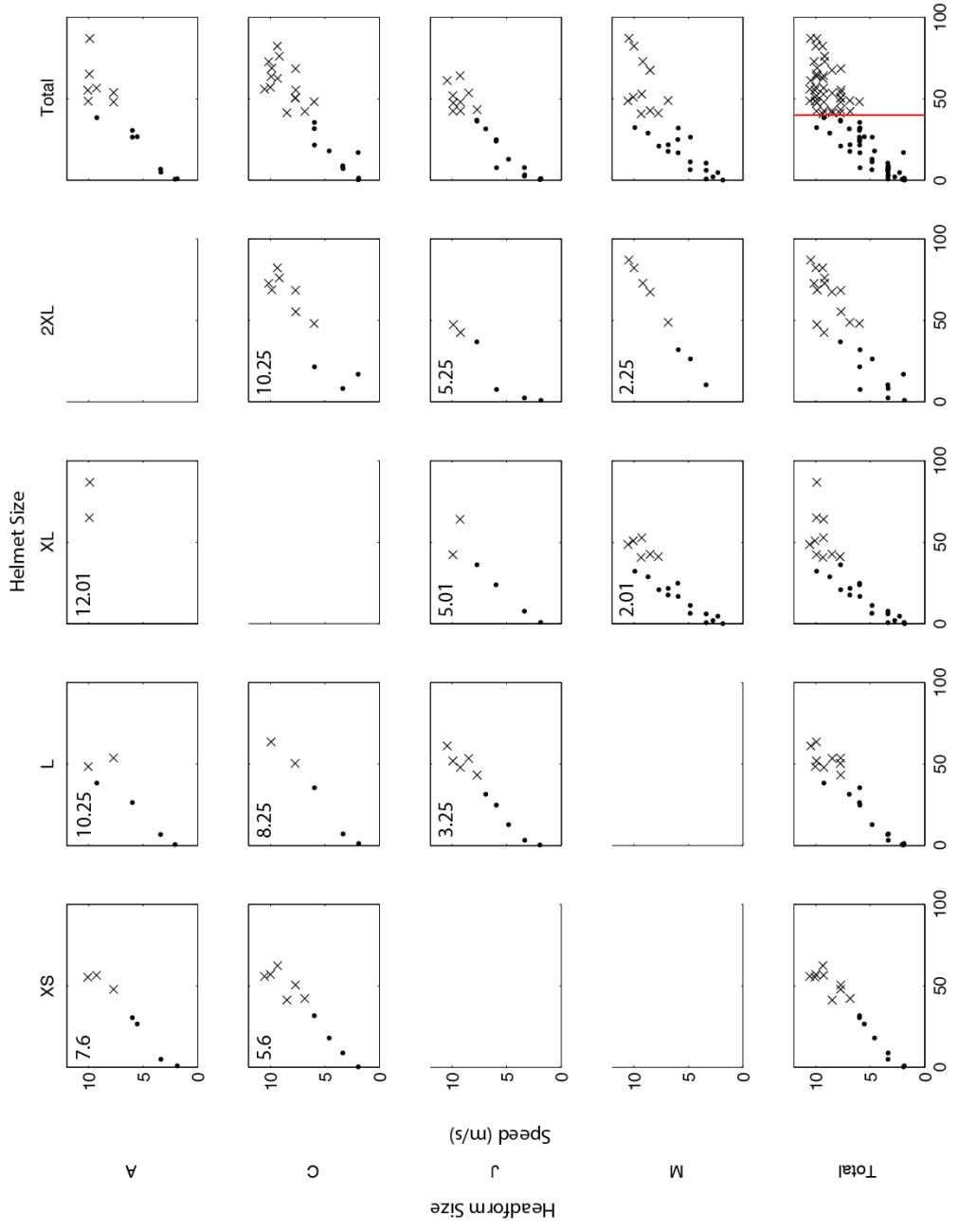

E6: Speed vs. crush volume (cm^3)

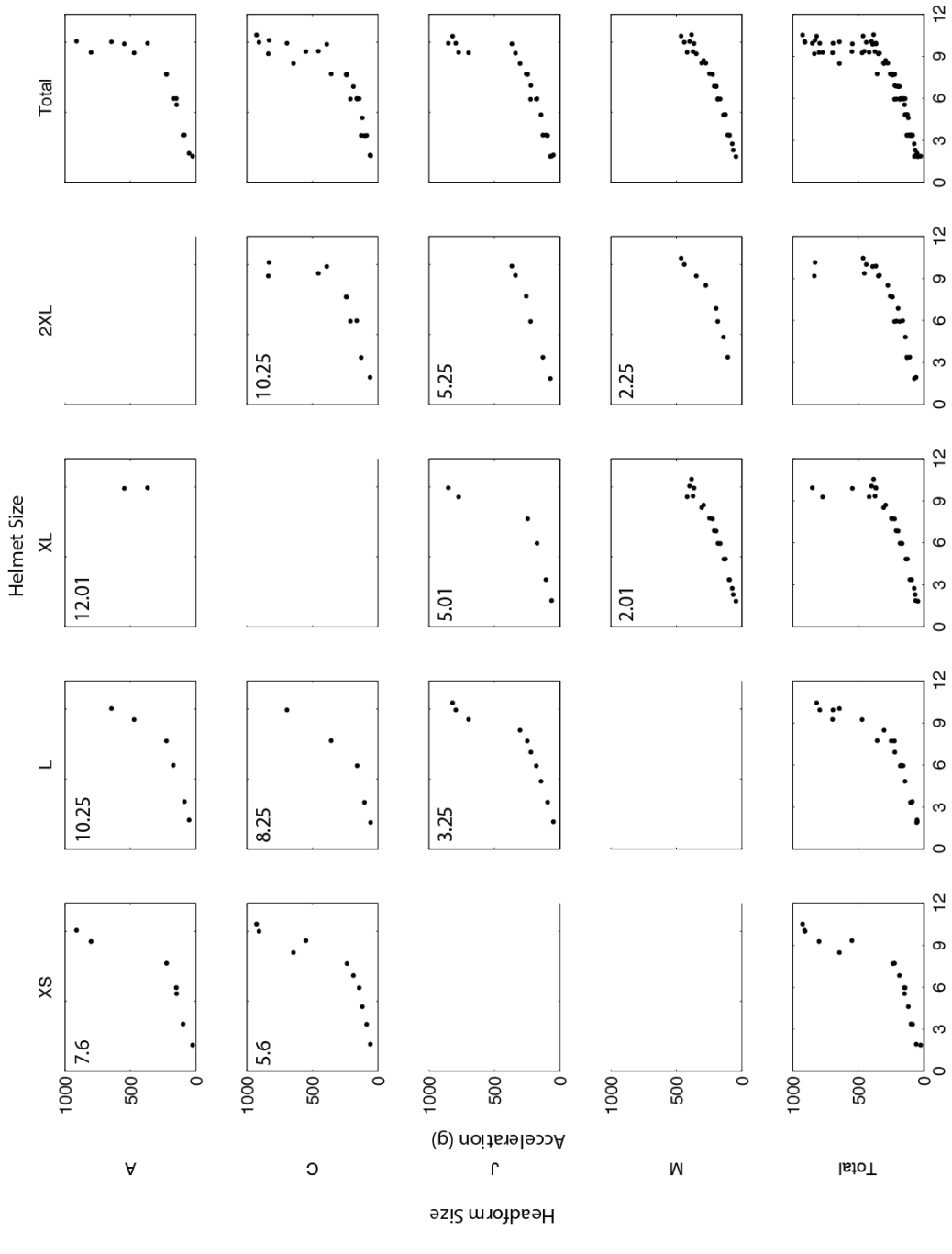

E7: Peak acceleration (g) vs. speed (m/s)